University of Southampton

Faculty of Engineering and Physical Sciences

Engineering Materials

Micro-mechanisms of fatigue and corrosion in a laser shock peened aerospace aluminium alloy

DOI [https://doi.org/10.5258/SOTON/T0030]

by

Alvaro Gonzalo Sanchez Araujo

ORCID ID 0000-0002-7246-7000

Thesis for the degree of Doctor of Philosophy

February 2021

I. Abstract

A laser shock peening treatment with ablative layer (LSP), and one without an ablative layer (LSPwC) were performed on AA7075-T651 (UNS A97075) to investigate their effects on the micro-mechanisms of fatigue, corrosion and fatigue of pre-corroded pits. Surface and microstructural characterisation techniques (micro-hardness, SEM-EBSD, contact-profilometry, incremental hole drilling, X-ray diffraction) showed the laser shock peening treatments generated high residual stress fields of up to –400 MPa, with LSPwC having 14% higher subsurface compressive residual stresses than LSP. Both showed limited hardness increase, with a limited surface roughness increase for LSP, and moderate for LSPwC. Fatigue testing showed a two-order magnitude increase in LSP AA7075-T651 overall life, due to the mechanism of crack initiation changing from surface second-phase particles to subsurface crack initiation dependent on the local stress field. Laser peening-induced defects in LSP (in some cases), and the surface roughness in LSPwC, were able to prevent AA7075-T651 from achieving maximum fatigue performance enhancement. This highlighted the importance of the interplay between surface features and residual stress on the micro-mechanism of crack initiation, and provided new insights into using this knowledge to maximise fatigue life extension. Modelling work by collaborators has used this experimental data to quantitatively evaluate the proposed mechanisms and is briefly reported in the discussion of the PhD results. LSP and LSPwC AA7075-T651 were also exposed to 3.5 wt.% sodium chloride solution under several electrochemical protocols (open-circuit potential, potentiodynamic sweep, galvanostatic control). The compressive residual stresses did not significantly affect the corrosion behaviour, corrosion pit morphology or pit depth. Additionally, laser shock peening-induced surface roughness was shown to have the most detrimental impact on corrosion performance. However, there was no clear indication of long-term changes in corrosion performance. The fatigue performance from pre-corroded pits in peened AA7075-T651 was also studied. It showed pits act as stress concentrations, causing cracks to initiate shortly after dynamic loading, reducing fatigue life by 50%. The laser shock peening treatments markedly increased fatigue life, by up to 400% compared to corroded untreated AA7075-T651, due to the residual stresses effectively counteracting the stress concentrations of the pits. Laser shock peened AA7075-T651, even after suffering subsequent pitting corrosion, can be expected to have fatigue performance as good as, or better than, standard untreated AA7075-T651.

II. Table of Contents

III. List of Figures

IV. List of Tables

V. List of equations

VI. List of accompanying materials

One portable storage hard drive containing all generated data and documents for this PhD thesis.

VII. Declaration of authorship

I, Alvaro Gonzalo Sanchez Araujo, declare that the thesis entitled:

Micro-mechanisms of fatigue and corrosion in a laser shock peened aerospace aluminium alloy

and the work presented in it are both my own, and have been generated by me as the result of my own original research. I confirm that:

- This work was done wholly or mainly while in candidature for a research degree at this University;
- Where any part of this thesis has previously been submitted for a degree or any other qualification at this University or any other institution, this has been clearly stated;
- Where I have consulted the published work of others, this is always clearly attributed;
- Where I have quoted from the work of others, the source is always given. With the exception of such quotations, this thesis is entirely my own work;
- I have acknowledged all main sources of help;
- Where the thesis is based on work done by myself jointly with others, I have made clear exactly what was done by others and what I have contributed myself;
- Parts of this work have been published as:

1. ‘Effects of laser shock peening on the mechanisms of fatigue short crack initiation and propagation of AA7075-T651’. International Journal of Fatigue. Accepted.
2. ‘Effect of ablative and non-ablative Laser Shock Peening on AA7075-T651 corrosion and fatigue performance’. NPJ Materials Degradation. Submitted.

Signed: Alvaro Gonzalo Sanchez Araujo

Date: 24/03/2021

VIII. Acknowledgements

I am very grateful to my supervisor Professor Philippa Reed for always being kind, patient, and supportive; and helping me achieve my PhD goals. Her dedication to her students, and their well-being, is admirable. I also want to thank my second supervisor Dr. Julian Wharton who had infinite patience answering my questions, as well as being available whenever I needed his support. I am also grateful to Dr. Domenico Furfari, and Airbus, for their sponsorship and technical feedback.

I would like to thank Professor Mike Fitzpatrick, Mitchell Leering, Dr. Daniel Glaser and Dr. Niall Smyth for their academic support and feedback, laboratory access and very importantly, laser shock peening my samples. I would also like to thank Dr. Shuncai Wang for his continuous support and help since supervising my IP project. I would like to mention Dr. Chao You, who through academic collaboration helped me strengthen my knowledge and understanding. Finally, I am grateful to Dr. Andrew Robinson and Dr. Terry Harvey for their laboratory help.

An invaluable part of the PhD experience was the friendship and support (both academically and personally) I had from my colleagues within and outside my research group. They made it a much more enjoyable journey. In no particular order I would like to thank Alex R., Chao, Marek, HRH the Duke Charlie, ‘is complicated’ Luis, angry Mike, Ara-dino, noob Angelos, el ‘che’ Diego, Anqi, Andreu, Stephen, Behrad, Kamran, crazy Som, Deepak ‘the electropolisher’, Corentin F.F., Antonio, Polo, Dan, Maruti 2.8, Maria T., Sebastian, Benito M., Song^2, Kim-Kim, and many others.

I would like to use this opportunity to express my deep gratitude and love for my wife and best friend Amy, who has always believed in me and supported me in every challenge I undertake. To my son Teo, who has added so much happiness to my life and, unaware, strongly motivated me to finish my thesis. To my in-laws David and Shirley, who have always made me feel welcome in their family.

Para mi querida madre Iracema, quien desde pequeño me ha dado amor y apoyo incondicional. Mi hermana Jimena quien siempre me ha hecho sentir que puedo lograrlo todo. Y mi abuela Elsa, mi segunda madre. Por último, para mi papá Teodoro, a quien extraño mucho, pero que siempre está conmigo, guiándome y empujándome a ser una mejor persona , como él.

IX. Nomenclature

2D	Two dimensional
3D	Three dimensional
2XXX	Two thousand series aluminium alloys
6XXX	Six thousand series aluminium alloys
7XXX	Seven thousand series aluminium alloys
BEI	Backscatter electron imaging
CSIR	Council for scientific and industrial research
CT	Computed tomography
EBSD	Electron backscatter diffraction
EDS	Energy dispersive spectroscopy
EPFM	Elastic-plastic fracture mechanics
HCF	High cycle fatigue
IGC	Intergranular corrosion
KAM	Kernel average misorientation
L	Longitudinal microstructural direction
LCF	Low cycle fatigue
LEFM	Linear elastic fracture mechanics
LSP	Ablative laser shock peening
LSPwC	Non-ablative laser shock peening
LT	Long transverse microstructural direction
NaCl	Sodium chloride
OCP	Open circuit potential
ORR	Oxygen reduction rate
PSB	Persistent slip band
SCC	Stress corrosion cracking
SEI	Secondary electron imaging
SEM	Scanning electron microscope
SiC	Silicon carbon grit paper
SR	Stress range
ST	Short transverse microstructural direction
XRD	X-ray diffraction

X. Terminology

ΔK	Stress intensity factor range
K_c	Critical stress intensity factor
K_{max}	Maximum stress intensity factor
K_{th}	Threshold stress intensity factor
da/dN	Crack growth vs number of cycles
E	Potential
E_{corr}	Corrosion potential
E'_{corr}	Corrosion potential of intermetallic
E_{pit}	Pitting potential
h	hours
Hv	Vickers hardness
j	current density
j_0	Exchange current density – equilibrium conditions
j_a	Anodic current density
j_c	Cathodic current density
keV	Kilo-electronvolt
$kg\text{-}f$	kilogram force
η	Strengthening precipitate $MgZn_2$
η_p	anodic polarisation
P_a	Mean primary profile
P_q	Root mean primary profile
P_z	Mean primary profile depth
R_a	Mean roughness
R_q	Root mean square roughness
R_{sk}	Skewness
R_t	Maximum roughness depth
R_v	Maximum valley height
R_z	Mean roughness depth
W_a	Mean waviness
W_q	Root mean waviness
W_z	Mean waviness depth
s	seconds
S_1	Compressive residual stress measurement direction parallel to L

S_3	Compressive residual stress measurement direction parallel to LT
$N_{R=0.1}$	Number of fatigue cycles in 0.1 load ratio
$N_{R=0.1}$	Number of fatigue cycles in 0.5 load ratio
N_{Total}	Total number of fatigue cycles

1 Introduction

1.1 Application background

According to a report by the Research and Technology Organisation (RTO) and the North Atlantic Treaty Organisation (NATO), all forms of corrosion and the interplay between fatigue and corrosion is a field of intense interest and research due to high repair and maintenance costs of their ageing aircraft [1].

The challenges from corrosion and fatigue degradation of aerospace aluminium alloys in-service parts are also present in commercial aircraft. According to the U.S. Department of Transport Federal Aviation Authority [2], localised corrosion nucleating at constituent particles in highly stressed areas of aluminium alloy parts cause clusters of fatigue inducing pits, which can reduce the fatigue life of an in-service part by a factor of ten. Consequently, localised corrosion is deemed a principal contributor to the early onset of multisite fatigue damage and this has an impact on structural integrity and thus flight safety of aircraft [2].

The aerospace industry is developing new technologies to improve the performance of their materials, to produce new longer-life aircraft parts or to extend in-service life through repair of old parts. One type of technology is surface treatment, widely used in engineering applications for the improvement of mechanical performance, most notably fatigue life.

Laser shock peening, or laser peening, is a relatively new form of mechanical surface treatment. It is similar to shot peening in terms of objective: Imparting beneficial compressive residual stresses to the surface and near surface of the material. Unlike shot peening, laser peening uses high power laser pulses to ionise the surface into a high pressure plasma within a transparent inertial confinement medium (typically water). The confined plasma generates a Giga Pascal (GPa) magnitude pressure, which transmits shock waves into the metal surface, causing constrained localised surface and subsurface plastic deformation, generating compressive residual stresses [3][4][5]. The manufacturing benefits of using laser peening over shot peening are the accuracy and precision it allows [3][6][7], improvements in the maximum level and depth of compressive residual stress achieved subsurface [3][6], beneficial decrease in detrimental surface modification and improvement in fatigue life in comparison to shot peening [3][8][9]. Therefore, laser peening is now an up and coming technology that is continually expanding in use in aerospace and other industries.

Aluminium alloys are used extensively in the aerospace industry and, naturally, laser peening is seen as a promising method for improving fatigue life of aerospace aluminium components [3]. However, there is limited research on the extent to which surface modification (roughness, hardness) and the level of laser peening residual stress, respectively, contribute to the overall fatigue life improvement, and how each of these influence possible changes in micro-mechanisms of crack initiation and propagation in aluminium alloys after laser peening. In addition, considering the susceptibility and exposure of aluminium alloys to corrosive environments in the aerospace industry [1], and the increased use of laser peening for fatigue improvement of aerospace components, it raises the question whether laser peening has an effect on corrosion performance of which users may not be fully aware. Thus, as laser shock peening has become more attractive, further research is being performed to replace the empirically led application of laser peening techniques developed by industry, to add a deeper understanding of how a material's microstructure, mechanical and corrosion properties are affected by this surface treatment [10].

1.2 Research focus area

Airbus currently employs laser shock peening as a surface treatment for airframe components manufactured from aluminium alloys. Aluminium alloys have lower strength and stiffness than other materials that are routinely peened. There is extensive work being performed to better understand the effects of laser shock peening in aluminium alloys and to understand how laser peening develops the level and distribution of residual stress without excessive reverse yielding that may lead to zero or low compressive stress at the surface. In addition, Airbus is interested in investigating the microstructural effects and surface modification of laser shock peening on aerospace aluminium alloys. Gaining a deeper understanding of how the interplay between these and the generated compressive residual stresses will affect the micro-mechanisms of fatigue crack initiation and propagation is necessary, enabling prediction of the effects on corrosion and corrosion with mechanical stimuli.

Airbus, Coventry University and the University of Southampton agreed a joint PhD collaboration programme to study the effects of laser shock peening on aluminium alloys used for aerospace applications. Coventry University focused on the development of ablative layers and the optimisation of laser parameters to improve the effectiveness of laser peening optimisation. The University of Southampton focussed on the effects of laser shock peening on the material's surface and microstructure, and how this may change its fatigue and corrosion micro-mechanisms and performance.

1.3 Aims and objectives

The aim of this study was to perform a representative laser shock peening on an aerospace grade 7XXX aluminium alloy to study its effects on the micro-mechanisms of fatigue crack initiation and propagation and corrosion behaviour.

The initial objectives were as follows:

- To understand how, and to what extent, the LSP and LSPwC generated residual stress, and the modified surface (hardness and roughness), will each influence changes in the micro-mechanisms of short crack fatigue initiation and growth in an aerospace grade 7XXX aluminium alloy.
- To understand to what extent the laser shock peening generated residual stresses and the modified surface (microstructure, hardness and roughness) influence the 7XXX aluminium alloy's electrochemical properties, corrosion pit formation and corrosion performance.
- To investigate how laser shock peening affects the mechanisms of crack initiation and growth from corrosion features in a laser peened 7XXX alloy.

A detailed review of the established knowledge of 7XXX series alloys, laser shock peening and relevant fatigue and corrosion research, has been performed with the aim of identifying knowledge gaps or opportunities for further study. Based on the literature survey, this PhD project's objectives are further reviewed and enhanced, to ensure the project aim is achieved in the available time and, more importantly, delivers concrete new findings that add novelty to the field of study.

2 Literature review

2.1 Introduction

The microstructure of a material is inexorably linked to its fatigue and corrosion behaviour. Thus, having a deep understanding of the project relevant 7XXX family of aluminium alloys is necessary. This will then lead to a detailed exploration of the micro-mechanisms of fatigue crack initiation and propagation, and corrosion feature development of the aforementioned alloy family. Deep understanding of the untreated material behaviour will be vital to subsequently identify any material modifications and altered performance by laser shock peening. Naturally, laser shock peening, as a technology, is explored in detail. A literature survey is performed to understand the development of laser peening, the peening parameters used, and the available literature on its effects on aluminium alloys. As this is a high energy surface treatment that plastically deforms a material, it is expected to affect both the alloy's microstructure and surface state, as well as generate a desired compressive residual stress field. Thus, there will be a focus on effects of laser peening surface modification, microstructure modification and residual stress field generation on fatigue and corrosion.

The following literature review assumes the reader has a basic understanding of wrought metal manufacture, aluminium alloys, fatigue theory and corrosion theory. Appendices with further information, particularly on fundamental theory, are available for further reading if required.

2.2 Aluminium alloys

Aluminium alloys are classified according to their mode of manufacture, and can be separated into wrought alloys and cast alloys. Eighty five percent (85%) of aluminium is used for wrought alloy products [11]. These alloys are produced from cast ingots and then changed by mechanical working operations and thermal treatment. This PhD project involves working with wrought alloys only, and therefore cast alloys are not discussed any further. Wrought alloys by themselves comprise a considerable number of alloy families and require careful designation to help engineers identify each alloy by their composition and mode of fabrication, and therefore their properties, allowing the selection of an appropriate alloy for the required application.

2.2.1 Wrought aluminium alloys

The international Alloy Designation System (IADS) is used to classify aluminium and aluminium alloys. For wrought aluminium alloys IADS gives a four digit number to the alloy, of which the first number is based on the major alloying element(s) [11][12]. The following series are shown in Table 2-1:

Table 2-1 – IADS aluminium alloy classification

Aluminium Alloy Series	Main Alloying Element
1XXX	Pure aluminium (>99%)
2XXX	Copper
3XXX	Manganese
4XXX	Silicon
5XXX	Magnesium
6XXX	Magnesium and silicon
7XXX	Zinc and magnesium
8XXX	Miscellaneous

This system deals separately with heat and non-heat treatable alloys. In the case of heat treatable alloys, all tempers are denoted either by the letter O, or more commonly by the letter T. This is followed by one or more digits that further specify the heat treatment method used to make the alloy, as show in Table 2-2 [11][12][13]:

Table 2-2 - IADS Aluminium alloy temper designation

Suffix letter	Condition
F	As fabricated
O	Annealed wrought products only
H	Cold-worked (strain hardened)
T	Heat treated (stable)

Of particular use to the aerospace industry are the precipitation hardenable 2XXX, 6XXX and 7XXX series alloys. Their high strength-to-weight ratio, lower fatigue sensitivity, higher damage tolerance and heat resistance, compared to other metals, has helped the industry fly faster, longer and with lower fuel consumption.

2.3 Aerospace aluminium alloys

2.3.1 2XXX series alloys

Together with the 7XXX alloys these are the most widely used in aerospace components. The first alloy family to be used for aircraft, 2XXX alloys have been generally favoured over 7XXX alloys when damage tolerance is required [14]. This alloy family has copper as the main alloying elements for precipitation strengthening, with common tempers being T3, T4 and T8. Several alloys are still used for aerospace including 2219, 2024-T62, 2024-T4, 2324-T39, 2524-T3, among many others [11]. Common applications are fuselage skins, lower wing covers, fuselage panels, aircraft bulkheads, etc. [14][15]. As these alloys contain copper, they can suffer from localised corrosion and stress corrosion cracking (particularly 2024-T3) [16][14]. This includes intergranular corrosion due to preferential dissolution at the precipitate free zone near the more cathodic (containing Al_2Cu) grain boundaries [17]. Similarly to 7XXX, the 2XXX alloy family can suffer from intergranular corrosion that can evolve into exfoliation corrosion due to elongated microstructure of cold worked alloys [17]. Thus, many applications of 2XXX alloys require cladding to provide corrosion protection.

2.3.2 6XXX series alloys

Al-Mg-Si alloys, are intermediate strength materials that have good weldability and have better corrosion performance, particularly stress corrosion cracking, than 2XXX and 7XXX alloys [17][16]. Their main alloying elements are Mg and Si, and the main precipitation strengthening particles is Mg_2Si. Although their use in aerospace is considerably lower than that of 2XXX and 7XXX alloys, there are several alloys used, including 6063, 6463, 6061,

6082-T6. In terms of applications, they are commonly used for architectural and decorative finishes, and used predominately in the form of extrusions and structural components such as angles, beams and tubes. Figure 2-1 compares yield, ultimate and fatigue strength against other common 2XXX and 7XXX alloys.

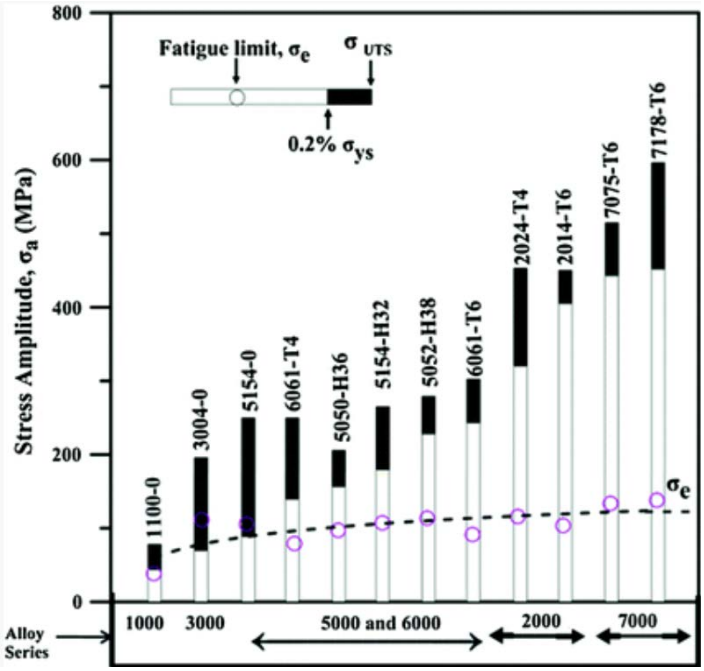

Figure 2-1 – Yield strength, ultimate strength and fatigue limit of some aluminium alloys (Rambabu et al., 2017) [15].

2.3.3 7XXX series alloys

Amongst the precipitation hardenable alloys, the 7XXX series alloys have been extensively used and studied due to their high strength [18]. They are used widely in airframe structures, mobile equipment and other highly stressed parts. Historically, the first 7XXX series alloys only had zinc (Zn) and magnesium (Mg) as their main alloying elements. These aluminium alloys became particularly interesting to engineers due to their enhanced ability to respond to age hardening in comparison to other aluminium alloys, and being readily weldable. However, they were also found to be susceptible to stress corrosion cracking (SCC) [11]. As new 7XXX alloys were created, small quantities of copper (Cu) were added to the Al-Zn-Mg system alloys, which gave an improved resistance to stress corrosion cracking. These Al-Zn-Mg-Cu alloys have received special attention due to their even greater response to age hardening compared to previous Al-Zn-Mg system alloys [18][11][19]. Figure 2-2 shows the relationship between some of the more commonly used 7XXX series alloys.

Despite the relative SCC improvement by the addition of copper, Al-Zn-Mg-Cu 7XXX alloys are still susceptible to stress corrosion cracking and localised corrosion [11][20]. These limitations are counterweighed by their high strength to weight ratio, and are therefore of great importance to the aerospace industry. Thus, many 7XXX alloys are approved for use in the construction of civil and military aircraft.

There are a variety of 7XXX aluminium alloys currently used for aerospace applications. This include AA7075, AA7050, AA7010, AA7150, AA7085, AA7475, etc. and commonly in peak and over-aged tempers. Table 2-3 details some actual and proposed uses of conventional 7XXX aluminium alloys in aerospace applications [15]. One of the oldest and most used alloys throughout the last 80 years is AA7075. Consequently, there is a breadth and depth of research and industrial data on this particular alloy, particularly of the T6 and T651 temper. Although these specific tempers have to a certain degree fallen out of a favour in aerospace (replaced by overaged tempers) it is one of the most well-established alloys and is often used as a benchmark.

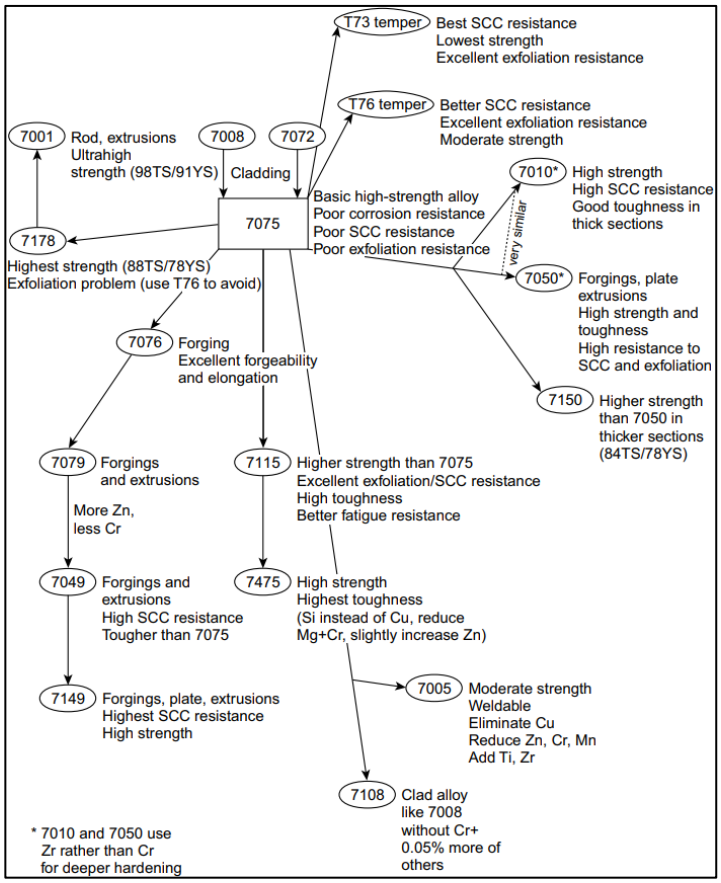

Figure 2-2 – Relationships among commonly used 7XXX series alloys. Tensile strength (TS) and yield strength (YS) are in ksi units (Davis, 2001) [19].

Table 2-3 – 7XXX aluminium alloy aerospace applications.

Product	Strength levels	Alloy/temper	Applications
Plate	Medium strength	7050-T7451, 7X75-T7XXX	Internal fuselage structures
	High strength	7150-T7751, 7055-T7751, 7055-T7951, 7255-T7951	Upper wing covers
	Medium strength	7050-T7451	Spars, ribs, other internal structures
Forgings	High strength	7175-T7351, 7050-T7452	Wing/fuselage attachments
Extrusions	Medium/high strength	7075-T73511, 7075-T79511, 7150-T6511, 7175-T79511, 7055-T77511, 7055-T79511	Fuselage stringers and frames, upper wing stringers, floor beams, seat rails

2.3.3.1 AA7075-T651

AA7075 is an Al-Zn-Mg-Cu alloy developed in the early 1940s as a high strength alternative to 2XXX series alloys [15][14]. The T6 and T651 tempers have been extensively used in both civil and military aircraft [14]. However, as early as 1954 the low damage tolerance of AA7075-T6 was made evident by the infamous Comet jet crashes caused by premature fatigue failure due to stress concentrations at fuselage windows [14]. This led to the decrease of 7XXX alloys for high tension applications and reintroduction of some 2XXX alloys for these specific applications. Furthermore, 7075-T6 showed to be susceptible to SCC in the short transverse direction, particularly in thick products, due to its microstructure [14]. New over-aging tempers were used to solve this problem at the cost of lowering strength. A subsequently developed temper, T77, was able to provide corrosion resistance without sacrificing strength. However, other alloys with some compositional modifications, were developed to improve SCC and fracture toughness. Examples of these are 7050, 7150 and 7055 [21]. Despite these newer alloys, 7075, including its T6 and T651 tempers, remains a benchmark alloy, and has a good balance of properties required for aerospace applications [22]. Therefore it is a good candidate for research studies involving new technologies. Benchmarking to a well-studied, highly-characterised baseline material is ideal for identifying the material modifications and performance variations introduced by the new technology. The remainder of the literature review is on 7XXX alloys with a focus on AA7075-T651, as the selected alloy for this project.

According to the IADS, the T6 temper defined as solution and artificial ageing. AA7075-T6 is tempered after solution treatment, at temperatures near 120°C for 12 to 24 hours, to obtain maximum strength and good ductility (peak-aged alloy) [23]. A T651 temper differs only slightly from a T6 temper in that it is solution heat-treated, stress-relieved by stretching and then artificially aged. In essence, T651 is an alloy which has been tempered to a T6 designation, and stretched 1-3% to relieve residual stresses [23]. Both of these tempers tend to be considered the same in terms of mechanical properties and their use in components. ASM International, and all aluminium alloy suppliers reviewed, list mechanical and other properties of AA7075-T6 and AA7075-T651, as the same [24].
Table 2-4 shows the chemical composition of AA7075. Whereas Table 2-5 shows a selection of mechanical properties taken from the open literature.

Table 2-4 – AA075-T651 alloy composition [25].

Element	Composition limits (% weight)
Copper	1.20 to 2.0
Magnesium	2.1 to 2.9
Manganese	Maximum of 0.30
Silicon	Maximum of 0.40
Iron	Maximum of 0.50
Chromium	0.18 to 0.28
Zinc	5.1 to 6.1
Titanium	Maximum of 0.20
Zirconium	NA
Any other	Maximum of 0.05
Others (total)	Maximum of 0.15

Table 2-5 - Mechanical properties of relevant 7075-T651 [26].

Property	***Values***
Density / $g \cdot cm^{-3}$	2.81
Hardness, Vickers / $kg\text{-}f \cdot mm^{-2}$	175
Ultimate Tensile Strength / MPa	572
Tensile Yield Strength / MPa	503
Elongation at Break / %	11
Modulus of Elasticity / GPa	71.7
Poisson's Ratio	0.33
Fatigue Strength (5×10^8 cycles, fully reversed loading) / MPa	159
Fracture Toughness (K_{Ic} in ST-L direction) / $MPa \cdot m^{1/2}$	20
Fracture Toughness (K_{Ic} in LT-L direction) / $MPa \cdot m^{1/2}$	25
Fracture Toughness (K_{Ic} in L-LT direction) / $MPa \cdot m^{1/2}$	29

2.4 7XXX series alloy microstructure

As 7XXX series alloys are precipitation strengthened the manufacturing steps are important in the development of the microstructure and therefore their fatigue and corrosion properties. Figure 2-3 shows the common steps performed for manufacturing 7XXX series alloys. A more detailed explanation of the manufacturing steps can be found in the appendix in section 9.1.1.1.

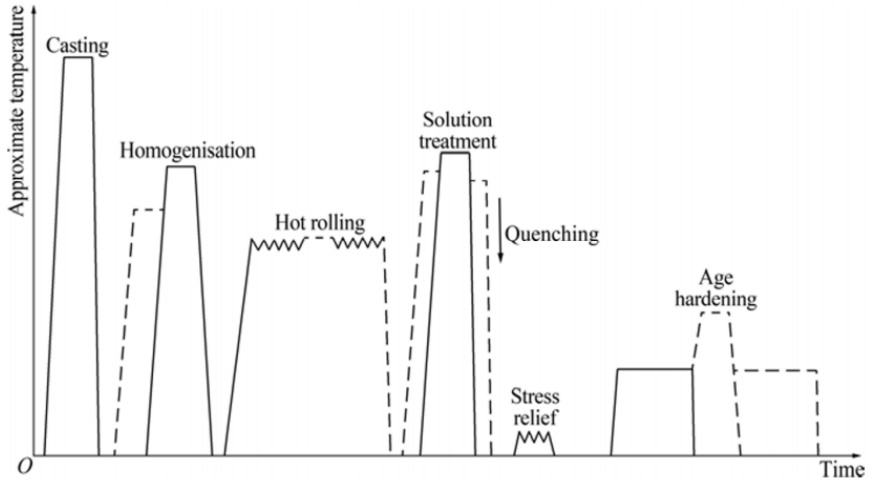

Figure 2-3 – Schematic of common 7XXX alloy manufacturing steps (Rometsch et al., 2014) [27].

Due to the manufacturing of 7XXX alloys, in particular hot rolling, it is common to identify the different orientations in the microstructure in terms of the longitudinal rolling direction. This direction is usually labelled as 'L' and the other orientations, which are at 90° to the L direction, are labelled as long transverse (LT, or sometimes T) and short transverse (ST, or sometimes S). Figure 2-4 and Figure 2-5 show examples of open literature images with one or more labelled directions. Figure 2-6 is a schematic of AA7075 microstructural planes according to labelled directions [28][29][30].

The manufacturing process will affect the grain structure. Hot rolling, extrusion and forging can affect grain size and shape by deforming grains and nucleating and growing recrystallised grains. For example, in a 100 mm thick extruded AA7150-T6 alloy Fan et al. [31] found mostly uncrystallised large grains in the middle (T/2) of the LS plane and, in contrast, many small recrystallised grains near the extruded surface. This variation in grain structure with plate depth can be an important variable in considering aluminium plate performance in components.

Manufacturing processes such as rolling tend to create anisotropic grain structures in 7XXX alloys, where grains tend to elongate in the rolling direction, becoming relatively wide in the long-transverse direction, and short in the short transverse direction. This type of grain shape is often called pancake shaped (see Figure 2-4 and Figure 2-5). The grain size can vary from 100µms to 10µms in size depending on the microstructural plane. It is very common for grains in the rolling or extruded direction to be in the 100µms. Despite there being large uncrystallised grains there are many small recrystallised grains giving a microstructure with a large grain size variation. Thus, studies of 7XXX alloys, such as AA7075 and AA7150, report typical microstructures with large quantities of uncrystallised grains, some small recrystallised grains which are highly anisotropic with elongated pancake shaped grains [32][28][33][34]. This can sometimes be difficult to quantify simply, with average grain sizes and ranges quoted depending on the characterisation technique used. One relatively straight-forward method uses linear intercept measurements (which intrinsically capture an average of several mean grain size determinations rather than the full range of grain sizes). This method relies on microscopy and visual observation and thus can be subjective. There are other more precise, but more work intensive, approaches to measure grain size variation such as the commonly used electron backscatter diffraction (EBSD). This method does not depend on visual observation and thus is more objective and avoids user bias. Consequently, the differing methods available means different studies have reported different grain sizes for nominally the same alloy heat treatment. Harrison et al. performed a qualitative assessment of the grain structure of AA7075-T6 sheet and an AA7057-T651 extrusion via visual inspection using optical microscopy. The AA7075-T651 mean grain dimensions were 13 µm × 8.3 µm × 2.8 µm; and AA7075-T6 mean grain dimensions as 79.9 µm × 59.7 µm × 12.5 µm [35]. These relatively smaller grain size values are not reported in other studies. In contrast, Jin et al. [28] reports considerably larger AA7075-T651 pancake-shaped grains, with an average size of 4502.8 µm × 376.6 µm × 45.8 µm in the L, LT and ST directions, respectively. For studies using the EBSD method Mohan et al. [34] reports the average grain size of their AA7075-T6 is 210-250 µm and 70-110 µm in thickness. Sintay [33] states according to the available literature AA7075-T651 has a pancake-shaped grain structure with average sizes of 600 µm × 150 µm × 30 µm. The EBSD characterisation did not attempt to calculate the average grain size, instead Sintay plotting grain size distribution for each microstructural plane. These distributions (see Figure 2-7) agree with the general consensus that the average grain size for the L, LT and ST directions (Figure 2-7) are likely in the 100µms, high 10µms and low 10µms, respectively. Additionally, although studies report different grain sizes, it is clear the microstructure is anisotropic. Finally, there are other causes for variation in average grain size, e.g., the sample location. The microstructure can vary through the plate thickness as

the number of small recrystallised grains (and sub-grains) can vary due to the manufacturing step such as rolling. The differences in grain size could also be attributed to small variations per manufacturing batch. This highlights the importance of being consistent with the location from where samples are taken (plate thickness), the batch used, and clearly report the grain size measurement method used. Finally, due to the variation in grain size reporting found in the literature, it is clear that characterisation of the grain size and overall microstructure is required for every study of 7XXX alloys that focuses on microstructural effects on material performance.

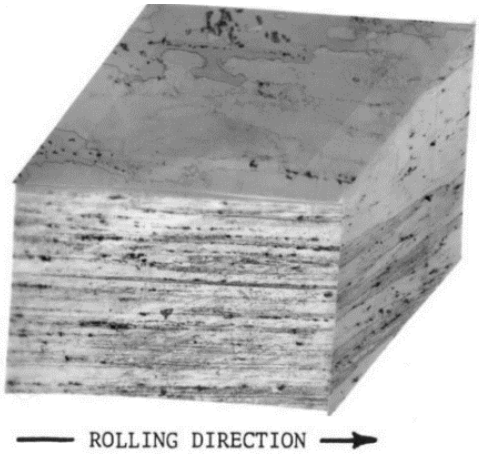

Figure 2-4 - Three dimensional microstructure of AA7075-T6 or T651 revealing the rolling texture (Lee, 1984) [23].

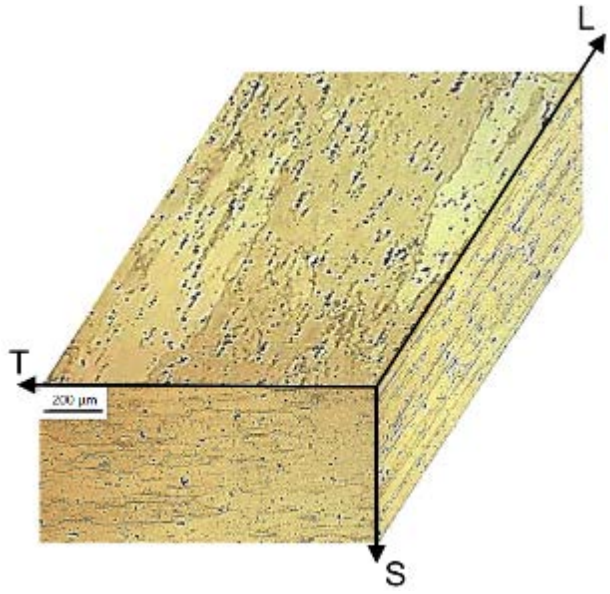

Figure 2-5 - Three dimensional microstructure of AA7075-T6 or T651 revealing the rolling texture (Jin et al., 2015) [28].

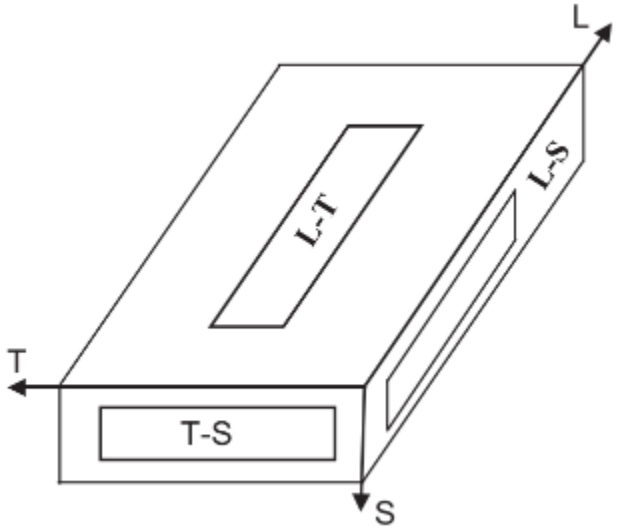

Figure 2-6 – AA7075 microstructural planes (Jin et al., 2015) [28].

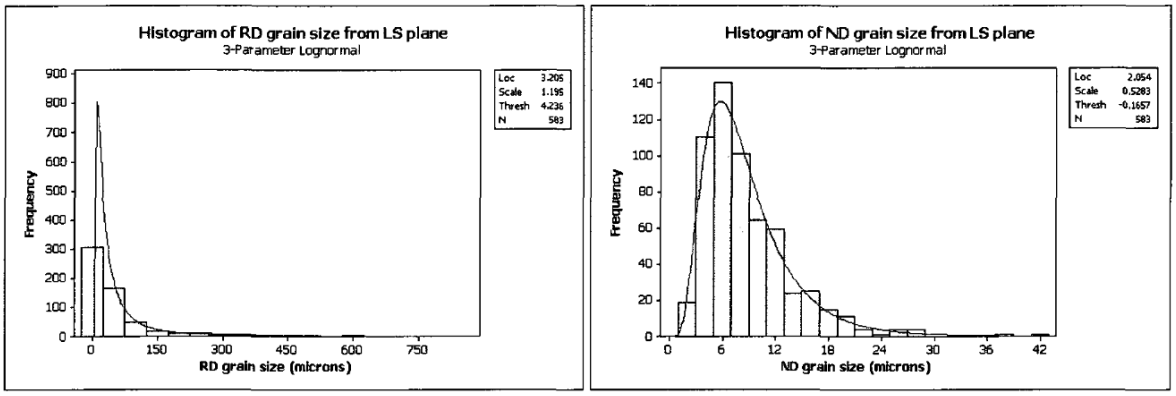

Figure 2-7 – Grain size distribution for the LT and ST directions of AA7075-T651 acquired from the EBSD LT-ST plane (Sintay, 2010) [33].

2.4.1 Second phase particles

During the alloy manufacturing steps several types of second phase particles are formed. These are separated into three categories: strengthening precipitates, dispersoids and coarse constituent particles. Strengthening precipitates and coarse constituent particles have important effects on fatigue and corrosion performance, whilst dispersoid effects are considered more limited.

2.4.1.1 Strengthening precipitates

These particles are the main mechanisms for alloy strengthening in 7XXX aluminium alloys. Zinc and magnesium provide increased strength through the precipitation of very fine precipitates of the eta (η') phase, a semi coherent metastable form of the equilibrium $MgZn_2$ phase. The precipitation sequence in Al-Zn-Mg-Cu alloys with relatively low Mg concentrations is generally accepted as α (SSSS) -> GP -> η' -> η [11]. This is from α in the super saturated state, to Guinier-Preston zones, to transition eta (η') particles, and finally to eta (η) equilibrium phase. The eta particles consist of $MgZn_2$ or $Mg(ZnCuAl_2)$ and are hexagonal close packed [11][19][36][37]. Park and Ardell found the fine plate η' seemed to be the most common precipitate in AA7075-T651 and these are usually semi-coherent with the matrix. Although some η' are heterogeneously nucleated on dislocation lines. They also observed precipitate η (non-coherent $MgZn_2$) [37]. The maximum hardness of the AA7075-T651 alloy is believed to be mainly due to the fine dispersion of η' particles, but the addition of copper also strengthens the alloy primarily by solid-solution strengthening as well as precipitation strengthening [23], [37]. These are generalisations of very complex processes, and the field of study is extensive, showing there is considerable variation according to heat treatment steps and chemical composition, for more information see Berg et al. [38].

The η precipitate size ranges from Angstroms to fractions of a micrometre. They are homogeneously dispersed in the matrix but may also concentrate at grain boundaries. These ageing precipitates are there to strengthen aluminium alloys and their effect on the alloy depends on size, modulus and interfacial, or surface energy, of the precipitates [11][13]. They can also be sites for localised corrosion, especially at grain boundaries where they can be present in high densities, promoting intergranular corrosion and stress corrosion cracking [39].

2.4.1.2 Dispersoids

Dispersoids contain aluminium and other intentionally added elements such as Cr, Ti, Zr and Mn. Chromium, present in older 7XXX alloys such as AA7075-T651, provides improved stress corrosion cracking resistance. Whilst manganese forms compounds that control grain structure, and it is an effective strengthener on an atomic basis. Typical dispersoids identified by TEM are Al_3Ti, Al_6Mn, $Al_{20}Cu_2Mn_3$ and Al_3Zr [11]. Newer alloys such as AA7150 replace Cr (used for AA7075) with Zr as an alloying element for dispersoid formation [27]. According to Rometsch [27], Zr-based dispersoids increase fracture toughness compared to Cr and Mg based dispersoids. Al_3Zr in particular is a preferred dispersoid as it inhibits recrystallisation without increasing quench sensitivity significantly.

Dispersoids tend to be formed during casting and homogenisation and can grow to considerably bigger sizes than strengthening precipitates, growing to several hundred nanometres in size and occupying a volume fraction of 0.05% − 0.02% [11][27]. Most dispersoids retard recrystallization and limit grain size. Full recrystallisation only occurs in the most highly stressed regions as dispersoids inhibit them in most areas by pinning the movement of dislocation-cell boundaries and grain boundaries. Thus, hot rolled alloys will contain both uncrystallised grains, and recrystallised grains distributed along the grain boundaries of uncrystallised grains [11][27]. Due to their incoherence with the matrix dispersoids may also act as sites for crack nucleation but are over-shadowed by the more crack-prone coarse constituent particles. In the case of corrosion, they have not been found to be particularly active [11][39].

2.4.1.3 Coarse constituent particles

During the manufacturing process insoluble and soluble coarse constituent particles are formed. Although there are a large number of particles with different compositions it is iron, copper and silicon impurities that form the most coarse intermetallic compounds in the

7XXX series alloys [36]. Particles sizes can range between 1 µm and 50 µm. AA7075-T651 is known to be particularly 'dirty' due to containing larger quantities of Fe and Si than the newer alloys, which are extremely common elements in constituent particles. Indeed, these modern alloys showed fatigue and corrosion improvements due to a purposeful design to limit Si and Fe [11][27]. Harris [36] used an automated image analysis method to characterise AA7075-T651 and distinguish the particles from the matrix, reporting a volume fraction in AA7075-T651 of approximately 1%, and an extremely inhomogeneous distribution. Singh et al. [40] performed a 3-D characterisation of AA7075-T651 constituent particles using X-ray tomography, see Figure 2-8. They found the total volume fraction of the particles in this alloy to be 1.63%. It is likely this is higher than that reported by Harris due to the 3D characterisation method being able to more accurately pick up the different sized particles as well as their full volume. Singh et al. also found pores to be present at a 0.06% volume fraction, and that these are nearly always associated with inclusions [40].

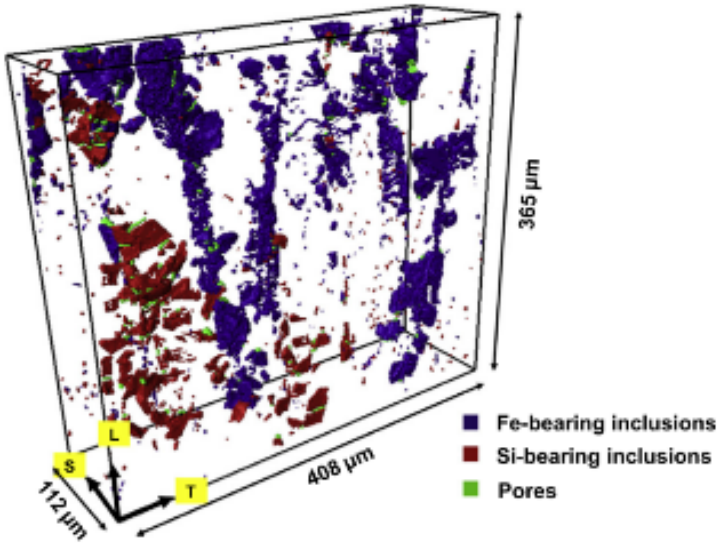

Figure 2-8 – Volume fraction of inclusion and pores in AA7075-T651 (Singh, 2014) [40].

Constituent particles can be divided into soluble and insoluble particles. A common soluble constituent particle in 7XXX alloys is the *S*-phase (Al_2CuMg) which forms due to the copper content. Therefore, copper quantities can be reduced to limit the formation of large *S*-phase particles that can be detrimental to both fracture toughness and corrosion properties of the material, but this is to the detriment of stress corrosion performance. Solution treatment has a limited impact on the dissolution of *S*-phase although there are newer multi-step surface treatments that can improve the dissolution of this phase. Nevertheless, there are often trade-offs, for example for AA7150 this increased dissolution can happen at the cost of increased grain recrystallisation [27].

It is during casting that insoluble coarse particles (often unwanted iron and silicon) are formed. Subsequent fabrication into cast ingots can make these compounds fracture, leading to the formation of stringers of 0.5 µm - 10 µm in size that are aligned with the direction of metal working [11]. These particles are brittle and therefore harmful to the fracture toughness of aluminium alloys. They have a negative effect on fatigue life of aluminium alloy parts when subjected to high stress intensities [41] as they are sites of crack initiation. They have also been found to have a negative effect in terms of resistance to localised corrosion due to micro-galvanic interactions between them and the aluminium matrix [39]. Insoluble constituent particles such as Al_7Fe_2Cu, Mg_2Si and $Al_{23}Cu_4Fe$, cannot be dissolved in subsequent manufacturing processes. Therefore, the best way to minimise these is by making the casting processes 'cleaner', thus introducing lower Fe and Si.

As seen in Figure 2-9, Fe-rich particles and Mg_2Si are always present in large quantities in AA7075. For AA7075-T651 Fe-rich Al_7Cu_2Fe in particular tends to be one of the most abundant intermetallics, whilst Mg_2Si is present in less abundance. Singh et al. [40] not only found the highest volume fraction of constituent particles in AA7075-T651 are composite inclusions of Al_7Cu_2Fe and $Al_{23}Fe_4Cu$ (0.58%), but they also are more brittle, with a Young's modulus and hardness (via nano-indentation) of the Fe-rich particles roughly 50% higher than Mg_2Si particles [36][40]. Furthermore, Fe-rich particles have complex shapes, are spatially non-uniform (clustered) and have partially anisotropic morphological orientations.

Fe-rich particles and Mg_2Si particles can also be differentiated by size and colour, in both optical and scanning electron microscopes. In an SEM, Fe-rich particles tend to be grey in colour, Mg_2Si tend to be very dark. Fe-rich particles are on average larger than Mg_2Si particles by an order of magnitude and, unlike the complex shapes of Fe-rich particles, Mg_2Si particles tend to be more circular in shape. Coarse intermetallic particles such as these generally decrease fracture toughness, fatigue resistance, and ductility. Indeed, plastic deformation and fracture of 7XXX series alloys in general is associated with cracking and void coalescence around these particles [2][36]. These particles are also associated with localised corrosion, especially pitting corrosion, due to galvanic coupling between the particles and the metal matrix [2][11][39][42]. The specific effects of these coarse constituent particles on fatigue and corrosion performance is explored in greater detail in subsequent chapters.

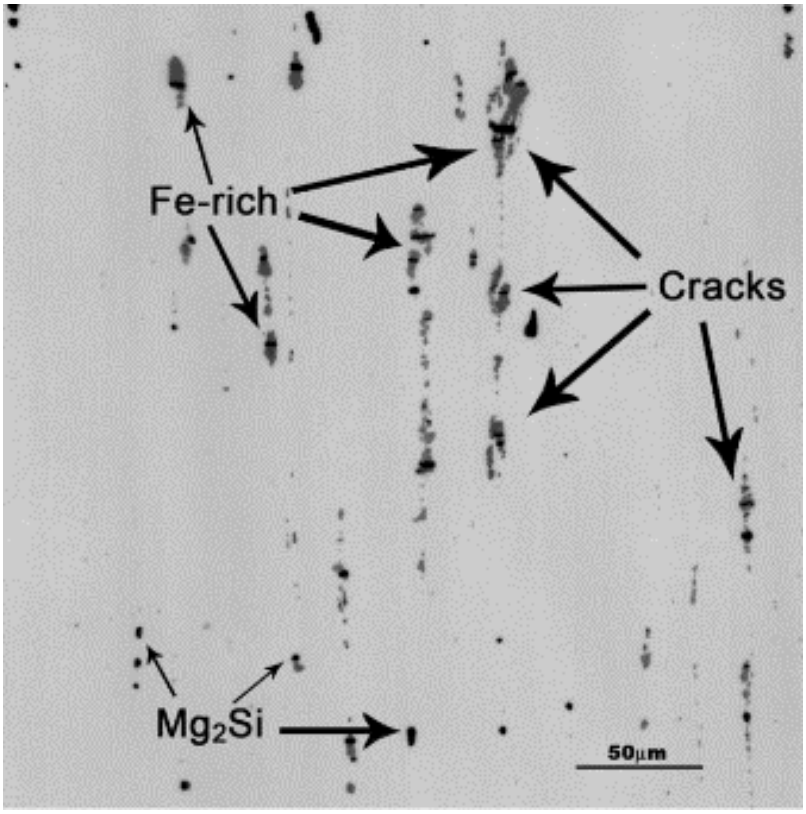

Figure 2-9 – Fe-rich and Mg_2Si particles in AA7075 (Harris, 2005) [36].

2.5 Fatigue behaviour of 7XXX alloys

According to Suresh and Ritchie, fatigue can be termed as the progressive fracture of a material via incipient growth of flaws under cyclic varying stresses [43]. In most engineering structures, due to the demand for more efficient and economic components and structures, the vast majority of in-service failures are caused by fatigue fractures [44]. Fatigue fractures can result from either pure mechanical loading or can be coupled with fretting fatigue (sliding and friction contact between surfaces), the effects of an aggressive environment (corrosion fatigue) or elevated temperatures (creep fatigue and/or oxidation fatigue) [43].

2.5.1 Fatigue Theory

Suresh and Ritchie categorised fatigue into the following phenomena [43]:

i. Initial cyclic damage by cyclic hardening or softening;
ii. Creation of initial microscopic flaws (micro-crack initiation);
iii. Coalescence of these microcracks to form an initial flaw (micro-crack growth);
iv. Subsequent slow macroscopic propagation of the flaw (macro crack growth);
v. Final catastrophic fast failure or instability.

Applying a simple, observable and consistent definition of crack initiation is non-trivial. Often, engineers will find it most practical to set stage iii as initiation, as this is where non-destructive testing equipment has enough resolution to identify cracks. On the other hand, materials scientists are likely to be more concerned with the localised effects of microstructure on fatigue, and therefore consider fatigue initiation to occur at a much earlier stages. The conditions for nucleation of microdefects and the propagation rate of the dominant fatigue crack are strongly influenced by a wide range of mechanical, microstructural and environmental factors. Engineers want to be able to predict fatigue life, which comprises the crack initiation stage and the crack propagation stage; and it is how this stages are quantitatively treated that has led to different design approaches assessing fatigue [45].

2.5.1.1 Fatigue Life Approaches

There are two well-known fatigue life approaches: The total life approach and the damage tolerant approach. Each approach provides different guidelines for the assessment of fatigue failure and hence the optimisation of microstructural variables for fatigue resistance. The fatigue life approach used depends on whether the component is safety or non-safety critical, simple or complex, expensive or inexpensive, etc., and these do not have to be

used separately, they can complement each other to get a full understanding of fatigue in the material in its service application [45][46].

Total life approach

Historically, the fatigue life approach was the first fatigue design approach, and was based on stress versus the number of cycles. That is, for a given stress, the total number of cycles it takes to initiate a crack and then propagate sub-critically to a final crack size. A total life approach involves characterising total fatigue life to failure in terms of cyclic stress (*S-N* curve) or the (plastic or total) strain range. In this approach crack initiation is very important/dominant, and to assess it carefully controlled conditions are required which may involve carefully calibrated test setup and well characterised surface conditions [47][45]. Within the total life approach there are two different approaches, these are the stress life approach and the strain life approach. Information on the strain life approach is given in the appendix in chapter 9.1.2.1 .

The stress life approach is typically used for components where high cycle fatigue (lifetimes of over 10^6 cycles) is a concern. The approach assumes that little plastic strain occurs. As there is little or no plastic strain, fatigue lifetimes are longer and hence these assumptions are linked to the high cycle fatigue regime [45].

In the stress life approach the number of cycles to failures (*N*) are related to the applied stress range and plotted on an *S-N* curve (maximum applied stress range versus number of cycles to failure). It is typically observed that the *S-N* collated data shows an exponential relationship. Therefore, it is common to re-plot the graph logarithmically. This shows a linear relationship between the logarithms of stress amplitude and the fatigue lifetime. Several empirical equations are used to predict fatigue life as a function of applied and/or mean stress. For example, the Basquin equation [45], applied to fully reversed loading, expresses a log-log relationship for *S-N* curves:

Equation 2-1

$$\frac{\Delta\boldsymbol{\sigma}}{\mathbf{2}} = \boldsymbol{\sigma_a} = \boldsymbol{\sigma'_f}(\mathbf{2}\boldsymbol{N_f})^{\boldsymbol{b}}$$

Where σ'_f is the fatigue strength coefficient (which approximately equals the true fracture strength σ_f, corrected for necking, in a monotonic tension test for most metals) and *b* is known as the fatigue strength exponent or Basquin exponent [45].

It is important to once again consider that the above relationships were observed for fully reversed loading ($\sigma_m = 0$, $R = -1$). Nevertheless, not all applications can be represented with a mean stress of zero and fully reversed stress cycles. Furthermore, it is known that mean stress plays an important role in influencing the fatigue behaviour of engineering materials. According to Suresh a decreasing fatigue life is observed when mean stress is increased [45]. Mean stress effects in fatigue can be represented in terms of constant-life diagrams, where different combinations of the stress amplitude and mean stress, providing a constant fatigue life, are plotted. Three very well-known models are those from Gerber (1874), Goodman (1899) and Soderberg (1939). These can be relevant or not depending on the ductility and loading of the material. For more information on these empirical expressions see Suresh (1998) [45].

Damage tolerant approach

Pre-existing defects are present in most real structures. A damage tolerant (or defect tolerant) approach was developed as a fatigue design approach. This starts with the premise that all engineering components will have inherent flaws. Pre-existing flaws are identified via the use of non-destructive flaw detection equipment (or assumed equal to the resolution of the non-destructive flaw-detecting equipment used) to characterise the defect population in a component structure. The life of the component is then taken to be the time or cycles it takes to go from the estimated initial crack, that is usually the size of the largest defect detected, to a critical crack size, based on empirically-derived crack growth laws [45][47]. The calculation of the critical crack size may be based on the fracture toughness of the material, the limit load, the allowable strain or the acceptable change in the compliance of the component. Fracture mechanics can be used to successfully evaluate fatigue life based on the defect tolerant approach. Two theories, linear elastic fracture mechanics (LEFM) and elastic-plastic fracture mechanics (EPFM), are widely used to describe the crack driving force [45]. It is a common engineering practice to start with LEFM assumptions, as it affords considerably simplification and can often adequately describe real life situations [45][47].

The critical conditions for crack growth can be described through the theory of linear elastic fracture mechanics in terms of defining the local stress distribution at the crack tip in terms of the stress intensity factor approach. It is first necessary to consider the different modes of crack opening before considering the variation of stress field around cracks [45][47]:

The displacement of crack surfaces during crack growth can happen in three opening modes:

- **Mode I:** The tensile opening mode, where the crack displaces in a direction normal to the crack plane.

- **Mode II:** The in-plane sliding mode, where the crack shears in a direction perpendicular to the crack front.

- **Mode III:** The anti-plane shear mode, the crack shears in a direction parallel to the crack front.

For a component subject to Mode I loading (see Figure 2-10), the local stresses at any coordinates close to the crack tip can be described mathematically as follows [45]:

Equation 2-2

$$\begin{Bmatrix} \boldsymbol{\sigma_{xx}} \\ \boldsymbol{\sigma_{yy}} \\ \boldsymbol{\sigma_{xy}} \end{Bmatrix} = \frac{\boldsymbol{k_I}}{\sqrt{\boldsymbol{2\pi r}}} \boldsymbol{cos}\left(\frac{\boldsymbol{\theta}}{\boldsymbol{2}}\right) \begin{Bmatrix} \boldsymbol{1 - sin\left(\frac{\theta}{2}\right) sin\left(\frac{3\theta}{2}\right)} \\ \boldsymbol{1 + sin\left(\frac{\theta}{2}\right) sin\left(\frac{3\theta}{2}\right)} \\ \boldsymbol{sin\left(\frac{\theta}{2}\right) cos\left(\frac{3\theta}{2}\right)} \end{Bmatrix}$$

where K_I is the stress intensity factor for Mode I loading. Griffith [48] and Orowan [43] developed theories regarding fracture from the extension of cracks on the basis of a global energy balance approach which they also linked to a description of the stress intensity factor. In the global energy balance approach it is defined in terms of the applied (far-field) stress (σ) and flaw length (a) as:

Equation 2-3

$$\boldsymbol{K_I = \sigma_{app}\sqrt{\pi a}\, f\left(\frac{a}{W}\right)}$$

where $f\left(\frac{a}{W}\right)$ is the compliance function and accounts for differing geometries and shapes in the component. The stress intensity factor then is a measure of the magnitude of the stress field close to the crack tip under linear elastic conditions that can be calculated from global stress information and the crack length [45].

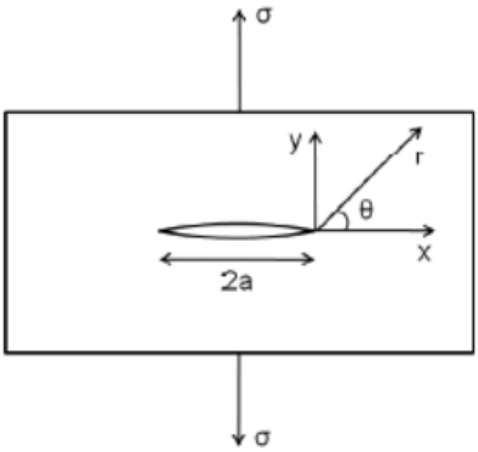

Figure 2-10 – Crack in a thin elastic plate under mode I loading (Evangelou, 2017) [49].

The region of "*K*-dominance" is the near crack area in which the stress field can be satisfactorily described by *K*. This region is an annular zone whose outer radius is defined as the point where the asymptotic solutions of the set of equations in Equation 2-2 deviate significantly from the solution of the fully elastic equation for the far field stresses (see Figure 2-11). The inner radius of the *K*-dominance region can be defined as the point where the near tip plastic zone ends. This plastic zone exists, because real materials, when subjected to loading, exhibit plastic yielding at the crack tip to relieve and redistribute the stresses. This invalidates the basis of linear elastic fracture mechanics. Nevertheless, it is generally accepted that as long as the plastic zone is significantly smaller than the specimen size and the crack length (less than $1/50^{th}$) the region of *K*-dominance essentially controls the behaviour of the crack [45].

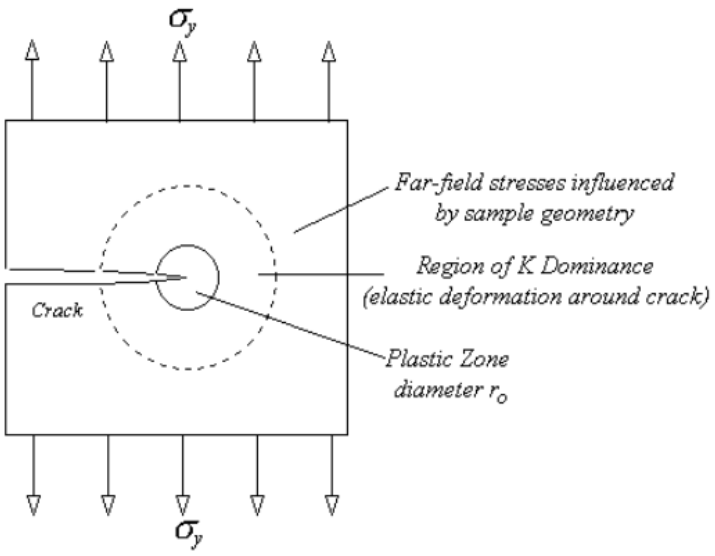

Figure 2-11 – Schematic of plastic and K-dominance zones (Evangelou, 2017) [49].

The critical stress intensity factor (K_c) is a critical value that characterises the ability of a material containing a crack to resist fracture. This value is a function of the mode of loading, material microstructure, strain rate, stress rate, environment and the temperature. Under plane strain conditions, K_c, is known as the fracture toughness of the material at a specific environment.

For fatigue loading, the crack growth behaviour is described by the stress intensity factor range ($\Delta K = K_{max} - K_{min}$), which is obtained from the applied stress range ($\Delta\sigma = \sigma_{max} - \sigma_{min}$). The crack growth data is obtained from test samples of the material containing a pre-existing defect of known dimensions. A log-log plot of crack growth rate (da/dN) against ΔK is produced where there are usually three distinct regions, as seen in Figure 2-12. Region A is characterised by low ΔK values and almost negligible crack growth rates. Nevertheless, crack growth rate is observed to increase rapidly with small changes in ΔK. A threshold value of stress intensity factor (ΔK_{th}) represents the smallest driving force to attain a detectable crack growth rate. Region B exhibits a steady crack growth rate and is governed by the Paris law [45][47]:

Equation 2-4:

$$\frac{da}{dN} = C\Delta K^m$$

The coefficient *C* and the exponential *m* are empirically determined and dependent on loading conditions and the environment, as well as the material itself [45][47].

Finally, in region C the material approaches its fracture toughness (K_c) and the crack growth rate increases rapidly. This region is heavily influenced by the microstructure and mean stress levels. However, this regime only exists for a relatively small number of cycles and therefore usually has a minor contribution to the overall fatigue lifetime [45][47].

It is important to mention these is a simplification, and there are other variables that can affect crack growth rate. According to Maddox [50] mean stress has been reported to have important effects on crack growth rate, however this can strongly depend on the load ratio used and the type of material tested. Furthermore there have been contrasting studies that report different effects of mean stress on crack growth rate.

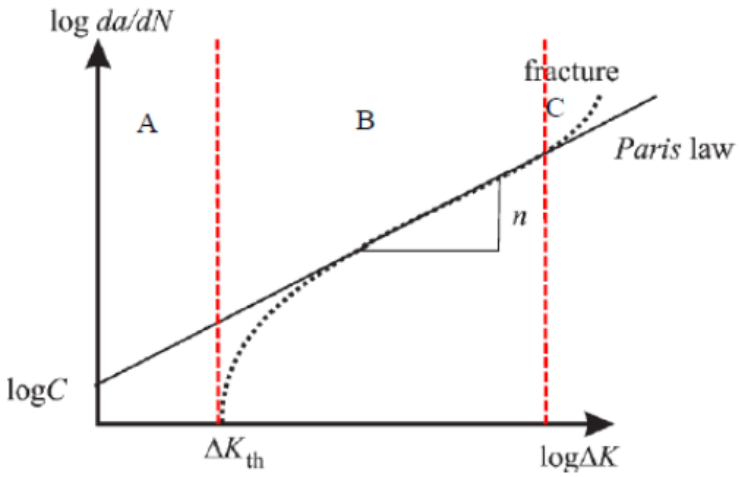

Figure 2-12 –Crack growth rate (da/dN) against stress intensity factor (ΔK) diagram illustrating the three different propagation regimes (Evangelou, 2017) [49].

2.5.1.2 Fatigue Crack Initiation

In a notionally defect free crystal, persistent slip bands (PSBs) form in the direction corresponding to the slip system with the greatest resolved stress. Under sufficient cyclic loading, there are irreversible deformations associated with slip along these PSBs. This results in the formation of extrusions and intrusions at the crystal surface, providing sites for micro-crack formation [45][51]. In real world components there are other features in a material's surface that are likely to cause crack initiation before PSB based mechanisms do. All components will have a degree of surface roughness, which is known to be

detrimental to fatigue performance [52]. This can be imagined as a surface with many small stress concentrations [45][51].

Influence of surface features

As with surface roughness, the influence of surface features is important for fatigue performance of a metal. It is common to find both pores and inclusions within a metal matrix. Pores and inclusions can be seen as existing microcracks within the metal. As these features are rarely avoidable, and depending on their size, they can have a dominant effect on the fatigue performance of the material. The size of these defects can be of great significance, particularly when they reach sizes approaching the grain size [45]. Tanaka proposes three types of fatigue crack initiations for high strength materials [53]:

- **Type A:** Crack initiation from debonded inclusions;
- **Type B:** Inclusion cracking from impinging slip bands;
- **Type C:** Slip band cracking emanating from uncracked inclusions.

Aluminium alloys contain different inclusions of different sizes, many are of significant size and band together as stringers. Therefore, it will be important to identify what type of fatigue crack initiation mechanisms dominate in this material.

2.5.1.3 Short Crack Fatigue

According to Suresh and Ritchie there are several ways to define a ‘short’ crack [43]:

- Cracks that are of a length that is comparable to the scale of the micro-structure (e.g., of the order of the grain size).
- Cracks which are of a length comparable to the scale of the plastic zone (e.g. small cracks embedded in the plastic zone of a notch of a length comparable with their own crack tip plastic zones. This is typically less or equal to 10^{-2} mm in ultra-high strength materials, and less or equal to 0.1 mm - 1 mm in low strength materials).
- Cracks that are physically small (e.g. less or equal to 0.5 mm – 1 mm).

Most metals appear to show a similar behaviour of small crack growth during cyclic loading. This is a faster growth rate than long cracks followed by growth retardation due to crack tips reaching grain boundaries, triple points and phase boundaries [43][53]. In general, smaller grain sizes lead to slower short crack growth, thus fine grained materials will have slower short crack growth rates than coarse grain materials [54]. Suresh and Ritchie stated that a study by Pearson (1975) also found that, for precipitation hardened aluminium alloys, cracks

of size similar to the average diameter of the alloy's grains grew several times as quickly as long cracks under nominally identical alternating local stresses, see Figure 2-13 [55].

According to Suresh and Ritchie, "differences in short crack and long crack behaviour is to be expected". Such differences can arise from a number of distinct phenomena [43]:

- Inadequate characterisation of the mechanics of crack tip stress and deformation field of short cracks, including neglecting elastic singularity higher order terms and the presence of extensive local crack tip plasticity;
- Notch tip stresses and deformation field effects (for cracks emanating from notches);
- The interaction, including deflection, of short cracks with microstructural features such as grain boundaries, inclusions and second phases, of dimension comparable in size with the crack length;
- Differences in crack shape and geometry;
- Differences in crack extension mechanism;
- The effect of crack closure varying with crack length;
- Differences in the local crack tip environments.

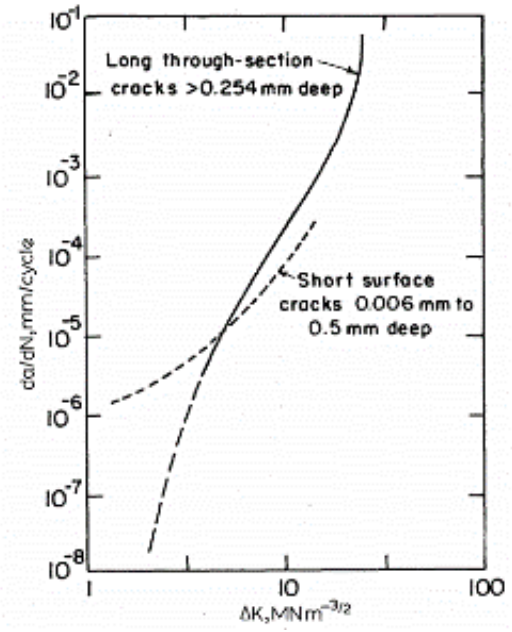

Figure 2-13- Difference in propagation rates da/dN of fatigue cracks as a function of stress intensity factor range ΔK for precipitation hardened aluminium alloys (Pearson, 1975) [55].

2.5.2 Micro-mechanisms of fatigue crack initiation and propagation in 7XXX alloys

The total fatigue life is divided between crack initiation and crack propagation. As with other precipitation hardenable aluminium alloys, both crack initiation and propagation in 7XXX aluminium alloys is influenced by the material microstructure (coarse constituent particles and the grain structure) and its surface state [11][56]. The microstructure and surface state of the material can depend on the alloy's chemical composition, manufacturing method (e.g. rolling, extrusion, forging, etc.) and temper.

One of the most important microstructural features for strength and fatigue performance are strengthening precipitates. As discussed in section 2.4.1.1 the size, coherence and distribution of these is strongly dependent on the temper [11][37]. For example, the T6 temper maximises strength but this affects fracture toughness and fatigue life. Whilst the over-aged tempers tend to sacrifice some yield strength to increase fracture toughness, and improve corrosion and fatigue performance. The literature on the effects of temper on material properties is substantial. However, as only one alloy, and temper, will be investigated in this project (AA7075-T651), effects of temper on material performance is not discussed any further. For an overview of temper effects on material performance see Polmear [11] and Bucci et al. [57].

Additionally, it is important to mention that over time better understanding of 7XXX aluminium alloys' interrelationship between microstructure and fracture mechanisms have led to newer, better alloys with optimum high strength and high toughness. Improvement in most of these alloys has been achieved through microstructural control obtained by increasing purity, modifying compositions and improving manufacturing steps [57]. Thus, compared to newer alloys AA7075-T651 performs relatively poorly in terms of fracture toughness, fatigue and corrosion performance. Some of these newer improved alloys are AA7475, AA7150-T77 and AA7055-T77 [57].

As AA7075-T651 has been chosen for this project due to the extensive body of knowledge on its performance, making it a good benchmark alloy, the specific mechanisms for crack initiation and propagation of AA7075-T651 will be discussed below. Further literature examples of other aerospace alloys will only be mentioned where similar mechanisms apply.

2.5.2.1 Influence of coarse constituent particles

As briefly mentioned in section 2.4, for commercial materials, short cracks tend to initiate at constituent particles such as inclusions and intermetallics [43]. Pearson [55] performed

extensive work on 7XXX aluminium alloys, and showed fatigue short crack initiation and growth in plane polished surfaces occur at the interface between a surface inclusion and the matrix and in some cases the inclusion would be pre-cracked due to prior cold working. Although there are several types of coarse constituent particles, of which Fe and Si-particles are the most common, Fe-rich particles are commonly attributed as the main mechanism for crack initiation [28][29][36][55][58][59][60]. Fe-rich particles are abundant compared to Si-bearing particles, have irregular forms, tend to be larger in size and appear in clusters as stringers. In AA7075-T651, Al_7Cu_2Fe appears to dominate crack incubation [28][36][55][58][59]. Although this is also dependent on the microstructural plane dynamically loaded. Due to the anisotropic grain structure of many 7XXX alloys, particularly rolled alloys such as AA7075-T651, the L-LT and L-ST microstructural planes not only have a larger distribution of Fe-bearing particles but many of these tend to be pre-cracked from the manufacturing process [28][55][59]. If not pre-cracked, these tend to crack within the first few cycles of dynamic loading. In contrast, the LT-ST plane contains fewer Fe-bearing particles (or at least less surface area), are less likely to be pre-cracked, and therefore these are less dominant. In this plane Mg_2Si becomes more important for fatigue behaviour [28]. These microstructural differences also cause fatigue behaviour anisotropy. Figure 2-14 and Figure 2-15 show *S-N* curves for all planes and number of cracks vs. maximum stress, for each plane. Fatigue strengths of L-LT, L-ST and LT-ST were measured to be 243.6 MPa, 273.0 MPa and 280.6 MPa, respectively (4-PB test, R:0.1, f = 20 Hz) [28]. It is clear from Figure 2-14 and Figure 2-16, the LT-ST plane has the highest fatigue limit and this appears to be due to the lesser dominance of pre-cracked Fe-rich particles, replaced by Mg_2Si, as the main mechanism of crack initiation [28].

Finally, in thick plates, the rolling step during manufacture does not affect the inside of the material as much as the outside. There can be differences in the distribution and size of constituent particles between the surface [61] due to rolling cracking particles near the plate surface, whilst the middle of the plate may have not suffered any rolling effects. This will clearly have an effect on fatigue performance. Thus, when fatigue testing AA7075-T651, or other alloys, that have been manufactured as thick plates, it is important to be aware of the location (plate thickness) from which any test samples are taken.

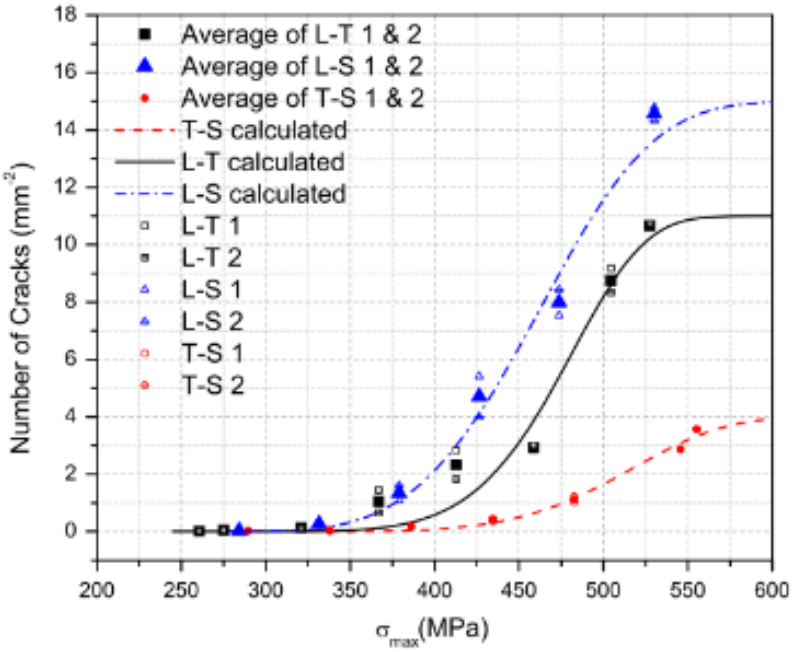

Figure 2-14 – Number of cracks vs. maximum stress (Jin et al., 2015) [28].

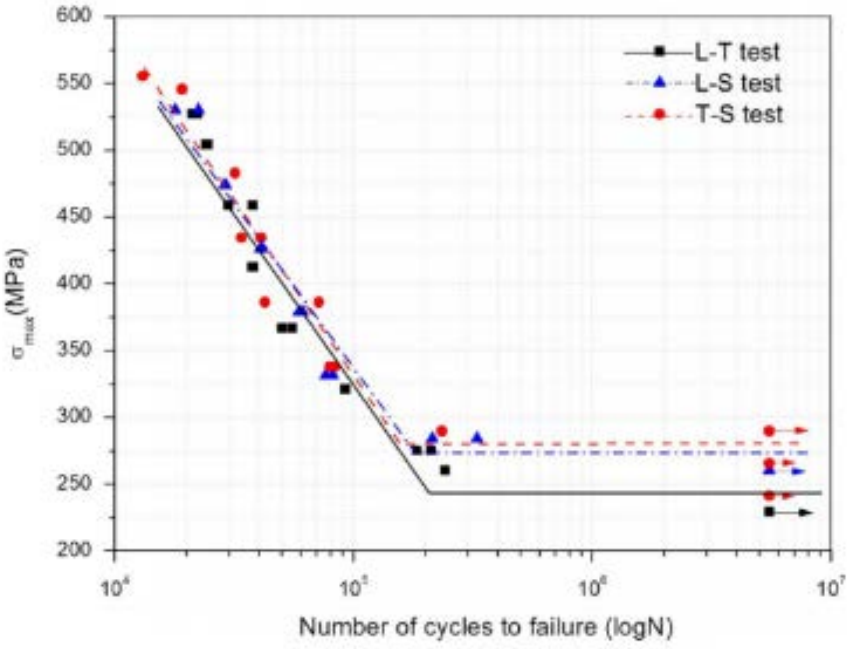

Figure 2-15 - S-N curves of samples in LT (L-LT), LS (L-ST) and TS (LT-ST) planes of AA7075-T651 by four-point bend fatigue (Jin et al., 2015) [28].

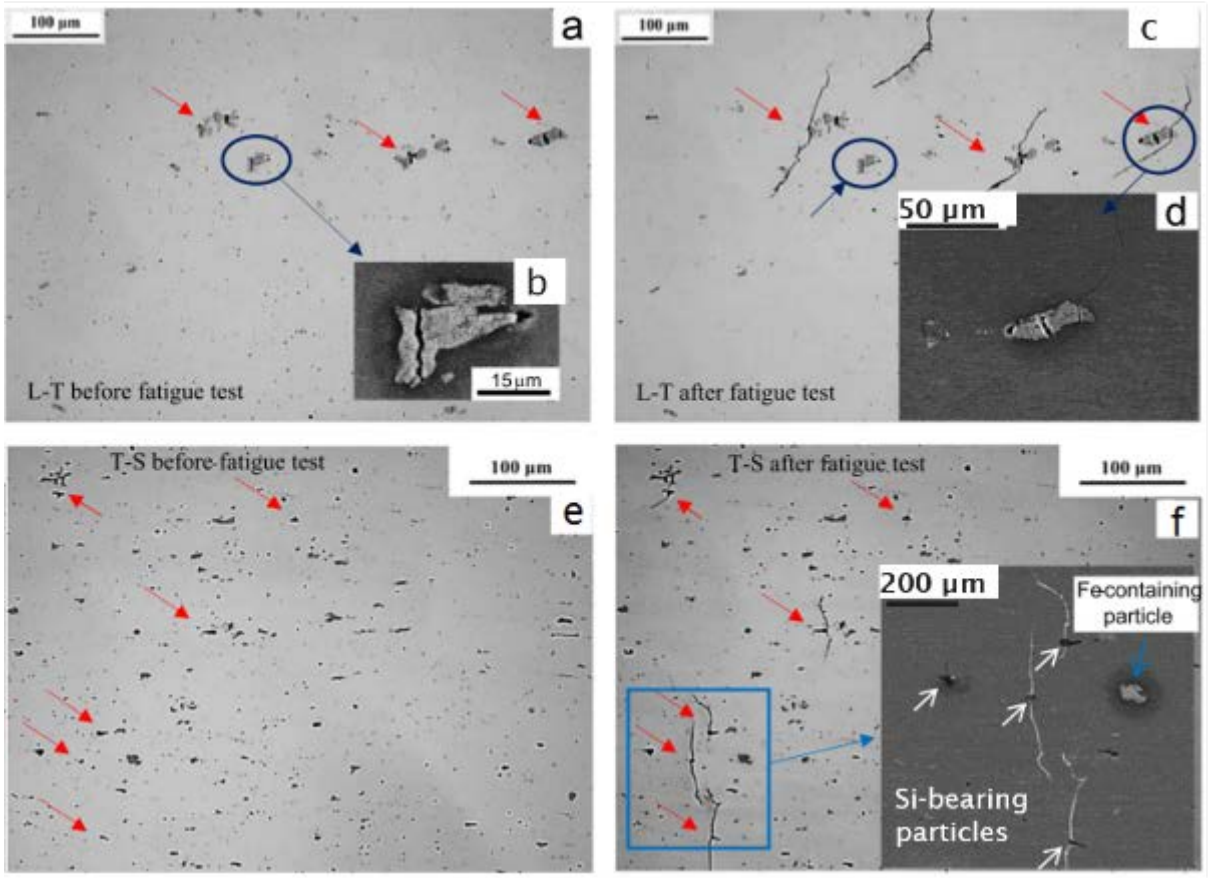

Figure 2-16 – AA7075-T651 microstructure before and after fatigue testing (Jin et al., 2015) [28].

a. Iron particles in L-LT plane, before fatigue. **b**. Pre-cracked Fe-containing particle before fatigue. **c**. Fe-containing particles in L-LT plane after fatigue. **d**. Pre-cracked Fe-cont. particle after fatigue. **e**. LT-ST plane before fatigue. **f**. LT-ST plane after fatigue.

2.5.2.2 Influence of grain microstructure

As mentioned previously, the manufacturing steps, including rolling in the case of AA7075-T651, will affect the fatigue performance as the consequent anisotropic microstructure will lead to marked grain size variation (discussed in section 2.4). Larger grain sizes, in the AA7075-T651 L-LT and L-ST microstructural planes can mean lower fracture toughness. The importance of grain size on short crack growth is shown by Pearson [55] who found 7XXX alloys experience high crack growth rates (above 10^{-6} mm per cycle) in comparison to LEFM predictions. This would then approach long crack growth behaviour when approaching 0.127 mm size, close to the average grain size of a common 7XXX alloy. Prior to approaching long crack growth behaviour crack growth tends to decelerate due to crack closure and due to interaction with microstructural features, in particular, grain boundaries. The crack growth blocking effect of grain boundaries is more frequent in fine grained material, thus fine grained alloys or microstructural planes with smaller grains such as the

AA7075-T651 LT-ST plane is expected to perform best compared to the other planes with larger grain size [31][54]. This is also seen in a study of pure aluminium, showing the smaller the grains the higher the fatigue strength as the grain boundaries acted as barriers to crack growth [62]. Due to the finer grains and the lower quantity of detrimental Fe-bearing particles it is well established that industrial applications of AA7075-T651 therefore tend to favour loading the LT-ST plane.

2.6 Corrosion behaviour of 7XXX alloys

2.6.1 Introduction

This chapter has a brief introduction to corrosion theory. If more information is required please see Trethewey and Chamberlain [63].

Corrosion can be defined as the degradation of a metal by an electrochemical reaction with its environment [63]. It is a complex phenomenon which depends on several factors, including the thermodynamics of the reaction, the kinetics of the reaction and the environment [63]. For corrosion to happen, the corroding metal's surface has to be part of an electrochemical cell. As can be seen in Figure 2-17, an electrochemical cell consists of two electrodes, or metal conductors, in contact with an electrolyte, an ionic conductor. If you remove any of these elements from the cell, corrosion will not happen [63]. In the electrochemical cell an anode is where electrons are lost (oxidation) and a cathode where electrons are absorbed (reduction) [63].

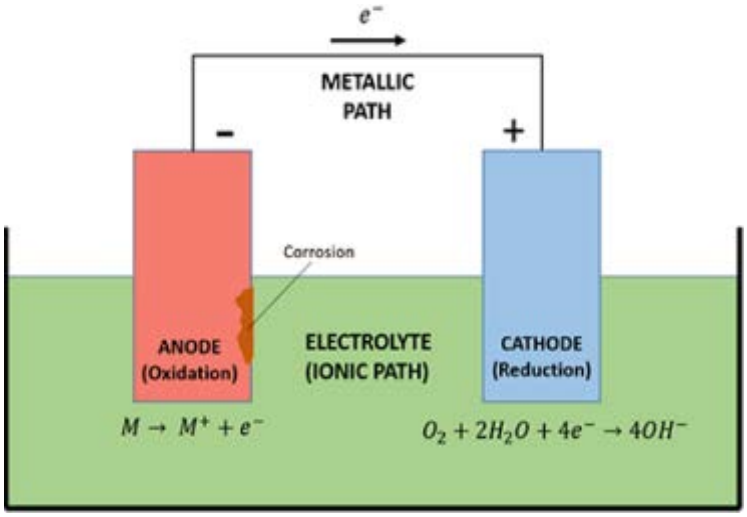

Figure 2-17 - Basic corrosion cell (Hays, 2017) [64].

Most metals are thermodynamically unstable in aqueous environments. Their corrosion in water, or an electrolytic solution, made by dissolving a salt, acid, or base in water, is an electrochemical process. It is most common for a metal to be the anode, losing electrons and ending up with corrosion products that can separate from the bulk, sometimes weakening the metal's surface. The cathode is where electrons are received, where there is a reduction process. A cathode could be a metal of a different electrochemical potential

(more noble) to the anodic metal, attracting electrons from the anode, forming a galvanic cell. Alternatively, the metal itself may have areas that are anodic and cathodic, forming micro-galvanic cells within the same metal. This can be due to, for example, differences in grain structure, composition or metal defects [63].

2.6.2 Standard electrode potentials

The electrochemical potential is the key expression connecting electrical measurements to the Gibbs free energy, and therefore the thermodynamic properties of a material. For more information on these please see appendix in section 9.1.3.2. In corrosion there needs to be a way to measure electrochemical potential in a standard form. Electrochemical potential will vary depending on the electrolyte used and the element with which it is coupled, as only the potential difference can be measured. Therefore a defined set of parameters are needed to define the standard potential of a reaction [63]. Hydrogen has been chosen in the corrosion-engineering field as the standard for reference with a potential defined as zero volts. This means the potential difference between any metal and hydrogen is the standard electrode potential for that element. This has given rise to the electrochemical series, which is listed in terms of reduction potentials and determined under standard conditions. The values are absolute and dependent of the electrolyte used [63].

Reduction potentials have now been measured so accurately there is no practical need for using hydrogen electrodes. Robust and very stable standard reference electrodes that are more convenient for use in laboratories and field measurements are now available. Some of these are the standard calomel electrode, the saturated calomel electrode, the silver/silver chloride (Ag/AgCl) electrode, among others [63]. Table 2-6 lists the standard reduction potentials measured against the standard hydrogen electrode:

Table 2-6 - Selected standard electrode potentials (E°) at 298.15 K (25 °C), and at a pressure of 101.325 kPa (1 atm), all chemical species being in their standard states at unit activity [63].

Reduction half-reaction	$E^{o}\ vs.\ \mathbf{SHE}$ / V
$\mathbf{Au^{+} + e^{-} \rightarrow Au}$	+1.692
$\mathbf{Cl_2 + 2e^{-} \rightarrow 2Cl^{-}}$	+1.358
$\mathbf{O_2 + 4H^{+} + 4e^{-} \rightarrow 2H_2O}$	+1.229
$\mathbf{Pt^{2+} + 2e^{-} \rightarrow Pt}$	+1.180
$\mathbf{Ag^{+} + e^{-} \rightarrow Ag}$	+0.800
$\mathbf{Fe^{3+} + e^{-} \rightarrow Fe^{2+}}$	+0.771
$\mathbf{Cu^{+} + e^{-} \rightarrow Cu}$	+0.521
$\mathbf{O_2 + 2H_2O + 4e^{-} \rightarrow 4OH^{-}}$	+0.401
$\mathbf{[Fe(CN)_6]^{3-} + e^{-} \rightarrow [Fe(CN)_6]^{4-}}$	+0.358
$\mathbf{Cu^{2+} + 2e^{-} \rightarrow Cu}$	+0.342
$\mathbf{Hg_2Cl_2 + 2e^{-} \rightarrow Hg + 2Cl^{-}}$	+0.268
$\mathbf{AgCl + e^{-} \rightarrow Ag + Cl^{-}}$	+0.222
$\mathbf{Cu^{2+} + e^{-} \rightarrow Cu^{+}}$	+0.153
$\mathbf{2H^{+} + 2e^{-} \rightarrow H_2}$	0.000 (by definition)
$\mathbf{Fe^{3+} + 3e^{-} \rightarrow Fe}$	–0.037
$\mathbf{O_2 + H_2O + 2e^{-} \rightarrow HO_2^{-} + OH^{-}}$	–0.076
$\mathbf{Ni^{2+} + 2e^{-} \rightarrow Ni}$	–0.257
$\mathbf{Co^{2+} + 2e^{-} \rightarrow Co}$	–0.280
$\mathbf{Fe^{2+} + 2e^{-} \rightarrow Fe}$	–0.447
$\mathbf{Cr^{3+} + 3e^{-} \rightarrow Cr}$	–0.744
$\mathbf{Zn^{2+} + 2e^{-} \rightarrow Zn}$	–0.762
$\mathbf{2H_2O + 2e^{-} \rightarrow H_2 + 2OH^{-}}$	–0.828
$\mathbf{Ti^{2+} + 2e^{-} \rightarrow Ti}$	–1.630
$\mathbf{Al^{3+} + 3e^{-} \rightarrow Al}$	–1.662
$\mathbf{Mg^{2+} + 2e^{-} \rightarrow Mg}$	–2.372

2.6.3 Polarisation and corrosion kinetics

When an electrochemical cell is in equilibrium potential, there is no net change in the Gibbs free energy (the thermodynamic state) of the material. When a metal is not in equilibrium with a solution of its ions the electrode potential, *E*, differs from the equilibrium potential by an amount known as polarisation, also termed overvoltage and overpotential. Polarisation is a very important corrosion parameter because it allows useful statements to be made about the rates of corrosion processes. When a metal is polarised, and therefore not in equilibrium, there is a net flow of electrons (from the anode to the cathode) and thus net current flowing in one direction. In an electrochemical cell where a metal is undergoing corrosion, the electric current signifies the rate of corrosion reactions. It is commonly divided by the exposed area and presented as current density. The experimental equation that links polarisation to the exchange current density is shown in Equation 2-5. It allows us to plot current density measurements against polarisation (For more information on the fundamental theory of corrosion kinetics and how Equation 2-5 is derived please see appendix in section 9.1.3.3). Thus, it allows for the experimental extrapolation of the

exchange current density, and in a more practical sense, it helps us find the corrosion rate of a specific material in a specific environment, specific roughness, etc., when in a steady-state.

Equation 2-5:

$$\eta_{p_a} = \beta_a ln\left(\frac{j_{meas} + j_c}{j_0}\right)$$

Where η_{p_a} is the polarisation at the anode (the metal), j_{meas} the experimentally measured current density which is the sum of the anodic and cathodic current densities, j_c is the cathodic current density, j_0 the exchange current density flowing in both directions (cathodic and anodic currents) at equilibrium conditions, and β_a an expression of polarisation and other constants related to temperature and the material's thermodynamics properties.

Additionally, by being able to measure current density, and therefore corrosion rates, at different polarisations, we can use several experimental electrochemical and surface characterisation techniques, that can shed light into the mechanisms of corrosion of a material in different conditions and how these may develop with the passage of time. One commonly used experimental method, for example, is a potentiodynamic polarisation, where the metal's potential is polarised by a fixed amount and the current density logged as an output. The resulting graph is a useful way to compare electrochemical behaviour between different materials and/or surface states. Figure 2-18 is a schematic of an experimental potentiodynamic polarisation plot [65].

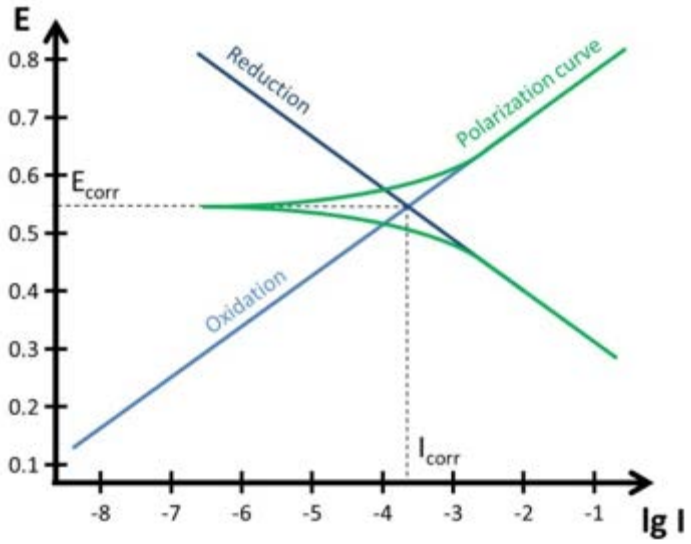

Figure 2-18 – Schematic of experimental Tafel plot with extrapolation of theoretical Tafel lines (PalmSens, 2017) [65].

2.6.3.1 Acidity and pH

The pH (a measure of the acidity or alkalinity) is another important parameter in corrosion as this can explain how chemically hostile the environment is to a metal's surface. Therefore giving us information on whether the environment the metal is exposed to can lead to corrosion degradation and what the rate of corrosion may be [63]. Acidity and alkalinity are linked to the concentration of hydrogen ions present in a solution. A high concentration of hydrogen ions means a more acidic solution and lower one a more alkaline solution [63].
Pure water is considered a neutral substance as it has equal quantities of hydrogen ions and hydroxyl ions, and has a pH value of 7. The pH scale can vary from 0 to 14. Figure 2-19 shows both the pH and pOH scale versus concentration of hydrogen and hydroxyl ions [63].

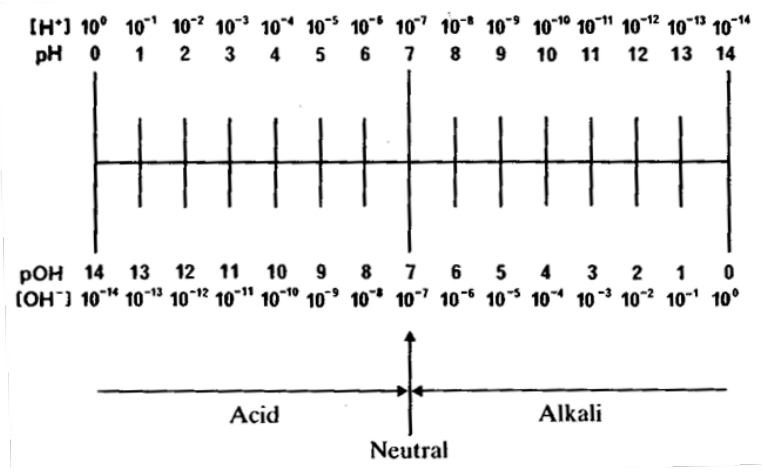

Figure 2-19 – pH and pOH Scale (Trethewey, 1988) [63].

2.6.4 Environmental corrosion in Aluminium Alloys

Aluminium is an active metal, which will readily oxidise and would be a very unstable metal in common environments if it were not for the formation of a natural oxide film of alumina on its surface. This oxide film inhibits corrosion of the bulk material. It is stable and protective in aqueous solutions in a pH range of 4.5 – 8.5. In exposed air, the oxide layer is very thin, measured at 2.5 nm. In aqueous solutions, it has been suggested the initial corrosion product is aluminium hydroxide, which then changes, in time, to hydrated aluminium oxide. This could lead to the oxide film being less adherent and less protective in water compared to in air. In strong acids and strong alkalis alumina becomes soluble, leading to rapid attack of the bulk aluminium [11].

By assessing the standard electrode potentials (*vs*. 0.1 M calomel reference electrode) in Table 2-7, we can get an idea of how aluminium and its alloys may react in comparison with other metals/alloys. It can be seen that aluminium has a potential of -0.850 V and aluminium alloys are in range from -0.690 V to -0.990 V. Magnesium can be seen to be more anodic then aluminium and its alloys, whilst a mild steel is more cathodic [11].

Table 2-7 - Electrode potentials of various metals and alloys (0.1 M calomel electrode) [66].

Metal or alloy	Potential / V
Magnesium	-1.730
Zinc	-1.100
Alclad 6061, Alclad 7075	-0.990
5456, 5083	-0.870
Aluminium (99.95%), 5052, 5086, 1099	-0.850
3004, 1060, 5050	-0.840
1100, 3003, 6063, 6061, Alclad 2024	-0.830
7075-T6	-0.810
2014-T4	-0.690
Cadmium	-0.820
Mild steel	-0.580
Lead	-0.550
Tin	-0.490
Copper	-0.200
Stainless steel (3xx series)	-0.090
Nickel	-0.070
Chromium	-0.490 to -0.180

In terms of corrosion, the following half-cell reactions of aluminium in water are considered common knowledge:

The basic anodic reaction of aluminium can be seen in Equation 2-6 :

Equation 2-6

$$Al \rightarrow Al^{3+} + 3e^{-}$$

The cathodic reaction is oxygen reduction for neutral to alkaline conditions is seen in Equation 2-7:

Equation 2-7

$$O_2 + H_2O + 4e^{-} \rightarrow 4OH^{-}$$

However, there would be hydrogen reduction (hydrogen evolution) in acidified solutions within a pit environment as a result of aluminium ion hydrolysis, as seen in Equation 2-8:

Equation 2-8

$$2H^{+} + 2e^{-} \rightarrow H_2$$

Due to the interaction of local cathodes and anodes and the local matrix nearly all forms of corrosion can occur in aluminium alloys. This includes pitting corrosion, selective dissolution, trenching, intermetallic particle etch out, intergranular attack and exfoliation corrosion [67].

2.6.5 Pitting corrosion

Pitting is localised corrosion, which selectively attacks areas of metal surface. It happens when there is:

- A surface scratch or mechanically induced break in an otherwise protective film;
- An emerging dislocation or slip step caused by applied or residual tensile stress;
- A compositional heterogeneity such as an inclusion, segregate or precipitate [63].

Pitting corrosion is distinguishable from crevice corrosion in the initiation phase. It is initiated by metallurgical factors alone whilst crevice corrosion is initiated by a differential concentration in oxygen ions in an electrolyte. Once the initiation phase is over the pits from

both corrosion types have very similar geometrical characteristics and the propagation electrochemistries converge [63].

Pits can nucleate and then stop due to loss of current. If the pit survives the nucleation phase, it is called a metastable pit, where the continuous survival of the pit depends on maintenance of an effective layer of corrosion product that prevents diffusion. If this pit cover is lost and the current density is not sufficient the pit also dies. If the pit survives then it is called a stable pit [63].

2.6.6 Intergranular and exfoliation corrosion

Intergranular corrosion is localised corrosion of grain boundaries and what is immediately around them [63][68]. For this to happen the chemical make-up of the grain boundary will differ from that of the bulk material leading to anodic activity in the grain boundary and preferential dissolution. Thus, intergranular corrosion is dependent on the alloy's microstructure [63][17].

Intergranular corrosion can develop into other forms of corrosion, in particular exfoliation corrosion. According to the Research and Technology Organisation and NATO [1] exfoliation corrosion is a form of severe intergranular corrosion which occurs in grain boundaries of elongated grains. It occurs where there is a combination of highly directional microstructure (such as 7XXX and 2XXX alloys), a preferential anodic path and a specific type of corrosive environment.

2.6.7 Localised corrosion in 7XXX aluminium alloys

According to Sukiman et al. [69], the presence of chloride ions make aluminium susceptible to localised corrosion. In aerated conditions the availability of oxygen means the metallic surface is readily polarised to its pitting potential, and chloride ions contribute to the formation of soluble chlorinated aluminium hydroxide, which interferes with the formation of a stable oxide film. The higher the chloride ion concentration in the environment the higher the pitting occurrence due to passive layer disruption [39][67].

Aluminium alloys are known to have a heterogeneous microstructure, with many different particles present, some of them coarse particles from the solidification process, others from the age hardening phase, such as precipitates. These micro constituents can be detrimental to corrosion resistance as those particles that will invariably be on the surface will cause non-uniform attack at specific areas of the alloy [67][11], due to high Volta potential difference between the intermetallics and the matrix [70]. Volta-mapping allows for the mapping of a surface's Volta potential, by scanning the electrical potential between different

points at a surface to and a specific point in air, for example the tip of a scanning Kelvin probe, a tool commonly used for Volta-mapping. The intermetallics with the highest Volta potential difference were those that have iron and copper present in the particle [70], such as Mg_2Si, $MgZn_2$, Al_7Cu_2Fe, Al_2CuMg, Al_2Cu and Al_3Fe. These intermetallics vary in size from angstroms ($MgZn_2$) to tens of microns (Al_7Cu_2Fe).

Several authors have attempted to categorise the different types of second phase particles present in 2XXX and 7XXX according to their micro-anodic or micro-cathodic behaviour against the aluminium matrix. Gao et al. [71] divides the constituent particles into two categories: 'A' particles, which act as anodic respect to the matrix and dissolve themselves. Whilst 'C' particles act as cathodic to the matrix and promote dissolution of the adjacent matrix. For AA7075, SEM and EDS have shown type 'A' particles contain Al, Cu, Mg, and Zn; and type 'C' particles contain Al, Fe, Cu, Mn and Zn. An example of a 'C' particle would be $Al_{23}CuFe_4$ [71] and of 'A' $MgZn_2$.

Birbilis and Buchheit [39] also classified intermetallics based on their electrochemical characteristics, cathodic or anodic, with respect to a high strength aluminium matrix:

- Noble particles with high electrochemical activity. E.g., Al_2Cu, Al_7Cu_2Fe. Where the corrosion potential of the intermetallic (E'_{corr}) is greater than that of the alloy's corrosion potential (E_{corr}) : $E'_{\mathrm{corr}} > E_{\mathrm{corr}}$, and with the ability to sustain high cathodic currents. These are the intermetallics thought to induce pitting corrosion in the surrounding matrix [39].
- Noble particles with low electrochemical activity. For example, dispersoid Al_3Zr. $E'_{\mathrm{corr}} > E_{\mathrm{corr}}$, but these particles are unable to sustain high cathodic currents [39].
- Active particles with high self-dissolution rates. E.g. $MgZn_2$. $E'_{\mathrm{corr}} < E_{\mathrm{corr}}$, with the ability to undergo dissolution at high rates [39].
- Active particles with low self-dissolution rates. No specific particles were observed, though Mg_2Al_3 may qualify in term of range of potentials [39].
- Active particles with a noble elemental component. For example, Al_2CuMg. De-alloying and incongruent dissolution may lead to polarity reversal. Therefore it can be selectively dissolved or lead to peripheral pitting [39].

In AA7X75 the coarse particle Mg_2Si and the precipitate $MgZn_2$ are sites for initiation of pitting; where the nobler particles such as Al_7Cu_2Fe would initiate pitting in the surrounding matrix [39][67][70][72]. Al_7Cu_2Fe in particular appears to be a dominant feature during pitting corrosion [39]. This intermetallic could sustain oxygen reduction reactions at high rates, three times greater than Al_2Cu and double that of $Al_{20}Cu_2Mn_3$ [39]. This leads to peripheral pitting of the intermetallic, with the bulk material as the anodic branch of this localised

corrosion, and this can happen at a potential range typical of the open circuit potential of these alloys in NaCl solutions [73]. The US FAA [2] adds weight to the idea of cathodic particles being more dominant in driving localised corrosion in AA7075-T651 due to the density of all second phase particles (1500 particles per mm^2) and that 80% of these are cathodic to the matrix [2]. Thus, the general consensus is that 2XXX and 7XXX aluminium alloy series contain intermetallics that act as both anodes and cathodes and can therefore cause different localised corrosion mechanisms [2][71][67][69]. Cathodic intermetallics, nobler than the bulk aluminium, will cause a ring of dissolved bulk material around the intermetallic. The reason for the trenching around the intermetallic could be due to micro-galvanic coupling or because of local pH elevation, or a combination of both of these. In some cases, if the trenching is severe, it can lead to the displacement of the intermetallic from the bulk material leaving a big cavity. In the case of anodic particles, this is dissolved leaving a cavity in the surface [67]. Figure 2-20 is a conceptual model showing the interactions of particles and the bulk material leading to localised corrosion [2].

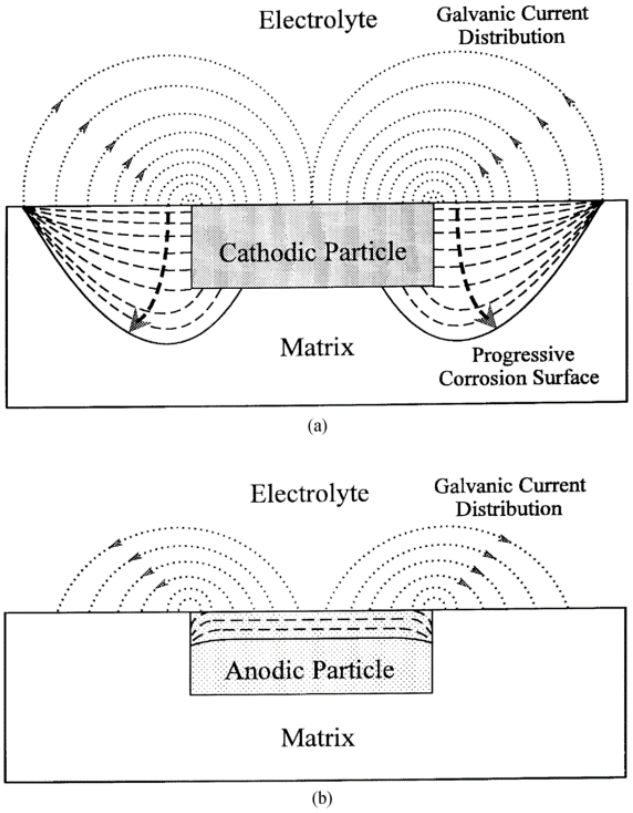

Figure 2-20 - Conceptual models of particle-matrix interactions. a) Cathodic particle, b) anodic particle (US DoT FAA, 2001) [2].

A third more complex corrosion mechanism of intermetallics occurs in some incongruent intermetallics, such as Al_2CuMg (S phase) and Mg_2Si. Here there is selective dissolution of

the more anodic element within the intermetallic [46]. For example for *S* phase (Al_2CuMg) this mean magnesium preferentially dissolving, leaving remnants of the nobler Cu at the bottom of the pit or near the particle site.

Aside from constituent particles, the 7XXX series alloy precipitates, $MgZn_2$, also appear to be important in corrosion mechanics due to being more anodic to the aluminium matrix, having no window of passivity and being finely dispersed throughout the material. In peak aged AA7075 these are also present in large quantities in grain boundaries, strongly affecting its resistance to intergranular corrosion [70][74][75].

On the other hand, it is also important to be aware of intermetallics that have little to no effect on localised corrosion in the alloy. Birbilis and Buchheit [39] found dispersoids did not appear to have a significant direct effect on localised corrosion susceptibility in high strength aluminium alloys; and that the literature available reveals no evidence of $Al_{20}Cu_2Mn_3$, Al_3Zr, Al_3Ti and $Al_{12}Mn_3Si$ having any adverse effect on the corrosion properties of commercial aluminium alloys. This may be, at least partially, due to the significantly smaller size of the aforementioned dispersoids in comparison to the Cu- and Fe-rich intermetallics, which are orders of magnitude larger in size and nominally capable of supporting oxygen reduction more efficiently [39].

2.6.7.1 Breakdown potentials in 7XXX alloys

As mentioned in Section 2.6.3, electrochemical polarisation tests are used to gain insight into the corrosion behaviour of a material in a particular corrosive environment. Potentiodynamic polarisation tests can show breakdown potentials in a material. A breakdown potential, or pitting potential, occurs when at a particular ‘threshold’ potential, the current density rapidly increases, pointing to the activation of a particular form of corrosion at the alloy’s surface.

There are two breakdown potentials in peak-aged AA7075 exposed to aerated NaCl: One which is approximately 50 – 60 mV above the free corrosion potential due to corrosion pitting and matrix dissolution [48][75][76] [77]. In this localised corrosion the solution can become acidified. For AA7075 in acidified solution it will suffer not only pitting but also intergranular corrosion, sub-surface pitting cracking and tunnelling [2][68][78].

There is a second breakdown potential soon after polarising above the free corrosion potential (-0.730 V). The cause of this has been previously attributed to grain boundary

corrosion due to higher nucleation of $MgZn_2$ (ɳ') precipitates at both grain interiors and grain boundaries [75]. However, later studies confirmed this was in fact due to an active surface layer that is susceptible to corrosion in polished AA7075. The surface is different to the bulk material as small hardening precipitates are absent and fine sub grains are present in tens of nm in size in the direction perpendicular to the final polishing direction, and hundreds of nm in size along the final polishing direction. Additionally, some nano-grains have higher concentration of Zn at the boundaries, possibly initiating activity and leading to grain dissolution [48][76] [77]. These presence of active surface Zn-rich bands after polishing depends on the ageing of AA7075, with peak aged alloys being susceptible [77].

2.6.8 Corrosion mechanisms in 7XXX aluminium alloys

This section attempts to summarise the main localised corrosion mechanisms for initiation and growth in 7XXX aluminium alloys, particularly for AA7075-T651. If immersed in a corrosive environment, such as a 3.5 wt.% NaCl solution, chloride ions within the solution will immediately start de-passivating the aluminium oxide that protects the bulk aluminium alloy [69]. Over time, hours or days, the depassivation will expose the bulk material to the corrosive environment, as seen in the schematic in Figure 2-21:

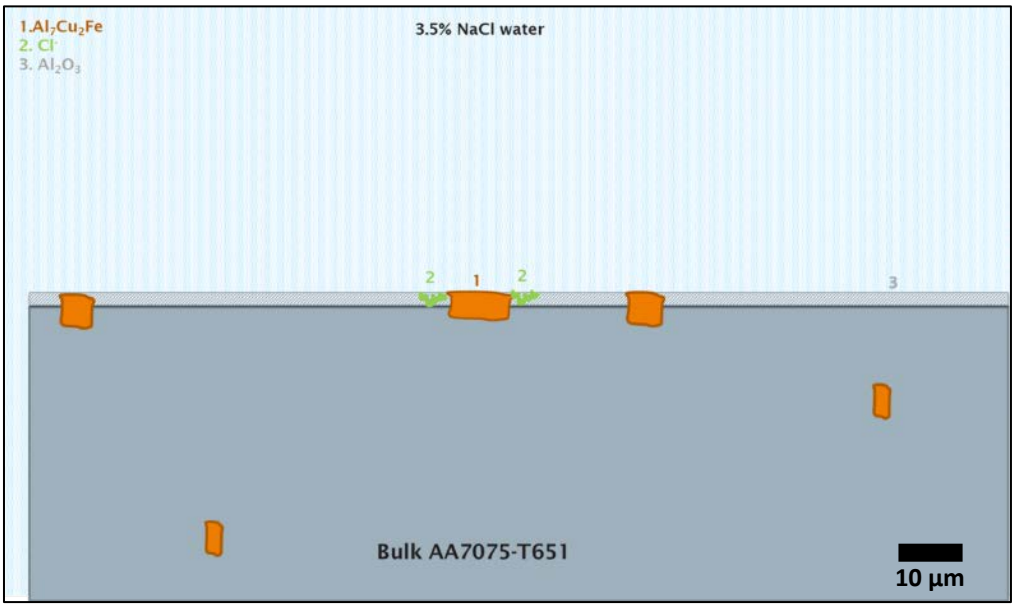

Figure 2-21 – Schematic of chloride ions de-passivating an aluminium alloy oxide layer.

If the surface has been mechanically polished the alloy's surface may suffer a transient uniform dissolution due to Zn rich bands in a nano-thin layer at the surface [48], [76]. Once this transient activity ends, the surface will become less electrochemically active until localised corrosion of the bulk material starts. According to the open literature,

strengthening precipitates $MgZn_2$ act as micro anodes, dissolving quite easily at the start of polarisation in a corrosive environment [39]. These act as micro-pits, which in the right environment can be incubators for pit initiation and growth [39]. The likelihood of these micro-pits becoming pits depends on the availability of corrosion promoters. This is where large cathodic and anodic intermetallics can act as current reservoirs, aiding in the electrochemical reaction. Thus, it is likely that micro-pits from $MgZn_2$ sites near intermetallics are the sites most likely to develop into pits due to their proximity to the cathodic intermetallics. This may explain why some cathodic intermetallics do not appear active (no material dissolution around it) whilst others are. Once micro-galvanic couplings are formed between bulk material and intermetallics this leads to the bulk material oxidising, with oxygen reduction at the cathodic particle, leading to bulk material dissolution around the cathodic particle, as shown in Figure 2-22. Intergranular corrosion also develops due to the presence of Zn-rich bands at the grain boundaries, leading to grain boundary and adjacent nano-grains dissolution. This stops once it reaches the bulk matrix which is less susceptible to corrosion [77]. Nevertheless, a mixture of intergranular corrosion near dissolution of $MgZn_2$ close to highly cathodic particles such as Al_7Cu_2Fe could lead to rapid (within days) formation of corrosion features that are mechanically damaging.

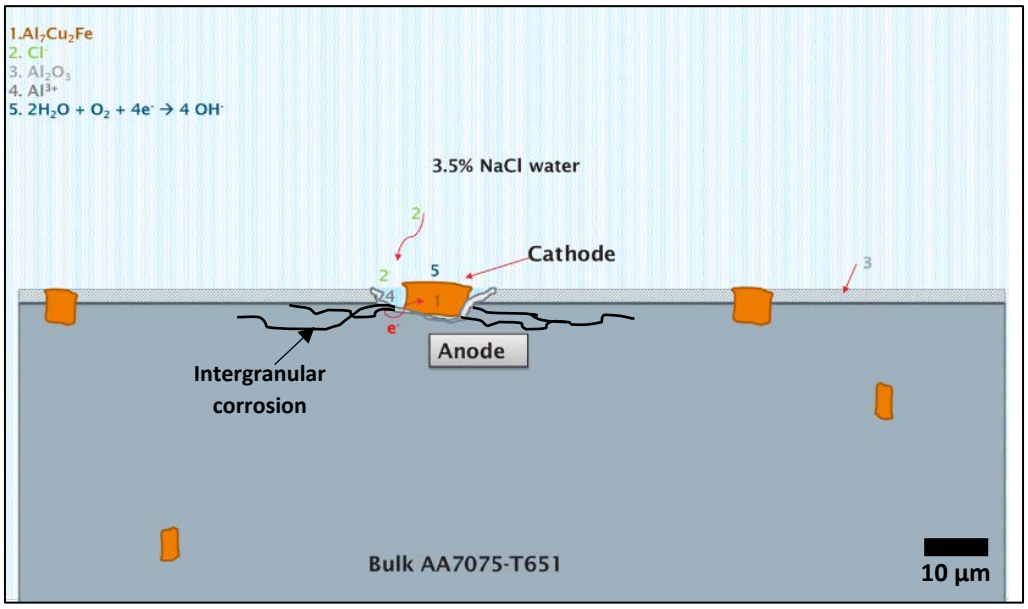

Figure 2-22 – Bulk material dissolution near cathodic particle.

As the dissolution of bulk material continues and a pit starts forming, the pit can become sufficiently large to lead to cathodic particle detachment from the bulk material. It may then float off into the solution or drop into the pit. Nevertheless, the pit has developed its own complex chemistry that is different from the rest of the solution, and any adjacent large

coarse intermetallics, in particular Al_7Cu_2Fe can act as dissolution promoters by sustaining large cathodic current densities [39][68]. The exact chemistry and what chemical reactions may dominate are still debated [63]. The pit becomes self-propagating or autonomous. It will continue to propagate for several hours or days, and there will be other cathodic particles present to act as locations for oxygen reduction. Figure 2-23 provides a schematic representation of the pitting process. Intergranular corrosion, can also develop into tunnelling and exfoliation corrosion [1][78][79] and is often present with pits.

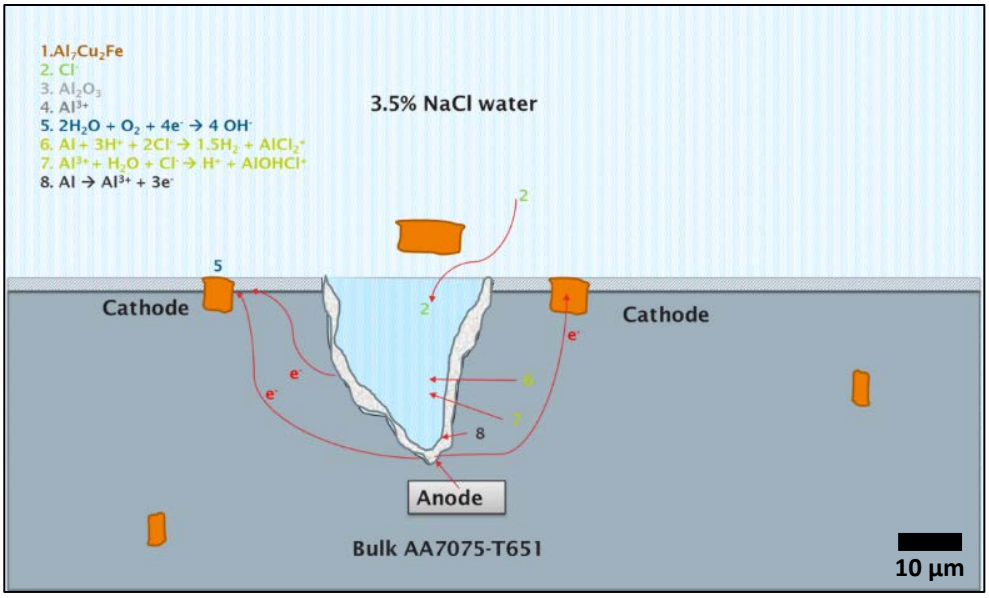

Figure 2-23 – Schematic of propagating pit in aluminium alloy.

In many pits, a layer of corrosion products builds up on the pit surface, partially blocking the entrance to the pit. This can serve as a shielding mechanism for the complex pit chemistry, by reducing the diffusion of substance between the pit and the rest of the environment. This can lead to the pit becoming acidic due to the evolution of hydrogen within the pit [63]. A schematic of this is shown in Figure 2-24.

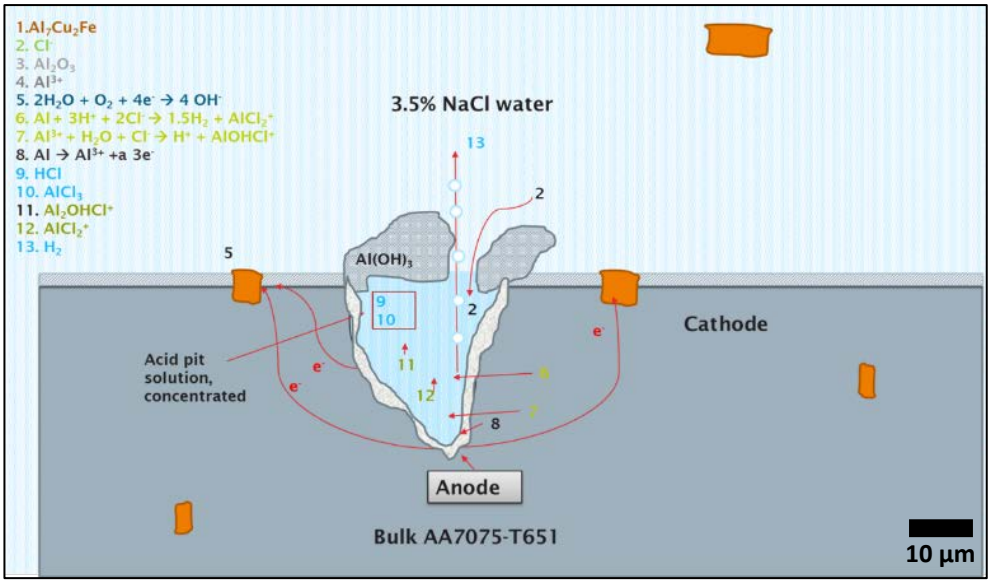

Figure 2-24 – Schematic of partially capped self-propagating pit.

Finally, a pit will cease to develop when its complex chemistry disappears. This can happen due to the pit becoming fully capped, which can stop the diffusion of chloride ions into the pit [63]. Alternatively, if cathodic particles cannot support the reduction of oxygen required to maintain the corrosion reactions occurring at the pit; or, if the material is removed from the corrosive environment and left in a neutral environment, see Figure 2-24. As mentioned previously, pitting corrosion will be one of several localised corrosion mechanisms occurring surface and sub-surface and the accumulation of all these different features increases the level of mechanical damage on the surface.

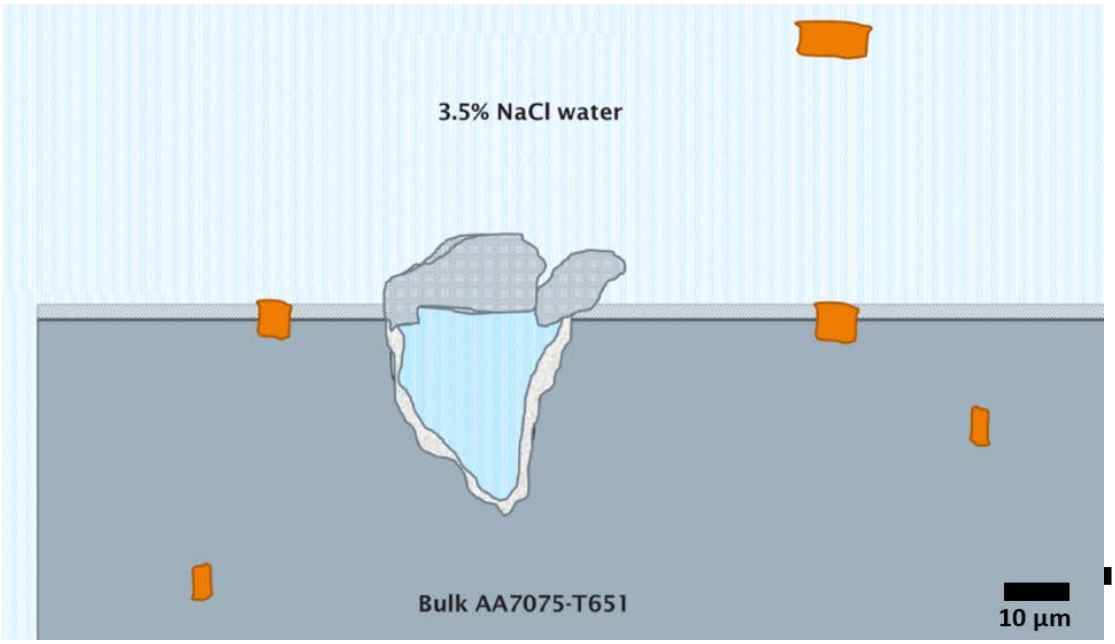

Figure 2-25– Schematic of dead pit due to being fully capped by corrosion product.

2.7 Fatigue performance in pre-corroded material

There are different ways a metal alloy can suffer from the combined effects of fatigue and corrosion. An alloy can be initially exposed to corrosion where features are then generated, removed from this exposure and subsequently suffer from fatigue loading. In this type of material degradation both corrosion and fatigue affect the material but at separate periods of time. In the literature this type of material degradation is named fatigue of pre-corroded material. In other scenarios, corrosion and stress act concomitantly, interacting in a more complex manner and often acting synergistically. If the metal alloy is undergoing corrosion and static loading it can suffer from stress corrosion cracking (SCC). If the metal is undergoing corrosion and dynamic loading it can suffer from corrosion fatigue. Numerous studies show that 7XXX series alloys are susceptible to stress corrosion cracking [80][81][82][83][84][85][86][87] and corrosion fatigue [80][88][89][90][91][92]. In the case of AA7075-T651 which is particularly susceptible to corrosion and relatively weak in terms of damage tolerance, it is known to be more susceptible to these phenomena than other tempers, particularly overaged tempers and its use in highly stressed areas or for thick components has been limited since the 1960s [14]. Although corrosion fatigue and SCC are serious issues in the aerospace industry and require deep understanding, the simpler problem of fatigue cracks initiating from pre-existing corrosion damage also requires better understanding. This PhD project aims to understand fatigue performance of pre-corroded AA7075-T651, as understanding of this simpler corrosion and fatigue issue (and the effects on this of laser shock peening) is deemed a necessary first step before delving into the more complex corrosion with mechanical stimuli phenomena. Thus, this chapter will not discuss corrosion fatigue or stress corrosion cracking any further, focusing only on fatigue of pre-corroded aluminium alloys.

Pits act as extreme forms of surface roughness, and can generate significant stress concentrations [93], as such dominating the crack initiation mechanism and replacing constituent particles that are known to be associated with crack initiation in aluminium alloys [30]. DuQuesnay et al. [20] studied the fatigue performance of pre-corroded AA7075-T651 under variable loading conditions. Although it is important to be aware this study applied relatively severe loading conditions, it showed pits as small as 100 µm can lead to a decrease in fatigue performance. Other studies with more standard loading regimes, such as that of Genel [94], found pits as small as 15 µm – 20 µm were big enough to initiate cracks under dynamic loading.

Although there are studies, such as those of DuQuesnay and Genel [20][94], that show the most important relationship to fatigue degradation is pit depth; there are other studies reporting maximum pit depth is not necessarily an indication of a crack initiation site. Proximity to other pits, pit surface area and pit geometry are also important in determining the effectiveness of a pit as a stress concentration [95][79][96] and thus influence in fatigue degradation.

In terms of the level of fatigue life loss, Burns et al. found strong evidence that time to crack initiation tends to zero cycles with increasing maximum stress [97]. While Co and Burns [95] show at maximum applied stresses over 200 MPa the crack initiation time can be considered negligible, as can be seen in Figure 2-26.

In terms of crack propagation, several studies have shown it is very common for there to be multi-site crack initiation depending on the maximum stress [93][98], which leads to either single-crack fracture, multi-crack competition or multi-crack parallel growth [93]. In addition, the more severe the corrosion the more cracks are able to initiate due to more stress concentration sites being available, and these cracks tend to coalesce, affecting the main crack path [99][100]. According to Medved et al. [101], who fatigued clad AA7475, the pits greatly reduce the time it takes to reach a 100 µm crack depth due to multi-site initiation resulting in irregular growth. After 100 µm, or as the crack moves away from its initiation point, crack growth converges to comparable crack growth rate for corroded and uncorroded aluminium [95].

Overall, considering both loss of crack initiation and crack propagation time, the reduction in total fatigue life by corrosion pits in pre-corroded aluminium alloys varies from 27% to 60%, depending on the level of corrosion exposure (the size and shape of corrosion features) and the subsequent dynamic loading regime [30][93][101][94]. Therefore, the aerospace industry is always striving to either limit the material's exposure to fatigue and corrosion wherever possible, or more realistically, enhance its fatigue and corrosion resistance. There are many ways to achieve this, and one of the most common approaches is to use surface treatments for fatigue-enhancement.

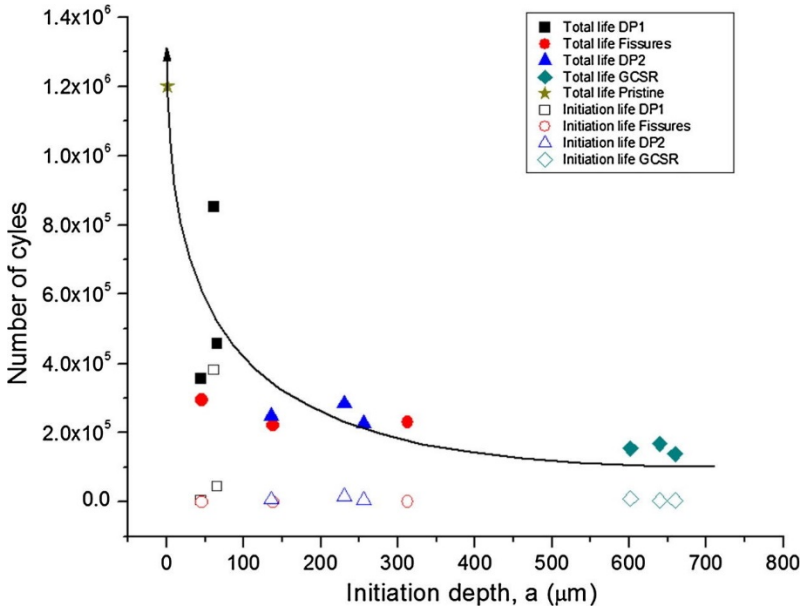

Figure 2-26 – Total fatigue life and initiation time of pre-corroded AA7050-T7451. DP1 and DP2 stand for discrete pits, GCSR stands for general corrosion with surface recessions (Co and Burns, 2017) [95].

2.8 Fatigue-enhancement by surface treatment

There are many types of surface treatments, used for various industrial applications and/or objectives, for example to improve wear resistance, corrosion protection, and avoid other forms of environmental degradation. Surface treatments are also commonly used to improve fatigue performance. One of the most successful approaches to fatigue enhancement surface treatment is by inducing beneficial compressive residual stresses in a component.

2.8.1 Residual stresses

Residual stresses are self-balanced forces in a material existing without external forces being applied. They are generated by creating inhomogeneous plastic deformation via thermal or mechanical loads [102]. They can be generated in components either intentionally by the use of surface treatments such as shot peening; or unintentionally by manufacturing processes such as casting, forging, milling, etc. They can also be generated by pre-service or in-service loading.

Tensile residual stresses are generally known to be detrimental to fatigue performance as most failures in fatigue are caused by tensile loads. Thus, tensile residual stresses exacerbate fatigue damage by acting in concert with applied loads, increasing the tensile stress levels experienced locally. In contrast, compressive residual stresses acting in areas of tensile loading can slow fatigue crack initiation and growth by reducing the mean stress during fatigue, as well as by their magnitude, gradient and position relative to locations for crack initiation [103][104]. Residual stresses can also affect cyclic fatigue crack growth and this depends on the crack size (they can have a greater effect on short crack growth than long cracks), mechanical load variables, and the environment [103]. Thus, it is common to add steps to manufacturing processes to eliminate harmful tensile residual stresses and/or to add beneficial compressive residual stresses to safety critical areas [105].

It is important to understand the level of residual stresses present in a component, to better assess how it may affect performance. Several residual stress measurement techniques exist today, and these can be either destructive or non-destructive. Destructive techniques are based on removal of material and measuring the consequent elastic stress relaxation and associated strain [106][107]. Non-destructive techniques are based on microstructural characterisation such as atomic-*d* spacing (distance between crystallographic planes) or responses by the material to sound or magnetism. The most commonly used destructive

techniques are hole drilling, slitting and the contour method. Non-destructive techniques are X-ray diffraction, synchrotron X-ray diffraction, neutron diffraction and Raman spectroscopy [105][107][108].

One of the most well established surface treatments used for compressive residual stress generation is shot peening, whilst a relatively newer treatment is laser shock peening. To be able to assess their effect on fatigue lifetimes accurately, detailed knowledge of residual stress profiles generated by these surface treatments are required to generate fatigue life models that accurately incorporate the effects of residual stresses fatigue crack initiation and growth.

It is common nowadays for residual stresses to be reconstructed in finite element (FE) modelling. Both LEFM and EPFM have been used to modify dependent variables (such as $\Delta\sigma$ and ΔK) taking into account the effects of residual stresses. This includes accurate prediction of residual stress relaxation behaviour as neglecting this can result in fatigue life overestimation [109]. FE modelling has been increasingly used in residual stress reconstruction as its advantage over analytical approaches includes: the ability to investigate specimens with complex geometries and its effectiveness in reconstructing 2D and 3D profiles in the FE model; although the effectiveness strongly depends on the reliability of the experimental data input. One approach to introduce residual stresses into the FE model is the inverse Eigenstrain approach [110][111]. This requires prior knowledge of the existing residual stresses in the component of interest. Thus, experimentally acquired residual stress data is used to validate the inverse Eigenstrain approach and may require several iterations to reconstruct the 'best fit' compared to the experimental data. The FE model can then extrapolate residual stresses to the whole region of interest, and thus complement the discrete experimental data points, building a bigger picture of the residual stress profile generated by the surface treatment. By using FE modelling to then apply the relevant dynamic loading conditions selected driving parameters (e.g. $\Delta\sigma$, $\Delta\varepsilon$ and ΔKef) can be accurately calculated. Based on this, an effective lifing approach (total life or damage tolerant) can be applied to predict total life of the material. The available literature on fatigue life prediction and residual stress reconstruction of metal alloys is vast and diverse. As fatigue life prediction is not directly performed in this PhD project this topic is not discussed further. The reader is directed towards the literature review by Smyth [105] and You [109] for more information on fatigue life prediction approaches and residual stress reconstruction in metal alloys containing residual stresses.

2.8.2 Shot peening

Shot peening is a pre-stressing process that has been used for many years to strengthen metal machine parts against stress corrosion and fatigue failure. Some of the most commonly shot peened components are aircraft wings and empennages, as well as weld joints due to the significant (tensile) residual stresses introduced during welding [112].

Shot peening improves fatigue life by producing compressive self-stresses in the regions to which it is applied [113]. This is accomplished by firing a stream of small steel shots using a compressed air jet which bombard a surface. This is the equivalent of applying many tiny hammers onto the surface, where the kinematic energy of the shot indents the surface and causes it to yield (locally) in tension. After the shot rebounds from the surface the mismatch between the plastically deformed surface and the elastically unloading bulk material underneath, causes a compressive residual stress in the near surface region of the component [114]. These compressive stresses counter-balance existing or applied tensile stresses in the component. Therefore, shot peening is widely used in highly stressed components or in areas where there are high stress concentrations. As most cracks initiate at stress concentrations on the surface this provides resistance to both crack initiation and propagation, leading to an increase in the fatigue life of components. Shot peening has been an effective and widely used surface treatment that is relatively inexpensive, and uses robust and durable process equipment. However, its drawbacks are that its process is semi-quantitative in terms of determining the degree of compressive stresses or surface work hardening produced, and it induces roughness on the surface. Often this roughness needs to be removed prior to service, if this surface removal is extensive the beneficial compressive residual stresses can be decreased [115].

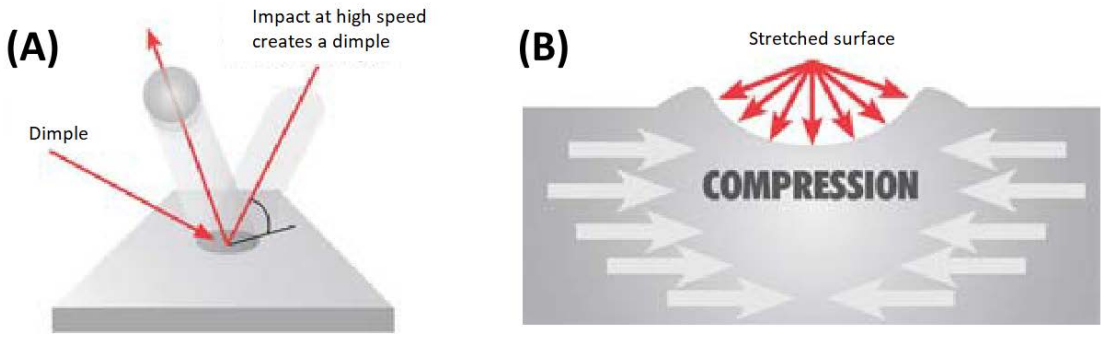

Figure 2-27 - (A) Dimple creation on material surface during shot peening and (B) formation of compressive residual stress around dimple (Smyth, 2014) [105].

The improvement of fatigue life by shot peening in different metal alloys is well documented [116][117][118][113][119][120][121][122][123][124][125][115]. It is understood improvement in fatigue life is mainly due to a delay in crack propagation. Crack initiation improvement is limited mainly due to surface roughness increases induced by shot peening, which if lightly polished can lead to a further improvement in fatigue life, presumably due to the decreased roughness and therefore increased crack initiation time [115]. See the further discussion in section 2.8.5 and section 2.8.6 on the effects of shot peening and laser shock peening on fatigue and corrosion performance, respectively.

2.8.3 Laser shock peening

Laser shock peening is a relatively new technology that is rapidly becoming a common surface treatment for the improvement of fatigue performance of metallic components, in particular in the aerospace industry. It is a very similar technique to shot peening in terms of the expected physical outcome of applying it to a surface, which is to generate a field of compressive residual stresses.

The first high-energy laser beams to produce recoil pressure by vaporising metal surfaces were achieved in 1960s, and in this decade there was considerable work performed to understand the physics behind laser induced shock waves. It was in the 1970s that laser shock peening was explored as a treatment to improve the properties of metal alloys. From then on a considerable amount of work has been done, supported by the automotive and aerospace industries, to study the laser-material interaction processes, in particular to improve fatigue and wear resistance [7]. For more information on the history and development of laser shock peening please see Clauer [126].

Laser shock peening (LSP) surface treatment works by inducing deep compressive residual stresses in a metal surface, increasing the hardness and yield strength of the material, improving fatigue performance under tensile loads. This is achieved by firing high intensity laser beams into the metal surface, causing material to evaporate due to the target surface being heated by the laser pulse [127]. Depending on the type of laser used, and the material to be peened, the range of laser power can be as low as 0.1 joules (J) and as high as 100 J; a pulse can be between 5 nanoseconds (ns) to 30 ns. The laser consists of an optical chain of mirrors and lenses that are used to direct the laser beam onto the surface part to be treated. As seen in the schematic in Figure 2-28, it is common in laser shock peening to have two types of overlays, one transparent, often called an inertial tamping layer; and one opaque, often named an ablative layer. The opaque overlay is placed directly on the surface to be peened and is commonly a black coating used as a thermo-protective layer. The transparent overlay is placed on top of the opaque overlay and is commonly water. The laser beam is fired into the transparent overlay, passing it and hitting the opaque overlay, which absorbs the energy and vaporises. The vapour then continues to absorb the laser beam energy, causing it to rapidly heat and consequently expand. As it is not able to expand outwards due to the space constraint from the transparent overlay, it causes it to increase in pressure and expand towards the material's surface as a shock wave. If the shock wave has a higher peak stress than the dynamic yield of the material it will cause the material to

plastically deform. The stress wave will propagate through the material and cause the material below the surface to deform as long as the wave's peak stress is above the dynamic yield of the material. At some depth, it will have dissipated enough to be below this dynamic yield and the deformation will stop. The deformation caused by the shock wave causes the material to strain harden, and compressive residual stresses are formed at the surface of the workpiece as well as below it, to a specific depth [127][6][7][3][4][5]. This increase in material properties is largely attributed to an increase in dislocation density [128][129][130][5][131][132][82]. There a number of studies that also attribute some of the improvement in yield strength and hardness to grain refinement [82][128][129][130][133][134].

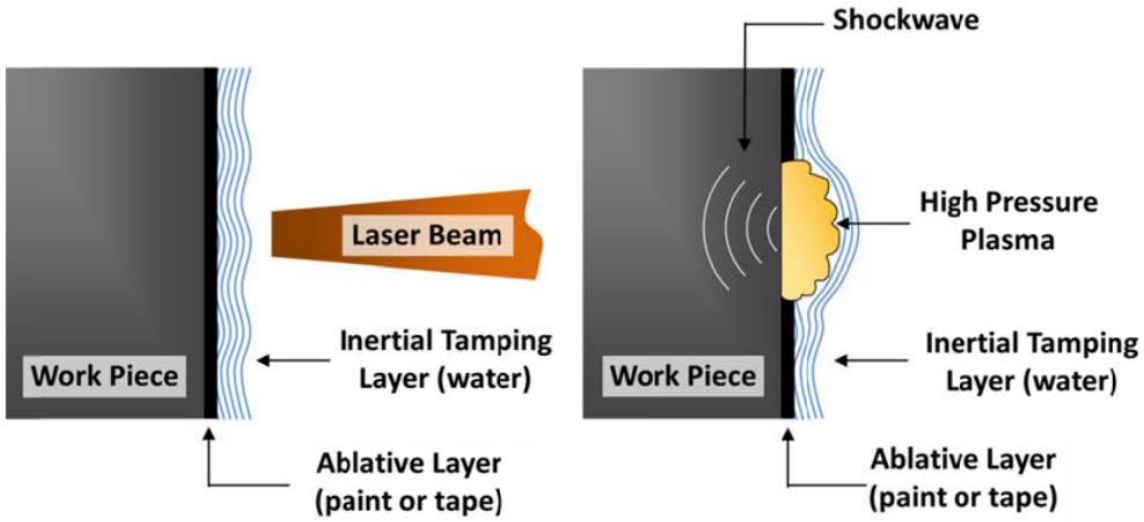

Figure 2-28 – Schematic of the LSP process (Smyth, 2014) [105].

Nowadays, two methods for laser shock peening are considered in existence: Laser shock peening with ablative coating (LSP), and without ablative coating (LSPwC). The more recently developed laser shock peening without ablative coating was originally developed for underwater laser peening to prevent stress corrosion cracking in power generation [135]. It has become increasingly interesting to industry in part due to reduction in setup time and therefore reduction in costs. In LSPwC a thin layer of the material's surface is ablated, generating the plasma shock wave which then imparts compressive residual stresses. This removes the need for an ablative layer and all the related setup logistics. Advantages of LSPwC versus the standard laser shock peening with ablative layer (hereinafter called LSP) are the ability to employ compact and commercial available lasers, deliver laser pulses through flexible optical fibre, ability to irradiate laser pulses to water immersed objects and a reduction in peening-processing time [135]. Aside from the expected fatigue improvement, some studies have also found LSPwC may improve the overall corrosion properties of

treated materials, despite a higher increase in surface roughness [136][137][138]. This is discussed further in section 2.8.6. In LSPwC grain refinement appears to be more prevalent due to ablation of the surface [132]. Additionally, there are studies that state the surface tends to be made more homogeneous due to plastic deformation removing or masking coarse constituent particles after LSPwC [134]. In LSP (with an ablative layer) this appears to be less likely, as studies with microscopy observation of the microstructure after laser peening have shown no apparent change in the number or size of second phase particles [139].

Aluminium alloys are used extensively in the aerospace industry and, naturally, LSP treatment is seen as a promising method for improving fatigue life of aerospace aluminium components [3]. There are several benefits to choosing laser shock peening over shot peening aluminium alloys, including: greater accuracy and precision [3][6][7]; greater depth and magnitude of the subsurface compressive residual stresses [3][6][115][140]; beneficial decrease in detrimental surface modification; and fatigue life improvements [3][8][9].

The effectiveness of laser shock peening on fatigue life of any alloys, including aluminium, depends on the combination of laser parameters chosen for a specific type of material, with the aim to minimise surface modification (particularly roughness) and maximise compressive residual stress, which in turn maximises fatigue life. Nevertheless, there are several laser shock peening parameters to consider (power density, spot shape, spot overlap, energy, etc.). Thus, knowing the appropriate combination of laser shock peening parameters prior to treatment is important for each specific material [3][7]. For further information on laser shock peening please see the following review papers by Montross et al. [10], Clauer and Lahrman [141] and Peyre et al. [142]. A brief description of the parameters used is given below:

Laser type: The gain medium used in the laser system to amplify the laser from its source. The most common types are Nd:YLF, Nd:YAG and Nd:Glass.

Wavelength: of the laser light. The most common are 355 nm (ultraviolet), 532 nm (green) and 1064 nm (infrared).

Laser frequency: refers the number of laser pulses per second and is measured in Hz.

Application time: is the duration of one laser pulse and is measured in nanoseconds.

Laser spot geometry: is the shape of the laser contact area on the surface of the component. It is common for this to be either circular or square.

Laser spot size: is the diameter of the circular spot or the width of a square spot.

Energy of the laser beam, measured in joules.

Power density: is the power per unit area of the laser beam. It is calculated according to Equation 2-9 and expressed in W cm^{-2}.

Equation 2-9

$$\text{Power density} = \frac{\text{Energy (J)}}{\text{Pulse time} \times \text{Laser spot area}}$$

Overlap: is the percentage area that is spot overlap when peening, and is done to avoid heterogeneity at the edges between adjacent peened spots.

Number of impacts or repeat impacts, are the number of laser peening impacts performed on the same area.

2.8.3.1 Laser shock peening residual stresses in aluminium alloys

Several authors, including Peyre et al. [8], Dorman et al. [143] and Zabeen et al. [144], showed the maximum, and the depth, of residual stresses generated in aluminium alloys depend on the laser peening parameters. Particularly the power density and number of repeat impacts, shown in Figure 2-29. Although some studies quote energy instead of power density, these two are linked as shown in Equation 2-9, and thus higher energy laser also leads to an increase in level of residual stresses [145]. Most of the laser shock peening parameters have been shown to vary residual stress generation. These include overlap, spot size, spot geometry, type of coating, etc. [146]. However, there can be a limit to the maximum residual stresses that can be generated for a given material. At some point, due to reverse yielding, increasing power density will not generate higher residual stresses [144] and has even caused internal cracking, damaging fatigue performance [147]. Therefore, to generate the maximum residual stresses at the surface and subsurface, laser shock peening parameters require not maximisation, but optimisation. This optimisation is required

for each aluminium alloy and temper [8]. For example, for a given set of laser peening parameters, under and over-aged alloys will see higher deformation and generation of residual stresses compared to peak aged alloys [148]. This is attributed to the fact that peak aged alloys are already near saturated with dislocations, and thus laser shock induced dislocations are more limited.

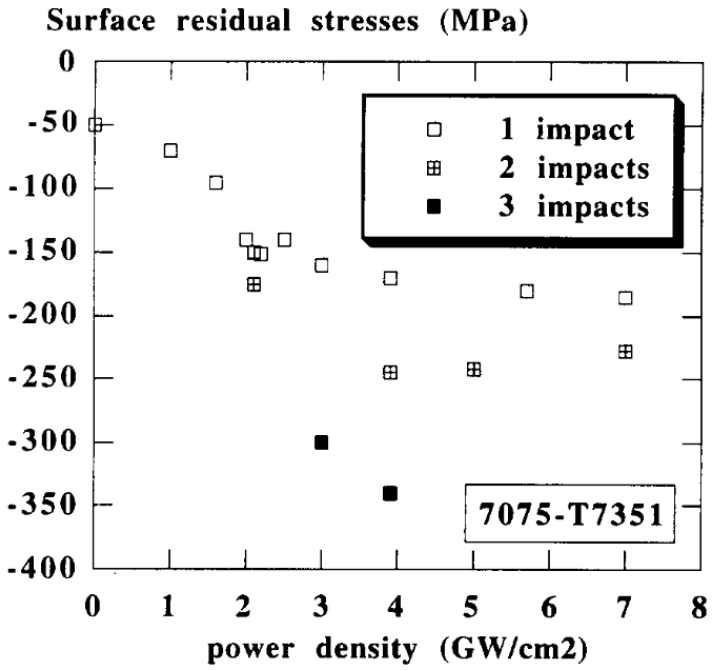

Figure 2-29 – Laser shock peening surface residual stresses in AA7075-T7351 for different power densities and repeat impacts (Peyre et al., 1996) [8].

2.8.4 Laser shock peening material modification

It is evident that, as with shot peening, laser shock peening will modify the shocked material at and below the surface. As well as varying residual stress, varying levels of surface roughness and hardening after LSP treatment have been seen in previous studies of aerospace grade aluminium alloys, including 7XXX alloys. This is discussed below with a focus on aerospace grade aluminium alloys.

2.8.4.1 Effects on surface roughness

It is well established that higher surface roughness detrimentally affects fatigue performance of a material. The surface roughness features act as high stress concentrations and thus are a source of crack initiation. Studies on aluminium alloys with rough surfaces have shown cracks usually are initiated by coarse constituent particles. However, surface roughness features will exacerbate the stress concentrations at these locations, decreasing the time it takes for fatigue cracks to initiate. Thus, there will be an inverse relationship between surface roughness and fatigue life [52][149][150][151][105][125][152]. This is shown to be most pronounced in high cycle fatigue where a major part of the total life is in crack initiation time [52][153].

It is known many types of surface treatments can increase surface roughness, and this includes shot peening and laser shock peening. The surface roughness competes against any fatigue-enhancement generated by the treatments: Several studies use surface treatments to introduce compressive residual stresses whilst acknowledging this will increase surface roughness [8][125][154][152][155]. However, it is difficult to disentangle the specific contributions to fatigue performance of beneficial compressive residual stresses and detrimental surface roughness, and whether there is a cut-off point where surface roughness becomes active.

As with residual stresses, the extent of surface roughness will vary depending on the laser peening parameters used. In particular, power density and number of repeat impacts, as increasing these will increase the level of plastic deformation [154]. Additionally, there have been studies where surface characterisation after laser shock peening has identified possible small defects, or damaged zones, caused by the surface treatment and associated to shock wave pressure [125][154][156].

One of the often-cited advantages of laser peening is the improved surface roughness in comparison to shot peening [115][6][148][9]. Peyre et al. [8] performed laser peening with ablative coating on AA7075-T7351 and compared it to a standard shot peening treatment. Increased roughness was the main difference between them. As shown in Table 2-8, shot peening sees a considerable increase in surface roughness, particularly R_t. In comparison, laser peened surfaces sees only a doubling in R_a and R_t parameters from as-milled. Laser peening also leaves 5 µm – 15 µm homogeneous depressions.

Table 2-8 - Comparative roughening effects of LSP and SP on A356 and 7075 alloys [8].

Material and processing	R_a (µm)	R_t (µm)
A356 as milled	0.7	6.2
A356 + SP F38-50 N (0.3 mm beads)	5.8	33
A356 + LSP 2 GW cm^{-2} (2 impacts)	1.1	7.5
7075 as milled	0.6	5.2
7075 + SP F20-23A (125%. 0.6 mm beads)	5.7	42
7075 + LSP 4 GW cm^{-2} (3 impacts)	1.3	11

Similar surface roughness comparisons have been found in other studies, including aluminium alloys. Hatamleh, Lyons and Forman [157], compared laser peening and shot peening on stir-welded AA7075-T7351. Their 2 GW cm^{-2} laser peening treatment had little effect on surface roughness (R_a = 0.24 µm for baseline, R_a=0.347 µm for laser peening), compared to shot peening which led to comparatively significant change in roughness (R_a = 3.865 µm). Becker [115] investigated this on AA7075 annealed and T6 temper, also finding surface roughness to be worse for shot peening (R_a = 8.53 and 11.49 µm, for T6 and annealed, respectively) compared to laser peening (R_a = 2.28 and 3.29 µm, for T6 and annealed, respectively). There is a general consensus that laser peening on aluminium alloys has a significantly lower surface roughening effect compared to shot peening, and that this is likely to give laser peening an advantage over shot peening in terms of fatigue performance.

Finally, Becker [115] and Hill and Luong [125] performed fatigue tests on lightly polished laser peened AA7XXX samples and compared them to un-polished samples. All polished samples had a considerable increase in fatigue life compared to unpolished laser peened. This highlighted how even with laser peening the small to moderate surface roughness increase does lead to fatigue life reduction. In addition, it shows laser peening compressive residual stresses are deep enough to not be significantly affected by small amounts of

surface removal. This opens the possibility of polishing as a post-laser peening step to remove surface roughness and further improve fatigue life.

2.8.4.2 Effects on hardness

As with residual stresses and surface roughness, surface hardness has been shown to increase with an increase in laser peening parameters such as power density and number of repeat impacts [8][154]. For example, Peyre et al. [8] performed a 2 GW cm^{-2} laser peen on over-aged AA7075-T7351, and compared it to a standard shot peening surface treatment on the same material. Whilst shot peened AA7075-T7351 hardness increased 20%, the laser peened material was subject to only a 10% increase. A more recent study on laser peening of AA7075-T6 [115], suggests laser peening on AA7075-T6 produces severe surface plastic deformation, but only limited evidence of hardness increase. An equivalent shot peening treatment does give an increase in AA7075-T6 hardness, attributed to longer pressure duration resulting in greater plastic deformation. This may be due to differences in surface treatment pressure duration resulting in higher dislocation generation and motion, and higher numbers of activated slip planes by the shot peening treatment. However, no further surface characterisation work is performed, although TEM is suggested as a possible method to confirm this.

It is apparent that for most aluminium alloy tempers, laser shock peening leads to surface hardening [158][144]. However, some studies on peak aged alloys have shown no change [8][115][148]. Fairand and Clauer [4] showed underaged AA7075 alloy experienced surface hardening from laser peening, but both 2XXX and 7XXX (including 7075) peak aged alloys did not see any surface hardening effects when using comparable power densities as the underaged alloys. They hypothesise that precipitation hardening in peak aged aluminium alloys is significantly high enough to mask any shock wave strain hardening. It is also hypothesized there would be a threshold power density where, above this, a peak aged aluminium alloy would experience surface hardening [4]. Thus, it is apparent from the previous studies that for a given material (and temper) the combination of parameters needed to generate surface hardness, will vary. Furthermore, that increase in surface hardness does not necessarily indicate high residual stresses or correlate with higher fatigue performance, particularly as laser peened peak aged alloys with no surface hardening have shown beneficial fatigue life improvements [8][115][148]. In contrast, for under-aged or over-aged aluminium alloys, surface hardening would also improve fatigue performance in addition to the generated compressive residual stresses. However, these studies also suggest the effects of surface hardening on fatigue life may be minor compared to the effects of surface roughness (negative) and particularly compressive residual stresses (positive) [8][148][115].

2.8.5 Effects on fatigue behaviour

Considering the different laser peening treatments and their different effects on each alloy and temper, the effectiveness of these on fatigue performance would be expected to vary considerably. The available literature indicates varying improvements in peened 2XXX alloys [143][144], [159][160] and 7XXX alloys [161][6][8][155]. In the case of AA7075, studies show fatigue life improvements have varied from 11% to over 100% compared to untreated samples [6][115][162][157].

In terms of crack initiation mechanism, a number of studies have seen changes due to laser shock peening. Zhang *et al.* [155] and Gao [140] found peened AA7075-T6 and AA7050-T7451 fatigue life improvements attributed to a change from surface (for untreated) to sub-surface crack initiation. Nevertheless, this change in crack initiation mechanisms has not been seen in most peened aluminium alloy studies surveyed. One study on a high-carbon chromium-bearing steel alloy showed how changing the mechanism of fatigue crack initiation from the surface to subsurface (not due to laser peening effects) was directly linked to a change from low to ultra-high cycle fatigue regime. In addition, this fatigue life improvement due to a change in mechanism of crack initiation was most pronounced at higher applied stresses [163], suggesting the fatigue life improvement is strongly linked to a considerable delay in crack initiation time (see Figure 2-30). A study by Shiozawa et al. [164] on the same steel showed how shot peening residual stresses can cause this same change in fatigue regime but for higher applied stresses, significantly increasing their fatigue performance, as seen in Figure 2-31.

In terms of laser peened materials, Zhang et al. [155] and Gao [140] report subsurface crack initiation will not necessarily lead to a change in fatigue regime, suggesting there are other factors affecting fatigue life. For example, the peening by Gao [140] results in relatively shallow compressive residual stress profiles, and the subsurface crack initiation point starts in an area with expected tensile residual stresses, resulting in a modest increase in fatigue life (10^4 to 10^5 cycles). Consequently, although crack initiation is subsurface, the surrounding tensile residual stresses may contribute to a relatively fast crack initiation and propagation, and thus lead to a low cycle fatigue regime. This behaviour would be expected to vary depending on the residual stress profile, the loading conditions and the surface state.

Other relevant laser shock peening studies do not report changes in micro-mechanisms of fatigue crack initiation and therefore attribute fatigue life increase to a delay in crack initiation

and crack propagation time. For these fatigue life improvements, with no change in mechanisms, the change is no higher than an order of magnitude, as can be seen in the study performed by Luong and Hill [156] on AA7085 (see Figure 2-32).

It is clear from the discussion in section 2.5.1.2 that surface roughness and any other induced surface features will have a detrimental effect on fatigue performance. It is also understood, and discussed in section 2.8.4.1, laser shock peening will induce surface roughness and this will increase the likelihood of cracks initiating at the surface. Nevertheless, changing the micro-mechanism of crack initiation is possible despite surface roughness increases. A study by Oguri [165] with fine particle shot peening showed how, despite relatively low compressive residual stresses compared to shot peening, by limiting surface roughness, crack initiation is moved subsurface.

Overall, it is yet unclear the extent to which roughness, hardness and the level of laser shock peening residual stress, *individually* contribute to the overall fatigue life improvement, and how each of these influence the possible change in micro-mechanisms of crack initiation and propagation in aluminium alloys after LSP treatment.

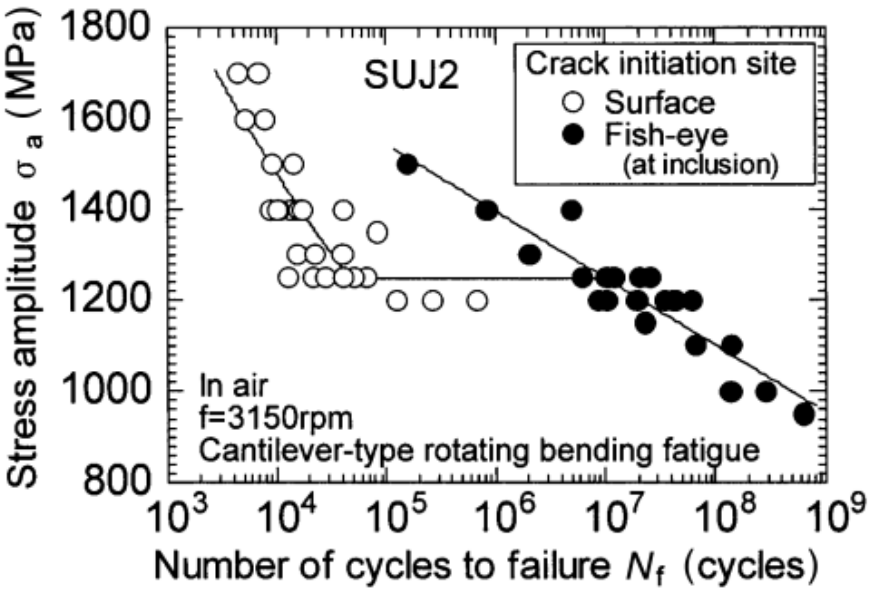

Figure 2-30 – Differences in fatigue life of a high carbon chromium-bearing steel. Subsurface (fish-eye) crack initiation leads to high cycle fatigue regime compared to surface cracks (Shiozawa et al., 2001) [163].

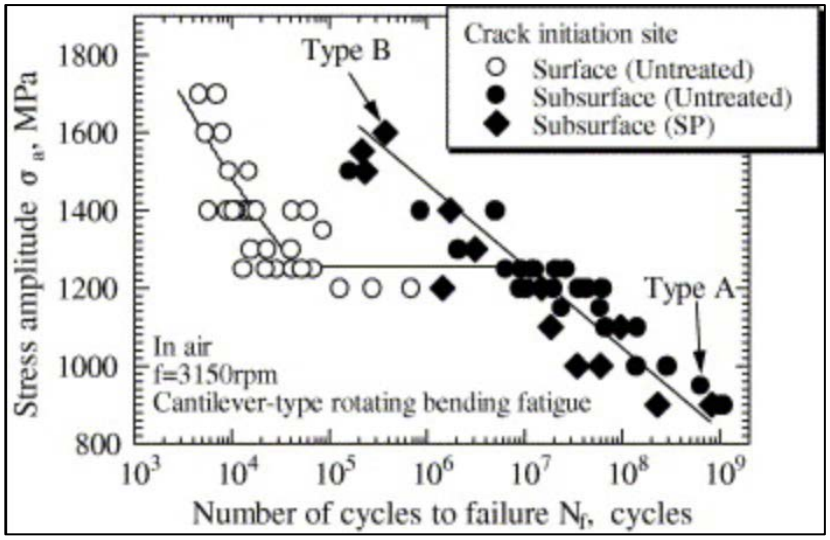

Figure 2-31 - The S–N curves of high-carbon–chromium bearing steel, untreated and shot-peened (Shiozawa et al., 2006) [164].

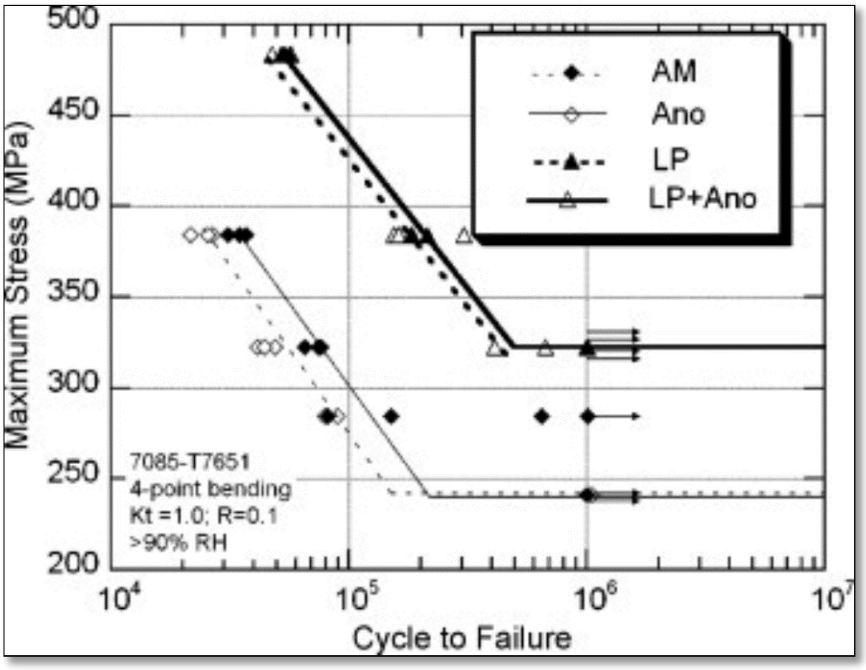

Figure 2-32 - 7085 S–N curves for all surface conditions. Run-outs are indicated by arrows, with grouped arrows indicating multiple run-outs at the same stress level. AM is as machined, untreated. Ano is anodised. LP is laser peened. LP+Ano is laser peened and anodised (Luong and Hill, 2008) [156].

2.8.6 Effects on corrosion behaviour

Considering the susceptibility and exposure of aluminium alloys to corrosive environments in the aerospace industry [1], and the increased use of laser shock peening for fatigue improvement of aerospace components, it raises the question of whether laser peening can have an effect on corrosion performance. AA7075-T651 is known to be particularly susceptible not only to SCC, but also localised corrosion, such as pitting and intergranular corrosion [14]. It has been established that compressive residual stresses are beneficial in retarding corrosion phenomena that requires mechanical stimuli, such as stress corrosion cracking [80][81][82][83][84][85][86][87] and corrosion fatigue [80][88][89][90][91][92]. This appears to be primarily due to the effect of residual stresses acting specifically against mechanical stimuli. In terms of effects of residual stresses on pre-corroded material (material exposed to corrosion to generate features and then removed from exposure prior to fatigue) literature review was challenging as it is dominated by papers on corrosion with mechanical stimuli. One specific study by Lv et al. [166] is highlighted as it shows shot peening residual stresses improves fatigue life of pre-corroded AA7075-T7451. Although it demonstrated higher peening intensity increased fatigue life, this improvement was within the same magnitude (from an average of 20,000 cycles in baseline to near 30,000 for the highest peening intensity). Additionally, it showed crack initiation was always at corrosion pits regardless of the residual stresses present.

In the case of electrochemical process without mechanical stimuli, such as pitting and intergranular corrosion, the effect of residual stresses is more nuanced. The literature review showed limited number of studies focused on the effects of laser shock peening with ablative layer (LSP) on corrosion performance without mechanical stimuli of aluminium alloys. Peyre et al. [167] found a decrease in cathodic currents in NaCl + Na_2SO_4 solution after LSP. Krawiec and Vignal [168] showed LSP improved the electrochemical impedance of AA2050-T8 in sodium chloride solution and this is attributed to residual stresses. They came to this conclusion due their finding that LSP did not change the impedance at areas where the matrix contained constituent particles, which are considered the main mechanisms for localised corrosion. In contrast, Amar et al. [139] found LSP increased pitting potential at constituent particles by -50 mV, whilst the aluminium matrix was passive due to compressive residual stresses. In addition, although there was an increase in pitting potential there was a favourable decrease in intergranular corrosion, attributed to compressive residual stresses. Thus, surveying the limited number of studies shows contradictory and limited evidence whether LSP does have an effect on corrosion

performance and there is evidence whether this is due to the compressive residual stresses, the effect on local microstructure, the matrix or the combination of all or some of these.

There are more numerous studies that report LSPwC can improve corrosion performance. For example, studies on laser peened aerospace aluminium alloys [169][170] and aluminium-silicon alloys [171] show improvement in pit numbers and size after laser peening, as well as more stable open-circuit potentials compared to untreated material [170]. This despite LSPwC increasing surface roughness which in most cases promoted higher corrosion current densities (corrosion rates), with higher power density clearly causing higher surface roughness [169][170]. In the case of AA7075, one study [172] shows a small (50 mV) ennoblement in open-circuit potential after shot peening. Another study reported a more varied performance, a slight increase in corrosion current density but a decrease in number of pits compared to the baseline [88]. There are studies that attributed the improvement in corrosion performance due to LSPwC leading to enrichment of the oxide layer [170].

It is clear from the literature surveyed there is are only a limited number of studies assessing LSP (laser peening with ablative layer) effects on corrosion performance, and where there are studies any improvement seen is solely attributed to compressive residual stresses. The exact mechanism in which residual stresses may have changed the electrochemical behaviour for the material is not discussed. In the case of LSPwC, there are more numerous studies on effects of corrosion performance. There is a general consensus that it can improve corrosion performance and this is attributed to not only compressive residual stresses but possibly also to a more homogeneous surface and an enriched oxide layer. In addition, for all laser shock peening treatments it is clear surface roughness increases with increase in laser peening power density, and this will be detrimental to corrosion performance. However, the degree to which each of: laser shock peening compressive residual stresses, increased surface roughness, possible formation of oxide layer enrichment and, to a lesser degree, changes in surface microstructure, affect any mechanisms of localised corrosion and their individual contribution to the material's corrosion performance has not been studied in detail.

2.9 Summary and updated PhD objectives

The initial focus of this study was on laser shock peening of 7XXX series alloys. The literature review confirms that despite there being general commonalities in 7XXX alloys microstructure, fatigue and corrosion behaviour, there are still sufficient differences to make generic conclusions difficult. The mode of manufacture, chemical composition and temper (all interconnected) can cause specific microstructural, fatigue and corrosion challenges for each alloy. Taking this into account, to perform a successful experimental study in the timeframe required, and considering the wealth of existing data on AA7075-T6T51, a well-established alloy, it was selected for study. Additionally, it is also clear the anisotropy of this alloy is likely to show differences in performance when studying different microstructural planes. From a research point of view it would be ideal to test all planes, however the timeframe available only allowed for one to be studied in depth. The L-LT microstructural plane was chosen in part to maximise the number of samples as there was relatively limited available material. This focused testing allowed for in depth comparison of the effects of laser shock peening to the already existing wealth of literature on untreated AA7075-T651 microstructure, fatigue and corrosion performance.

The literature review has made clear there are two different types of laser shock peening (LSP and LSPwC) which can have different effects on the material's surface and consequently differ in terms of fatigue and corrosion performance. Thus, both types of peening will be studied in this project to identify any differences in surface modification and consequently in fatigue or corrosion performance.

This material characterisation will be performed by using established material characterisation techniques (SEM-EDS, EBSD, variable focus microscopy, XRD, incremental hole drilling) to have a solid understanding of the microstructure and surface of the untreated, LSP and LSPwC conditions.

In terms of fatigue performance of laser shock peened materials, the available literature clearly shows this is dependent on the peening parameters used, as these will affect the level and depth of residual stresses generated, and the level of surface modification. Thus, the two laser shock peening treatments (LSP and LSPwC), which were undertaken by an external institution with the necessary expertise (CSIR in South Africa), were performed with parameters set up to generate the highest possible residual stresses whilst limiting as much as possible surface modification. The focus for this study is to fill some knowledge

gaps in the surveyed literature. This is achieved by exploring separately the individual contributions of surface roughness and compressive residual stresses on fatigue micro-mechanisms and overall performance.

Additionally, the literature review has shown there are limited studies on corrosion performance of laser shock peened 7XXX alloys. Thus, as with the fatigue objective, this project will attempt to separate the effects (if any) of LSP and LSPwC induced surface modification and compressive residual stresses on corrosion micro-mechanisms and corrosion performance.

Finally, the complexity of corrosion with mechanical stimuli phenomena in aluminium alloys, and the vast and varied literature on this subject, means it is necessary to focus on a realistic objective. This is to first focus on the relatively simpler phenomena of fatigue crack initiation and propagation in pre-corroded AA7075-T651, and the possible effects of laser shock peening. Future studies on laser shock peening effects in more complex corrosion phenomena can then be investigated backed up by deep understanding of the themes in this project.

The following updated objectives are given:

- To understand how, and to what extent, the LSP and LSPwC generated residual stresses, and the modified surface (hardness and roughness), will each influence changes in the micro-mechanisms of short crack fatigue initiation and growth in AA7075-T651.
- To understand to what extent the laser shock peening generated residual stresses and the modified surface (microstructure, hardness and roughness) influence the electrochemical properties, corrosion pit formation and corrosion performance of AA7075-T651.
- To investigate how pre-corroded pit features can affect fatigue performance, crack initiation mechanisms and crack growth, of laser peened AA07075-T651.

3 Material Characterisation

3.1 Introduction

This chapter is a self-contained study focused on presenting and discussing in detail the microstructural and surface changes, as well as generated residual stresses, on AA7075-T651 caused by LSP and LSPwC. This includes characterising surface hardness, surface roughness (and other laser peening induced surface features), microstructural changes and generated compressive residual stresses at the surface and subsurface. Deep understanding of the effects of laser peening on the material selected will in subsequent chapters help to understand how, and to what extent, the laser shock peening generated residual stress, and the modified surface (microstructure, hardness and roughness), could influence changes in fatigue and corrosion behaviour.

3.2 Material and methods

3.2.1 AA7075-T651

The material in this study was sourced from a 40 mm thick AA7075 plate with T651 temper. According to the literature its properties are as follows: tensile strength of 572 MPa; yield strength of 503 MPa; Vickers hardness of approximately 175; and fracture toughness of 20 to 29 MPa$\sqrt{m}$ depending on the microstructural plane loaded [173]. The major alloying elements are zinc, magnesium and copper. The T651 temper condition implies solution heat treatment, artificial ageing and stretching (to relieve internal residual stresses). A 15 mm × 5 mm × 5 mm sized sample was sent to MTT Testing, based in Sheffield, to perform Inductively Coupled Plasma Mass Spectrometry (ICP-MS) analysis. This was performed to confirm the chemical composition and weight percentage of the AA7075-T651 block of aluminium alloy (see Table 3-1).

Table 3-1 - AA7075-T651 Chemical Composition Test Results – Inductively Coupled Plasma Optical Emission Spectroscopy (MTT LTD) and AA7075-T651 expected chemical composition

Element	Measured value (%)
Al	89.7
Zn	5.64
Mg	2.15
Cu	1.79
Cr	0.19
Mn	0.016
Ti	0.029
Fe	0.10
Si	0.35
Zr	-

All samples tested in this study were removed from an AA7075-T651 50 mm thick plate, at T/4 (one quarter thickness). The AA7075-T651 microstructural directions and planes are shown in Figure 3-1 and are labelled as follows:

- L: Rolling direction.
- LT: Long transverse direction.
- ST: Short transverse direction.
- L-LT: Rolling – Long transverse plane.
- L-ST: Rolling – Short transverse plane.
- LT-ST: Long Transverse – Short transverse plane.

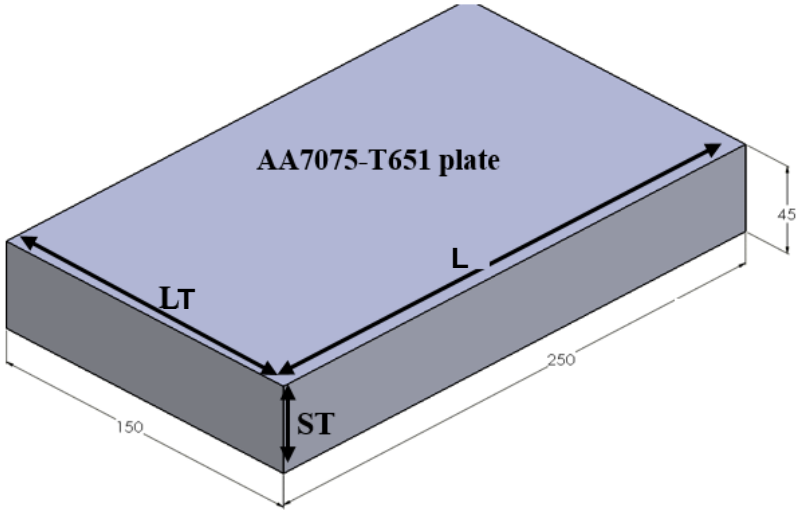

Figure 3-1 – AA7075-T651 plate where all samples used in this project have been sourced from (T/4 thickness).

3.2.2 Sample type and condition

There are three type of AA7075-T651 condition:

- Baseline: Untreated AA7075-T651.
- LSP: Ablative laser shock peening of AA7075-T651.
- LSPwC: Non-ablative laser shock peening of AA7075-T651, plus oxide layer removal (see section 3.2.3 for more information).

For each laser peened condition (LSP or LSPwC) there are two sample types:

- **Type A**: Fatigue bend bars with dimensions shown in Figure 3-2. Their laser peening compressive residual stresses are considered intact. This was a variation of the specimen geometry used by Luong and Hill [156]. The bend bar specimens were cut from the longitudinal – long transverse (L-LT) plane of the AA7075 plate.
- **Type B**: These were sourced from laser peened blocks as shown in Figure 3-2. It is well known that removing volume from a region of residual stresses will relieve these, and the larger the volume removed the greater the stress relief [174]. Thus, Type B samples are assumed to contain limited, or no, residual stresses.

- **Baseline** test samples are not labelled as Type A or B samples as there are no residual stresses present or modified surface in either sample type.

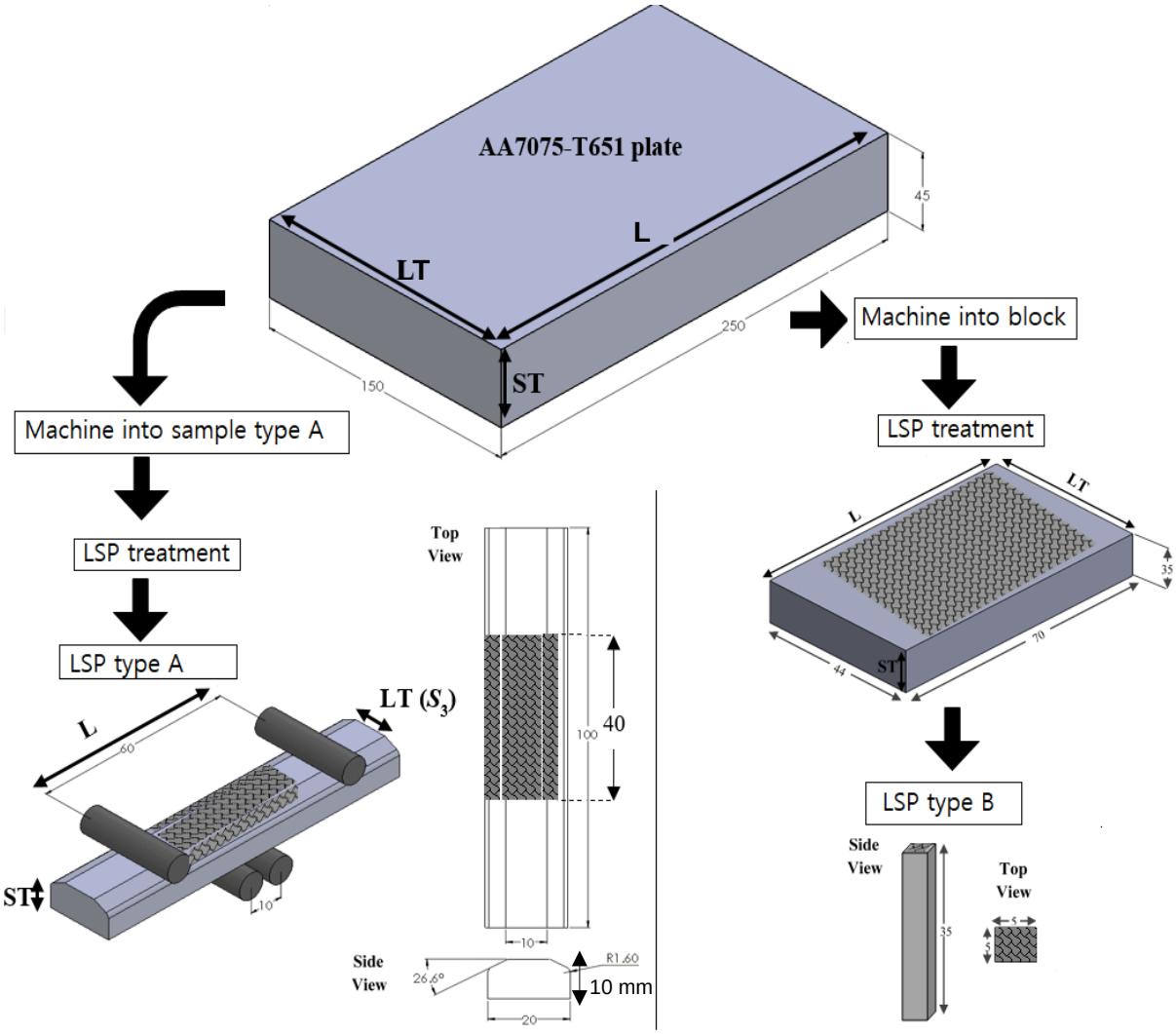

Figure 3-2 – Schematic of Type A and Type B sample manufacture, sourced from AA7075-T651 plate.

For some characterisation tests, samples were tested as-received, whilst in some cases samples were polished to a 1 µm surface finish (e.g. hardness test). Thus, when relevant, sample surface finish is labelled as:

- As-received (No change after LSP treatment. For LSPwC no change after LSP treatment and oxide layer removal).
- 1 µm (polished to 1 µm surface finish post-laser peening).

Table 3-2 – All types of samples in baseline, LSP and LSPwC.

Sample Notation	Residual stresses present	Cut (reduced/no RS)	As received	Polished 1µm
Baseline-AR	NA	NA	x	
Baseline-1µm	NA	NA		x
LSP-TypeA-AR	x		x	
LSP-TypeA-1µm	x			x
LSP-TypeB-AR		x	x	
LSP-TypeB-1µm		x		x
LSPwC-TypeA-AR	x		x	
LSPwC-TypeA-1µm	x			x
LSPwC-TypeB-AR		x	x	
LSPwC-TypeB-1µm		x		x

3.2.3 Laser shock peening treatment

Laser Shock Peening was performed at the Council for Scientific and Industrial Research (CSIR), South Africa. The laser peening configuration used a frequency doubled Nd:YAG laser (Thales SAGA HP) to deliver parameters shown in Table 3-3. A thin water layer was used to achieve inertial confinement, for LSP a black tape (around 100 µm thick with a 30 µm adhesive) was used as a sacrificial overlay. Spot overlap is achieved by sample motion in a conventional (X-Y) raster pattern by scanning (in the LT direction) and stepping (in the L directions) to achieve equal spot overlap (of 48.4% in the LT and L directions). To homogenise any periodic features such as residual stress between sequential overlays [9], subsequent sequential layers of LSP were applied with a spot offset (one third of the spot-to-spot distance to achieve 48.4% overlap). In total, three sequential applications of LSP were applied (each with a new tape) to achieve a total coverage of 5 spots per mm^2. The samples were peened across the top surface and the chamfered sides, as shown in Figure 3-2, to avoid crack formation outside the top flat surface.

LSPwC had one additional step involving the mechanical removal of a thin oxide layer present to improve the surface compressive residual stress. The oxide removal was performed at the CSIR, using a robot arm combined with a deburring brush (a very fine Scotch-Brite™ 'red' pad), a method used in industry. Further removal details can be found in Niknam and Songmene [175].

In Type A samples, the top surface and the chamfer surfaces were peened to avoid crack formation outside the top surface, as shown in Figure 3-2. Type B samples were cut from

peened blocks, as seen in Figure 3-2. The same peening parameters were used for Type A and B samples.

Table 3-3 – Laser peening parameters selected after CSIR trialled parameters on spare samples, best parameters for minimal surface modification were chosen.

Parameter	Value
Power Density / GW cm–2	4
Wavelength / nm	532
Spot Shape	Circular
Dimension / mm	1.5 dia.
Spot offset / %	0.225
Spot overlap / %	166.7 spots cm–2 (≈ 48.4%)
Energy / mJ	364
Sacrificial coating	Black vinyl tape (LSP) / No coating (LSPwC)

3.2.4 Residual stress measurement

Two residual stress measurements methods were used to, in combination, help understand the residual stress fields present after LSP and LSPwC. X-ray diffraction was performed to obtain measurements at the surface. Incremental centre hole drilling to obtain measurements through the depth of the material.

3.2.4.1 Incremental centre hole drilling

The hole drilling measurements were made with a Stresscraft three axis drilling device. A drilling feed rate of 10 µm s–1 was used with a 1.2 mm diameter drill on a 0.3 mm orbital eccentricity to create a hole diameter of 1.8-2.0 mm. The measurements were created with twenty-three surface biased (smaller increments near the surface) incremental depths using an orbital drilling motion. The measurements were taken in the centre of the LSP region on the bend bar sample. Strain readings were taken up to 1.024 mm from the surface in the longitudinal (S_1) and transverse (S_3) directions of the samples. S_1 was also the direction of loading in 4-point bend bar fatigue tests (See Figure 3-2). As it is well known that centre hole drilling measurements at, or very close, to the surface can be inaccurate [106][176], only values from 16 µm below the surface are shown.

3.2.4.2 X-ray diffraction

X-ray Diffraction (XRD) and incremental centre hole drilling were used in a complementary manner, to assess the residual stresses present in the laser peened samples at and below the surface [106][176]. The XRD measurements were completed with a Stresstech Xstress diffractometers on an articulated robot, which uses the d vs. $\sin^2\psi$ technique to determine the

stress. A chromium X-ray source was used with a 1 mm diameter collimator and count time of 20 s at each of the fourteen tilt locations evenly spaced between −45/45°. Additionally, a ±2.5° tilt angle was used at each measurement location to increase the number of sampled grains. The 0° and 90° measurement angles were aligned with the longitudinal (S_1) and transverse (S_3) directions of the samples (See Figure 3-2). The measurement distance was calibrated based on a stress free aluminium powder sample and was set at a calibration stress of −22 ± 10 MPa (0° direction) and −14 ± 11 MPa (90° direction).

3.2.5 Test sample preparation

Different characterisation techniques required different material preparation steps: General microscopy required Type B samples due to space limitations. Type B sample cross-sections were hot mounted in conductive phenolic resin, mechanically polished and etched. For samples characterised using electron backscatter diffraction (EBSD) Type B cross-sections were not mounted, only ground and polished to 3 µm finish followed by electropolishing. Hardness Type A and Type B samples were tested in the as-received and 1 µm polished surface finish. Surface roughness Type A samples only required an ultrasonic clean. See Table 3-4 for more details.

Table 3-4 – Material preparation details

Type of characterisation	Microscopy	EBSD	Hardness	Hardness	Surface roughness
Sample Condition	Type B (Cross-section)	Type B (Cross-section)	Type A*	Type B	Type A
Preparation step					
Hot mount	x	-	x	-	-
Cold mount	-	-	-	-	-
Grind - 1200SiC paper	x	x	x	-	-
Ultrasonic clean (10 min)	x	x	x	x	x
Polishing: 3 µm diamond suspension (10 N, 80 rpm, 10 min)	x	x	x	-	-
Ultrasonic clean (10 min)	x	x	x	-	-
Polishing: 1 µm diamond suspension (10 N, 40 rpm, 5 – 20 min)	x	-	x	-	-
Ultrasonic clean (10 min)	x	-	x	-	-
Light wash, gentle rubbing on 1 µm cloth, to remove any leftover diamond suspension	x	-	x	-	-
Keller's etchant: Time: 30 – 80 s	x	-	-	-	-
Electropolish (2:1 methanol – nitric acid, 25 – 30 V, -25° – -35°C, 2 – 5 s)	-	x	-	-	-
*** Some Type A hardness samples were polished to 1 µm surface finish and the preparation steps are shown above. Otherwise, the samples were as-received and only had an ultrasonically clean.**					

3.2.6 Microscopy

3.2.6.1 Optical microscopy

Surface characterisation of all three planes was performed using an Olympus BX41M-LED optical microscope. Images were used for visualisation purposes and grain size measurement. The images of each plane (L-LT, L-ST and LT-ST) were rotated using Microsoft PowerPoint 'Picture Tools' to create a three-dimensional (3D) representation of each alloy.

The line intercept method was used to measure grain dimensions for all material types (baseline, LSP, LSPwC). ImageJ software [177] was used to scale optical microscope images and measure lines drawn across the images. The number of grain boundaries the lines intercepted were counted, and the grain size given by dividing the number of grain boundaries intercepts by the line length, according to the ASTM-E112-12 planimetric method. Each line drawn intercepted a minimum of 10 grain boundaries, and the average grain size was calculated by dividing the total line length by the number of grain boundaries crossed. This was successfully performed on baseline samples. However, the grain boundaries were very faint and small grains (microns in size) may have been missed due to visual analysis limitations. The method was not successful for LSP and LSPwC surfaces, where the grain boundary faintness was very pronounced and visual analysis would have been too subjective. Thus, only baseline line intercept measurements are presented.

To assess the intermetallic surface area, an Olympus BX41M-LED microscope with a variable focus imaging capability was used to capture fully focused images. Quantitative analysis of the intermetallic surface area was performed on ImageJ using '3D trainable WEKA segmentation' [178] and 'Measure' [177] commands.

3.2.6.2 Variable focus microscopy

Background information

Focus variation microscopy allows for topographical and colour information. It uses a beam-splitting mirror, a small depth of focus, a light sensitive sensor that captures reflected light, a movable vertical stage, and complex algorithms to identify regions of image focus, see Figure 3-3.

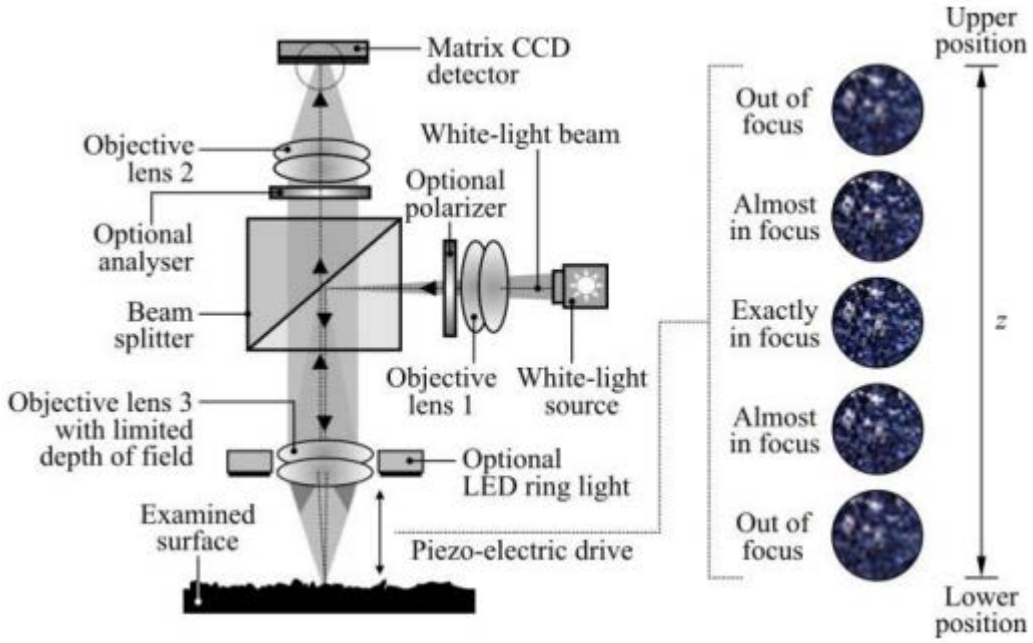

Figure 3-3 – Focus variation microscopy schematic diagram showing the principal of operation [179].

A beam of light is projected onto a relatively small surface of the sample. The light reflected from the sample surface returns to the microscope optical system, where it is directed by the beam splitter to the active area of the photoelectric detector. Here it forms a photometric image, containing colour, brightens and contrast information, as well as geometric character (length and width). The microscope processor searches for only parts of the image that have a focused beam of light. It then reconstructs a final 3D image by connecting the focused sections of the images together. By carrying out the scan process using a highly precise *z*-axis stage the processor can link an area of focus to a particular *z*-plane, thus being able to also provide surface micro-topography [180][179].

Some of the advantages of using this type of microscope are fast and automated surface imaging, colour imaging, ability to capture a large surface area by using the 'General Image Field' setting, which allows for automatic reconstruction of a set of adjacent surface images into one large image, and providing high resolution topography which allows for metrological measurements. Some disadvantages are problems measuring surfaces at high angle slopes (above 85°), large irregularities, very smooth surfaces and transparent or semi-transparent surfaces such as glass [179].

Test procedure

The Alicona InfiniteFocus™ focus variation microscope was used to capture 2D and surface topography (3D) images of characterisation samples. Typical settings used during imaging are shown below in Table 3-5.

Table 3-5 – Alicona InfiniteFocus™ imaging settings

Type of Alicona Image	General Image field
Magnification	×20
Horizontal resolution	1.5 µm
Vertical resolution	150 nm
Other information	Linear polariser

3.2.6.3 Scanning electron microscopy

A JEOL JSM-6500F scanning electron microscope (SEM) was used for secondary electron imaging (SEI) and backscatter electron imaging (BEI), including energy dispersive X-ray spectroscopy (EDS) and electron backscatter diffraction (EBSD). Voltages used for SEI imaging, BEI and EDS, and EBSD were 10, 15 and 20 keV, respectively. SEI was used for general image capture, and BEI to image secondary phases (intermetallics). Semi-quantitative identification of secondary phases in terms of chemical composition was carried out using EDS and SEI, and INCA software by Oxford Instruments. The chemical composition of a scanned point would be given in atomic percentages. This would then be used to compare to the chemical composition of known intermetallics present in AA7075-T651 to deduce the most likely intermetallic present. As an example, if an atomic percentage of Al = 7.3, Cu = 1.8 and Fe = 1.2 was found, this would be deemed an approximation of intermetallic Al_7Cu_2Fe.

Electron backscatter diffraction

For EBSD characterisation, LSP and LSPwC samples were mechanically polished and electropolished as detailed in section 3.2.5. Initials scans were performed on relatively large areas (500 µm × 500 µm) of LSP and LSPwC L-LT planes at scan step sizes of 2.3 µm and 1.87 µm, respectively. The level of indexing on these surfaces was consistently low (<50%). It is well-known highly deformed surfaces, such as the laser peened surfaces in this study, are very difficult to index using conventional EBSD techniques [181][182]. Therefore the data is used as a tool for semi-quantitative comparison between different surfaces. A more accurate scan of an LSP cross-section (L-ST plane) was performed to attempt to capture the microstructure, and change in local misorientation (and therefore infer change in plastic deformation) with respect to distance from the LSP surface, up to 1 mm subsurface. To be

able to build a profile of the grain structure to this depth in a realistic timeframe, whilst achieving as high as possible indexing percentage near the LSP surface, the following settings were chosen: A scanned area (145 µm long by 100 µm wide) considerably smaller than previous EBSD scans. A relatively small scan step (0.4 µm) was chosen to allow a larger number of indexed points: The indexing rate in the first 20 µm from the LSP surface is low due to very high deformation, but this subsequently improves rapidly to above 90% indexing.
Oxford Instruments Tango software was used to analyse the grain misorientation profile of the scanned surfaces. To calculate grain misorientation percentages, grains are classified as deformed if the average misorientation between all points within a grain is above 1 degree. Grains are classified as substructured if the average misorientation angle of a grain is 1 degree, but the misorientation angle between any two points within the grain is higher than 1 degree. Finally, grains are classified as recrystallised if the average misorientation angle of the grain is below 1 degree [183].

EBSD data was also processed in Matlab using MTex Toolbox [184] to calculate the kernel average misorientation (KAM), particularly in the LSP cross-section. KAM is a quantitative method to measure the local grain misorientation by treating low angle misorientation as evidence for dislocations. It does this by measuring the misorientation between a centre point (Represented as the number zero in Figure 3-4) and all its neighbouring points and returns the average number misorientation value for the centre point. The KAM obtained can depend on the number of neighbouring points included in the calculation. Thus, consistency is required to able to compare accurately. For this study, KAM is calculated up to second order neighbouring points, or ‘next-nearest’ neighbours (Points labelled one and two in Figure 3-4).

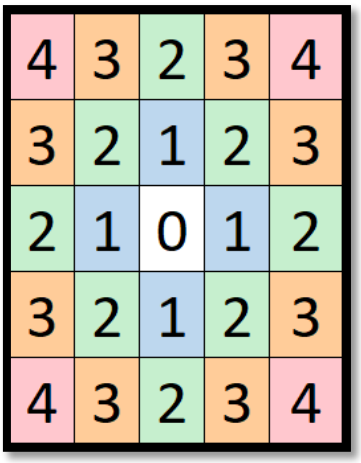

Figure 3-4 – Representation of a kernel's centre and neighbouring points in a kernel in the kernel average misorientation (KAM) technique.

3.2.7 Micro-hardness

The hardness test determines the resistance of the material to penetration of a non-deformable indenter with a specific shape. Macro-indentation is a well-established test for hardness in the engineering industry. The relatively large size of the indents is seen as large enough to give hardness values for the bulk material. Tests tend to be performed with loads of 1 to 120 kg-f. In a Vickers hardness test a diamond shaped indenter is used to load the sample. It uses the indenter load and the surface of the impression A_c to calculate hardness.

Equation 3-1

$$HV = \frac{L}{A_C} = 1.8544 \frac{L}{d^2}$$

Where L is measured in kg-force and d, in millimetres, is equal to the average of the two diagonals measured, from corner to corner, of the residual impression left by the indenter. The constant 1.8544 is based on the square-based pyramid-shaped indenter, with opposite sides that meet at the apex at a 136° angle. In macro-hardness testing loads can vary between 1 and 120 kg-force, force application time 2 - 8 s, and test force is maintained for 10 – 30 s [185]. Micro-hardness can also be performed using the Vickers method and is characterised by loads lower than 2 kg-f and penetrations of above 0.2 µm. The main difference between macro and micro Vickers tests are the forces used [185].

For this study only micro-hardness tests were performed, with a 0.5 kg-f load and 30 s hold time. Ten to fifteen readings were taken from each sample's L-LT plane. Baseline, LSP and

LSPwC conditions in Type A and B samples were tested. One or two samples per condition were indented, depending on sample availability. A minimum of 8 micro-indentations per sample type were performed. Indentations within a sample were at least 300 µm apart, a distance greater than three times the indent diagonal length (approximately 60 – 80 µm for these tests), performed according to ISO 6507. As discussed in section 3.2.2, it is assumed hardness testing on Type B samples give hardness values based mostly on microstructural changes, with reduced effects from any remaining residual stress.

3.2.8 Surface roughness

A Talysurf contact profilometer, with a 1 mm stylus of 4 nm resolution, was used to perform surface roughness testing to ISO4287 standard on baseline, LSP and LSPwC Type A samples. The roughness parameters captured and compared between different conditions are shown in Table 3-6. R_a and R_q are parameters commonly used for surface roughness comparison. However, as fatigue life is susceptible to stress concentrations, and corrosion life susceptible to localised corrosion, small but deep features are important to this study. The aforementioned roughness parameters do not capture the likelihood of these features being present in a sample. Thus, R_z and R_t were also deemed relevant surface roughness parameters for this study.

Table 3-6 – Surface profile parameters.

Profile parameter	**Description**
P_a	Average primary profile
P_q	Root mean square of primary profile
P_z	Mean peak to valley height of primary profile
R_a	Average roughness
R_q	Root mean square roughness
R_z	Mean peak to valley height
R_v	Maximum valley height
R_t	Maximum peak to valley height
R_{sk}	Roughness skewness (indicates whether the surface has more valleys then peaks or vice versa)
W_a	Average surface waviness
W_q	Root mean square of surface waviness
W_z	Mean peak to valley height of surface waviness

To complement the contact profilometer data an Alicona focus variation microscope was used to reconstruct macro-images of AA7075-T651 baseline, LSP and LSPwC surfaces, allowing for better visual understanding of the surface topography of the different material conditions. Primary and waviness profiles are also shown to investigate any changes to the overall shape of the surface or generation of medium frequency irregularities by LSP or LSPwC.

3.2.9 Three-dimensional x-ray computed tomography

3D X-ray tomography was used to capture percentage and size distribution of intermetallics in the baseline material.

3.2.9.1 Background information

Although X-ray computed tomography is widely known for its use in non-invasive medical testing, it has also become important and quite widely used in engineering for non-destructive characterisation of a variety of materials and in different applications. Its ability to generate 3D internal structure reconstructions makes it a very advantageous technique, for example, X-ray synchrotron tomography has been used to quantitatively characterise constituents in different aluminium alloys [40][186][187].

X-ray CT scans are used for microstructure characterisation as they can show features that give different X-ray attenuation within the bulk material. It does so by acquiring many radiographs of a rotating sample (typically between 0° and 180°) and then using a filtered back-projection algorithm to reconstruct the volume of the sample using these radiographs, see Figure 3-5. This reconstructed image is a quantified map of the linear X-ray attenuation coefficient at each point in the material. The X-ray attenuation at each point depends on the density, atomic number and electron density of the material it travels through. Thus, it is able to distinguish the bulk material from secondary phases and other feature such as porosity. The larger the difference in the aforementioned properties between two materials the higher the X-ray attenuation difference between the materials, making other features more easily distinguishable from the bulk material.

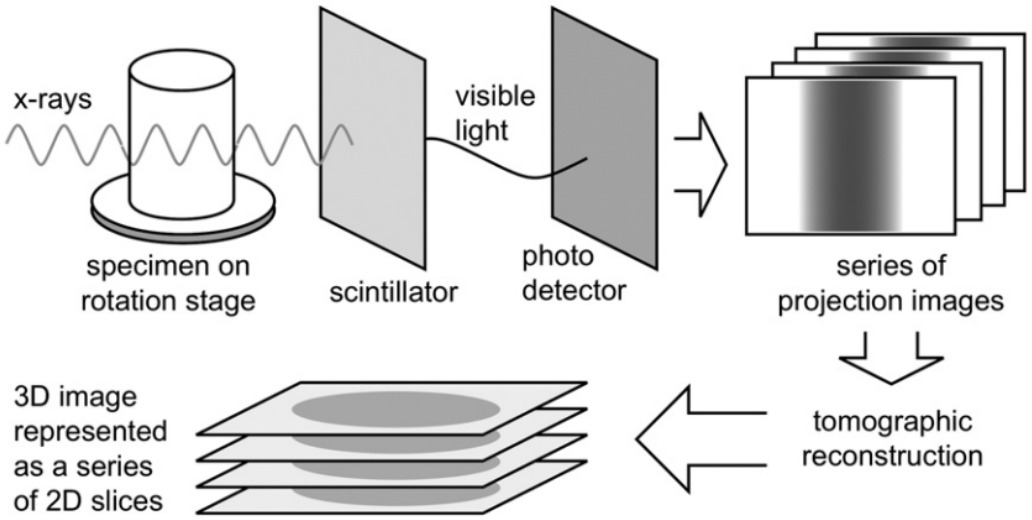

Figure 3-5 - Schematic illustration of X-ray CT acquisition and reconstruction process [188].

Limitations for CT scanning are:

- Features with similar atomic number and density are likely to have similar attenuation coefficients and thus can be hard to distinguish from each other;
- The quality and resolution of the scan reconstruction depends on the size and shape of the scanned material.
- Large samples lead to longer X-ray paths through the material, leading to overall higher X-ray attenuation, which affects the voxel resolution of the scan, or alternatively can lead to long scans to achieve the same resolution.
- A heterogeneous (non-circular) sample shape leads to varying X-ray paths leading to X-ray attenuation caused by the X-ray path rather than features in the material, which can lead to artificial features in the reconstructed scan.

Therefore, the ideal CT scan sample, particularly for microstructural characterisation, is as small as possible, and cylindrical in shape, for maximum resolution and minimum artificial features. This leads to the need for a delicate compromise between maximising scan resolution and accuracy, with the need for minimum sample preparation (and alteration).

3.2.9.2 Test procedure

A micro-focus CT with a polychromatic divergent X-ray beam was used to acquire high-resolution 3D reconstructions (below 5 µm voxel resolution). Typical X-ray energy used for AA7075-T651 were 80 – 110 keV. A low energy filter was used to decrease beam hardening issues, as well as ×4 objective magnification, placing the X-ray source and detector as close as possible to the sample (millimetres apart) and taking 1500 – 4000 projections to maximise voxel resolution, leading to scanning times of 18 – 24 h.

CT scan sample cross-sections were between 3 mm × 3 mm and 5 mm × 5 mm. The field of view varied according to the cross section, between 1 mm and 4 mm diameter. The voxel resolution achieved varied from 800 nm to 2000 nm.

Data visualisation and analysis software Avizo™ and ImageJ [177] were used to process 3D CT scan reconstructions. ImageJ was used for thresholding different material phases. First, several commands (Adjust Brightness/Contrast, Median Filter, Crop, Rotation, Reslice, Erode, Dilate) were used to decrease the volume size, reduce noise, improve image quality and facilitate visual analysis. Segmentation of the required material phases was then performed using the Threshold command and visual analysis. Quantitative analysis was performed by using the Analyse Particles command and processing the output data on Microsoft Excel. Avizo™ was used for 3D-visualisation. In these cases, a previously ImageJ-segmented material (including intermetallics, material matrix, and air) would be saved as a 'Tif' file and uploaded into Avizo™ for 3-D visual reconstruction.

3.2.10 Tensile testing

AA7075-T651 tensile tests were performed to generate yield strength data for comparison to the open literature. Samples were manufactured as a sub-size specimen according to ASTM-E8/E8M-09 standard. These sub-size specimens were chosen taking into account the limited source material available. See Figure 3-6 for AA7075-T651 dog-bone sub-size specimen dimensions.

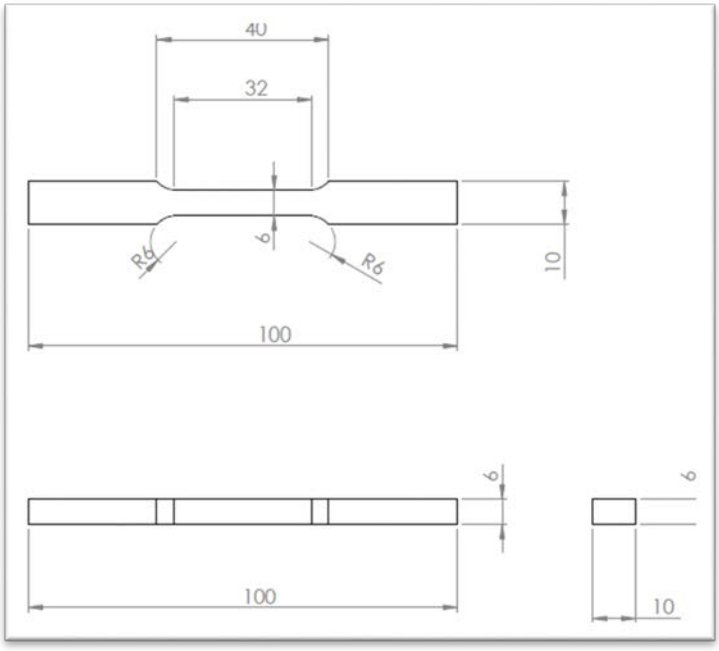

Figure 3-6 - AA7075-T651 sub-size tensile test specimen (dimensions in mm).

AA7075-T651 dog-bone specimens were tested, to failure, according to standard ASTM-E8/E8M-09. The tests were performed on an Instron 5569 with a load cell of 50 kN. The crosshead speed was 8 mm per minute. An extensometer was used to measure strain data. Instron Bluehill™ 3 [189] software captured load, extension and strain data. Specimen gauge length, gauge width and thickness, were input into the data before testing, for the software to output stress and strain data. The data was then plotted as a stress-strain curve in Microsoft Excel, and used to find the 0.2% offset yield stress of the material.

3.3 Results

3.3.1 Baseline material characterisation

Figure 3-7 shows a 3D representation of the AA7075-T651 microstructure. The microstructural planes are L-LT, L-ST and LT-ST. The L direction is the rolling direction, which makes the grains anisotropic, in the shape in what is commonly known as ‘elongated pancakes’. From visual inspection the L-LT plane appears to have grains between 200 µm and 300 µm in length (L direction) and up to 100 µm - 150 µm wide (LT direction). Nonetheless, there appears to be a wide distribution of grain sizes. This includes possible fine sub-grains present in the uncrystallised grains (lighter coloured grains). These sub-grains appear to have dimensions in the range of 1 µm to 10 µm. Line intercept measurements give an average of 227 × 67 × 14 μm^3 for the L, LT and ST directions, respectively.

The dark features (1s – 10s µm in size) seen in Figure 3-7 are coarse particles, also known as intermetallics. Semi-quantitative results from SEM-EDS suggest Al_7Cu_2Fe and $Al_{23}Fe_4Cu$ are the most abundant particles. Al_7Cu_2Fe (Figure 3-8) is the dominant intermetallic in the LT and LS planes, whilst in the TS plane $Al_{23}Fe_4Cu$ (Figure 3-10) is also present in significant quantities. In addition the size and shape of Fe and Cu based particles appear to be very heterogeneous. Mg_2Si (Figure 3-11) is also present but to a lesser degree, typically in the 1 – 10 µm size and tends to have more homogeneous shape compared to Fe and Cu based particles.

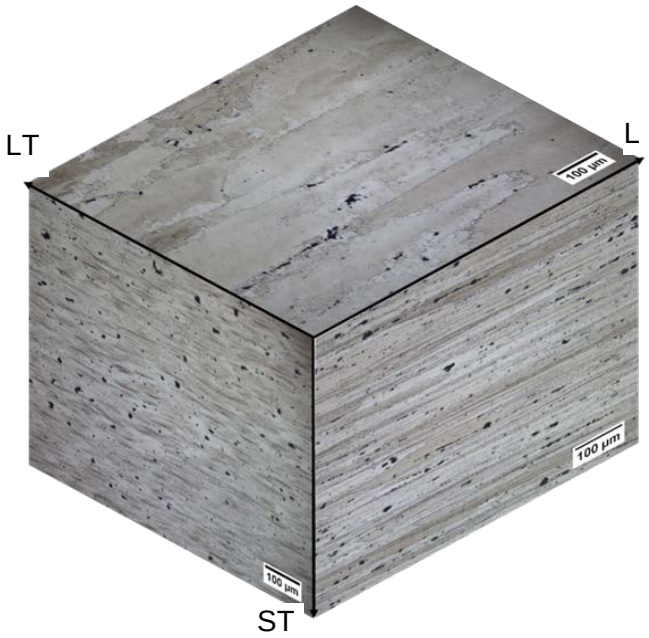

Figure 3-7 – AA7075-T651 microstructural planes representation.

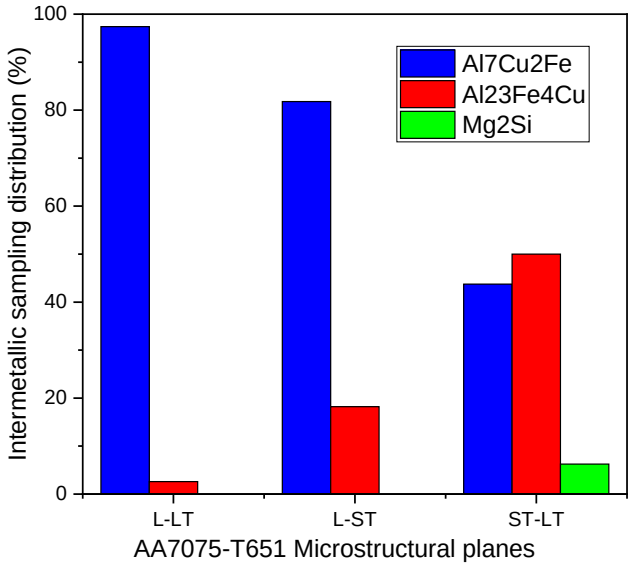

Figure 3-8 - SEM-EDS random sampling of intermetallics present in microstructural planes.

Table 3-7 - AA7075-T651 average grain size. Line intercept method

Average	L / µm	LT / µm	ST / µm
From L-LT plane	141	66.7	
From LT-ST plane		53.2	14.8
From L-ST plane	312		14.0
Final	227	66.7	14.4
Comments on grain size	100s microns	High 10s to low 100s microns	10s microns

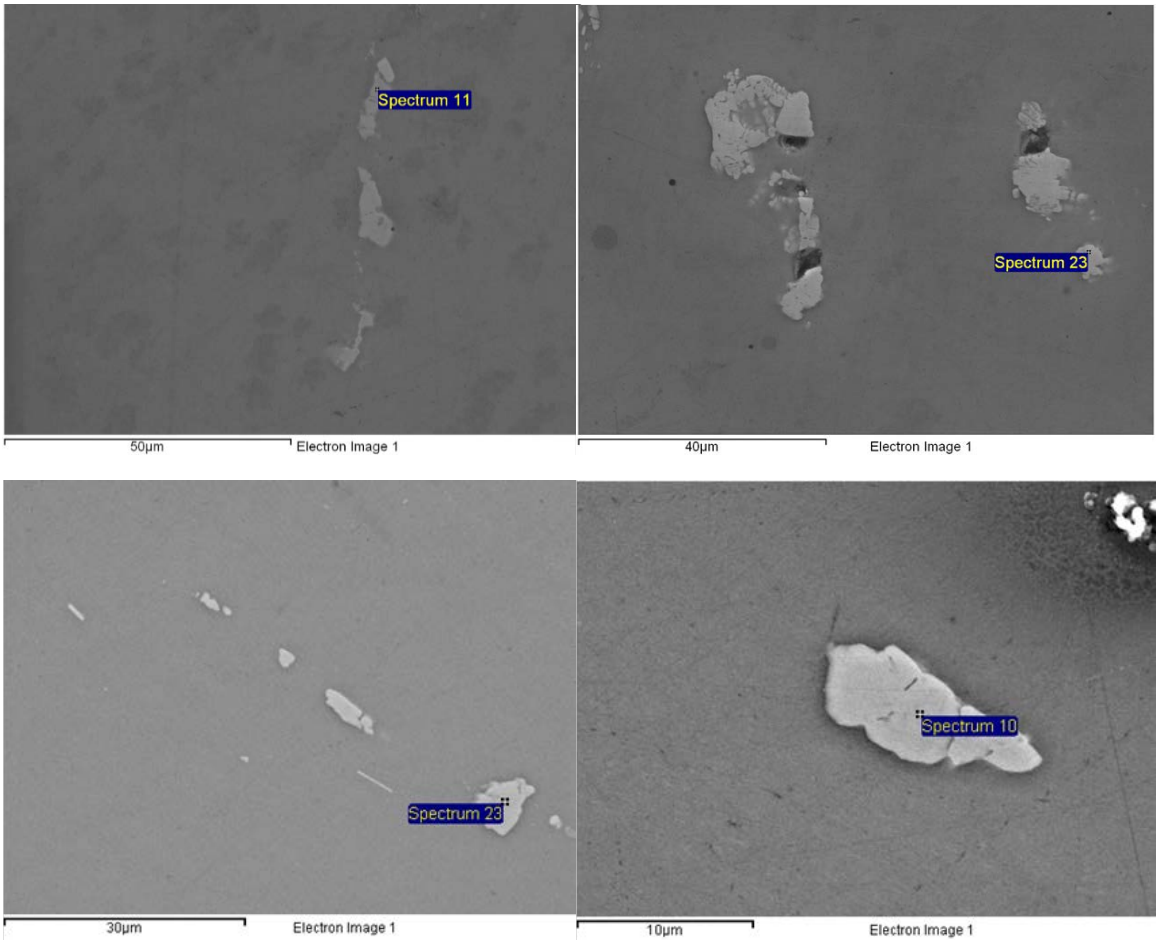

Figure 3-9 – SEM-EDS images of typical Al_7Cu_2Fe intermetallics, showing high shape heterogeneity.

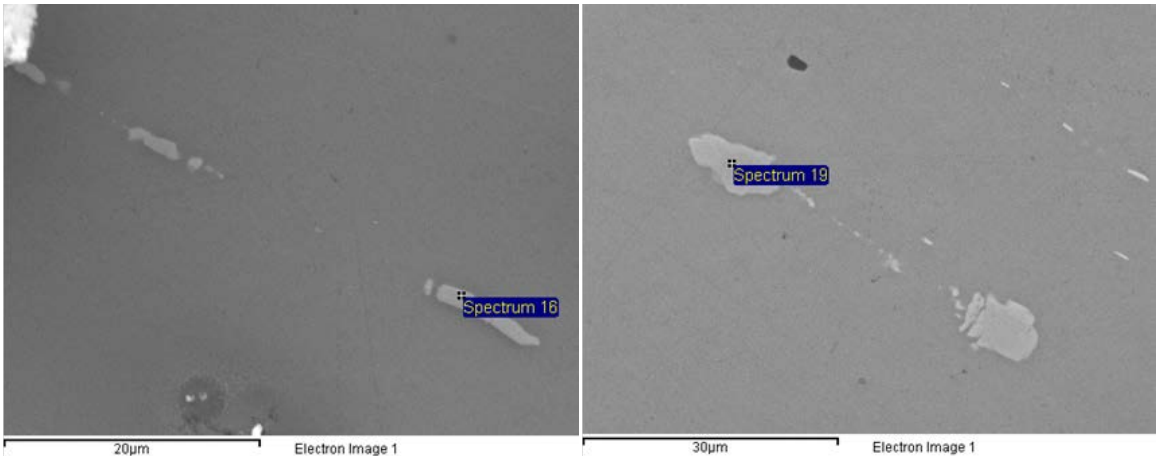

Figure 3-10 – SEM-EDS images of typical $Al_{23}Fe_4Cu$ intermetallics.

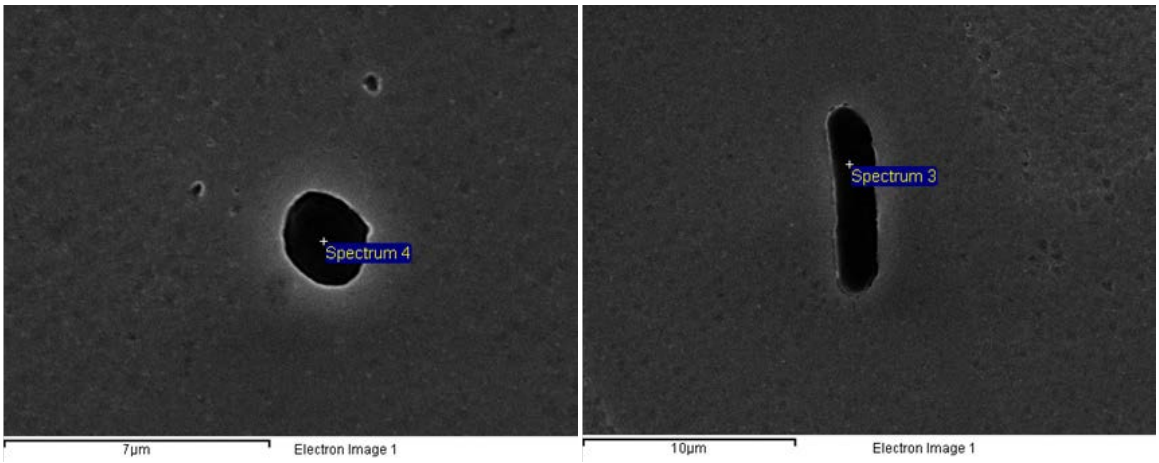

Figure 3-11 – SEM-EDS images of typical Mg_2Si intermetallics

3.3.1.1 Intermetallic distribution

According to Table 3-8, the AA7075-T651 intermetallic surface fractions for each plane have similar values. In addition, the L-LT plane has a higher intermetallic surface fraction than the LT-ST and L-ST planes.

Table 3-8 – AA7075-T651 microstructural plane intermetallic surface fraction.

	L-LT plane (%)	**L-ST plane (%)**	**LT-ST plane (%)**
Image 1	0.275	0.252	0.258
Image 2	0.362	0.21	0.210
Image 3	0.384	0.292	
Average	0.340	0.251	0.234

The intermetallic volume fraction established from X-ray CT scan is 0.85%, see Figure 3-12. Visual analysis suggests the intermetallics' shape and size are inhomogeneous. A histogram of particle volume shows the majority of particles are below 1000 μm^3, with a small number of very large particles, likely mega-clusters (several clusters of particles close together), see Figure 3-13.

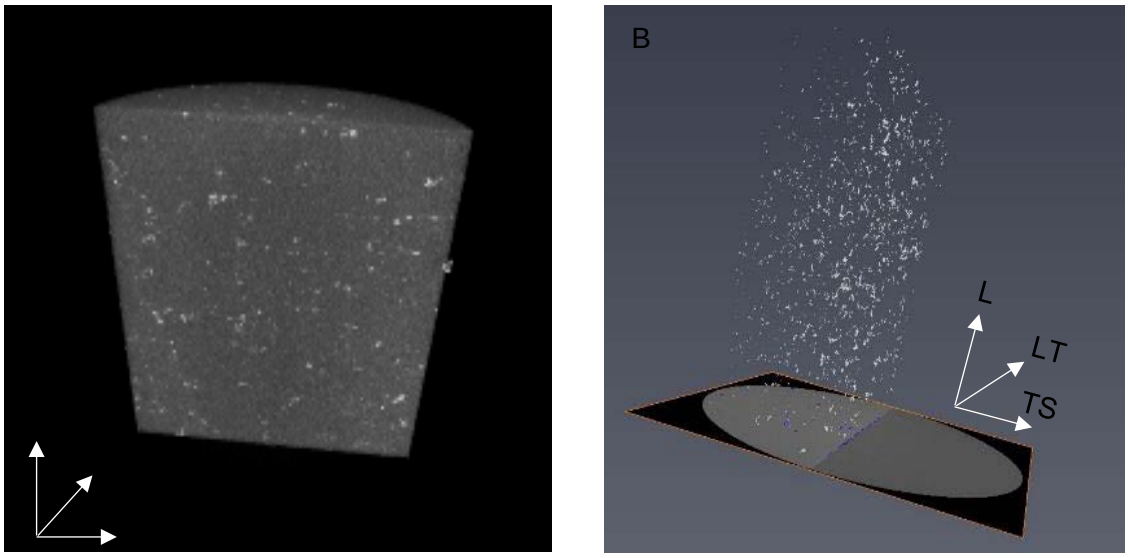

Figure 3-12 – Image A: AA7075-T651 volume visualisation with bulk matrix. Image B: Image visualisation without aluminium matrix, intermetallics only.

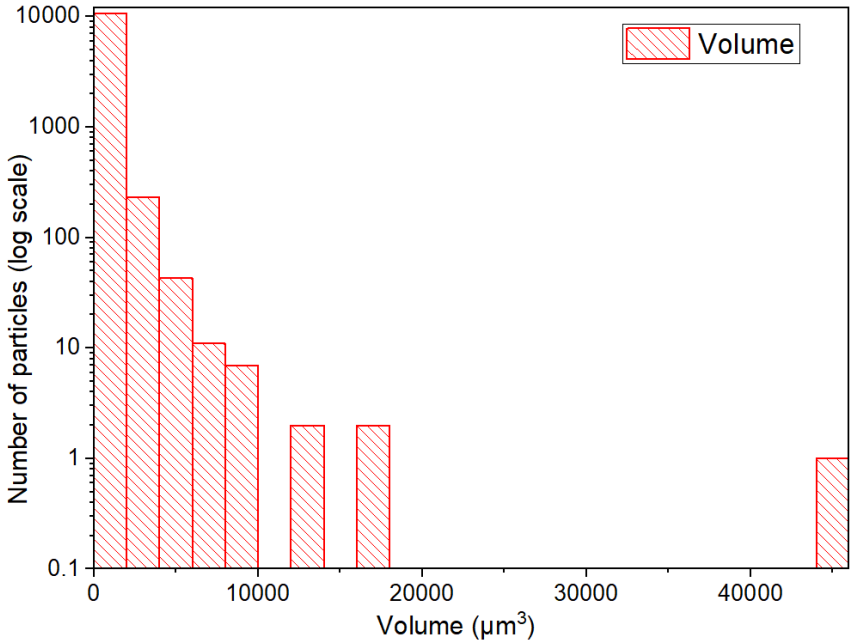

Figure 3-13 – Particle volume distribution taken from 3D CT-scan of AA7075-T651 volume.

3.3.1.2 Tensile strength

Table 3-9 shows AA7075-T651 yield strength data generated by tensile testing. The average proof-stress (0.2%) of AA7075-T651 is 444 MPa, with the maximum value being 455 MPa. This is within the expected range from the available literature [190].

Table 3-9 – Yield strength from tensile tests vs. expected from literature

Offset Yield Strength (0.2%)	444 ± 11
Range expected from literature	372 – 503

3.3.2 Compressive residual stresses

The LSP centre hole drilling data in Figure 3-14 shows longitudinal (S_1) and transverse direction (S_3) compressive residual stresses of up to –350 MPa below the surface. XRD surface measurements show surface residual stresses between –400 MPa and –325 MPa, progressively decreasing away from the surface, to -52 MPa, at 1 mm below the surface. For LSPwC, XRD measurements of residual stresses before oxide layer removal give -87 MPa. After oxide removal (see method in section 3.2.3) the maximum compressive residual stress at the surface is approximately –333 MPa. The centre hole drilling data for LSPwC in Figure 3-14 show compressive residual stresses of up to –405 MPa in the first 56 µm below the surface, progressively decreasing away from the surface. The measurements suggest LSPwC

has higher compressive residual stresses then LSP, by a range of approximately 100 MPa within the first 800 µm, with the difference been most pronounced in the first 400 µm.

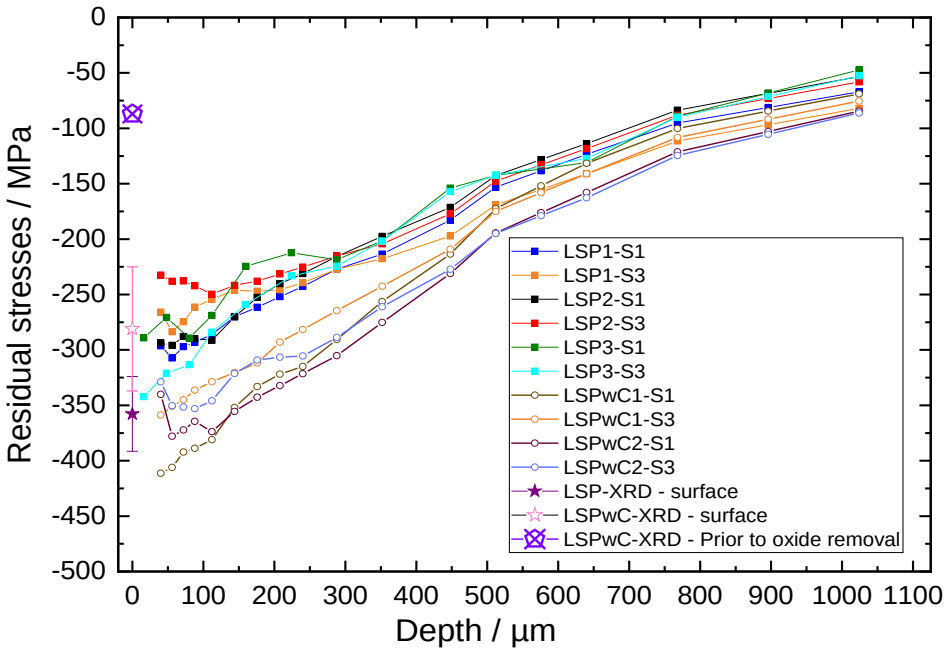

Figure 3-14 – Residual stress data for AA7075-T651 LSP and LSPwC. From centre hole drilling and XRD measurements. S_1 in the longitudinal direction, S_3 in the long transverse direction

3.3.3 Surface modification by laser shock peening

3.3.3.1 Hardness

According to Figure 3-15, LSP Type A average micro-hardness is 188 Hv, a 11% increase compared to baseline average hardness of 170 Hv. Average hardness for LSP Type B (residual stresses relieved) is 175 Hv. For LSPwC Type A and B average hardness is 176 Hv and 171 Hv, respectively. Unlike LSP Type A and baseline results, the interquartile range of values in LSPwC Type A is much larger, suggesting high variability. When LSP and LSPwC Type A samples are polished to 1 µm (removing less than 100 µm from the surface) the hardness values and the mean increase, with LSPwC having a slightly higher mean than LSP. However, the high variability seen in other LSPwC samples is repeated for the polished sample.

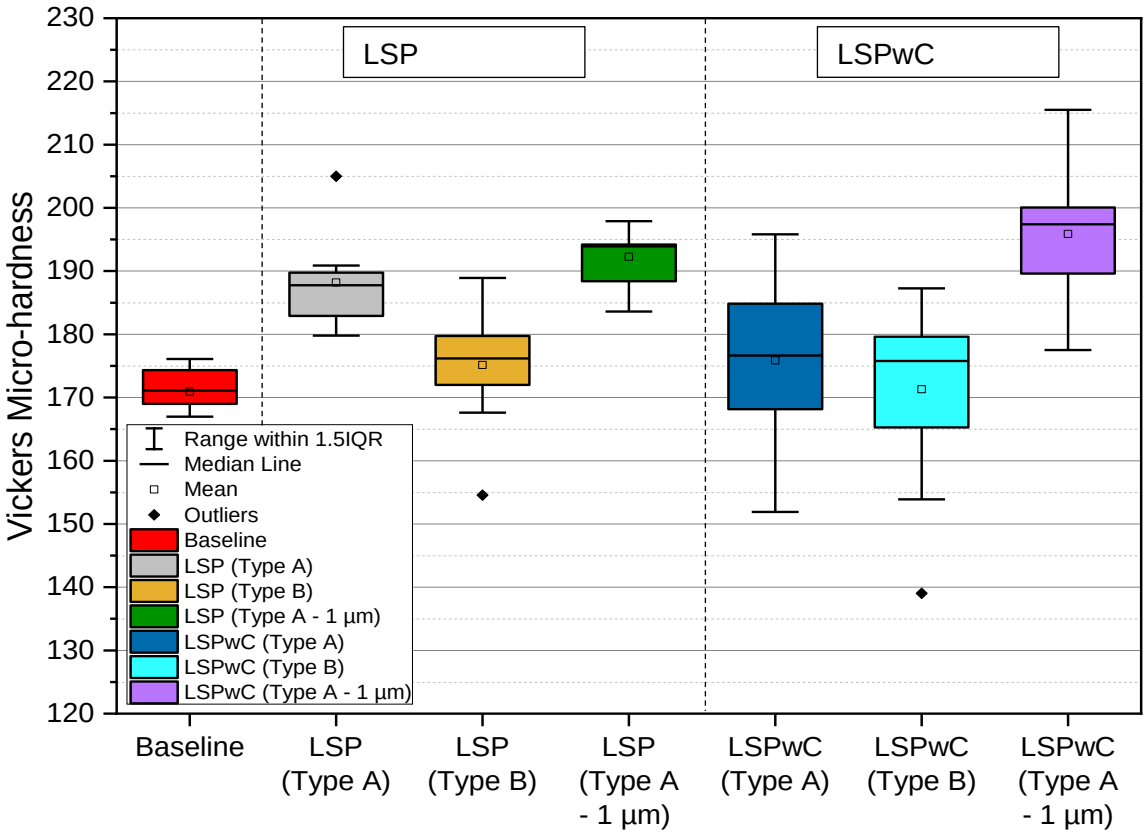

Figure 3-15 – Vickers micro-hardness measurements of baseline, LSP and LSPwC Type A (as received and 1 µm) and Type B samples.

3.3.3.2 Surface roughness

Roughness values are shown in Table 3-10. For each roughness parameter (except for R_{sk}) there is roughly a doubling (LSP) or tripling (LSPwC) of R_z, R_t values; and tripling (LSP) or quadrupling (LSPwC) of R_a, R_q values. There has been an increase in roughness from baseline to LSP, and even higher for LSPwC. Nevertheless, most of these values are in the same order of magnitude.

Table 3-10 – Contact profilometer surface roughness measurements

Roughness parameter	Baseline (1 µm)	Baseline (1200 SiC grind)	LSP	LSPwC
R_a (µm)	0.04	0.23	0.76	1.03
R_q (µm)	0.04	0.29	0.90	1.24
R_z (µm)	0.17	1.62	3.69	5.28
R_t (µm)	0.25	2.64	5.52	7.94
R_{sk}	0.06	-0.10	-0.11	0.03

Variable focus microscope macro-images, Figure 3-16 for LSP and Figure 3-17 for LSPwC, show both peened surfaces have a characteristic dimpled pattern left by laser peening. Although both LSP and LSPwC have a similar roughness range (+8 to -10 µm for LSP, +12 to -12 µm for LSPwC) according to contact profilometry, the variable focus microscopy measurements suggest the roughness may be higher for LSPwC, up to 19 µm (see Appendix A in section 9.2.1). In addition, LSPwC shows a clear pattern of medium-size valleys and peaks in the LT direction, observable when evaluating the 2D surface waviness 'rippled' profile (see Figure 3-19). In contrast, LSP surface topography (Figure 3-18) has a fainter ripple pattern, with minor surface waviness in the L direction. However, it has many small discrete features that appear to be small pits.

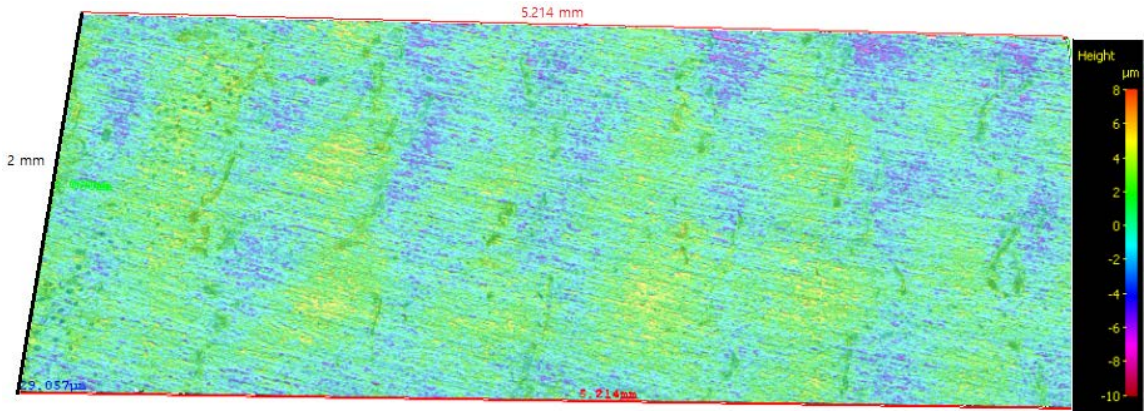

Figure 3-16 – LSP macro-image take with variable focus microscope. Surface topography shows a depth range of +8 µm to -10 µm.

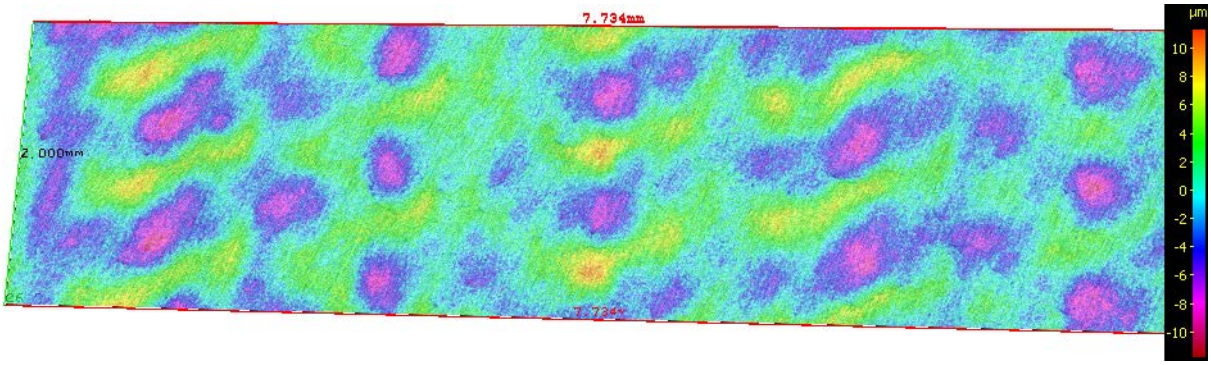

Figure 3-17 - LSPwC macro-image take with variable focus microscope. Surface topography shows a depth range of +12 µm to -12 µm.

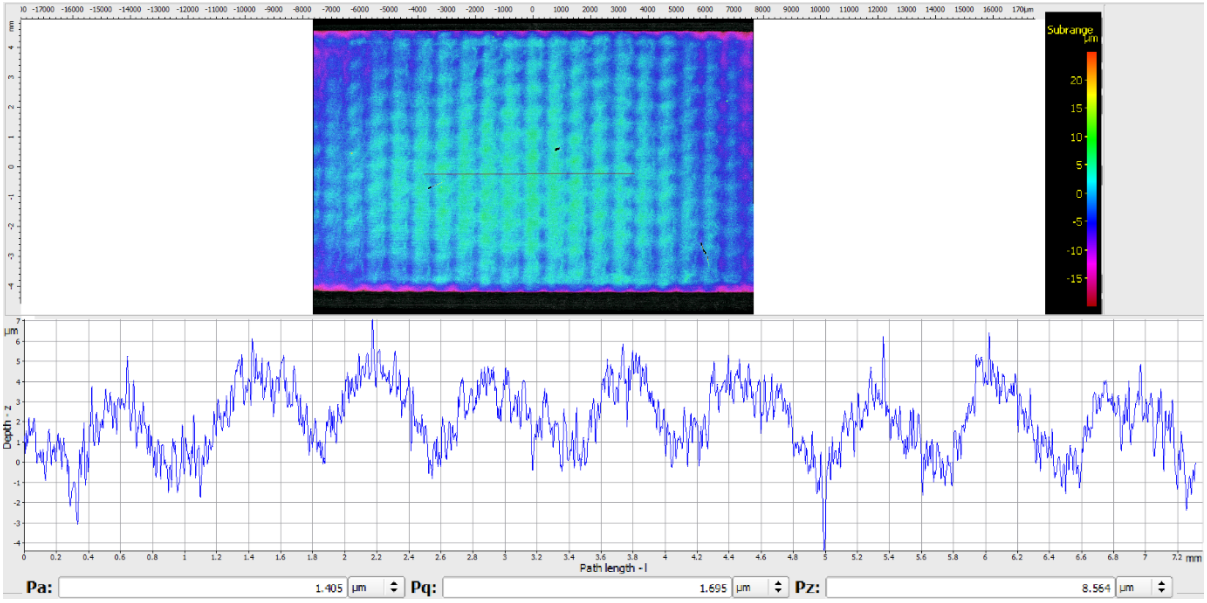

Figure 3-18 - Primary profile of LSP in L direction. From variable focus optical microscope.

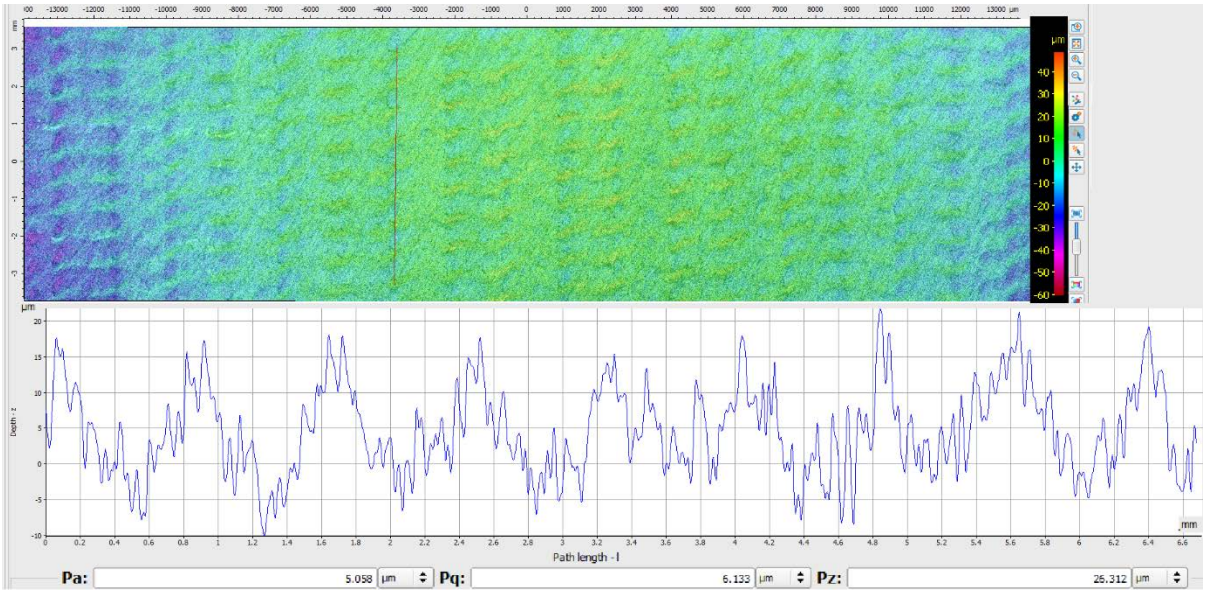

Figure 3-19 - Primary profile of LSPwC in LT direction. From variable focus optical microscope.

3.3.3.3 Laser shock peening generated pits

Small depressions found on LSP (Figure 3-16) led to more investigation of the topography. High magnification microscopy (see Figure 3-20) showed the LSP process has generated a small number of laser peening-process pits. Sampling of LSP Type A surfaces showed laser shock peening generated pits of 2 – 12 µm depth. Although the number of pits per area is random, it appears to be low. In some images (see Figure 3-21) there were indications the pits were aligned with the edges of the LSP ablative layer (black vinyl tape). High magnification of LSPwC images did not appear to show any clear discrete features as has been seen for LSP, if this exist they are masked by the higher roughness and waviness profile of the surface.

In addition, it is possible any LSPwC generated pits, or other features, may have been partially removed during mechanical removal of the oxide layer (see section 3.2.3).

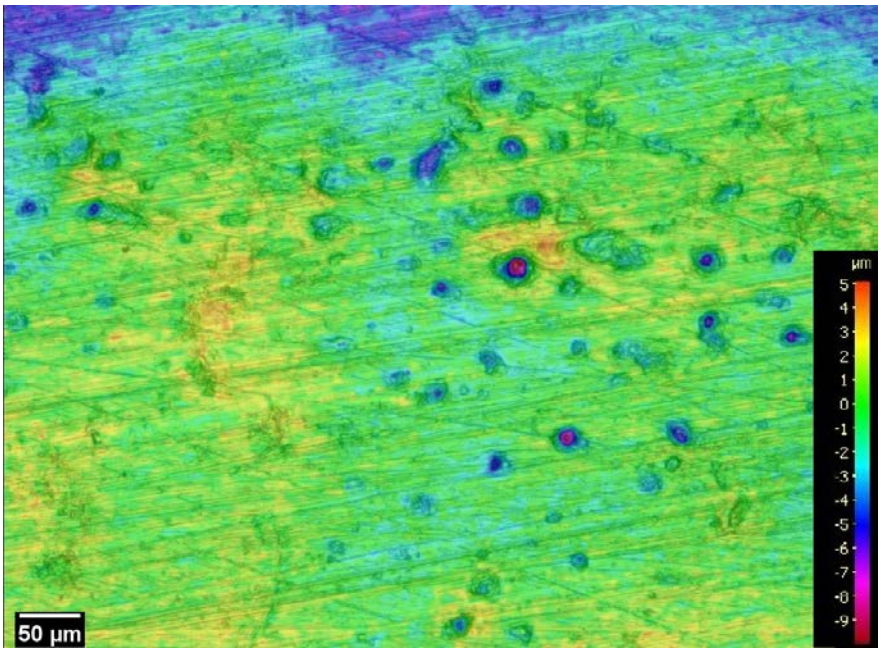

Figure 3-20 - An example of a bend bar surface with pits generated by LSP process. Number of pits per area differs greatly but is generally considered low. Captured by variable focus microscopy.

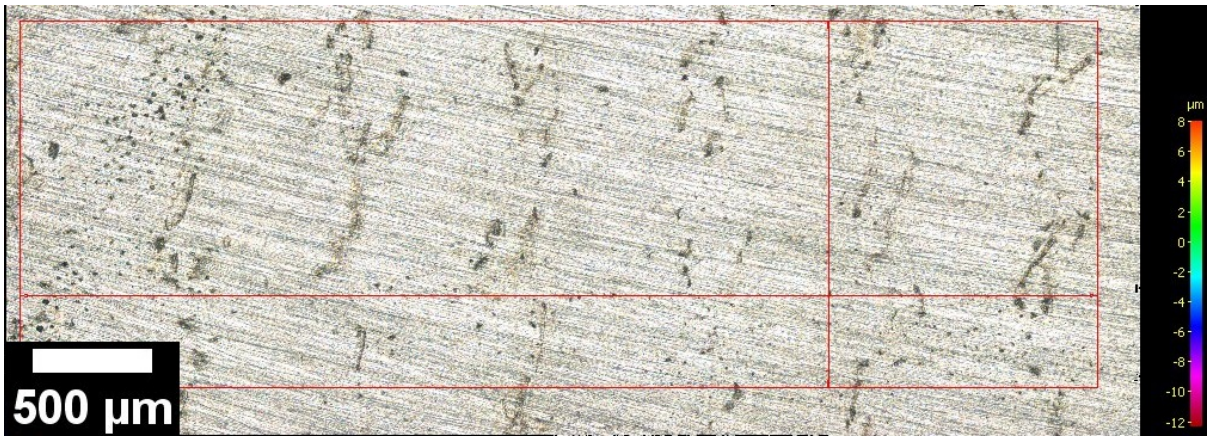

Figure 3-21 – LSP surface macro-image showing peening-generated pits may be aligned with ablative layer edges.

3.3.3.4 Grain characterisation after LSP

Line intercept measurements were not possible for LSP and LSPwC surfaces as the grain boundaries in microscopy images were difficult to separate from other features. This is likely due to the high level of deformation, recrystallisation and dislocation formation from laser peening. This made any possible measurements too subjective. In addition, a line intercept method of EBSD cross-sections images was not performed as indexing of highly deformed

areas, in this case at and up to 20 µm from the surface, is known to be a technique limitation [182][181]. Thus, the area most likely to have laser shock peening-induced grain refinement, and change in grain size, could not be accurately assessed.

EBSD recrystallization maps and graphs for baseline and LSP cross-sections (LT-ST microstructural plane) are shown in Figure 3-22, respectively. The recrystallisation analysis shows there has been a significant increase in deformed grains compared to baseline AA7075-T651. The baseline material appears to contain up to 30 – 35% retained deformed grains, which are expected to remain due to rolling during the manufacturing process. The LSP samples however contain up to 55% deformed grains, a significant increase in grain deformation levels. The largest concentration of deformed grains in the recrystallisation map appear at or near the surface. The percentage of deformed grains clearly decreases progressively moving away from the surface. Scans of the LSP LT-ST cross-section at 140 µm below the surface, or even further away, show similar percentage grain deformation as seen in the baseline material. Kernel average misorientation data shown in Figure 3-23 indicates there is clear grain deformation up to 100 µm under the surface, with the first 50 µm having the highest deformation. This grain deformation reflects the local microstructural change caused by LSP that has induced compressive residual stresses.

Figure 3-24 shows the kernel average misorientation (KAM) of LSP (A) and LSPwC (B) L-LT peened surfaces. As shown in Figure 3-23 the KAM of LSP cross-section clearly shows there is higher grain deformation near the surfaces (above 1.5° closest to surface) and progressively decreases to a stable 0.5° – 1.0°. The KAM values in Figure 3-24 (A) and Figure 3-24 (B) show grain deformation is highest at the LSP surfaces (constantly near to 2°). These suggests, that as shown in EBSD recrystallization maps of the LSP cross-section (Figure 3-23), LSP has caused grain deformation that is highest at the surface and progressively decreasing away from the surface.

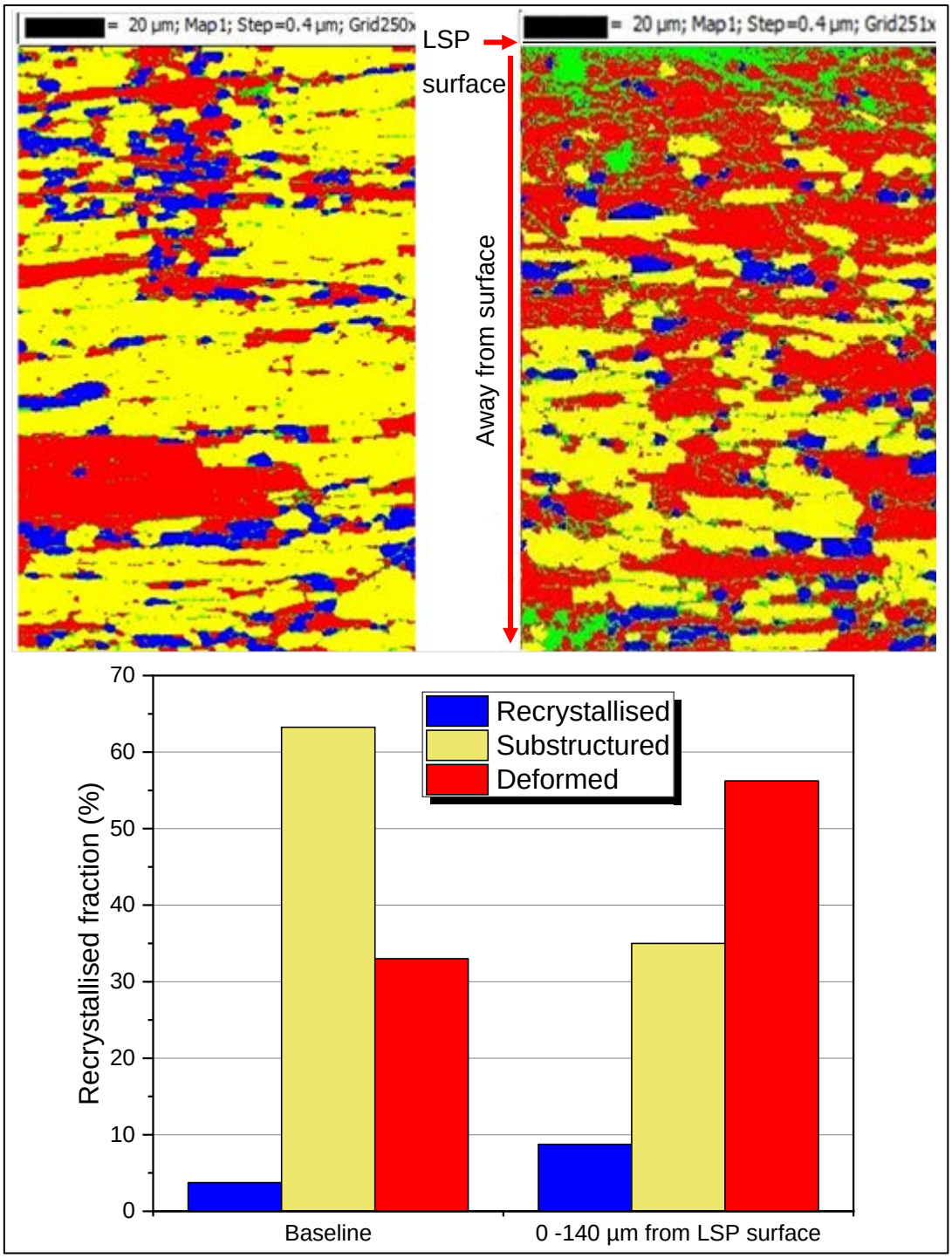

Figure 3-22 – EBSD recrystallisation maps showing cross-sections (LT-ST plane, LSP treated surface is in L-LT plane). Left: Baseline cross-section. Right: LSP cross-section. Bottom: recrystallisation percentages.

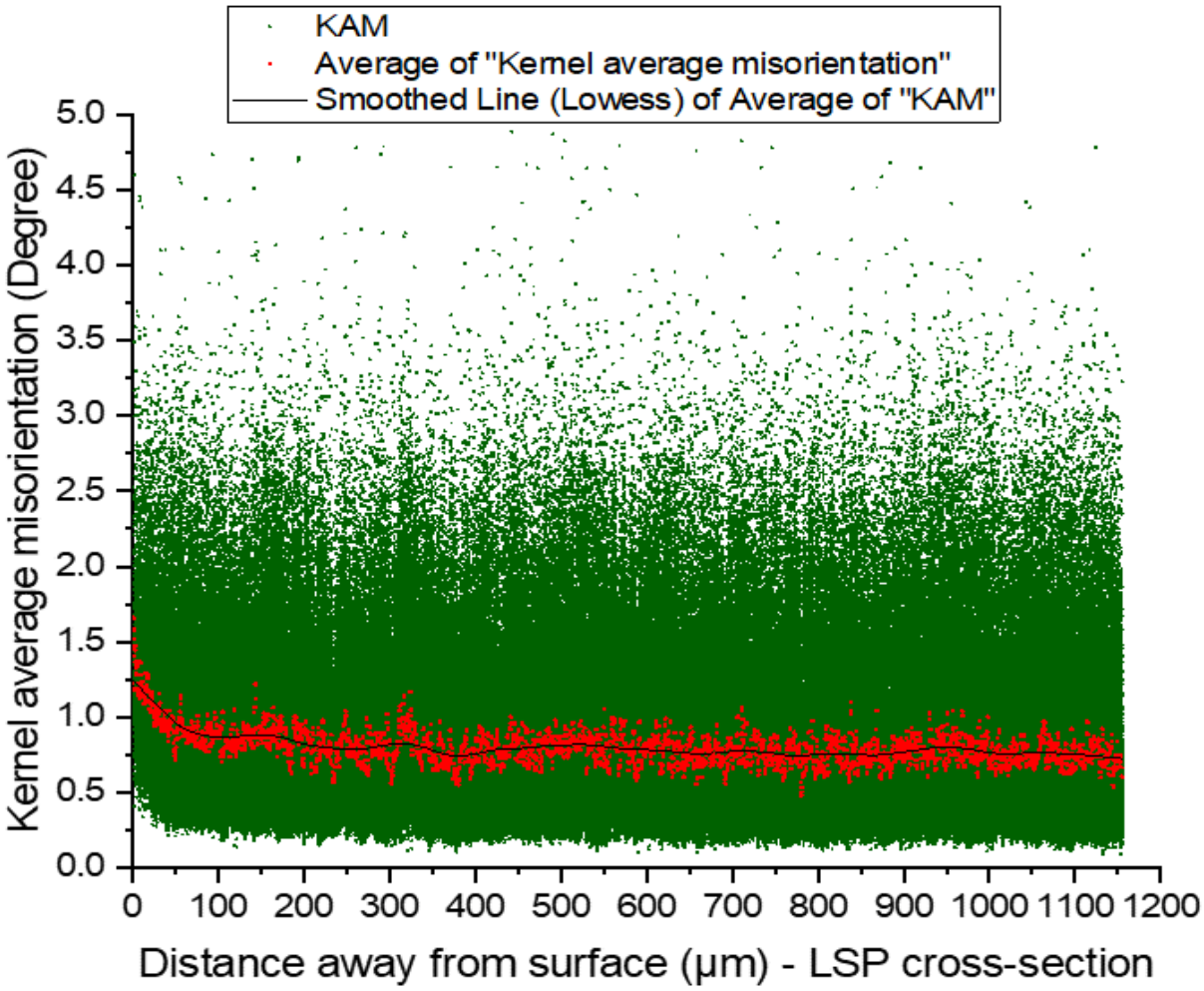

Figure 3-23 – LSP cross-section: Kernel average misorientation vs. distance away from LSP surface. Lowess is a local polynomial regression to create a smooth line through a scatter plot.

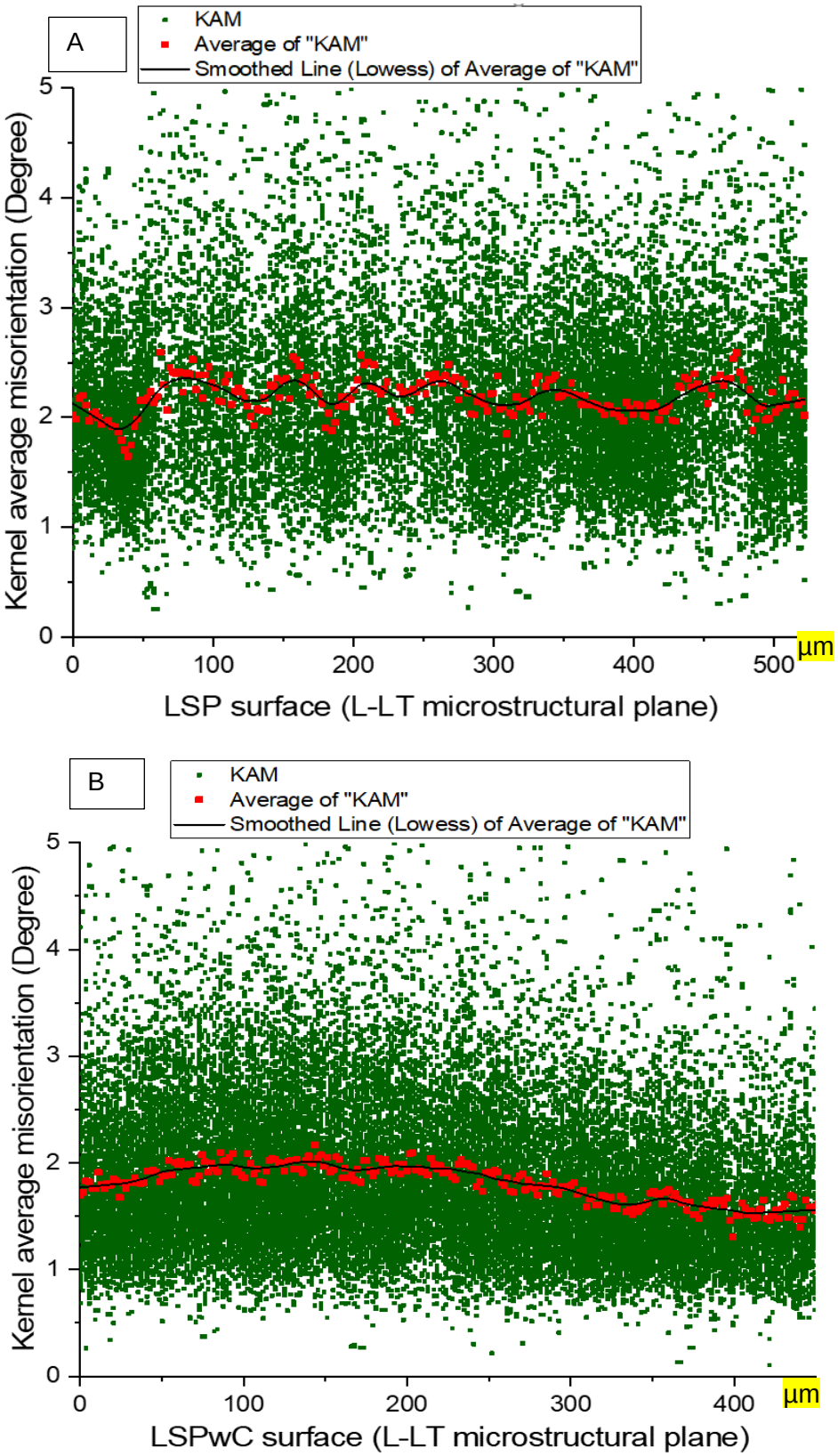

Figure 3-24 - Kernel average misorientation (KAM) data, average and smooth lines of (A) LSP surface (L-LT microstructural plane). (B) LSPwC surface (L-LT microstructural plane).

3.4 Discussion

3.4.1 Baseline AA7075-T651

Results in section 3.3.1 confirm this is a typical AA7075-T651 alloy with anisotropic microstructure and contains coarse particles typical of 7X75 aluminium alloys [39] [13][54]. These grain sizes calculated using the line intercept broadly agrees with previous studies [28][191][32][35] of 7XXX aluminium alloy rolled plate, where grains are reported to be in the order of 10s to 100s microns in the L direction, whilst being smaller in the other two directions, and smallest in the ST direction.

The intermetallic distribution found via X-ray tomography is consistent with previous studies: close to the 1% volume fraction mentioned by Harris [36], whilst Singh et al [40] reports 1.67%. The larger difference in percentage compared to Singh et al. could be attributed to their use of an X-ray synchrotron, which gives higher resolution and contrast, enabling smaller particle segmentation, such as $MgSi_2$. Figure 3-13 suggests a relatively small number of particles have very large volumes, the highest being near 45000 μm^3. This could be the equivalent of a 100 µm × 20 µm × 20 µm particle. Although this may seem large, previous studies [11][186] have shown particles cluster and align themselves in the rolling direction as stringers. It is likely the largest particles captured in this study are particle clusters and image segmentation could not distinguish individual particles.

3.4.2 Laser shock peening surface modification of AA7075-T651

Residual stresses in LSP are higher or equal to previous LSP or shot peen generated residual stresses in 7XXX alloys [8][155][192][125][156][82][90][172][193][130][194][195]. Figure 3-14 shows LSPwC residual stresses through the depth are higher than for LSP by up to 14%. Thus, also higher than previously reported residual stresses in 7XXX alloys. The exception is the surface, which is attributed to the LSPwC oxide layer formation leading to weak residual stress generation (-85 MPa). The subsequent mechanical polish partly solves this surface issue but does not produce residual stresses as high as the LSP surface. This surface modification difference between the two LSP types is also reflected in the KAM data (Figure 3-24), which shows a higher degree of angle misorientation in LSP surfaces compared to LSPwC, suggesting higher grain deformation at the LSP surface. For comparison, Figure 3-23 shows how the LSP KAM, and therefore plastic deformation, progressively decreases below the surface to considerably lower values, from near 2° at the LSP surface, to 0.75° at 1 mm

below the surface, where no LSP-generated plastic deformation is expected. This illustrates a shallow but relatively high level of plastic deformation (cold work) concentrated near the surface.

Table 3-6 shows the laser peening treatment at CSIR was successful in minimising surface roughness modification for LSP samples. The R_t, at 5.52 µm, is lower than a key paper on AA7075 laser peening by Peyre et al. [8], which used a similar power density (4 GW cm^{-2}) and reported R_t = 11 µm post-peening. In the same study, a shot peening treatment on AA7075 performed to generate similar compressive residual stress as the current LSP treatment, produced roughness of R_t = 42 µm. Other studies of shot peening also show higher surface roughness on AA7075 [172][194][193]. The increased roughness seen in these studies are closer to the values seen for LSPwC. Both the nature of non-ablative laser peening (ablation of alloy surface) and the subsequent mechanical polish to remove the oxide layer, lead to this increased roughness. According to the contact profilometer measurements this is mostly within the same magnitude as the baseline, although four times higher (for R_z and R_t). If the variable focus microscope measurements are considered, the R_t values (the maximum peak to valley) are nearly a magnitude higher than baseline, at 19 µm. This higher roughness, in conjunction with the waviness profile (likely caused by LSPwC plastic deformation) makes the overall (primary) peaks and troughs even higher than the roughness measurements suggest. These more pronounced surface features means the LSPwC surface is likely to have a stronger effect on other properties (such as corrosion or fatigue) compared to baseline or LSP.

An unintended effect of LSP treatment (using an ablative coating) has been the formation of small pits. As shown in Figure 3-20 and Figure 3-21, pits of up to 12 µm depth were found on LSP bend bar surfaces. Most pits were smaller than 10 µm depth. These pits contribute to the surface roughness of the material and will act as local stress concentration features during fatigue testing. This phenomena has been reported previously by Luong and Hill [156][125], during LSP treatment of similar aluminium alloys. These discreet pit phenomena are not seen in LSPwC. However, the LSPwC periodic profile and higher roughness (see Figure 3-16 and Figure 3-17) may make discrete features that act as stress concentrations harder to identify. Both LSP and LSPwC contain surface features that may promote early fatigue crack initiation, and localised corrosion at the troughs.

Hardness results (Figure 3-15) suggest AA7075-T651 surface hardness has increased after LSP. However, it is important to take into account the manner in which residual stresses may be affecting hardness testing. Simes et al. [196] reports that hardness testing in loaded material (either applied or residual stresses) will over-estimate hardness values if these are

compressively loaded. This agrees with the results seen in LSP Type A samples. However, the hardness overestimation is diminished when testing Type B samples. In these, the residual stress are expected to have been mostly relieved by the sample extraction process, confirming that hardness changes from LSP microstructure modification is likely limited. Considering LSPwC used similar peening parameters, residual stresses and KAM, LSPwC Type A and Type B hardness values would be expected to be similar to LSP. Instead, the LSPwC average and median hardness values are marginally higher than baseline. However, the variation level in both Type A and B LSPwC samples is very large compared to baseline and LSP values. It is possible there is an issue with testing accuracy due to the higher roughness, and profile waviness, in LSPwC.

The higher hardness values for the LSPwC Type A vs. LSP Type A in the 1 µm surface finish (in both cases material has been removed up to a maximum of 100 µm depth) strengthens the hypothesis that the hardness increase is linked to residual stresses. Residual stress measurements have shown LSPwC has higher subsurface residual stresses than LSP, suggesting a direct link between residual stress and hardness. In addition, comparing the residual stresses for LSP and LSPwC as-received finish with the 1 µm finish samples, also suggest a link: An increase in LSPwC 1 µm hardness compared to as-received hardness, due to residual stresses being higher subsurface; whilst for LSP the hardness difference is slightly lower, as the residual stress difference between the surface and near-surface is similar.

The way residual stress overestimates hardness is not completely clear. Simes et al. [196] study suggests the perceived hardness change is due to the residual stress modifying the stress state during hardness indentation. In contrast, Tsui et al. [197] performed a nano-indentation study that suggests the cause of overestimated values could be incorrect area deduction by material pile up. In addition, they showed once the pile-up area is taken into account, the hardness underestimation, or overestimation, disappears. Thus, it is possible the apparent increase in hardness seen in the LSP Type A samples is due to area underestimation caused by material pile-up on the indent's edges. Finally, Khan et al. [198][199] not only show residual stress affects indentation measurements but also present a methodology to extract residual stresses from experimental nano-indentation data.

It is difficult to compare the LSP and LSPwC hardness results unequivocally to other studies, as most do not make it clear whether the tests are done taking into account the residual stress effects on apparent hardness values. Hardness tests performed with 25g-f by Peyre et al. show limited (<10%) increase in surface hardness for AA7075-T651, which agrees with the LSP results in this study. A key paper on LSP by Clauer [5] does not see an increase in

hardness on AA7075 –T73 or T6 conditions. Clauer suggests this is due to the peak-aged alloy's high dislocation density, from precipitation hardening, limiting the ability of LSP to generate new dislocations. Longer pulse pressure duration is suggested as a way to increase dislocation density and surface hardness. Shot peening has higher pressure duration and tends to increase surface hardening more markedly [5]. An example of this on AA7075-T6 is a study by Becker [115] which sees no increase in surface hardness for LSP AA7075-T6 and a 20% increase from shot peening. In contrast Zupanc and Grum [194] do see a 25% increase on AA7075-T651 after LSPwC. Nevertheless, the effects of compressive residual stress on hardness values for some of these studies is not discussed, therefore it is not possible to assume these values are solely related to surface hardening rather than compressive residual stresses acting against indentation. Taking this into consideration, the limited surface hardness increase seen on AA7075-T651 correlates with what is reported in the literature.

3.5 Conclusions

1. Microstructural characterisation of untreated AA7075-T65 shows a typical 7XXX series alloy with anisotropic microstructure and coarse particles typical of 7X75 aluminium alloys.
2. LSP and LSPwC generated deep compressive residual stress fields of up to 400 MPa in AA7075-T651, whilst also causing a small increase in surface roughness for LSP (R_t = 5.52), and a moderate increase for LSPwC (R_t = 7.94 and pronounced waviness profile). In addition, LSPwC has a periodic profile of wide troughs and peaks not seen in LSP.
3. LSP treatment generated discrete pits of up to 12 µm depth, aligned with the ablative layer edges that could act as stress concentrations.
4. Laser peening caused a small increase in surface hardness for LSP (up to 11%) and likely for LSPwC. Nevertheless, when performing hardness tests the effect of residual stresses needs to be taken to account to understand whether surface hardness increases seen are in most part due to residual stresses or due to modification of the material's microstructure.

4 Fatigue

4.1 Introduction

As discussed in Chapter 2 the available literature surveyed suggests varying laser shock peening parameters will change the level of residual stress field and surface roughness in the material, and this in turn can vary the potential fatigue improvement. In addition, in some cases the micro-mechanisms of fatigue crack initiation appear to have been changed. However, this modification in crack initiation mechanisms has not been seen in most peened aluminium alloy studies surveyed. Overall, it is unclear the extent to which roughness, hardness and the level of residual stress, respectively, contribute to the overall fatigue life improvement, and how each of these influence the possible change in micro-mechanisms of crack initiation and propagation in aluminium alloys after peening. The following chapter is therefore dedicated to investigate the fatigue response of AA7075-T651 after laser shock peening performed to maximise fatigue improvement. To understand how, and to what extent, LSP and LSPwC generated residual stress, and the modified surface (microstructure, hardness and roughness), will each influence changes in the micro-mechanisms of short crack fatigue initiation and growth in aerospace grade AA7075-T651. The understanding gained (in Chapter 3) regarding LSP, and LSPwC, surface modification (grain structure, hardness, roughness) and residual stresses will be used to understand how each of these can affect fatigue behaviour.

4.2 Experimental methods

The materials used for this study, and fatigue sample manufacture are discussed in section 3.2. This section presents the methodology and methods used for fatigue testing, fractography and calculation of crack growth rate vs. stress intensity factor.

4.2.1 Fatigue testing

A servo-hydraulic Instron machine was used for four-point bend testing. The 4-point bend test was performed at 20 Hz frequency, with a load ratio of 0.1. The load setup is shown in Figure 4-1. After laser peening, bend bars (type A samples) were tested either as-received (1200 SiC grind followed by LSP treatment), or polished post-LSP to a 1 µm surface finish. See section 3.2 for more details on sample preparation and labelling. In total, twelve baseline, eight LSP and three LSPwC fatigue tests were performed.

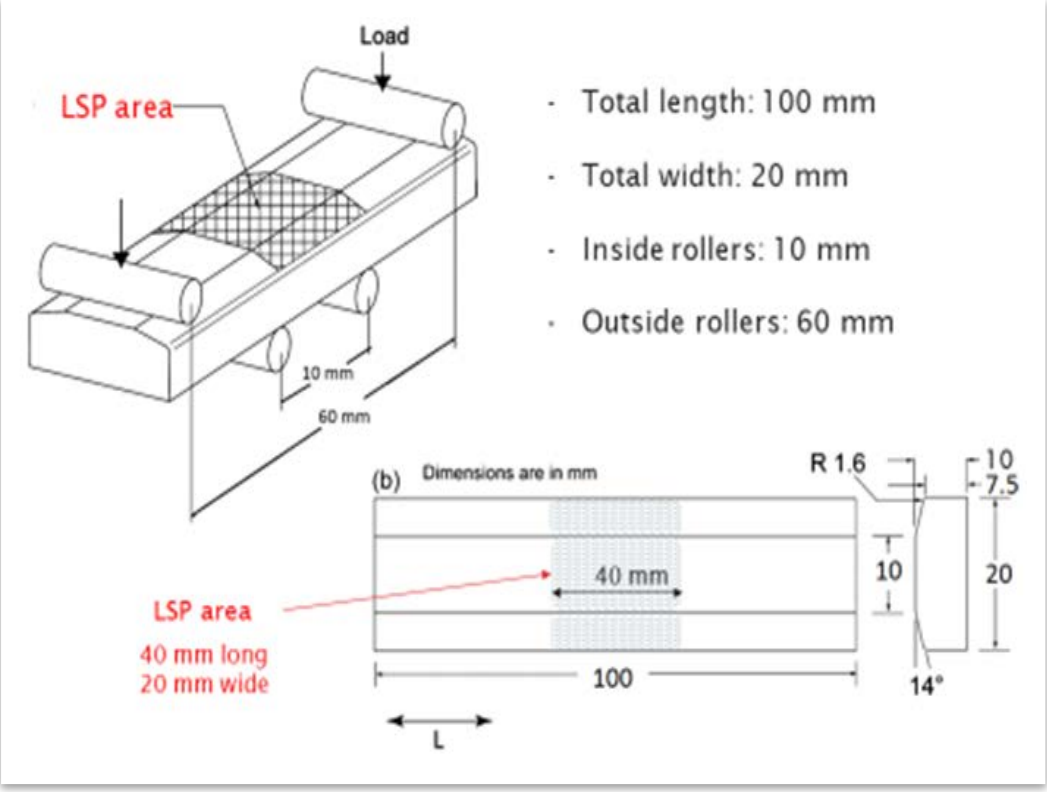

Figure 4-1 – Laser shock peening samples (Type A) and peening region.

A number of samples were initially tested below yield stress values to compare fatigue performance and analyse mechanisms of crack initiation and growth in a predominantly elastically loaded sample, with limited plastic strain ranges.

A smaller number of baseline and LSP samples were also tested at above yield stress values to understand how the LSP compressive residual stresses' beneficial effects may change due to higher subsequently applied plastic strain ranges. Overall, for both baseline and LSP tests, the nominal stress ranges (derived from beam theory) used for testing varied from 360 MPa to 595 MPa. Additionally, three LSPwC samples were tested, two as-received and one polished to 1 µm surface finish, at 400 MPa stress range, to investigate whether there were any fatigue behaviour differences between LSP and LSPwC.

Table 4-1 – List of fatigue test samples

Type	ID	Surface finish	Applied stress in MPa	Stress range for R = 0.1 / MPa	Test settings (All at f = 20 Hz)
Baseline	FLT5	1 µm	640	576	R: 0.1
	FLT2	1 µm	450	405	R: 0.1
	FPB-LT50	1 µm	453	407	R:0.5
	FPB-LT51	1 µm	453	407	R:0.1, R:0.5
	FPB-LT56	1 µm	400	360	R: 0.1
	FPB-LT52	1200 SiC grit paper	453	407	R:0.1, R:0.5
	FLT8	1200 SiC grit paper	450	405	R: 0.1
	FPB-LT1	1200 SiC grit paper	423	381	R: 0.1
	SBB-LT1	1200 SiC grit paper	428	385	R: 0.1
	SBB-LT4	1200 SiC grit paper	428	385	R: 0.1
	SBB-LT3	1200 SiC grit paper	402	362	R: 0.1
	SBB-LT5	1200 SiC grit paper	392	353	R: 0.1
LSP	FPB-LT8	As received	650	585	R:0.1, R:0.5
	FPB-LT14	As received	650	585	R:0.1, R:0.5
	FPB-LT4	As received	600	540	R:0.1, R:0.5
	FPB-LT5	As received	452.7	407	R: 0.1
	FPB-LT10	As received	452.7	407	R:0.1, R:0.9
	FPB-LT13	1 µm	490	441	R:0.1, R:0.5
	FPB-LT17	1 µm	545	491	R:0.1, R:0.5
	FPB-LT11	1 µm	452.7	407	R:0.1, R:0.9
LSPwC	FPB-LT18	As received	452.7	407	R:0.1
	FPB-LT21	As received	452.7	407	R:0.1
	FPB-LT25	1 µm	452.7	407	R:0.1, R:0.9

4.2.2 Fatigue crack growth capture

Two methods were used to assess crack propagation, (*i*) the replica method and (*ii*) the beach marking method.

4.2.2.1 Silicone rubber replica

The replica method consists of using ready-made replica material Struers F5. This material is applied during intermittent fatigue cycling of samples to obtain a visual record of the sample top surface and creating a series of snap shots of surface crack initiation and growth processes throughout the sample lifetime. After application of replica to the surface, it takes 20 minutes to harden and capture the sample's surface to a 1 µm resolution. This replica can subsequently be observed using optical microscopy. Successive crack lengths are measured and used to calculate crack growth rate d*a*/d*N* versus stress intensity factor (ΔK), assuming a crack aspect ratio of 1. Although this is expected to change in samples with laser shock peening, the crack aspect ratio is still assumed to be 1 due to lack of knowledge of possible variation from to peening.

4.2.2.2 Beach marking

For some laser peened samples, the replica method was not effective in monitoring crack behaviour due to subsurface crack initiation and growth. In this case, the beach marking method was used. Instron wave matrix was used to set up a regime where the load ratio was varied from R = 0.1 to R = 0.5, or R = 0.1 to R = 0.9 between blocks of cycling. This variation in load ratio was performed by increasing the minimum load, keeping the maximum load, and therefore K_{max}, constant during the whole test. The number of cycles for each load ratio was chosen based on expected total life and via experimental trials. For the 'R = 0.1 to R = 0.5' tests, fatigue life is presented as an estimate with error bars. The estimated life (N_{Total}) is equal to the cycles under 'R = 0.1' ($N_{R=0.1}$) plus a third of the cycles under 'R = 0.5' ($N_{R=0.5}$).

Equation 4-1

$$\boldsymbol{N_{Total} = N_{R=0.1} + \left[\frac{N_{R=0.5}}{3}\right]}$$

This method was presented in a paper by Sanchez et al. [200]. It is based on the Walker equation used for AA7075-T651 by Dowling et al [201], and a set of AA7075-T651 uniaxial data reported in [202], to estimate fatigue life for different load ratios. One fatigue bend bar was tested at R = 0.5 only, to confirm if this estimate is valid. This fatigue life estimate approach

was also assumed for the laser peened bend bars tested. Error bars are also presented to show the minimum fatigue life ($N_{R=0.1}$) and the maximum fatigue life ($N_{R=0.1} + N_{R=0.5}$). For tests performed with variation of R = 0.1 to R = 0.9, the number of cycles at R = 0.1 ($N_{R=0.1}$) is presented as total life, assuming a very limited contribution by loading at R = 0.9.

4.2.3 Microscopy

Optical microscopy and scanning electron microscopy were used to analyse fracture surfaces of fatigue samples, for both baseline and laser peened samples. The SEM microscopy settings are detailed in section 3.2.6.3. Optical and SEM microscopy, ImageJ processing [177], and fatigue data (number of cycles and load ratio) captured by Instron® Wavematrix were used to measure crack size and calculate crack growth rate versus ΔK.

4.3 Results

4.3.1.1 Fatigue life

Figure 4-2 shows all the fatigue tests performed in an *S-N* curve. Generally, fatigue data from baseline bend bar tests fall within the expected scatter of the data reported in the literature [28]. Baseline tests at 407 MPa stress range have fatigue life of 2 - 6 × 10^4 cycles. Data points with an error bar are tests performed using the beach marking method. The fatigue life error bars represent the variation of fatigue cycle counting as mentioned in section 4.2.1.

The LSP bend bars, as received and 1 µm polished, tested at 407 MPa applied stress range, failed at 1 – 3 × 10^6 cycles, a two orders of magnitude increase in total life. Fatigue lives of LSP 'as received' and 1 µm polished bend bars tested at 407 MPa stress range are in the same order of magnitude. There is one exception, where an 'as received' bend bar failed at 10^5 cycles. The causes of this are explored in more detail in section 4.3.1.2.

As the stress range at which samples are tested is increased by steps of approximately 50 MPa, the 10^6 cycles fatigue life is maintained until the stress range reaches 490 MPa. At this point fatigue life sees a significant drop, to 10^5 cycles. A further increase to 540 MPa and 595 MPa stress range (note this is above AA7075-T651 theoretical yield stress of 503 MPa) produces another large drop in fatigue life, down to 10^4 cycles. These values are now similar to baseline samples tested in the 407 MPa stress range.

For as-received LSPwC fatigue life increase is more limited compare to the gains seen for LSP, failing at 2 × 10^5 cycles, making it more comparable with the LSP sample exception that also failed at the surface. Polishing the sample to a 1 µm surface makes LSPwC fatigue life, at 2 × 10^6 cycles, comparable to LSP tested at the same stress range.

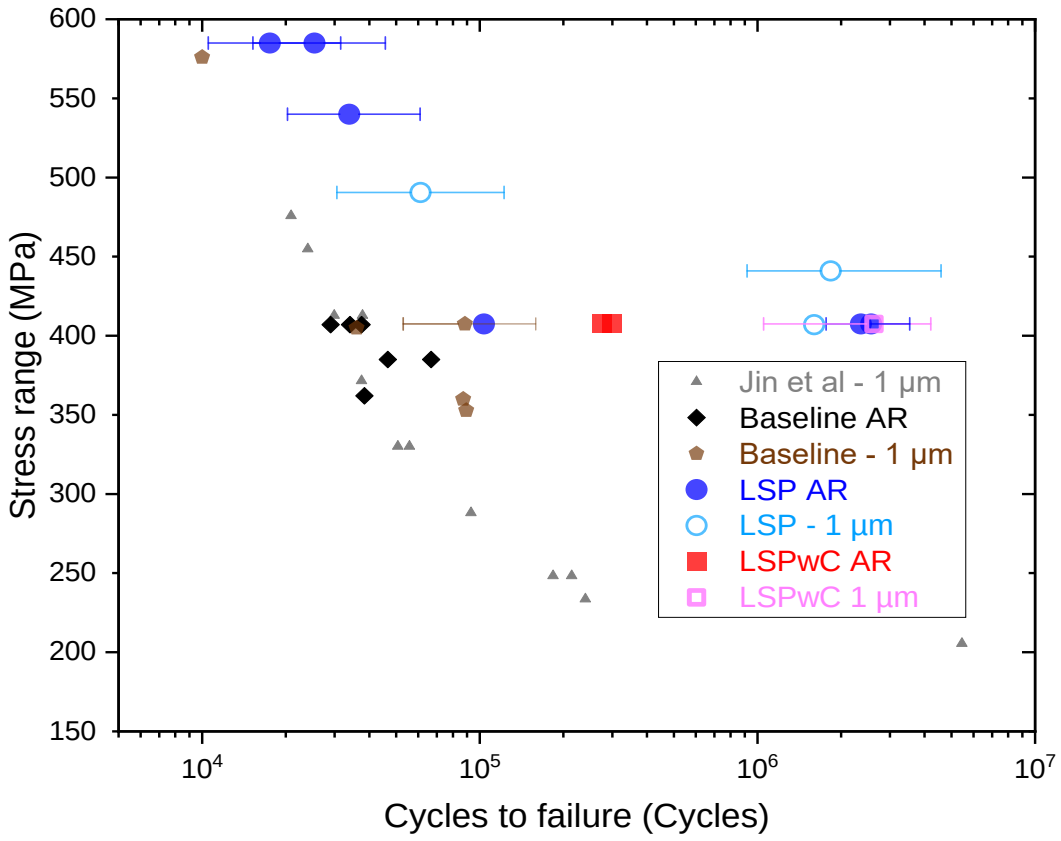

Figure 4-2 – Stress range vs. cycles to failure for baseline, LSP and LSPwC.

4.3.1.2 Fractography

Figure 4-3 (a)(b) shows typical crack initiation sites of fatigue tested baseline AA7075-T651. All of these crack initiation sites are at the surface, associated with the presence of coarse particles. SEM-EDS semi-quantitative analysis of these coarse particles predominantly found Al_7Cu_2Fe, and occasionally $Al_{23}Fe_4Cu$.

In the case of LSP fatigue tests at 407 MPa and 440 MPa stress range, the fracture surfaces show crack initiation points considerably below the surface, as shown in Figure 4-3 (c)(d). The initiation site depth varies between 200 µm and 400 µm below the surface. Furthermore, high magnification SEM showed there were no coarse particles present at these locations.

As mentioned in section 4.3.1.1 there was one exception to the above results. One 'as received' LSP bend bar tested at 407 MPa failed at 10^5 cycles, not 10^6. The fracture surface, Figure 4-3, show that the crack initiation site is not the same as other LSP fatigue tested samples previously shown. As shown in Figure 4-4, the crack initiation site is from a surface pit of 12 µm depth and approximately 20 µm width.

The fatigue bend bar tested at 490 MPa, which also saw a drop in fatigue life to 10^5 cycles, exhibited crack initiation from a pit located at the chamfer, as shown in Figure 4-3 (g)(h). All LSP bend bars fatigue tested at 545 MPa and 595 MPa failed from initiation at the top surface. As seen in Figure 4-3(i)(j), all crack initiation sites were at coarse particles, similar to baseline behaviour. SEM-EDS analysis confirmed these crack initiating particles were Al_7Cu_2Fe.

In the case of LSPwC fatigue behaviour, unlike LSP (apart from the exception mentioned above), crack initiation of as-received samples in the 407 MPa stress range occurs at the surface. As seen in Figure 4-5, the samples that failed at 2×10^5 cycles have failed on what appear to be either shallow pits or pronounced roughness features. In one case, in combination with a coarse particle sitting just beneath the surface feature. The 1 µm polished LSPwC sees crack initiation at approximately 475 µm subsurface, without coarse particles present, behaving in a very similar manner to polished LSP samples.

Baseline: All stress ranges above 360 MPa. Crack initiation at surface coarse particles.	a	b
LSP: Stress range 407 MPa. Sub-surface crack initiation, no coarse particles found.	c	d
LSP exception: Stress range 407 MPa. Crack initiation at mechanical pit.	e	f
LSP: Stress range 490 MPa. Crack initiation at corrosion pit at chamfer.	g	h
LSP: Stress range 545 MPa or above. Crack initiation at surface coarse particles.	i	j

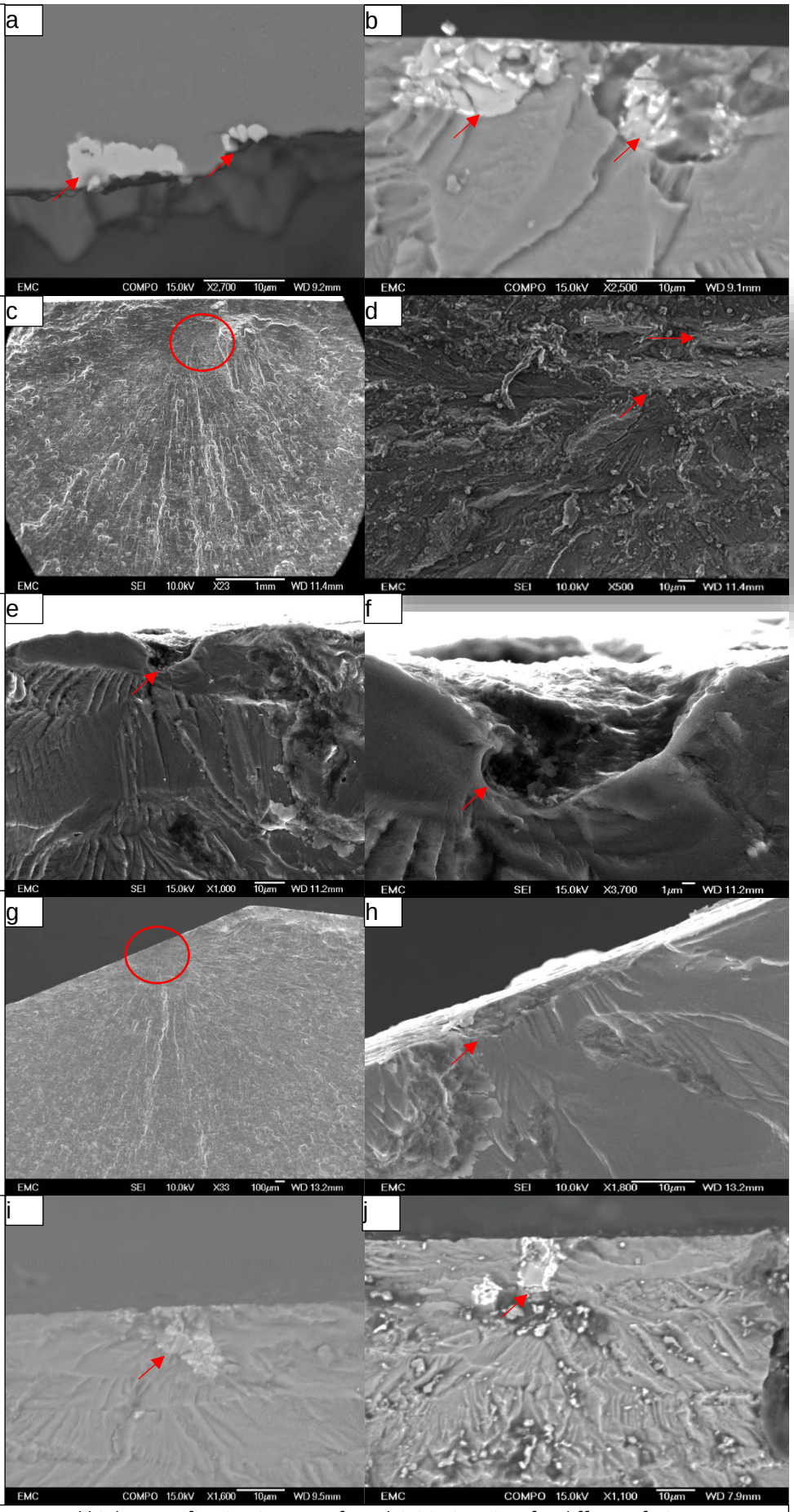

Figure 4-3 – Low and high magnification images of crack initiation sites for different fatigue test conditions. a-b: All baseline tests. c-d: LSP tests at 407 MPa stress range. e-f: One LSP test at 407 MPa which was an exception to the previous tests. g-h: LSP test at 490 MPa stress range. i-j: LSP tests at or above 545 MPa stress range.

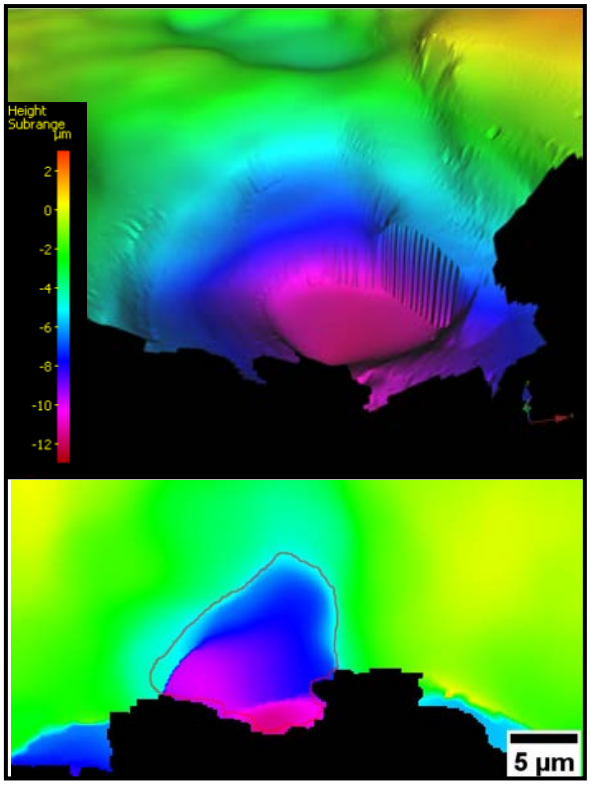

Figure 4-4 – Topographical images of both sides of pit acting as initiation site of LSP bend bar. Tested at 407 MPa stress range. Failed at 10^5 cycles. Taken from top surface (L-LT plane).

LSPwC: Stress range 407 MPa. Crack initiation at surface features.	a	b
LSPwC: Stress range 407 MPa. Sub-surface crack initiation, no coarse particles	c	d

Figure 4-5 - Low and high magnification images of crack initiation sites for the two LSPwC fatigue test conditions at 400 MPa stress range. a-b: LSPwC As-received. c-d: LSPwC 1 µm surface finish.

4.3.1.3 Crack propagation

The crack propagation rate vs. Δ*K* data, shown in Figure 4-6, suggests there is no clear difference in crack propagation rate between baseline and LSP fatigue tests. Furthermore, Figure 4-7 indicates LSP at high cycle fatigue shows crack initiation time is markedly higher than that of baseline samples when comparing applied stress range (SR) of 407 MPa. The beneficial effect of LSP compressive residual stress on crack initiation decreases as the applied stress is increased, as seen by the decreased initiation time in the LSP transition sample (490 MPa) and LSP low cycle fatigue samples (above 540 MPa). However, it is important to mention beach marking of subsurface crack growth was limited and visual inspection of fracture surfaces did not show clear marks. This meant, for the below yield strength applied loads, crack growth data was only captured when the cracks were large (in stage II). In the case of LSPwC, the crack propagation rate vs. Δ*K* data, although only three data points are available, is clearly lower than the baseline trend and the LSP values. In addition, the crack length at the first Δ*K* value is approximately 600 µm long, where residual stresses are not as high as they are near the surface. This would imply at or near the surface, due to the higher residual stresses, crack growth rate could be considerably slower than what is seen in these results. Thus, it could be suggested LSPwC has significantly slowed down crack growth, particularly near the surface.

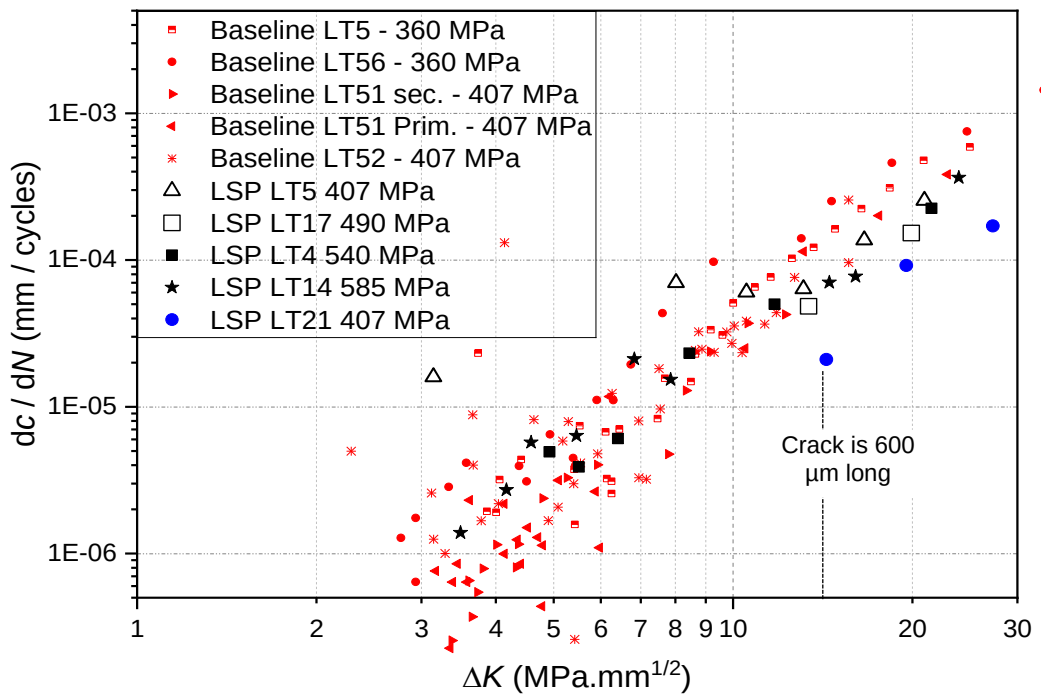

Figure 4-6 - Crack growth data vs. stress intensity factor for baseline, LSP and LSPwC fatigue tested samples. This includes crack propagation data captured by replica method and the beach marking

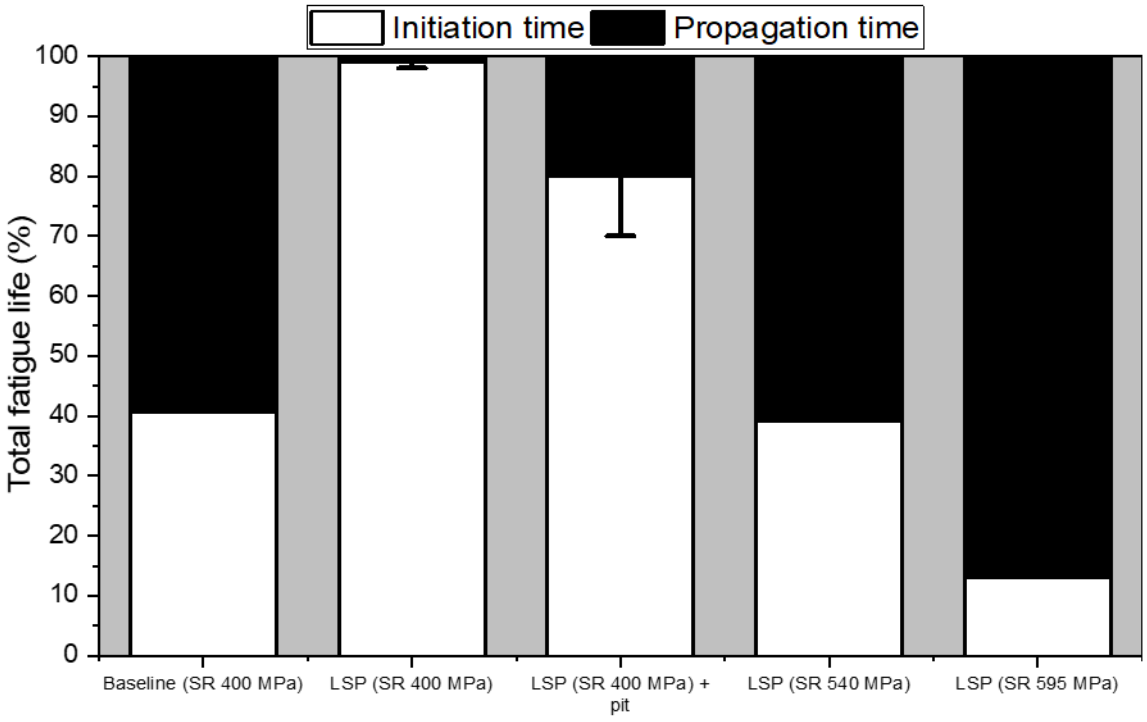

Figure 4-7 - Crack initiation and crack propagation as a percentage of total life. Baseline (SR 400), LSP (SR 400 – 595 MPa) and LSP (400 MPa) + pit. Crack initiation is defined as a crack of 50 – 100 µm. Due to the difficulty capturing crack initiation for LSP (SR 400 MPa) samples, with and without pits, these have error bars showing an estimate of the minimum crack initiation time. Estimates are based on extrapolating the crack growth rate vs ΔK logarithmic equations generated by the existing data.

4.4 Discussion

According to Figure 4-2, there is a substantial improvement in fatigue life of samples tested at 407 MPa stress range once they have been LSP treated. In effect, LSP treatment moves the fatigue performance of AA7075-T651 from the low cycle fatigue (LCF) regime to the high cycle fatigue (HCF) regime for the same applied stress range. Fractography indicates this is related to a change in the micro-mechanism of crack initiation. The LSP-induced compressive residual stress de-activates crack initiation from the coarse particles at the surface, and crack initiation is moved subsurface (0.2 mm – 0.4 mm in depth), dependent only on the local stress field for initiation. Sanchez et al.[1] [200] investigated this associated mechanism by using an FE model to predict the mean stress distributions in baseline and LSP samples at SR 407 MPa, shown in Figure 4-8 (a).

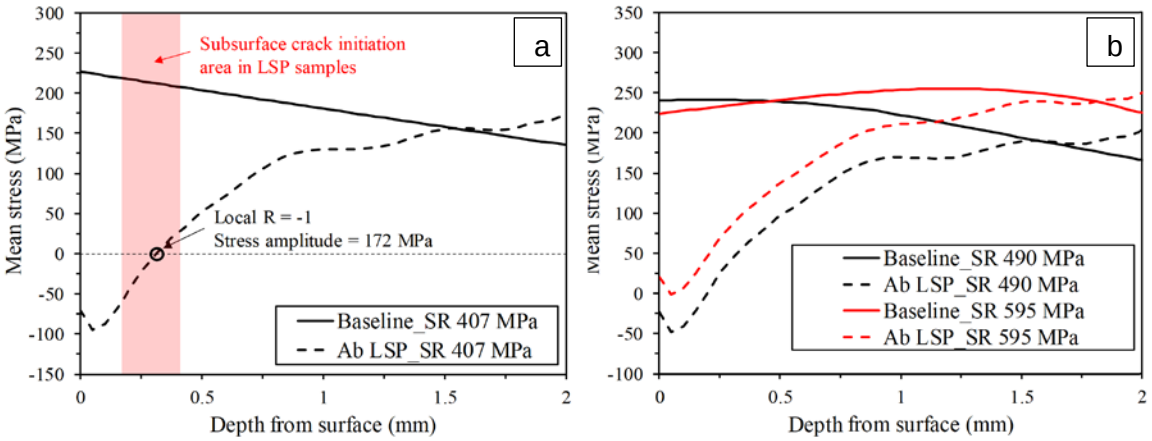

Figure 4-8 – FE-predicted mean stress distributions in baseline and LSP samples at (a) 407 (b) 490 and 595 MPa stress ranges. (Taken from Sanchez et al.[200]*)*

Clear benefits resulting from the LSP-induced compressive residual stress can be seen up to a depth of 1.0 mm, particularly at the near-surface area where the mean stress becomes negative. This implies that surface crack initiation at coarse particles in the LSP samples tends to be resisted by the surface compressive residual stress. Figure 4-8(a) further shows that the effects of the compressive residual stress start to quickly diminish with increasing depth from 0.2 mm, leading to the transition from negative to positive local mean stress. It is particularly noted that the local stress amplitude at zero mean stress point (at the depth of 0.31 mm) is 172 MPa with a local R = -1, according to the FE analysis. This stress value is greater than the fatigue limit (i.e. 159 MPa in stress amplitude) of AA7075-T651 under fully reversed

[1] This particular FE modelling work was performed by co-author Chao You.

uniaxial loading [31], suggesting the activation of local crack initiation and then subsequent growth. A previous study on shot peening of a high carbon chromium steel [164] showed a similar change in crack initiation mechanism from surface roughness cracks to subsurface inclusions when shot peened. There are similarities with this study in terms of the compressive residual stress being high enough to result in the local effective cyclic stress range being low enough to not activate surface initiation at coarse particles. Unlike the aforementioned study, the present study shows coarse particles are not involved in subsequent subsurface crack initiation in the LSP samples.

One LSP sample tested at a stress range of 407 MPa does not behave as previous tests, dropping from the HCF regime to LCF. The cause of this drop in fatigue life is crack initiation due to a pit generated during the LSP process. Figure 3-20 shows all LSP samples have these pits, although most appear to be smaller than 10 µm. The LSP sample tested at a stress range of 407 MPa, which failed in LCF, had an activated pit of 12 µm depth. It is possible there is a critical depth at which a LSP process pit acts as a large enough stress concentration to overcome the effects of the compressive residual stress and suppress the LSP benefits seen in other samples. This theory is reinforced by the as-received LSPwC fatigue test results. In this case, the surface features, which appear to be caused by higher surface roughness, leads to surface crack initiation and LCF behaviour. Although these are only two tests, it suggests LSPwC causes more deformation than LSP and thus a more heterogeneous surface (P_z = 26 µm). This in turn causes surface stress concentrations that are as effective as the 10 µm depth discrete LSP pits.

Polished LSP and LSPwC tests in stress ranges between 407 MPa and 440 MPa show the effectiveness of a light polish and the removal of both surface roughness and particularly LSP process pits. It is apparent that polishing LSP and LSPwC samples ensures they achieve their full potential of changing to the HCF regime and substantially increasing fatigue life. Furthermore, the test at stress range of 440 MPa shows the fatigue life for samples tested close to the yield strength of AA7075-T651 (theoretical 503 MPa, experimental 444 MPa) can receive the full benefits of LSP. Becker [115] performed 3-point bend fatigue tests on LSP treated AA7075-T6 which saw a relatively modest improvement in fatigue life when polishing the surface, and with no change in crack initiation mechanism. These suggest that the change in crack initiation mechanism and therefore the substantial gain in fatigue life is due to a complex interplay between surface roughness and residual stress. As an interesting example, Peyre et al. [8] fatigue tested LSP and shot peened treated AA7075-T73 and saw no subsurface cracking in the LSP samples. Compared to the present study the difference is likely due to slightly lower compressive residual stress (especially through the depth) and

higher surface roughness. Shot peened AA7075-T73 on the other hand saw some subsurface crack initiation due to a combination of high compressive residual stress at the surface, very low compressive residual stress through the depth and low applied loads, despite a much higher surface roughness compared to LSP [8]. Luong and Hill performed fatigue testing on AA7050-T7451 [125], where samples had lower compressive residual stresses (approx. 250 MPa) at the surface, and higher at 0.1 mm depth (400 MPa). All cracks initiated at the surface, in some cases pits of 5 mm depth were reported as crack initiation points, and polishing the surface did not move the initiation site sub-surface, likely due to the fact that compressive residual stress were lower at the surface, promoting surface crack initiation. This in turn led to a more modest fatigue improvement in their LSP samples, and no change in fatigue regime (although several test samples, tested at lower applied loads, were stopped at one million cycles and failure mechanisms were therefore not captured).

For the fatigue test with a stress range of 490 MPa, where the maximum applied stress is above the yield strength of the material, the surface stress may be high enough to cause some plastic strain, reducing the effectiveness of any pre-existing compressive residual stress at and near the surface. The high applied stress in particular is expected to cause a return to “untreated” fatigue behaviour: crack initiation at the surface. Nevertheless, for a stress range of 490 MPa, fatigue crack initiation occurs at a pit in the bend bar chamfer, where no polishing was performed. The pit produced a high enough stress concentration to move crack initiation from the top surface to a chamfer. Further tests with a polish of all top surfaces including chamfers would be important to understand if a stress range of 490 MPa is a transition zone, or whether at this stress range the LSP-induced compressive residual stresses are still high enough to produce HCF behaviour.

At stress ranges above the yield strength (545 – 595 MPa) all tests fail at the surface from coarse particles. This is a return to the crack initiation mechanism seen in baseline material. Figure 4-8 (b) suggests that the effects of LSP-induced compressive residual stress seem to be retained at stress ranges between 490 – 595 MPa in terms of the mean stress level. Nevertheless, Sanchez et al.[2] [200] FE model (see Figure 4-9) showed plastic deformation starts to accumulate in the surface layer at a stress range of 595 MPa in LSP samples, because the applied tensile stresses at the surface are too high to be compensated effectively by the compressive residual stress. This implies the transition of the crack initiation site from subsurface to the surface at high loads. Under such circumstances, the benefits of LSP tend to be greatly reduced compared to lower load levels (e.g. stress ranges between 407 MPa

[2] This particular FE model work was performed by co-author Chao You.

and 440 MPa), as demonstrated in Figure 4-2. Surface roughness, particularly the pits as shown in Figure 4-3(e)-(h), is also likely to further accelerate surface crack initiation, again suggesting there is a interplay between surface roughness (stress concentrations), applied tensile stress, and residual stress at both the surface and subsurface.

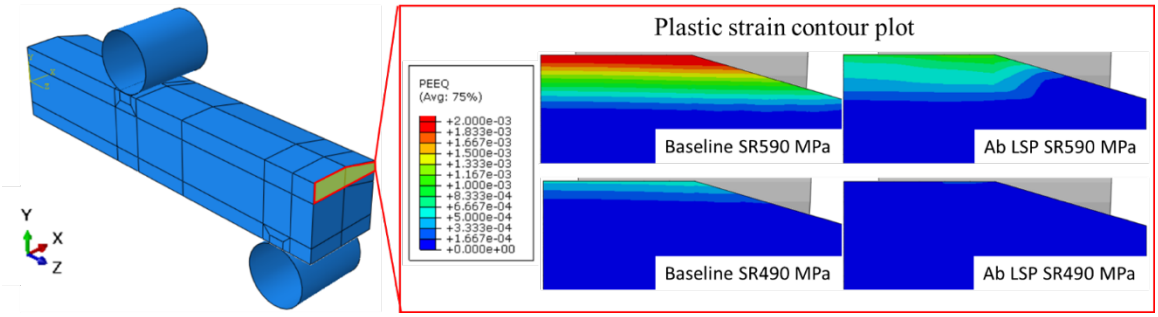

Figure 4-9 - FE-predicted plastic strain distribution near the surface of baseline and LSP samples at SR 490 and 595 MPa (no plastic strain is generated in either baseline or LSP samples at SR 360-440 MPa).

In terms of crack propagation determination, the beach marking method had mixed success. Particularly for LSP and LSPwC treated samples with sub-surface initiation. It is possible the shape of subsurface cracks (assumed semi-elliptical for the Δ*K* calculation) also leads to Δ*K* estimation inaccuracies. In addition, sub-surface crack propagation within a compressive residual stress field might reduce the effectiveness of beach marking as well as the calculation of Δ*K*. The LSP-induced compressive residual stress could be reducing the effectiveness of changing load ratio (R = 0.1 to R = 0.5) by reducing the difference in local mean Δ*K*. This means the microscopic roughness that differentiates fatigue growth for different load ratios may be too similar to produce clear beach marks [203]. There is also the possibility that (due to residual stress) the local stress field goes through compressive stresses that cause contact between the two sides of the crack, which would remove beach marking evidence due to friction. This may explain why only a small number of samples had clear beach marks, and this was indeed more likely in tests where the maximum stress was above yield stress.

The LSP crack growth rate vs Δ*K* data compiled suggests all LSP crack propagation is essentially within the baseline data trend. Due to the possible inaccuracies mentioned above it is possible that any crack growth rate delay by LSP is underestimated. The existing deep compressive residual stress in the samples would be expected to delay crack propagation. Previous literature [8] suggest this would be the case for AA7075-T651 and that LSP would slow crack propagation but this will probably be a small contribution to overall fatigue life improvement. In the case of LSPwC, although only a very small number of data points were obtained (three) and these were at relatively large cracks, there is a clear indication of crack

growth delay, and its crack growth rate is, relative to LSP, slower due to LSPwC having higher compressive residual stresses. In addition, Figure 4-7 shows LSP-induced compressive residual stress vastly increases initiation time, but this also depends on the applied stress range. The higher the applied stress range, the less effective LSP-induced compressive residual stress are at delaying crack initiation. In addition, the LSP-induced residual stress field and depth profile, as well as the shape and depth of defects (including pits) appear to be important variables influencing fatigue crack initiation mechanisms (surface or sub-surface) and thus changes in fatigue regime.

Thus, the main conclusion that can be taken from this study's crack growth data is that crack initiation is the main cause of the observed fatigue life increase. There is likely to be an improvement in crack propagation but this is assumed relatively small compared to crack initiation and has been hard to determine explicitly. Further work is required to accurately capture crack propagation data (short crack shape, growth rate and ΔK) in LSP and LSPwC samples under high cycle fatigue. One possibility being considered is using X-ray tomography (ex- and/or in-situ) in combination with other characterisation techniques (SEM, FIB), as this has been shown to produce high resolution data of fatigue cracks and surrounding microstructure [204][205][206].

4.5 Conclusions

1. The largest improvement in fatigue performance is for cases where the maximum applied stresses were below the yield strength of AA7075-T651, and where a change was observed in fatigue crack initiation mechanism (from surface coarse particles for baseline, to subsurface and dependent on the local stress field for LSP and, if polished, for both LSP and LSPwC). This transition also pushed the fatigue behaviour into the high cycle fatigue regime.
2. At high loads, where maximum applied stresses were above the yield strength, the combination of high applied loads and plastic strain at the surface relieve the LSP compressive residual stress benefits. This returned the observed fatigue behaviour to the low cycle fatigue regime, where coarse particles at the surface are the main crack initiation sites. Thus, fatigue life improvement from LSP is small under these loading conditions.
3. An increase in crack propagation time for laser peened samples is expected, and clearly seen for LSPwC, but appears relatively small compared to the much larger increase observed in crack initiation time (at the same nominal applied stress ranges). However, characterising crack propagation time is very challenging with the techniques used in this study.
4. The surface condition of the material is critical to obtaining the maximum benefits from laser peened compressive residual stresses. More investigation is required to understand the interplay between a critical depth at which a surface feature acts as a stress concentration and counteracts a given laser peened-induced compressive residual stress profile enough to prevent a change to sub-surface crack initiation, drastically reducing the potential for increased fatigue performance.

5 Corrosion and subsequent fatigue

5.1 Introduction

The effects of LSP and LSPwC, on the corrosion performance and fatigue performance of corroded AA7075-T651 will be investigated. The objectives of this study are to understand to what extent the laser peening generated residual stresses and the modified surface (hardness and roughness) influence the electrochemical properties and corrosion performance of AA7075-T651. Additionally, to understand if the formation of corrosion pits is hindered or encouraged by laser peening. Finally, to investigate how corrosion pits might affect the fatigue performance, and crack initiation mechanisms, previously seen in peened AA7075-T651.

5.2 Experimental methods

The materials used for this study, and sample manufacture are discussed in Chapter 3.2. In addition, fatigue sample preparation and fatigue testing is discussed in Chapter 4.2. Therefore, this chapter presents the methodology for corrosion testing only. As in previous chapters, both type A and type B samples are tested. As explained in section 3.2.2, it is assumed type B samples have limited residual stresses due to stress relaxation from cutting, unlike type A samples which have intact residual stresses.

5.3 Electrochemical testing

To characterise the electrochemical properties of the AA7075-T651 laser peened surface the remaining sample surface was masked using a mixture of beeswax and colophony resin (3:1 ratio), leaving only 25 mm^2 unmasked. All electrochemical tests are performed in ambient temperature and atmospheric conditions. After corrosion exposure, the samples are ultrasonically cleaned in ethanol (45 minutes at 50°C) to remove soluble corrosion products. Electrochemical measurements were carried out in a Faraday cage, in a single compartment three-electrode cell with a silver/silver chloride (Ag/AgCl) reference electrode, a graphite counter electrode, and a 3.5 wt.% NaCl test solution. A VMP3 Biologic VSP multi-channel potentiostat and EC-Lab v11.10 software were used to perform the tests and interpret data.

The electrochemical tests were:

- Open circuit potential at 30 min and 24 h, on type A and type B. These were performed to understand the short term and long term effects of a corrosive environment (3.5% NaCl in water) on the electrochemical response (corrosion potential) of each surface. Additionally a small number of samples were exposed for 72 h for subsequent microscopy analysis of corrosion feature initiation mechanisms (Table 5-1).
- Potentiodynamic polarisation, performed on both type A and B samples (Table 5-2). These were performed to understand the kinetic properties of each surface when polarised and is a useful tool for comparison of electrochemical properties.
- Galvanostatic control: These tests were performed to understand the electrochemical response, and study the degradation, of each surface after accelerated corrosion. Two galvanostatic control exposures were performed with the aim to capture corrosion behaviour at two different regimes. High galvanostatic control is performed on both type A and B samples. Low galvanostatic control is a smaller study performed on type A only.

The total charge was the same for both low and high galvanostatic control (144 C) (Table 5-3).

Table 5-1 – Open circuit potential test details

Open circuit potential	Parameters	Comments
Rest time	30 min	Short-term response
	24 h	Long-term response
	72 h	Investigate corrosion feature initiation
pH	6.5 − 7.5	Ambient temperature and humidity
Electrolyte	3.5 wt.% NaCl	-

Table 5-2 – Potentiodynamic polarisation test details

Potentiodynamic Polarisation	Parameters
Rest time	30 min
Potential sweep rate	0.2 mV s^{-1}
Potential range	-0.250 < E_{corr}< +0.350 V
pH	6.5 − 7.58
Electrolyte	3.5 wt.% sodium chloride (NaCl) solution

Table 5-3 – Galvanostatic control test details

Galvanostatic control	Parameters
Rest time	30 min
Current density (low galvanostatic control)	0.167 mA cm^{-2}
Time (low)	24 h
Current density (high galvanostatic control)	2 mA cm^{-2}
Time (high)	2 h
pH	6.5 − 7.5
Electrolyte	3.5wt.% NaCl solution

5.3.1 Accelerated corrosion pit generation and characterisation

Corroded baseline and laser peened samples (Type A and B) were exposed to the high galvanostatic control (2 mA cm^{-2} for 2 h) to generate corrosion features at ambient conditions (see section 5.3). After corrosion exposure, the samples are ultrasonically cleaned in ethanol (45 minutes at 50°C) to remove soluble corrosion products. All pits bigger than 10 µm are

assumed to be corrosion-generated (not laser peening-generated mechanical pits – smaller than 10 µm) and are characterised as such. This is to focus on capturing pits of the same order of magnitude as of the damaging mechanical pits found in LSP samples, shown in section 3.3.3.3. Additionally, due to the roughness of LSP, and particularly LSPwC surfaces, and the limitations of the variable focus microscope, surface roughness features pre-corrosion that are less than 10 µm deep could be mis-interpreted as corrosion pits.

Images of a corroded area were assessed using ImageJ software [177], where the following steps are followed to quantify the pit features: rotate, crop, colour threshold, eight-bit image, threshold and analyse particles. The data generated in ImageJ is processed in Origin(pro) 2020 to generate graphs of corrosion pit area fractions (the sum of all corroded surfaces over the measurement area) and pit density (pits per mm^2) for comparison between baseline, LSP and LSPwC.

5.3.2 Fatigue testing of pre-corroded AA7075-T651

The fatigue testing methodology used for corroded samples is the same as shown in Chapter 4.2. Pre-corroded baseline, LSP and LSPwC are fatigue tested at 407 MPa stress range. Uncorroded fatigue data (performed in Chapter 4) is included in the study for comparison. The type of fatigue samples tested presented in this study are:

Table 5-4 – Type of fatigue samples tested

Sample Type	Details	Comments
Baseline	Untreated	From chapter 4
LSP	Ablative LSP treatment	From chapter 4
LSPwC	non-Ablative LSP treatment	From chapter 4
Base+Corr	Untreated + corrosion exposure	-
LSP+Corr	Ablative LSP treatment + corrosion exposure	-
LSPwC+Corr	non-Ablative LSP treatment+ corrosion exposure	-

As performed in Chapter 4, two methods were used for crack propagation capture. The replica method was used for baseline samples only. For LSP samples and corroded samples, the replica method was not effective in monitoring crack behaviour due to subsurface crack initiation and growth. In this case, the beach marking method was used.

Variable focus optical microscopy (settings shown in Table 3-5 in Chapter 3.2.6.2) and scanning electron microscopy (settings shown in section 3.2.6.3) were used to analyse fracture surfaces of fatigue samples, for both baseline and laser peened samples. SEM

microscopy (10 - 15 keV), ImageJ processing [177], and fatigue data (number of cycles and load ratio) are used to measure crack size and calculate crack growth rate d*a*/d*N* versus its stress intensity factor (ΔK). For more information on the replica method, beach marking method and crack growth rate vs. ΔK calculations see section 4.2.

5.4 Results

5.4.1 Open circuit potential

Figure 5-1, Figure 5-2, Figure 5-3 and Figure 5-4 show the OCP measurements for the baseline, LSP and LSPwC in Type A and Type B. As previously noted, some (if not all) residual stress loss is expected for Type B. Initial OCP for the baseline was similar for the three replicates, between –0.730 V and –0.740 V. In contrast, initially for LSP and LSPwC the corrosion potentials varied between –0.730 V and –0.690 V, leading to a more transient response caused by the peened surface. Nevertheless, overall, during the initial 30 minutes (Figure 5-4 and Figure 5-2) the OCPs for all surfaces were relatively similar (within 30 mV). Whereas, after 24 h (Figure 5-3 and Figure 5-4) the OCPs for all peened surfaces tend to decrease to between –0.775 and –0.800 V, unlike baseline which stayed relatively uniform.

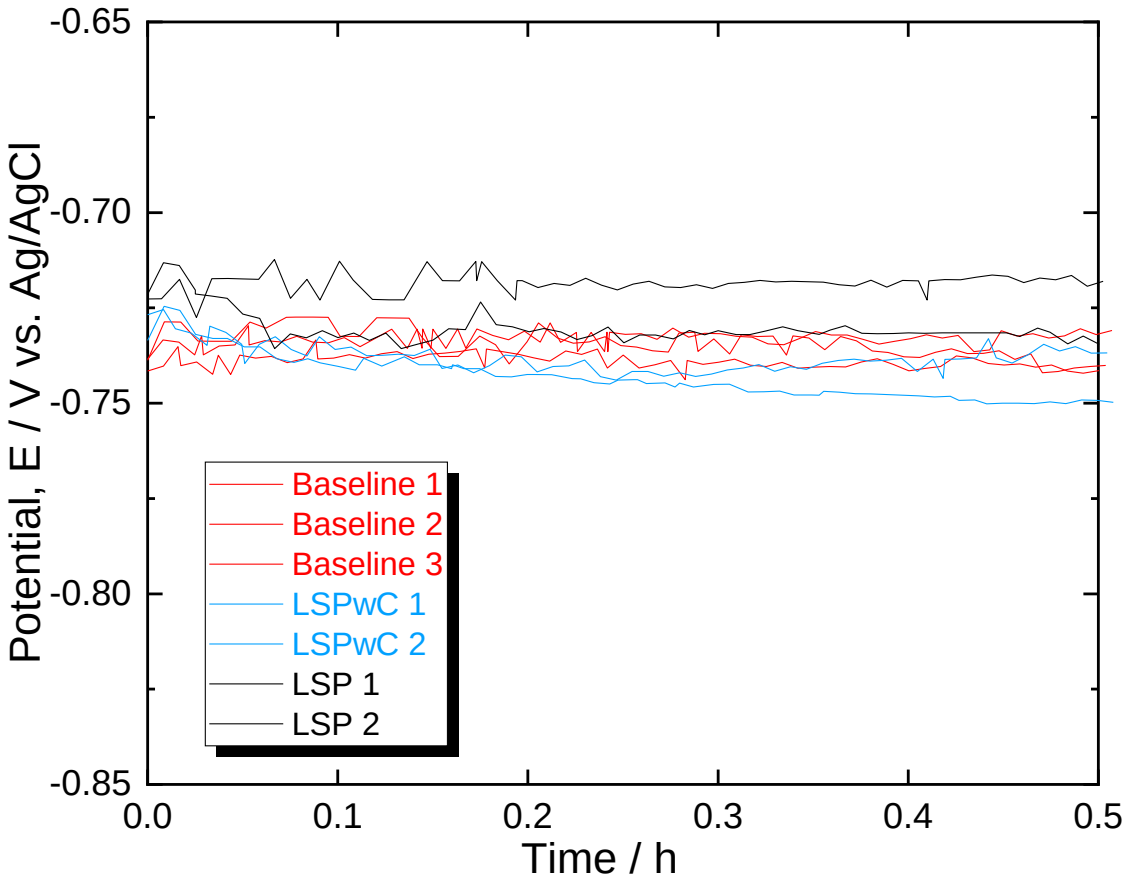

Figure 5-1 – Open circuit potential, Type A, 30 minutes, for baseline, LSP and LSPwC.

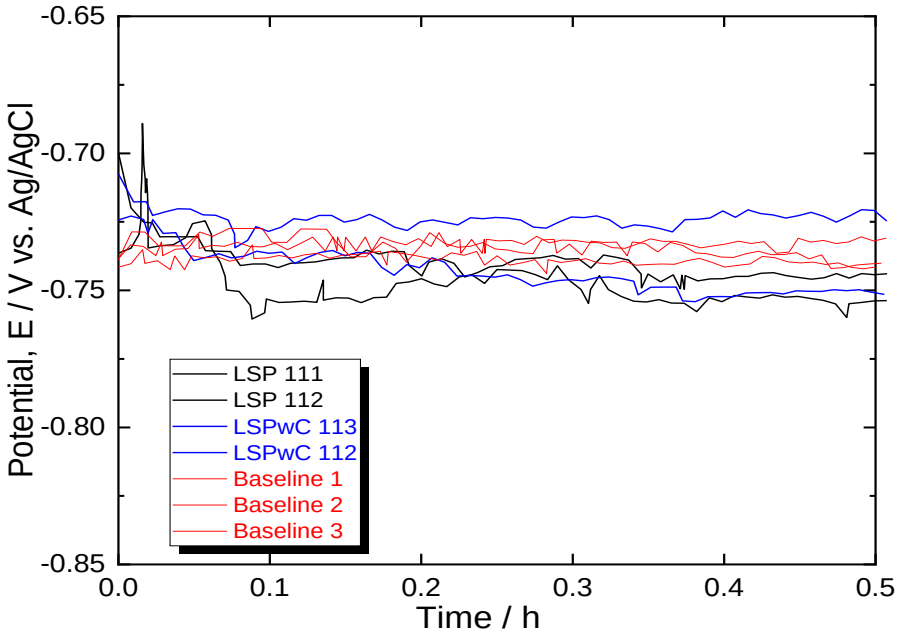

Figure 5-2 – Open circuit potential, Type B, 30 min, for baseline, LSP and LSPwC.

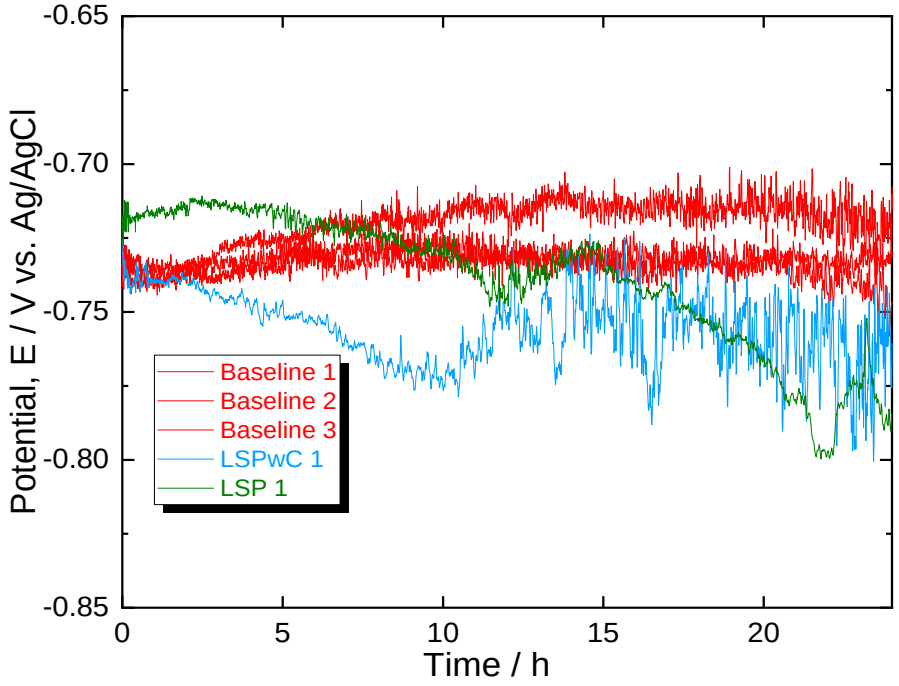

Figure 5-3 – Open circuit potential, Type A, 24 h, for baseline, LSP and LSPwC.

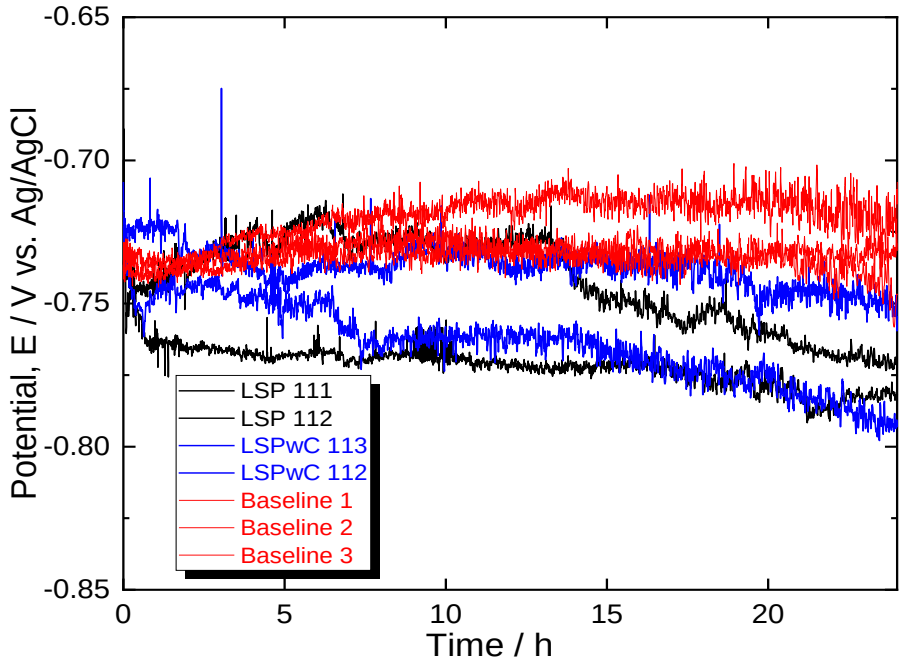

Figure 5-4 - Open-circuit potential, Type B, 24 h, for baseline, LSP and LSPwC.

5.4.2 Potentiodynamic polarisation

Figure 5-5 shows the potentiodynamic polarisations for untreated AA7075 (baseline), LSP and LSPwC Type A and B. In terms of corrosion potential, the baseline tests are similar, between –0.750 and –0.735 V; whilst LSP values are generally more variable. LSP Type B are in the same range as, if not slightly above, baseline. In contrast, LSP Type A appear to have more varied free corrosion potential, and are generally nobler than the baseline, by no more than 40 mV. The anodic curves for all samples are similar, suggesting no particular difference in the anodic corrosion kinetics between baseline and LSP. Additionally, the cathodic slopes of all LSP and LSPwC sample A and sample B cathodic branches are within or close to that of baseline. This suggests there has been no change in the oxygen reduction kinetics after laser shock peening (LSP and LSPwC), and not significantly affected by either residual stresses or the increased surface roughness.

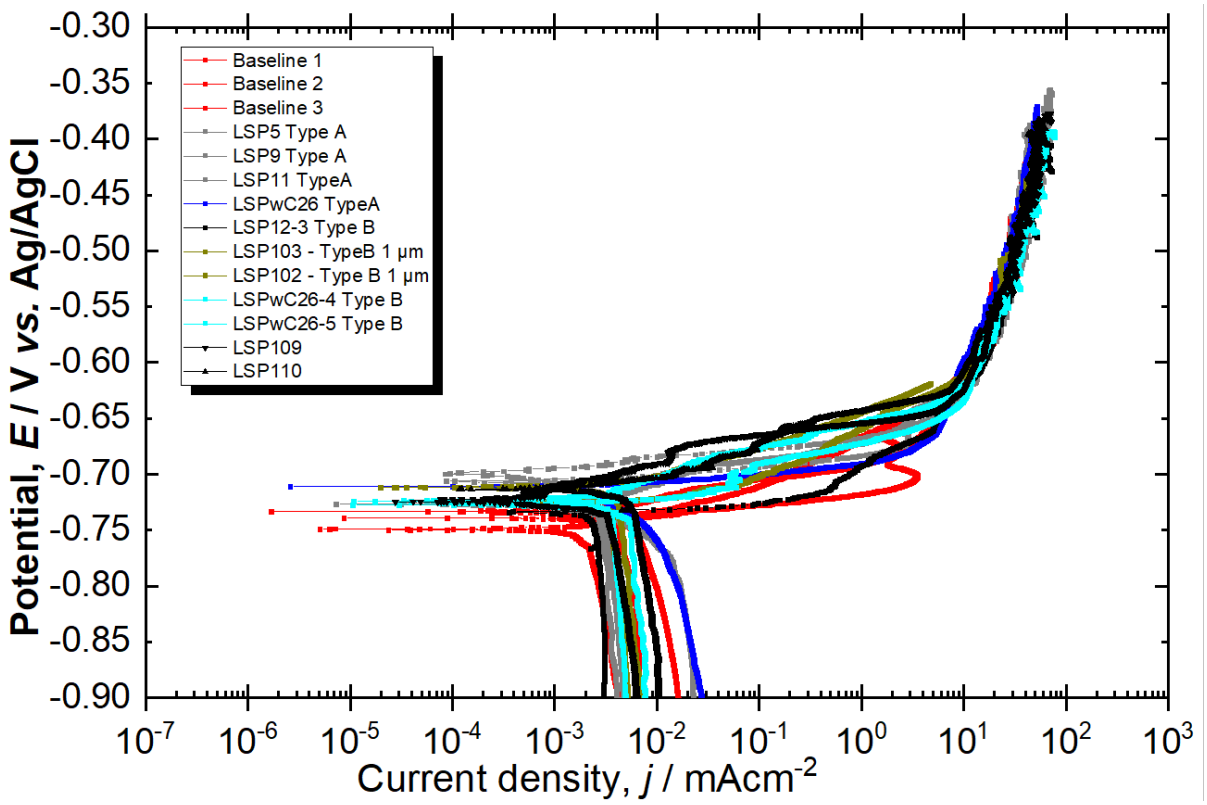

Figure 5-5 - Potentiodynamic polarisation of untreated AA7075 (baseline), LSP and LSPwC Type A and B.

Table 5-5 – Comparison of average equilibrium corrosion potential and corrosion current density, as well as pitting potential.

Sample type	E_{corr} (V)	I_{corr} (10^{-3} × mA)	E_{pit} (V)
Baseline	-736	1.66	-0.675
LSP Type A	-707	1.19	-0.650
LSPwC Type A	-708	1.88	0.625
LSP Type B	-727	6.43	-0.701
LSPwC Type B	-726	7.54	-0.673

5.4.3 Galvanostatic polarisation

Figure 5-6 shows untreated AA7075 (baseline), LSP and LSPwC Type A and B under high galvanostatic control (2 h at 2 mA cm^{-2}). LSP and LSPwC are either within the baseline range or less than 50 mV from baseline. LSPwC shows a transient behaviour where in the first 10 – 15 minutes, the potential is lower by 10 mV – 20 mV than baseline. From approximately 1 h into the galvanostatic control the potentials for all samples are within the baseline range, with some variation per sample (e.g. one LSPwC sample slightly higher by 20 mV).

Figure 5-7 shows a set of low galvanostatic control tests (all Type A), performed to view the change in potential for sample surfaces with a slower corrosion acceleration. The difference in potential values between baseline and LSP samples is less than 50 mV.

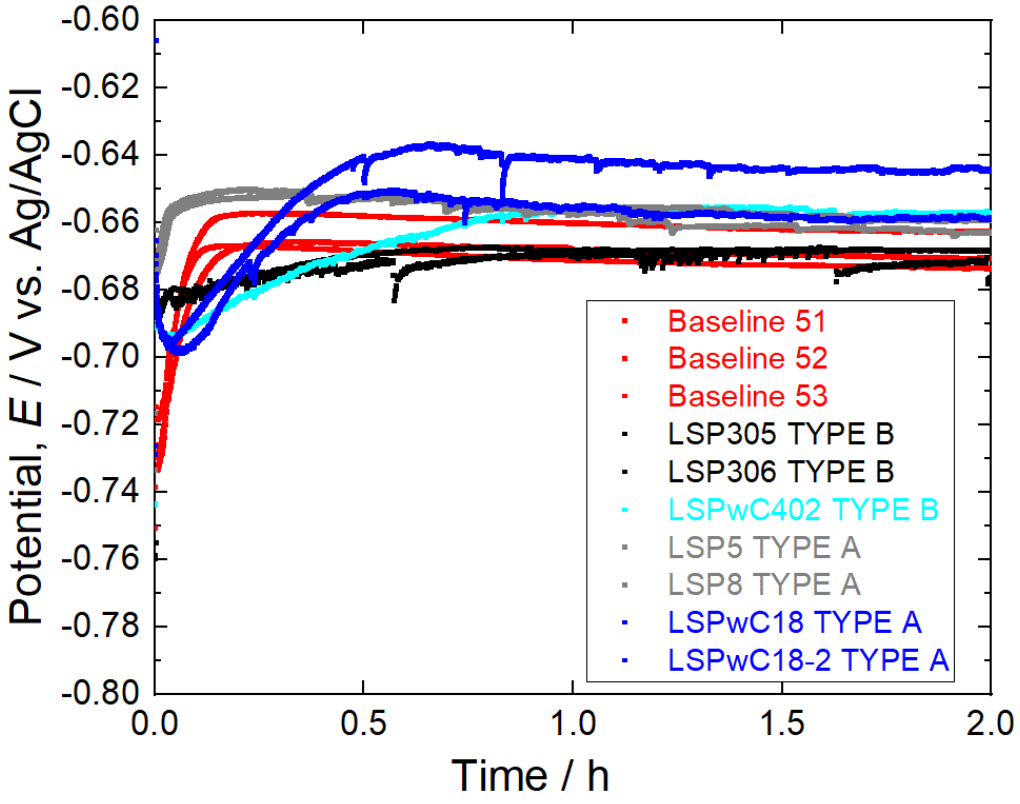

Figure 5-6 - High galvanostatic control (2 h) for the baseline, LSP, and LSPwC Type A and B samples.

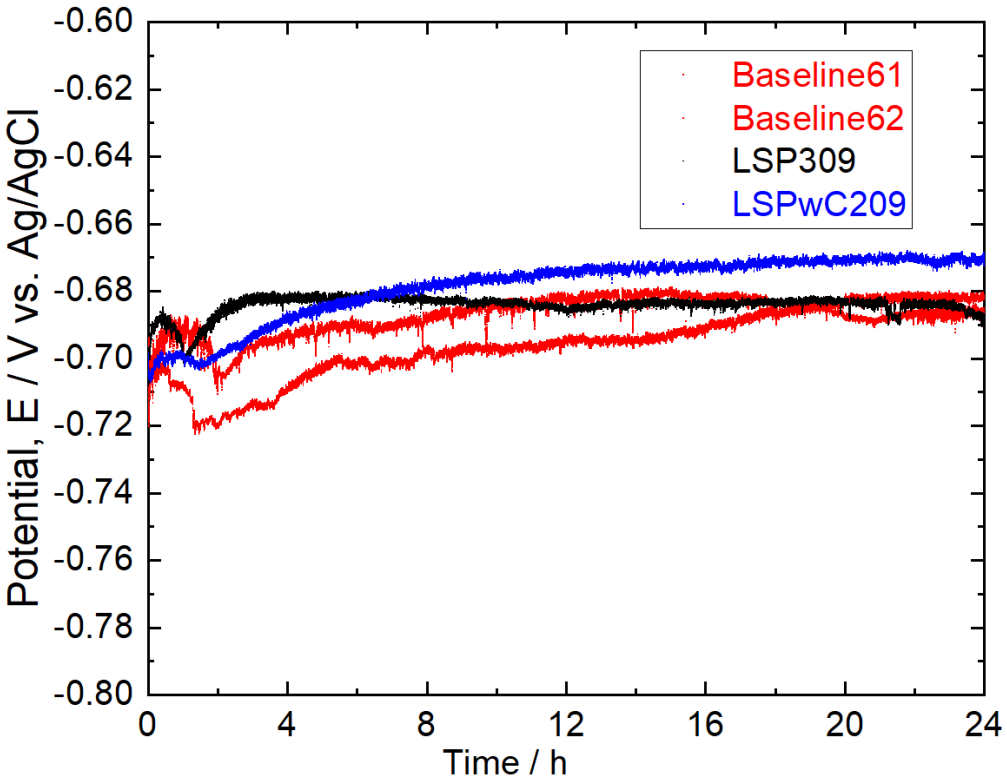

Figure 5-7 - Low galvanostatic control (24 h) for the baseline, LSP and LSPwC Type A.

5.4.4 Corrosion pit characterisation

5.4.4.1 Corrosion pit initiation

Figure 5-8 and Figure 5-9 show typical AA7075-T651 corrosion pit initiation sites (after 72 h OCP) found at the surface both baseline and LSP samples. The experimental results are in agreement with what is seen in the literature, as described in section 2.6.8. Both LSP and LSPwC show matrix dissolution adjacent to coarse intermetallics, due to micro-galvanic coupling between the aluminium matrix and the coarse intermetallics, particularly Al_7Cu_2Fe. Additionally, from microscopy observation there is no indication of a reduction in size or population of intermetallics at the surface, suggesting laser peening has not had an effect on these particles acting as efficient local cathodes and corrosion pit initiation sites.

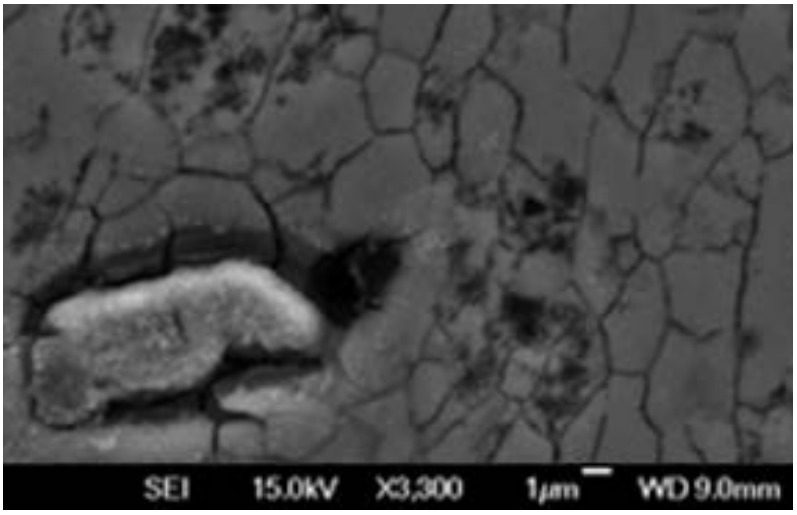

Figure 5-8 – Baseline (untreated) surface pit initiation site at coarse constituent particles. Dissolution of aluminium alloy around cathodic particle due micro-galvanic coupling.

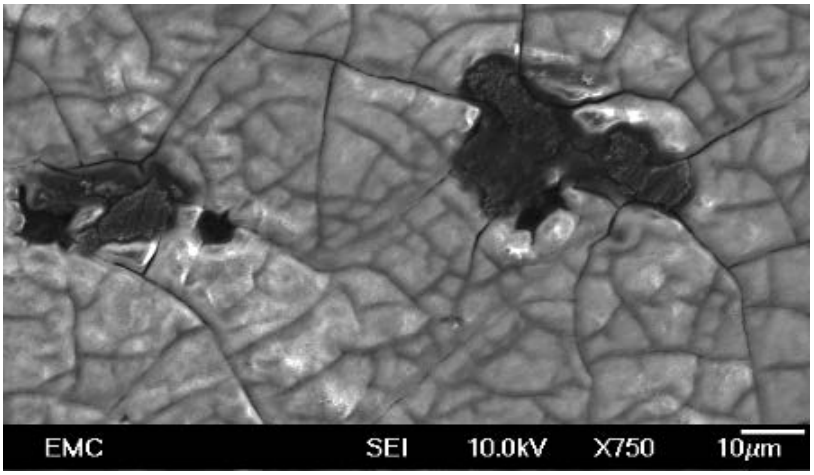

Figure 5-9 – LSP surface pit initiation site at coarse constituent particles. Similar to what is seen for baseline.

5.4.4.2 Pit topography

Figure 5-10 and Figure 5-11 provide representative topographical maps for the baseline and LSPwC samples before and after galvanostatic control (low). It is evident for all cases there are numerous pits 10 µm to 20 µm in depth. Visual inspection suggests LSPwC has more corrosion pits than the baseline. In addition, it suggests LSPwC may have more corroded areas than baseline. This is similarly seen for LSP. It is important to note LSPwC and LSP samples already have some small pits, or depressions, present before corrosion exposure. These are assumed to be mechanical pits (<10 µm) generated during the laser peening surface treatment or in the case of LSPwC features generated due to surface ablation.

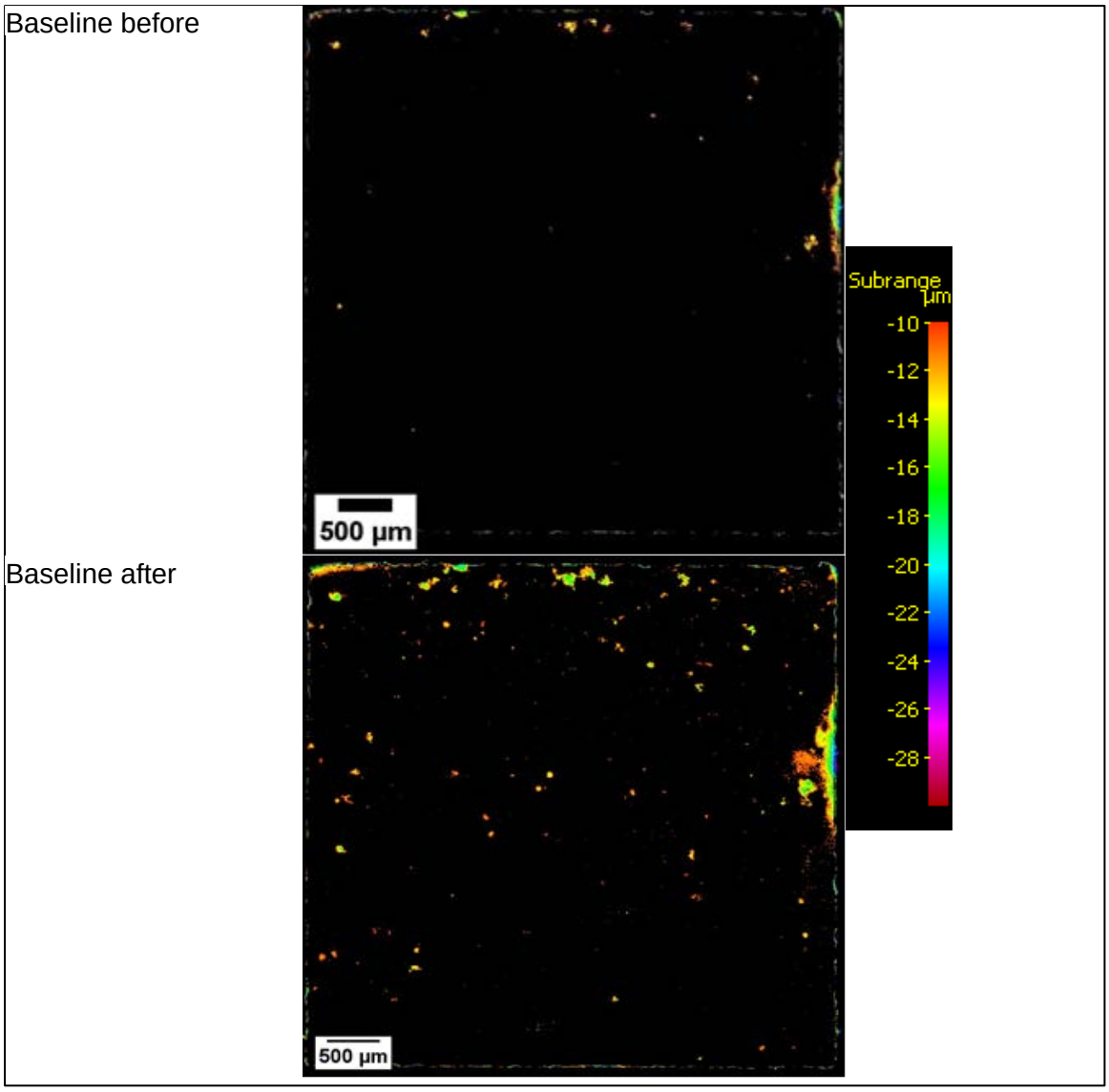

Figure 5-10 – Surface topography of AA7075 baseline surfaces before and after 24 h galvanostatic control.

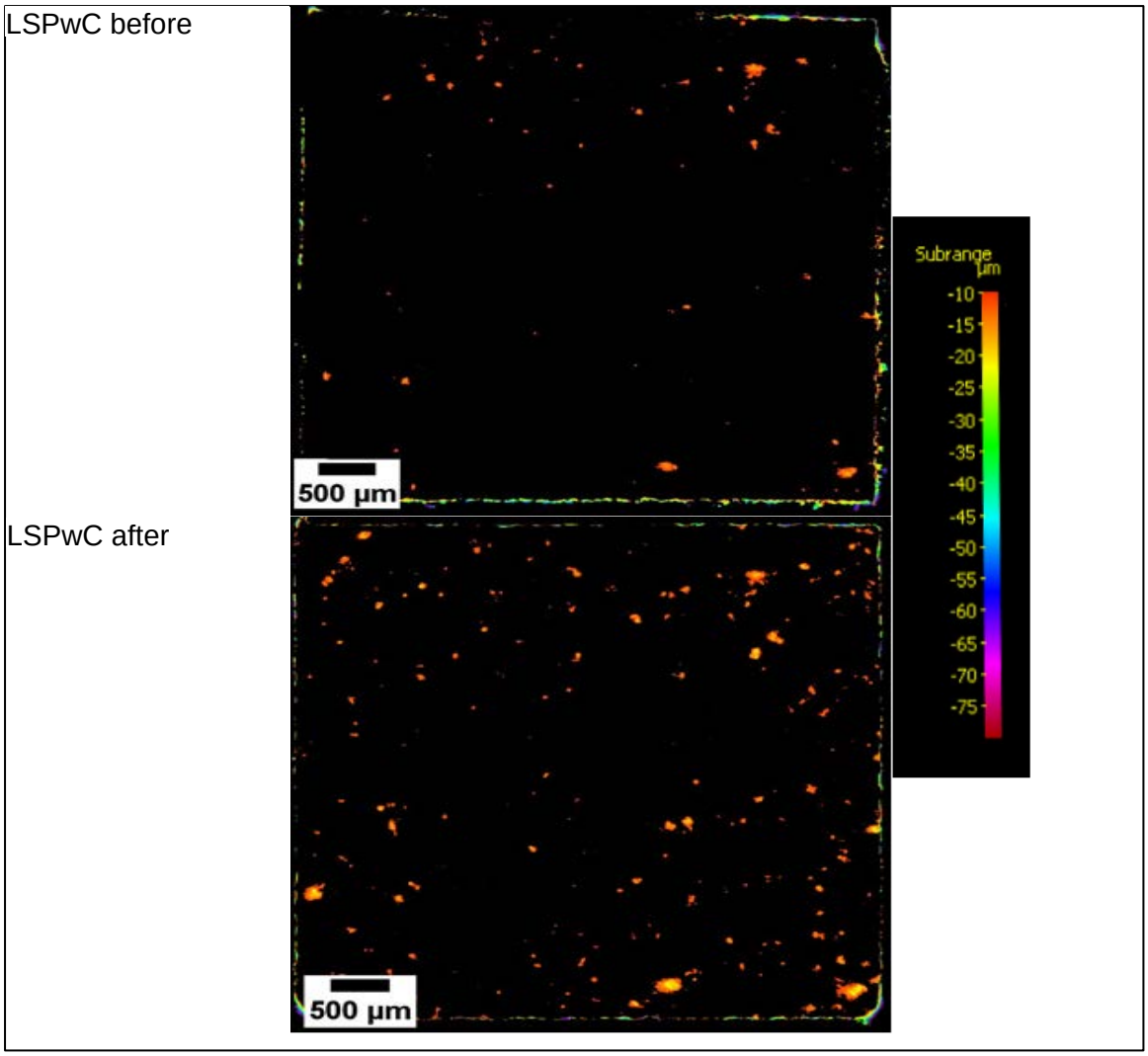

Figure 5-11 - Surface topography of AA7075 LSPwC surfaces before and after 24 h galvanostatic control.

5.4.5 Corrosion pit characterisation

The pit density (number of pits per mm^2), and the corroded area divided by the total projected area (pit area fraction) captured using the topographical images were assessed quantitatively, see Figure 5-12 and Figure 5-13. Although there is some variation within each sample type (baseline, LSP or LSPwC), overall the LSP and LSPwC Type A show equivalent (high) or worse (low exposure) values to baseline. Type B show they are all similar than untreated AA7075 (baseline).

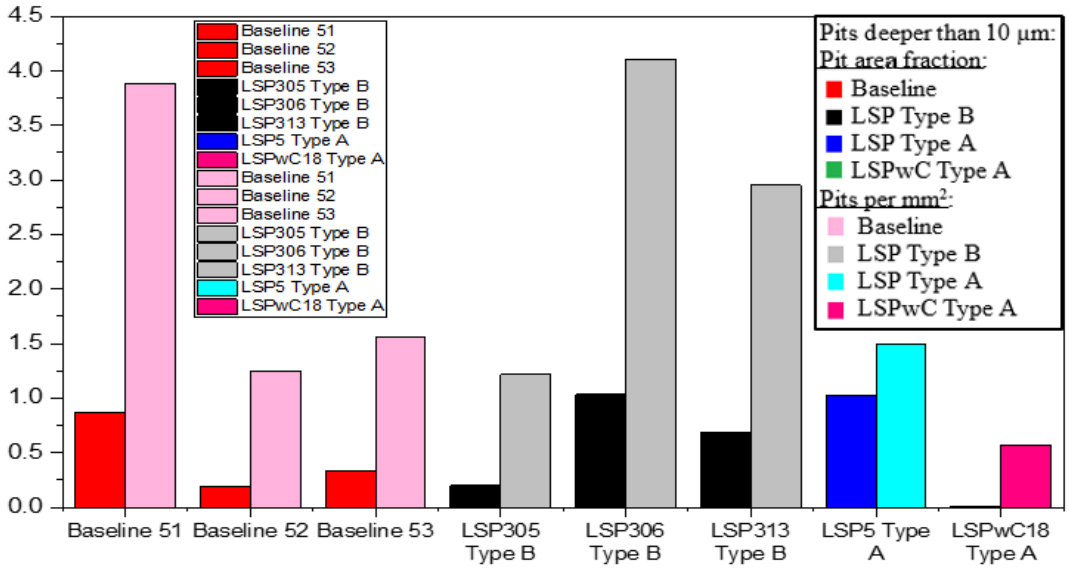

Figure 5-12 - Baseline, LSPwC and LSP Type A samples only (24 h, 0.167 mA cm^{-2}).

Areas equal or larger than 10 µm depth are considered to be associated with corrosion features.

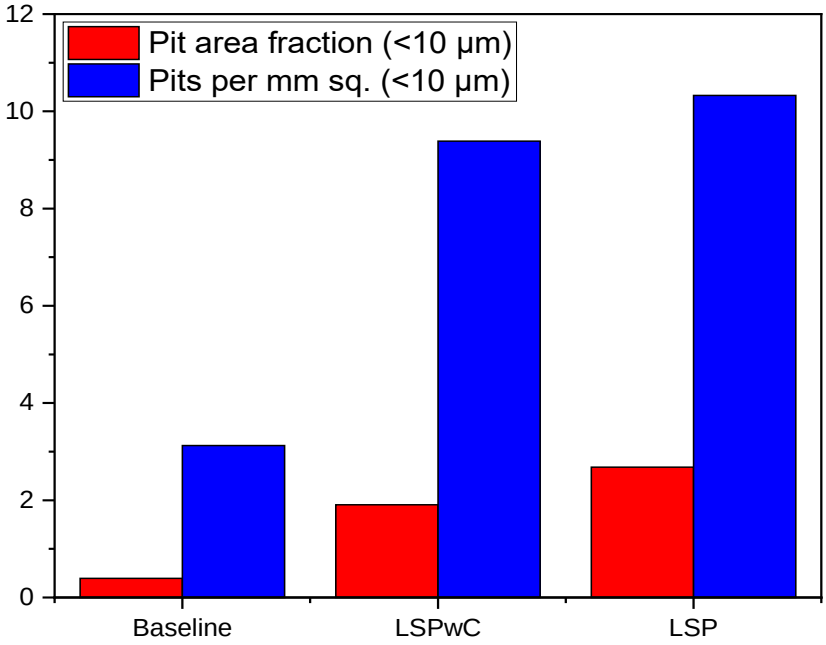

Figure 5-13 - Baseline, LSPwC and LSP Type A samples only (24 h, 0.167 mA cm^{-2}). Areas equal or larger than 10 µm depth are considered to be associated with corrosion features.

SEM imaging of corrosion pit cross-sections generated by galvanostatic control (Figure 5-14, Figure 5-15 and Figure 5-16) show, as expected, pit depths are deeper than that assessed via topographical imaging. In all cases, irrespective of whether they are baseline or laser peened, the depth of pits are near 50 µm, despite surface topography imaging showing pits of 10 µm – 30 µm deep.

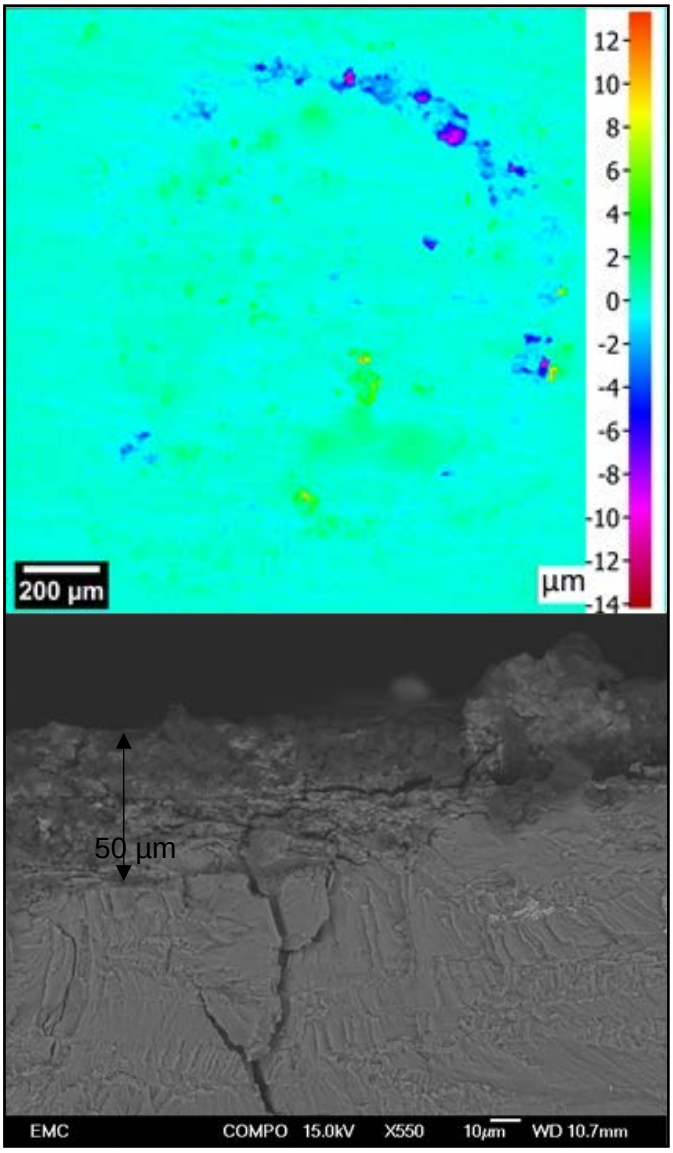

Figure 5-14 - Top: Variable focus optical microscopy of pre-corroded baseline Type A sample. Bottom: SEM cross section of pre-corroded pit feature in LSP sample showing the true pit depth.

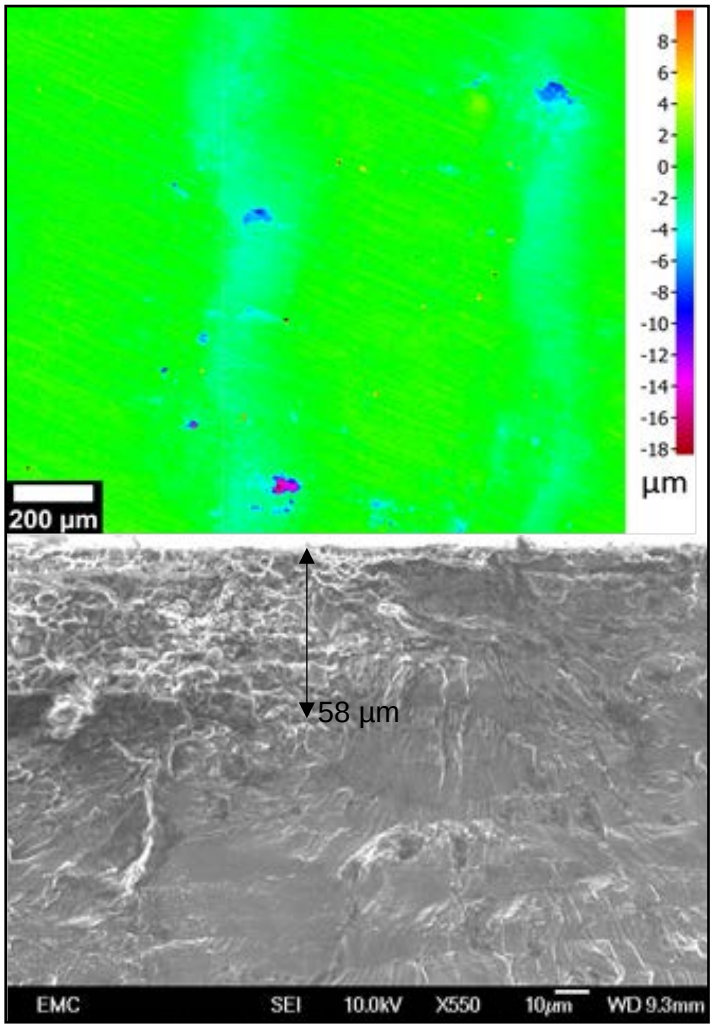

Figure 5-15 – Top: Variable focus optical microscopy of pre-corroded LSP Type A sample. Bottom: SEM cross section of pre-corroded pit feature in LSP sample showing the true pit depth.

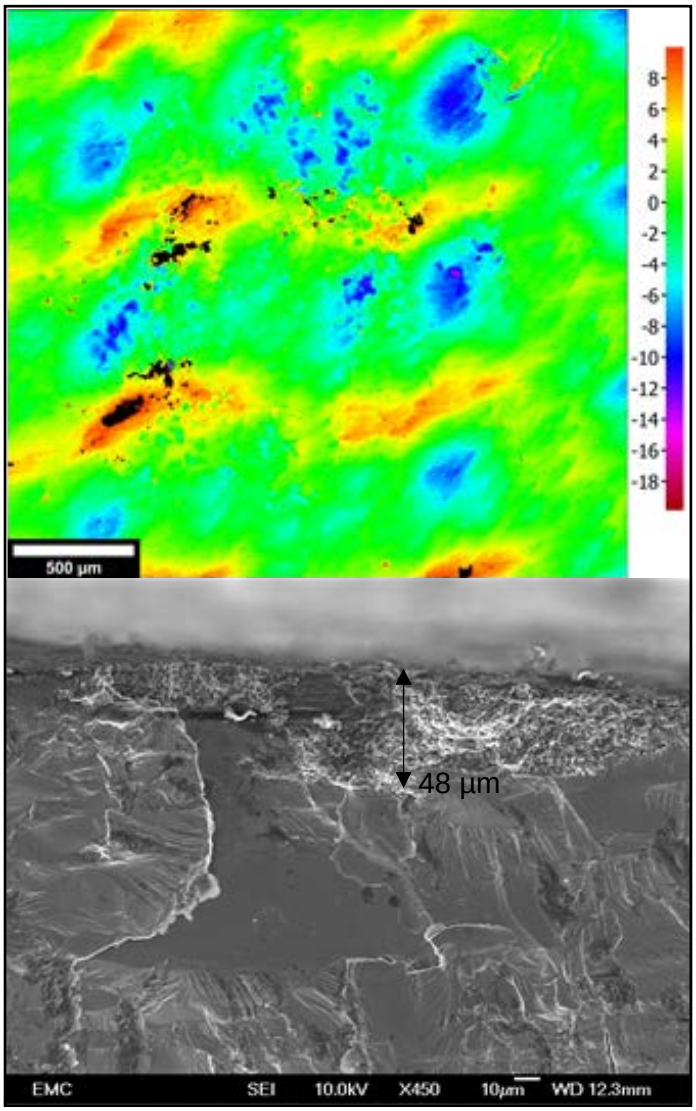

Figure 5-16 - Top: Variable focus optical microscopy of pre-corroded LSPwC Type A sample. Bottom: SEM cross section of pre-corroded pit feature in LSP sample showing true pit depth.

5.4.6 Fatigue life of corroded AA7075-T651

Figure 5-17, Figure 5-18 and Figure 5-19 present typical examples of a pre-corroded Type A samples before and after fatigue testing, for baseline, LSP and LSPwC. According to the topographical examination fatigue cracks do not necessarily initiate at the biggest or deepest pit, irrespective of whether it has or has not undergone laser shock peening.

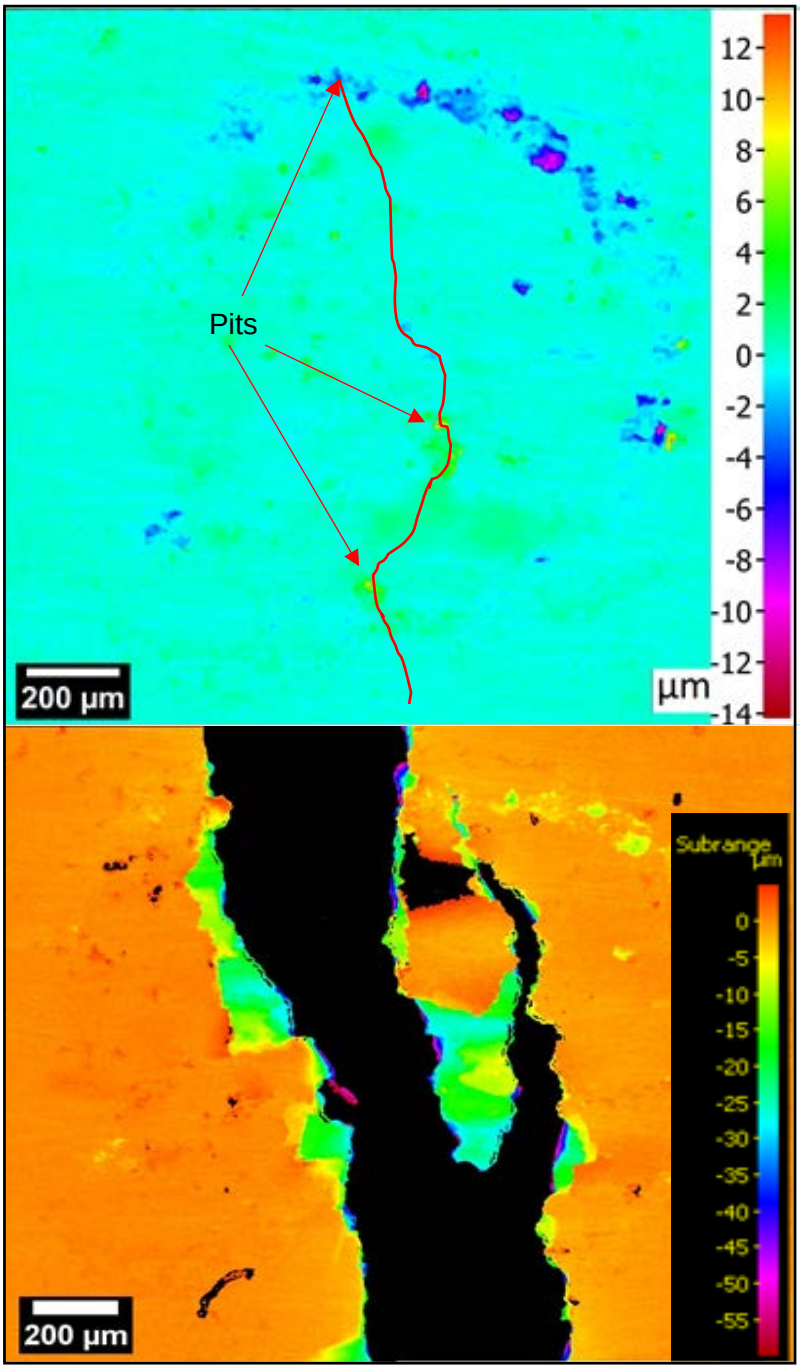

Figure 5-17 – Variable focus optical microscopy image of baseline Type A. Top: pre-corroded sample before with approximate fracture line super-imposed on top, drawn in red. Fatigue cracks initiate at pits. Bottom: Sample after fatigue fracture.

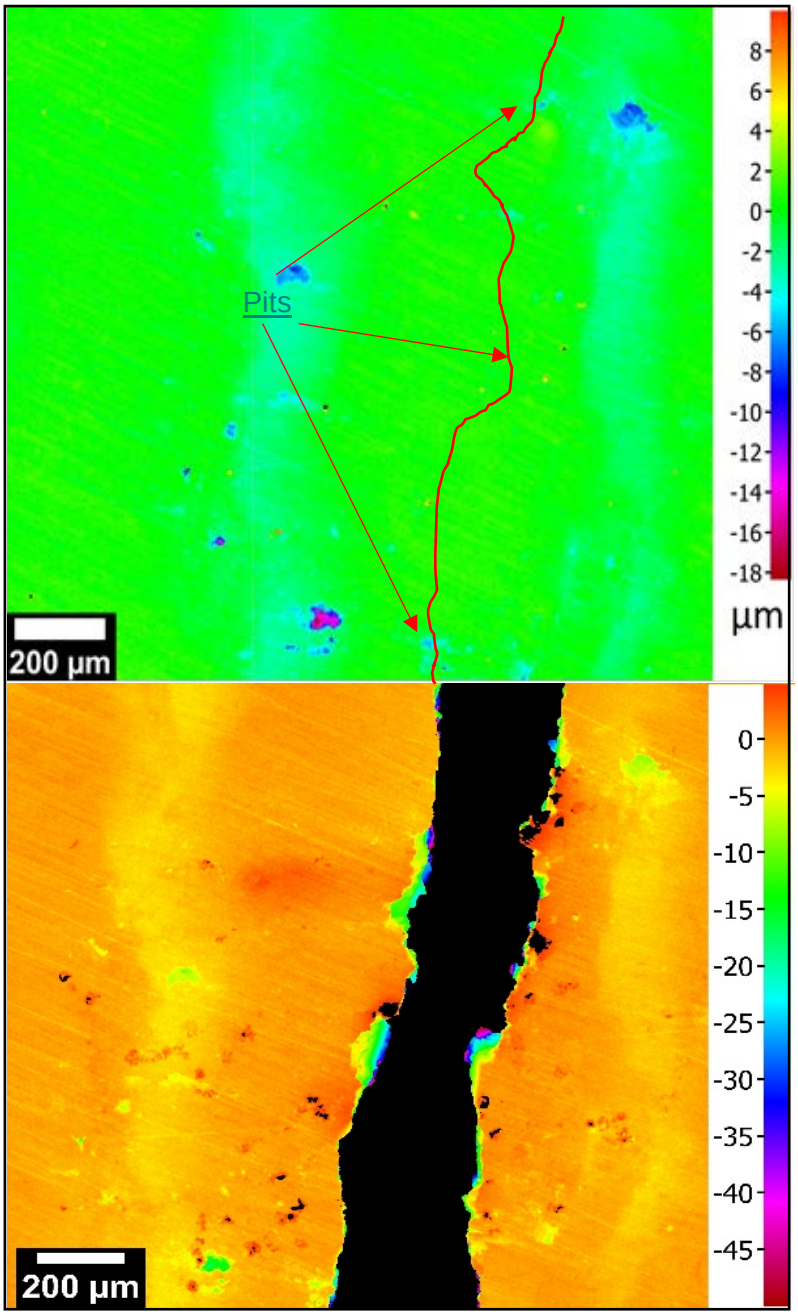

Figure 5-18 - Variable focus optical microscopy image of LSP Type A. Top: pre-corroded sample before with approximate fracture line super-imposed on top, drawn in red. Fatigue cracks initiate at pits. Bottom: Sample after fatigue fracture.

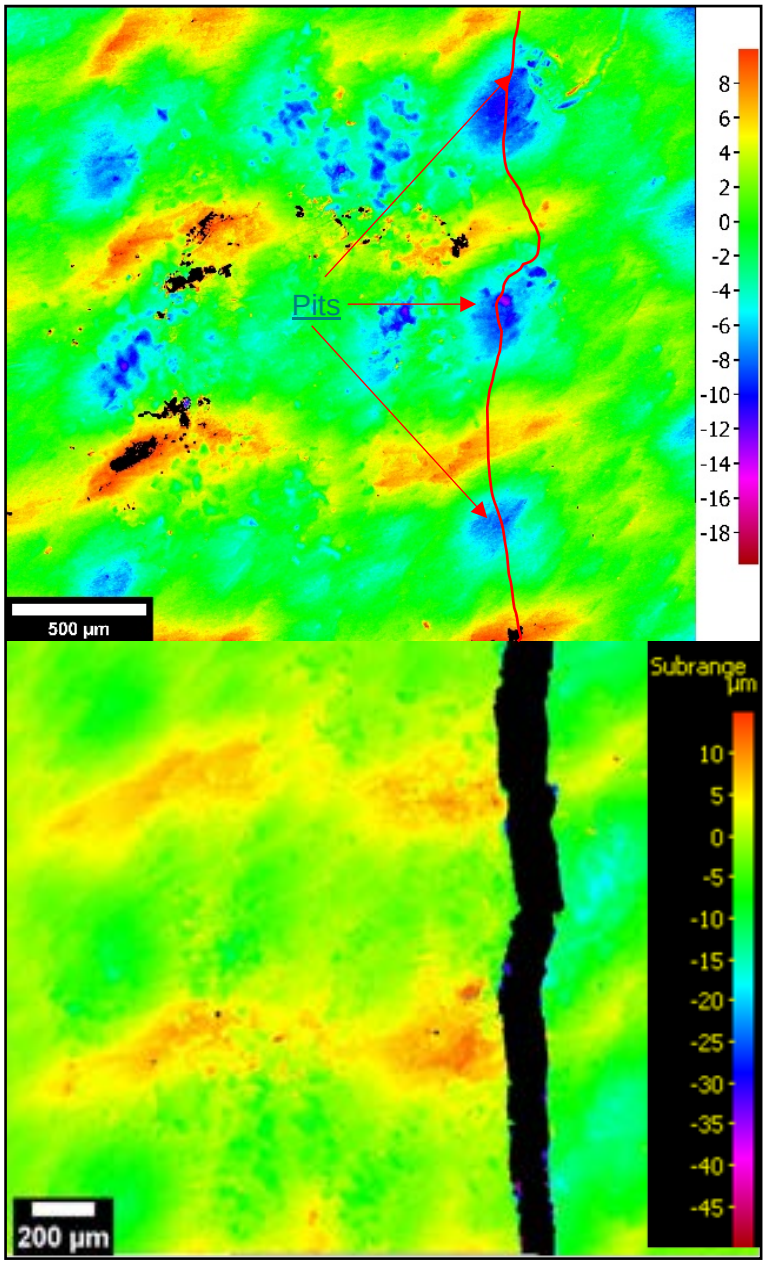

Figure 5-19 - Variable focus optical microscopy image of LSPwC Type A. Top: pre-corroded sample before with approximate fracture line super-imposed on top, drawn in red. Fatigue cracks initiate at pits. Bottom: Sample after fatigue fracture.

Figure 5-20 shows the baseline (untreated and uncorroded) AA7075 as-received (R_t = 2.64 µm) and 1 µm polished (R_t = 0.25 µm) fatigue life are quite similar. In contrast, baseline fatigue life decreased by at least 50% in the presence of pre-corroded pits. The crack propagation of corroded baseline (Figure 5-21) is at the top of the uncorroded baseline trend, suggesting it occurs slighter faster than for the uncorroded untreated AA7075 baseline surface condition. Figure 5-22 shows crack initiation occurs almost immediately and at least 95% of fatigue life is spent in crack propagation. The pre-corroded LSP and LSPwC are subject to a magnitude decrease in fatigue life when compared to their uncorroded condition; from millions of cycles

to hundreds of thousands, thus indicating a change from a high cycle fatigue to a low cycle fatigue regime. Nevertheless, both LSP treatments have a better fatigue performance than the untreated AA7075 baseline (either pre-corroded or uncorroded). Crack propagation data, although limited, shows a clear decrease in crack propagation rate for LSPwC compared to the baseline. For LSP, the crack propagation trendline lies near the bottom of the baseline trend, and considerably lower than the pre-corroded baseline samples. Crack initiation in both LSP and LSPwC lasts for 30% of the total fatigue life, thus considerably increasing the fatigue initiation time: from near zero cycles in pre-corroded baseline to approximately 40,000 cycles in pre-corroded LSP. For crack propagation, life is increased from 40,000 cycles in corroded baseline to 80,000 for LSP and 160,000 cycles for LSPwC. This suggests a considerable delay in both crack initiation and propagation due to the laser peening generated residual stresses.

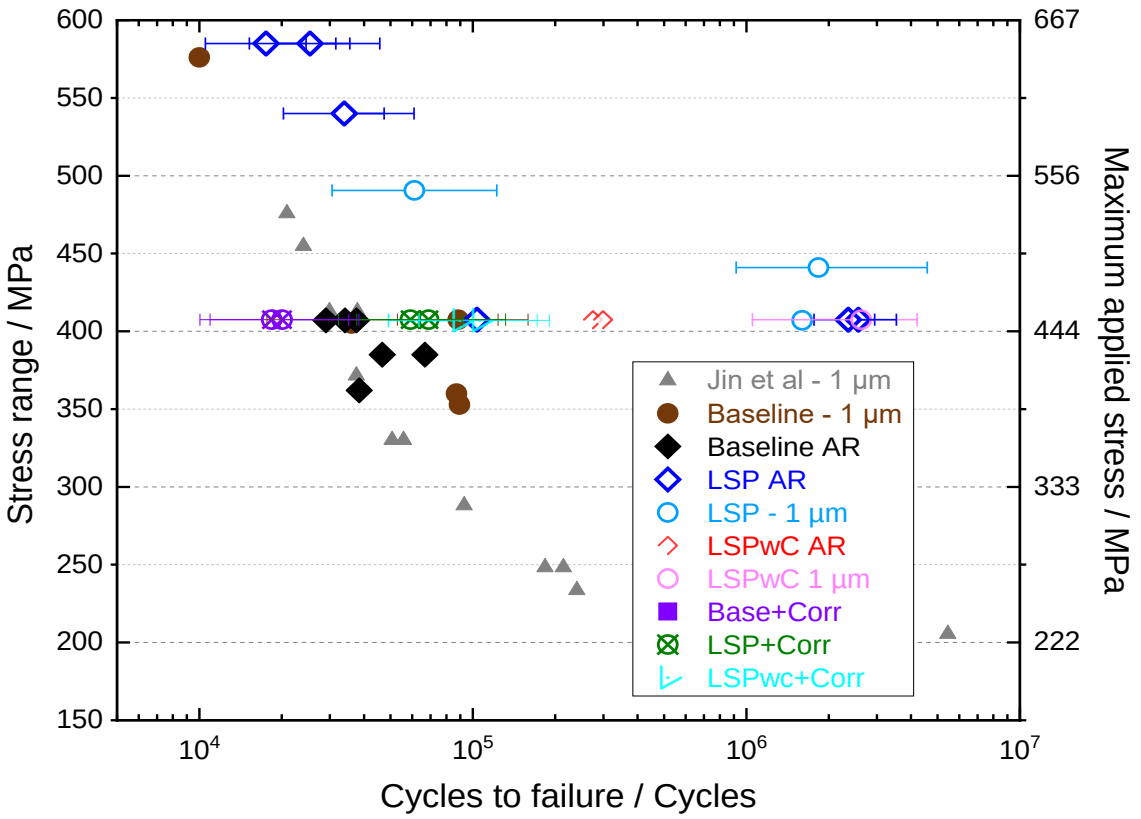

Figure 5-20 - Stress range vs. cycles to failure for AA7075 Type A (baseline), LSP and LSPwC samples (pre-corroded and uncorroded). Uncorroded baseline and LSP samples are included for comparison.

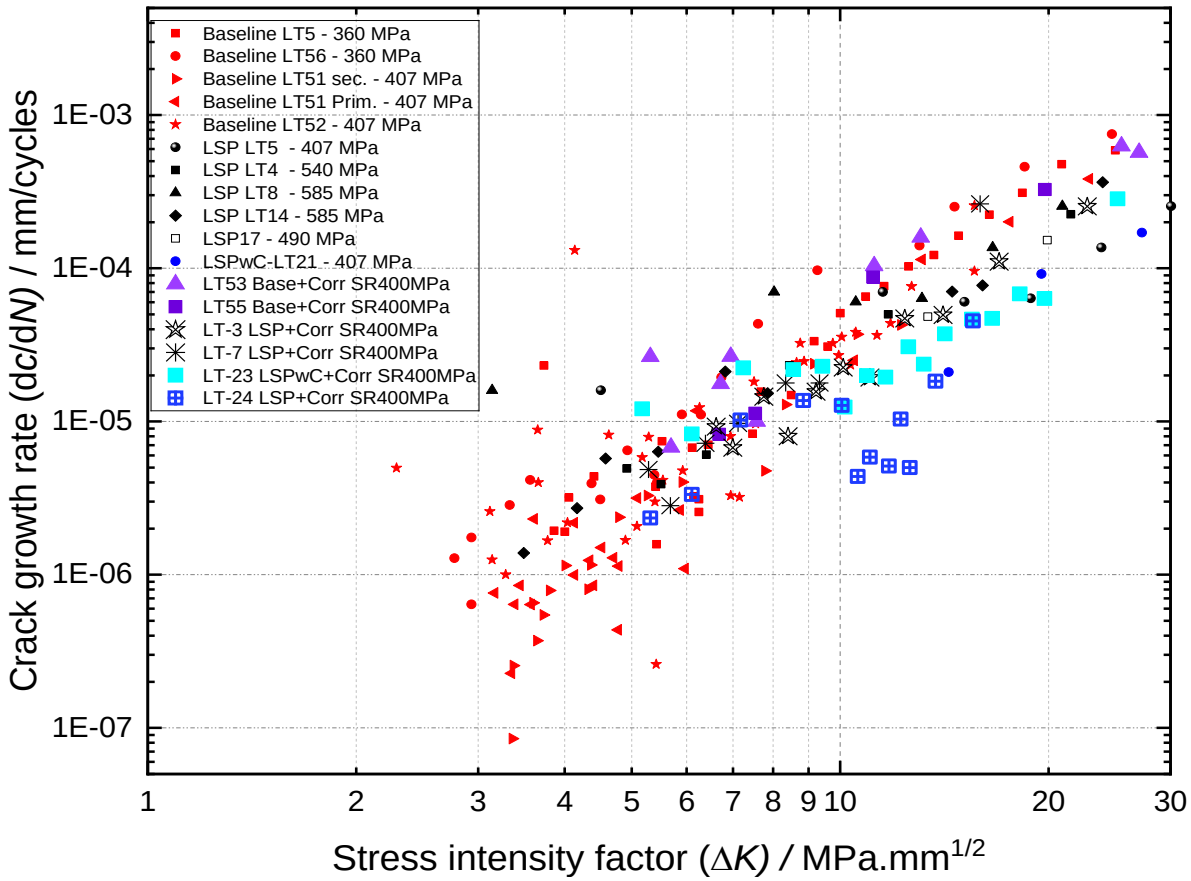

Figure 5-21 - Crack growth (dc/dN) vs. stress intensity factor range (ΔK) for baseline, LSP and LSPwC samples (pre-corroded and uncorroded). Baseline, LSP and LSPwC uncorroded samples are included for comparison.

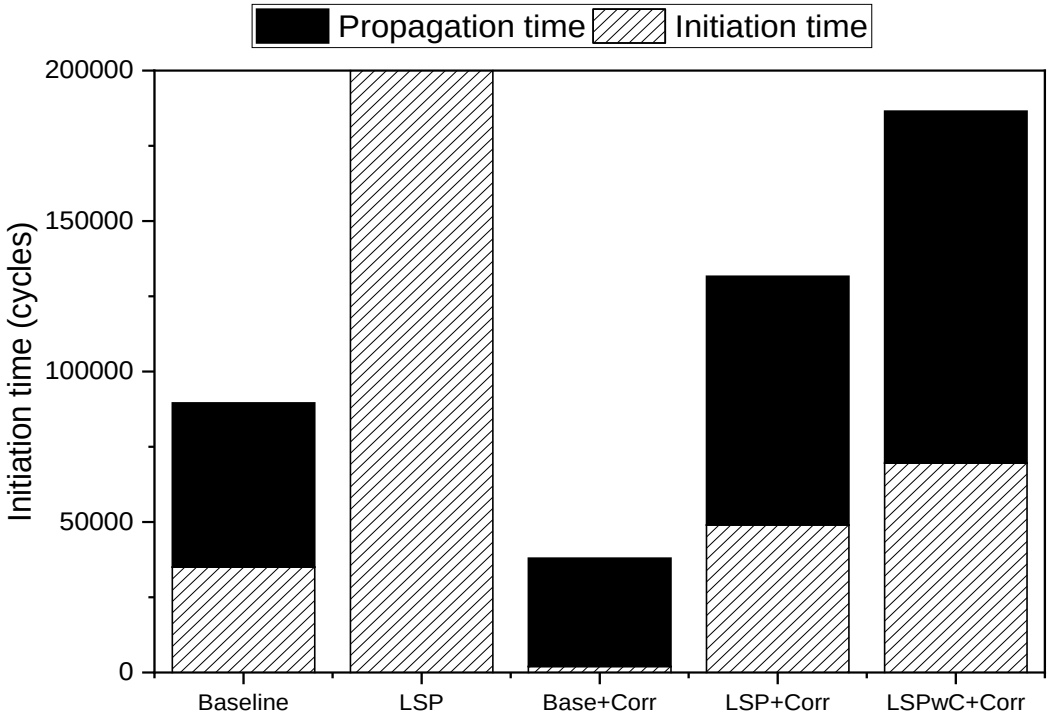

Figure 5-22 - Average initiation and propagation life of untreated AA7075 (baseline), LSP (LSPwC is expected to be the same), pre-corroded baseline, pre-corroded LSP and pre-corroded LSPwC. Columns show total fatigue life, including cycles at 0.1 and 0.5 load ratio.

5.5 Discussion

5.5.1 LSP effects on electrochemical and corrosion performance

The short-term OCP results agree with similar studies for AA6082 LSPwC by Trdan and Grum [169][170], where small potential changes are seen after peening (below 50 mV) within the first hour. However, the long-term (24 h) OCP shows relatively stable potentials for untreated AA7075 baseline, whereas potentials for all the LSP and LSPwC (A or B) decreased suggesting the modified surface (specifically roughness) may be detrimental in the longer term. Laser peening having a negative effect on corrosion is not universal; e.g., Trdan and Grum [170] found a favourable decrease in the current density of AA6082 LSPwC during polarisation tests. Other studies report only minor corrosion potential increases without changes in kinetic behaviour for AA6082 LSPwC [170][137] and low-plasticity burnished AA2024-T3 [207]. In terms of kinetic behaviour, the potentiodynamic polarisations in this study (Figure 5-5) appear to be consistent with the open-literature:; small increases in the corrosion potential (below 50 mV) of laser peened material and similar kinetic behaviour for untreated and laser peened material. No significant difference is found between the baseline and laser peened (Type A or B) anodic and cathodic branches. Although there is variation for all type of tested conditions, the kinetic behaviours of LSP and LSPwC are within the baseline range. This agrees with results from other electrochemical tests of this study: Overall it suggests no conclusive significant differences in behaviour between untreated and laser shock peened or between type A and B samples. Fundamentally, the LSP compressive residual stress will affect the thermodynamics of these electrochemical active surfaces, *i.e*., the 'free-energy state' which may promote the formation of oxide layers, and these may be the cause of the slight raised free corrosion potential of laser peened samples. The residual stress, plastic deformation and surface roughness will generally alter the corrosion either from enhanced cathodic kinetics, increased anodic dissolution (more initiation sites with increased surface activity) or via the formation of oxide layers (here subject to a compressive stress field). Overall, the combination of these conditions have not shown a conclusive kinetic effect on AA7075-T651. However, although the precise effect of laser peening induced surface roughness on AA7075-T651 corrosion is unclear, the only real conclusion that can be drawn is that roughness could affect the electrochemical potential long-term.

When galvanostatically controlled (Figure 5-6 and Figure 5-7), while there is no evidence of substantive localised corrosion, there are initially small transient differences, but subsequent pit characterisation shows no influence on pit density, pit size or depth for either LSP or LSPwC

conditions. This is also in contrast to that reported by Trdan and Grum [170][137], where a decrease in pit number and size was attributed to LSPwC surface melting changing the oxide layer (Al_2O_3) and residual stresses. Melting of aluminium surfaces using lasers has been shown to generate a more homogeneous surface, with fewer second phase particles [208][209], and to generate an oxide layer [170] [209][210]. For the present study, the LSP (due to the ablative layer) and LSPwC (due to the subsequent mechanical polish removing any shallow melted layer that may be present) are unlikely to have this laser-induced oxide layer. This difference in oxide layer may explain why there is no enhanced corrosion performance as seen in other LSPwC studies [169][170][137][210]. Thus, the small transient improvements in corrosion potential seen in this study could be attributed to compressive residual stresses, as this is not only seen in laser peened [169][170][137][210] but also in shot peened [172] and low-plasticity burnished [207] aluminium alloys. It is also likely that the laser peening induced roughness, particularly LSPwC, counteracts the residual stress benefits. Zagar and Grum [172] show that LSPwC treatment leads to surface roughness that promoted higher corrosion current densities, counteracting any possible peening benefits. Figure 5-6, showing the high galvanostatic control, suggests this is the case: LSP Type B (reduced or no residual stresses) shows higher pit area fraction and pit density compared to the Type A condition, where residual stresses may be counteracting the detrimental effects of roughness. In contrast, the low (less aggressive) galvanostatic control show a significant difference between baseline and laser peened Type A. In this instance, laser peened may have performed worse due to the slower kinetics allowing roughness to play a more dominant role. This corroborates the 24 h OCP data, suggesting in long-term, natural (non-aggressive) exposure, roughness plays a significant role in pit corrosion development, being more dominant than any beneficial residual stress effects. In addition, although grain refinement was not captured quantitatively, it is known changes in grain size can have an effect on corrosion performance [211]. However, the lack of conclusive evidence of changes in corrosion performance in this study suggest the expected grain refinement from both LSP and LSPwC has had a negligible effect in corrosion behaviour. Overall, this indicates surface roughness may be the most important variable in terms of electrochemical behaviour and long-term corrosion performance after laser peening, offsetting any residual stress effects. For LSPwC, if the oxide layer is not removed it may also provide an enhanced barrier to corrosion but this could not be evaluated in this study.

5.5.2 Mechanisms for AA7075-T651 corrosion initiation

From Figure 5-8 and Figure 5-9 it is evident there is no discernible change in pit corrosion mechanism after LSP or LSPwC. This agrees with the negligible minor effects seen in

electrochemical behaviour after both laser peening types. Aside for a few studies [169][170][172][137][210], residual stresses are reported to mostly have a significant effect only when retarding corrosion in processes where there is an external mechanical stimuli, such as corrosion fatigue and stress corrosion cracking [80][81][82][83][84][85][86][87][88][89][90][91][92]. In contrast, Liu and Frankel [207] evaluated the direction of compressive residual stress relative to the direction of intergranular corrosion (IGC). They observed compressive stresses (applied or residual) normal to the direction of preferred IGC (L-LT) reduced corrosion rates by closing intergranular sites. However, this benefit was not seen if the compressive stresses were parallel to the IGC direction. Unlike the Frankel study [207], the compressive residual stress in this study are expected to be mainly parallel to the electrochemically exposed L-LT surface and as such the benefits of compression on IGC were not seen. Thus, for this study, the dominant role of second phase intermetallics in corrosion pit initiation and growth, which is well documented [73][39], and the role of IGC, were clearly unchanged by the laser peening-induced residual stresses or the modified surface. Future work should study similar electrochemical tests on AA7075-T651 with laser peening, and thus compressive residual stresses, normal to the preferred direction of IGC (L-LT plane). Likewise, to investigate LSPwC without removing its generated oxide layer. This oxide layer and resulting homogenised surface caused by laser melting may change the overall electrochemical behaviour, give a small to moderate improvement in electrochemical properties and reduce the number and size of pits.

5.5.3 LSP effects on fatigue behaviour of pre-corroded AA7075-T651

Evaluation of the fractured fatigue samples (Figure 5-14, Figure 5-15 and Figure 5-16) showed cracks do not necessarily initiate at the deepest or widest pits within a pre-corroded surface. In several cases, cracks originated at what appear to be 10 µm deep pits. SEM microscopy of pit cross-sections show many of these apparent discreet pits are in fact connected to one another below the surface. Thus, the pit morphology under the surface is more complex. Cracks initiate subsurface and at the sharp edges of these complex pits, where the stress concentration is highest, in agreement with the literature [95][79][96].

Fatigue *S-N* data (Figure 5-20), and microscopy of beach marked fracture surfaces reveal the decrease in fatigue life of corroded baseline samples to be of at least 50% of uncorroded material, sitting at the top range of what has been reported in the literature [30][93][101][94]. This is due to a near complete absence of crack initiation time, caused by initiation pits, which has been previously shown by Burns et al. [97] and Easter and Burns [95]. This confirms pits

(mechanical or corrosion), act as effective stress concentrations, and initiating cracks shortly after dynamic loading starts. The crack growth rate *vs.* stress intensity factor (ΔK) data in Figure 5-21 suggests crack growth rate of corroded baseline is not particularly faster than uncorroded baseline, although it sits on the upper limits of this data trend. This may be due to all samples having at least two cracks initiating close together and coalescing shortly after. Thus, crack growth rates are marginally faster than uncorroded baseline due to multi-site cracking, which has been shown in past studies [99][100]. This, and the fact the cracks already start 50 µm below the surface (at pits) may explain why crack growth life is lower than for uncorroded baseline.

Pre-corroded LSP *S-N* and crack growth rate *vs*. ΔK data show compressive residual stresses delay crack initiation by effectively counteracting stress concentrations at pits. The higher compressive residual stresses in corroded LSPwC samples means crack initiation and crack propagation are delayed more effectively than corroded LSP, as seen in Figure 5-21. It is likely residual stresses are playing a part in delaying crack propagation of small cracks ($\Delta K \leq 10$); however, multi-site fatigue crack growth likely accelerates the overall crack growth rate. The overall increase in fatigue life is of +250% and 400% for LSP and LSPwC, respectively. Zupanc and Grum reported a similar improvement (a magnitude increase) in fatigue performance [88] in shot peened AA7075. A similar behaviour is found in an study of shot peened AA7075-T7451 by Lv et al. [166] although their fatigue improvement is relatively modest in comparison. Nevertheless, it is difficult to compare as they do not report the level and depth of compressive residual stresses in their material. However, they do report crack initiation is always from corrosion pits regardless of treatment. This agrees with this study that the fatigue life improvement from corroded surfaces is not due to laser peening changing the mechanism of fatigue crack initiation in pits. Instead, the improvement in fatigue life is solely connected to the level of residual stresses, and how effectively they delay crack initiation and propagation.

5.6 Conclusions

1. There is no conclusive evidence of long-term effects of compressive residual stresses on corrosion performance, changes in the corrosion pit initiation mechanism, or the number or depth of pits, for the LSP and LSPwC treated AA7075-T651, where no external mechanical stimuli is involved. This may not be the case if compressive residual stresses are normal to the direction of preferred IGC, and this should be investigated further.
2. Laser shock peening-induced surface roughness, can be a dominant feature and be detrimental to long-term corrosion performance.
3. LSPwC-induced oxide layer, not covered in this study, could be beneficial to corrosion performance and this should be investigated further in conjunction with its fatigue performance.
4. Corrosion pits in untreated AA7075-T651 act as stress concentrations causing at least a 50% loss in fatigue life, mainly due to a near complete absence of crack initiation time.
5. Laser shock peened generated residual stresses effectively counteract stress concentrations at pits, substantially delaying crack initiation by at least 40, 000 cycles.
6. The residual stresses also delay crack propagation, with LSPwC (160,000 cycles) performing better than LSP (80,000 cycles) due to the higher compressive residual stresses.
7. Overall, laser peened AA7075-T651 with corrosion pit degradation can be expected to have a fatigue performance and a life cycle as good as standard AA7075-T651.

6 Summary and conclusions

This project explored the possible changes caused by laser shock peening on the micro-mechanisms of fatigue, corrosion and fatigue from pre-corrosion in aerospace aluminium alloy 7075-T651. To achieve this the objectives were firstly: to understand how, and to what extent, the LSP and LSPwC generated residual stresses, and the modified surface (hardness and roughness), will each influence changes in the micro-mechanisms of short crack fatigue initiation and growth in AA7075-T651. Secondly, to understand to what extent the laser shock peening generated residual stresses and the modified surface (microstructure, hardness and roughness) influence the electrochemical properties, corrosion pit formation and corrosion performance of AA7075-T651. Finally, to investigate how pre-corroded pit features can affect fatigue performance, crack initiation mechanisms and crack growth, of laser peened AA07075-T651.

For the **first objective**, the laser peening treatments achieved their objective of generating the highest possible compressive residual stresses whilst minimising surface roughness. It was further demonstrated how LSPwC can generate higher residual stresses (up to 14% higher than LSP) subsurface, but with the compromise of increased surface roughness and profile. These laser treatments allowed for the investigation of possible significant changes in the micro-mechanisms of fatigue crack initiation. The outcome provides deeper insights of the full potential of laser peening on AA7057-T651. Changing fatigue behaviour from low to high fatigue regime by altering the crack initiation mechanism. In addition, this study highlighted the criticality of surface roughness in negating the full fatigue enhancement by laser peening, by reversing the change in micro-mechanism from sub-surface dependent on the local stress field to surface stress concentrations, a phenomenon more likely to happen for the rougher LSPwC compared to LSP. Finally, a post-laser peening mechanical polish, to remove surface features, returned the fatigue life of AA7075-T651 to the high cycle regime, for an applied stress range below the yield strength. This gives a possible solution if reliable maximum fatigue enhancement is required and the industrial application allows it. This study also established an interesting, industry relevant, avenue for further research. This is to investigate the interplay between the critical depth at which a surface feature acts as a stress concentration, which counteracts a given laser peened-induced compressive residual stress profile preventing changes to the sub-surface crack initiation, drastically reducing the potential

for increased fatigue performance. Quantifying these critical depths could allow for more accurate modelling and fatigue life prediction.

Although the highest fatigue performance gains are seen at below yield strength, another outcome of this project was to show that laser shock peening could allow this type of aluminium alloy to be loaded at above yield strength and perform with a fatigue life typically seen at below yield strength levels of fatigue loading. Thus, upwardly extending the loads at which the alloy can be used, for low cycle fatigue applications.

The benefits of laser shock peening are also present for crack propagation: both LSP and LSPwC indicate slowed growth, with LSPwC indicating a considerable delay (up to a magnitude difference compared to baseline) due to its higher compressive residual stresses. For below yield strength applied loads this crack propagating delay is dwarfed by the change in crack initiation mechanism. Whilst for above yield applied loads this becomes more significant in delaying fatigue failure. However, accurately characterising sub-surface crack propagation lives was very challenging, and further investigation with more precise techniques (e.g. interrupted CT-studies) could add considerable knowledge.

In terms of the **second objective**, there was no conclusive evidence that neither LSP nor LSPwC peening compressive residual stresses affect the corrosion behaviour of AA707-T651 in the L-LT microstructural plane. This includes no effects in the corrosion pit initiation mechanism, the density, or morphology of pits. From the various material modifications induced by laser shock peening (hardness, roughness, residual stresses) it is surface roughness that was the most dominant feature in electrochemical tests and could be most detrimental to long-term corrosion performance. However, aside from a decrease in open circuit potential for laser peened AA7075-T651, long-term detrimental effects were not seen. This is another interesting outcome, particularly for industrial application, as it indicates these laser shock peening treatments considerably improved fatigue performance without having a marked detrimental effect on corrosion performance: The aerospace industry may be able to use treatments for large improvements in fatigue and not have to make major adjustments for corrosion protection or life prediction. More investigation is required to fully characterise the fatigue and corrosion behaviour of the other AA7075-T651 microstructural planes, to understand if other planes respond differently to laser peening, and differ from the fatigue and corrosion behaviour studied in the AA7075-T651 L-LT microstructural plane.

The t**hird objective** provided a thorough characterisation of the effects of laser shock peening on fatigue mechanisms from pre-corroded AA7075-T651. This established the initial dataset

necessary for future work aimed at studying the more complex corrosion with mechanical stimuli. Firstly, the overall crack initiation mechanism from pre-corroded AA7075-T651 does not change despite high compressive residual stresses, due to the effectiveness of pits as stress concentrations. These stress concentrations cause at least a 50% loss in fatigue life in untreated material, mainly due to a near complete absence of crack initiation time. Laser shock peening generated residual stresses which effectively counteracted stress concentrations at pits, substantially delaying crack initiation by at least 40,000 cycles. The residual stresses were also effective at delaying crack propagation, with LSPwC (160,000 cycles) performing better than LSP (80,000 cycles) due to the higher compressive residual stresses. Thus, the main outcome was: if corrosion develops in an aerospace application the fatigue life of the laser peened material would be as good as, or better than, standard untreated AA7075-T651. In other words, laser shock peening would protect the aluminium alloy from early fatigue failure from subsequent corrosion. If applicable to components, it can improve the flight safety of aircraft and, pending more study, highlights the opportunity for the aerospace industry to use laser shock peening to increase the life of components where there is corrosion exposure. Indeed, the benefits of compressive residual stresses are very likely to extend to corrosion phenomena with mechanical stimuli, and future work to demonstrate this would be highly recommended.

As with non-corroded AA7075-T651, high-accuracy characterisation of fatigue crack growth from pits in AA7075-T651 with a surrounding residual stress field would enhance the understanding of crack propagation mechanisms in laser peened material and could lead to more accurate fatigue prediction models. Techniques such as three-dimensional X-ray tomography ex- and in-situ would be highly desirable. Therefore the next chapter presents methodology and early results on X-ray tomography (ex-situ) and recommendations based on lessons learnt, as well as other future work recommendations.

7 Future work

This chapter is divided into two sections. The first section details the incomplete work on ex-situ X-ray tomography of fatigue short-crack initiation and propagation from pre-corroded AA7075-T651. This work was planned as complementary to the third objective of this PhD project. However, the 2020 Covid-19 pandemic caused irrecoverable delays due to university laboratories being shut down for several months. This work was never completed and only contains work performed to understand its feasibility. Therefore the methodology does not have the same level of maturity as previous chapters. Thus, this section focuses on methodology, preliminary results and some discussion, including recommendations for successful completion of this work. The second section of this chapter details long-term future work recommendations based on the overall work completed in this PhD study.

7.1 Ex-situ X-ray tomography of fatigue in corroded AA7075-T651

7.1.1 Introduction

By using a combination of variable focus and electron microscopy Chapters 4 and 5 provide 2-dimensional data on corrosion features and fatigue crack initiation mechanisms of LSP and LSPwC. However, crack growth rates were difficult to capture using conventional methods (replica and beach marking) due to subsurface crack initiation and propagation, as well as non-semi elliptical crack shapes, in both laser peened and pre-corroded samples. In addition, microscopy data indicated corrosion feature morphology in the L-LT microstructural plane was more complex than what 2D techniques could accurately capture. Finally, one objective of this PhD project was to understand whether LSP and LSPwC could have an effect on corrosion performance including any effects on number and size of corrosion pits forming. The most common method to capture this data is progressive polishing of sample cross-sections whilst taking microscopy images at several intervals [1]. This is a very effective but time-intensive approach.

X-ray tomography can be an alternative approach that can capture feature morphology, such as corrosion pits, to a similar resolution in a fraction of the time. Most importantly, it can also

be used to capture the morphology of subsurface features such as corrosion pits and fatigue cracks, and can be done non-destructively [212][213][214][215][216].
The aim of this work was to provide 3D quantitative data of corrosion pit morphology, fatigue crack morphology and crack growth rates of pre-corroded AA7075-T651 in untreated, LSP and LSPwC condition by performing a programme of ex-situ high resolution X-ray CT scans at fatigue life intervals.

7.1.2 Methodology

A number of CT-scans, per sample, were required. First, to capture pit-morphology an ex-situ CT scan is required after corrosion exposure, prior to fatigue testing. Subsequently, a small number of CT-scans (3 – 5) are taken at fatigue life intervals in an attempt to capture cracks growing from pits, and through 3D data processing, calculate crack aspect ratios and crack growth rates at different fatigue intervals. Although the fatigue life (10,000 – 30,000) of pre-corroded baseline AA7075-T651 (loaded at 400 MPa stress range) was known at the time of initial testing, the crack initiation time had not yet been investigated. Thus, selecting the fatigue testing intervals, where the test is stopped to perform successful ex-situ scans of early crack growth, required a trial and error approach. This was also required for LSP and LSPwC, as there was no prior knowledge of fatigue life or crack initiation time of these samples (Type C, see next section). Consequently, during initial testing there was no knowledge of CT-scan timing (i.e. how to time the fatigue stop intervals to ensure early crack growth is not missed). Thus, two samples for each condition were manufactured, with the aim of using the first samples (of each condition) as trial samples, and using the second samples after having learnt the lessons of the first trial. Thus, accurately capturing early crack growth in each condition.

This work package required careful sample preparation, extensive use of several laboratories and considerable post-processing time. To achieve this as efficiently as possible, careful pre-planning and equipment booking was essential. This would allow the streamlining of the overall process and minimise time-loss.

7.1.2.1 Sample preparation

The fatigue sample size and shape to be selected for this study was heavily dependent on it being suitable for two contradicting requirements: fatigue testing (larger samples are preferred) and CT-scanning (smaller samples are strongly desired). See Section 3.2.4.2 for more for on CT scan requirements. In addition, several variables were also important when deciding sample parameters as they impacted project and laboratory logistics, e.g. available

laboratory time, number of scans required, project time availability. Table 7-1 details the four most important factors that influenced the choice of sample size.

Table 7-1 – Important factors influencing sample size choice.

	Larger sample	**Smaller Sample**	**Comments**
Ease of fitting in fatigue machine	x		Ideally 10 mm x 10 mm cross-section, or higher.
Leftover residual stresses	x		Ideally uncut LSP (e.g. Type A - 10 mm x 20 mm)
Increase Voxel resolution		x	Ideally 1 mm cross section or lower
Decrease scan time		x	Ideally 1 mm cross section or lower

Previous trial AA7075-T651 CT scans had showed a 1 µm voxel resolution can be achieved within a day scan (~20 h) if the sample cross-sections are no larger than 5 mm × 5 mm. Thus, Type C samples, shown in Figure 7-1, were manufactured with a 5 mm × 5 mm cross section and 70 mm length in the baseline, LSP and LSPwC condition. Baseline Type C samples were removed from the AA7075-T651 plate, whilst LSP and LSPwC samples are taken from the peened block that was also used for Type B samples (one block each for LSP and LSPwC), as shown in Figure 7-1. Consequently, the LSP and LSPwC Type C residual stress fields were expected to be different to the original peened block and required measuring to confirm if, and how much, residual stresses are present after cutting.

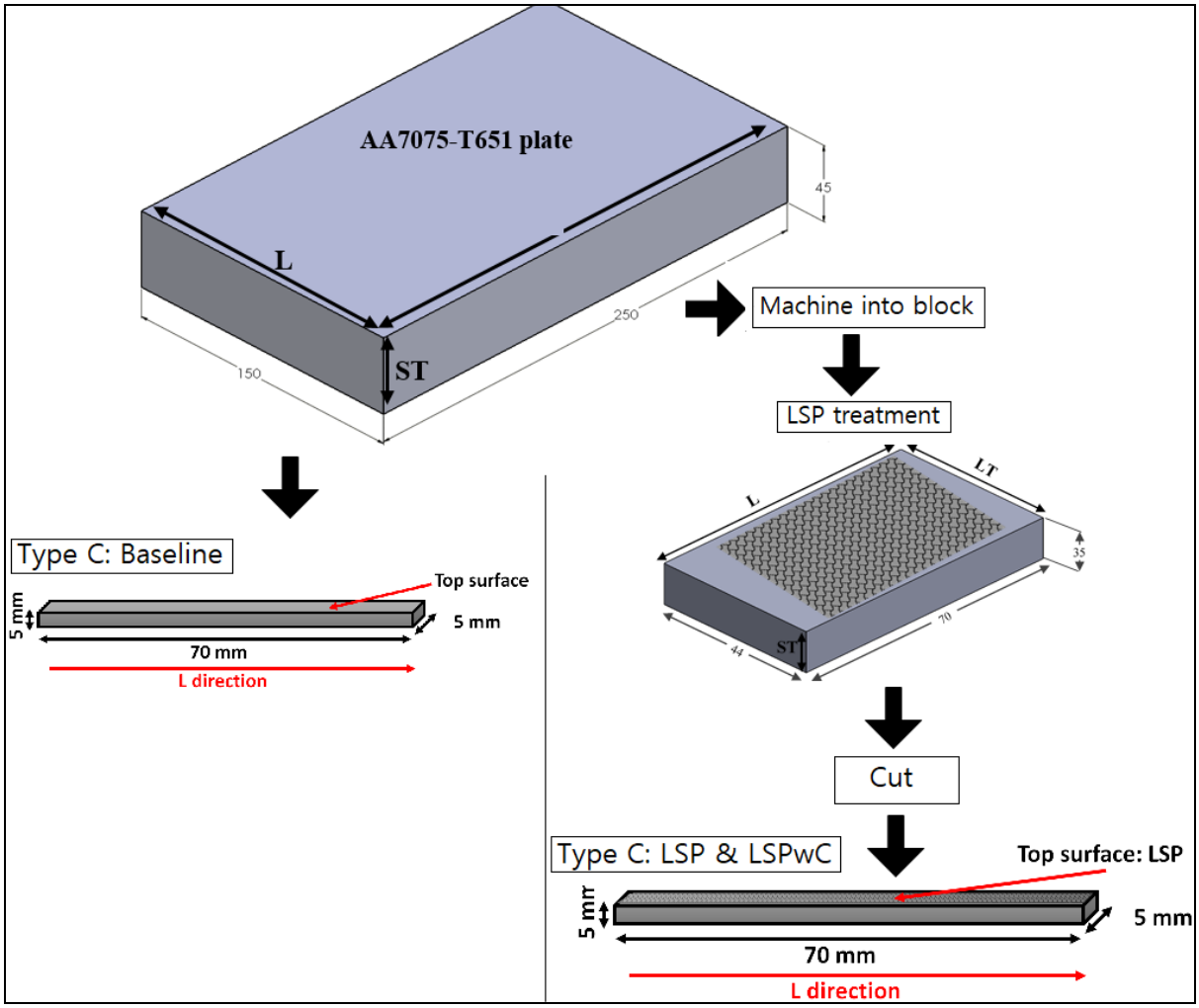

Figure 7-1 – Schematic of Type C sample manufacture sourced from AA7075-T651 plate

7.1.2.2 Residual stress measurements

X-ray diffraction residual stress measurements were performed with similar scan settings as shown in section 3.2.4. The number of surface locations scanned were reduced compared to Type A as Type C samples were considerably smaller in size. Subsurface residual stress measurements can be done by incremental hole drilling. However, as this technique is semi-destructive, and due to the limited number of samples, it was not used.

7.1.2.3 Corrosion testing

Prior to corrosion exposure sample surfaces were protected, to only expose a 1 mm diameter circle in the centre of the bar, using the same technique as performed for Type A samples in section 5.3.

Potentiostatic hold was chosen as a suitable electrochemical test to expose a controlled area to a corrosive environment and accelerate corrosion feature formation, such as corrosion pits [217][218][219][220]. In this corrosion protocol the sample is polarised (potential is changed away from its rest potential) with the output being current density. A number of trial tests on baseline Type B samples were performed to identify the best test settings, to generate pits no wider than 100 µm. This was particularly challenging as early tests showed, despite appearing to have a good electrical continuity, the open-circuit potential of Type C exposed surfaces was very unstable, and would vary by several 100 mV, possibly affected by the small size of the exposed area (1 mm diameter) relative to the reference electrodes. This led to the selection of a fixed potential hold of -0.655 V for 2 h (see Table 7-2) for all Type C bend bars. The assumption was that, as AA7075-T651 open circuit potential was approximately -0.735 V, this would ensure an overpotential of 0.080 V for all samples, exposing the samples to an aggressive corrosion regime. However, this assumed LSP and LSPwC samples would have a similar E_{corr} to the baseline.

Electrochemical data, such as voltage, current and time, were automatically saved by the EC-Lab software, which is used in conjunction with the multi-channel potentiostat. Origin(pro) 2020 was used to generate graphs of corrosion potential vs. current density and time. The Alicona variable focus microscope was used in the same manner as for material characterisation (see section 3.2.6.2) to visualise the corroded surface and obtain a 2-dimensional understanding of the corrosion features generated, prior to 3-dimensional evaluation.

Table 7-2 – Polarisation hold test settings

Test parameters	
Rest time before test start / minutes	30
Potential change from open current potential / mV	Fixed at -0.655 V
Time / h	2
Current limit / mA	200
pH	6.5 – 7.5
Electrolyte	3.5 wt.% NaCl solution

7.1.2.4 Fatigue testing

Fatigue testing was performed using the same methodology as indicated in section 4.2.1. A five (5) kN cell (instead of 50 kN used for Type A), was used to fatigue test the small Type C

samples. The fatigue testing setup is shown in Figure 7-2. The replica method was not used as it would be ineffective for the expected subsurface crack initiation. Beach marking was used to calculate crack growth rates based on fracture surfaces, to be subsequently compared to crack growth values calculated from CT scan processed data.

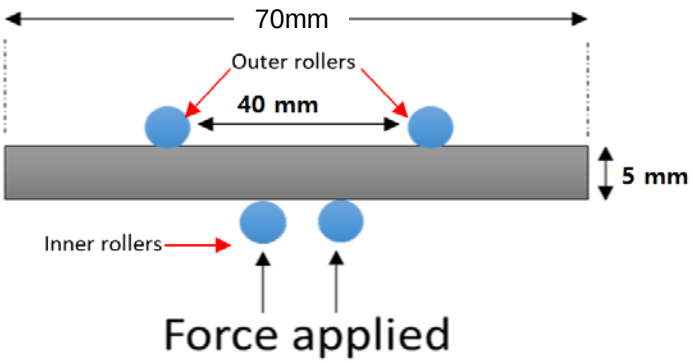

Figure 7-2 – Schematic of Type C fatigue testing setup.

To capture crack shape and early fatigue crack growth from corrosion using X-ray CT-scanning, fatigue testing was paused at several intervals. The fatigue life interval at which CT scans were performed are shown in Table 7-3. As mentioned previously, this study was not completed and therefore the table only shows a limited number of CT scans: Only two conditions, baseline and LSP, reached the first trial sample fatigue testing stage. Of these, only the baseline sample has been completed. LSP testing was started but end of life has not been completed.

Table 7-3 – Type C testing steps. No raw data available (-), raw data available (o), data processed (x).

	Steps	Baseline	LSP	LSPwC
1	Potentiostatic hold	x	x	x
2	2D microscopy	x	x	x
3	CT-scan (pre-corroded)	x	x	-
4	First fatigue test interval	x	o	-
5	CT-scan	x	o	-
6	Second fatigue test interval	x	o	-
7	CT scan	x	o	-
8	Third fatigue test interval	x	o	-
9	CT scan	x	o	-

7.1.2.5 X-ray CT-scan test procedure

A micro-focus CT with a polychromatic divergent X-ray beam was used to acquire high-resolution 3D reconstructions (below 5 µm voxel resolution). Typical X-ray energies used for AA7075-T651 were 80 – 110 keV. A low energy filter was used to decrease beam hardening issues, as well as ×4 objective magnification, placing the X-ray source and detector as close as possible to the sample (millimetres apart) and taking between 1500 and 4000 projections to maximise voxel resolution, leading to scanning times of 18 – 24 h.

Type C sample cross-sections scanned were 5 mm × 5 mm. The field of view varied between 1 and 1.5 mm diameter. The voxel resolution achieved varied between 900 nm and 1100 nm. Initially, several ImageJ commands (Adjust Brightness/Contrast, Median Filter, Crop, Rotation, Reslice, Erode, Dilate) were used to decrease the volume size, reduce noise, improve image quality and facilitate visual analysis. This data was then exported to Python, where a programme code (see appendix in section 9.2.2) was used to remove any features that are not pits or cracks (e.g. porosity, artefacts). The resulting data is then imported back to ImageJ were segmentation of corrosion pits and fatigue cracks is performed using the Threshold command. To attempt to quantitatively assess any differences in corrosion morphology between the different material conditions (baseline, LSP and LSPwC) the BoneJ plugin [221] was used. This plugin was chosen to assess the complex pit morphology, which contain several subsurface interconnected branches that are either intergranular corrosion and / or subsurface pitting from preferential grain dissolution. Plugin commands ‘3D-skeletonise’ and ‘Analyse skeleton’ were used to transform each pit into a set of 3D skeletons that reduce the complex pit morphology into a one pixel-wide feature (See Figure 90). Thus, each pit is converted into a ‘stem and branches feature, which allows for relatively easier quantitative analysis whilst still capturing pit morphology data. Average branch length per pit distribution and maximum branch length per pit distribution is calculated and compared between baseline, LSP and LSPwC. Differences in this distribution may indicate differences in pit morphologies for the different conditions.

Figure 3 – Example of skeletonised binary image [221].

Fatigue cracks growing from pits were to be separated from corrosion pits by visual analysis. This was selected over an automated process once the first scans were performed, as it became clear automatic thresholding would be difficult due to cracks being one to two pixels wide (low resolution) and were difficult to separate from corrosion pits' thinner branches.

Four CT scans each have been performed for the baseline and LSP bend bars. A large amount of data has been gathered. However, full analysis and the full methodology to capture early crack growth, has not been completed.

7.1.3 Results

Due to aforementioned time limitations, this section presents incomplete test data from baseline, LSP, and to a lesser extent, LSPwC.

7.1.3.1 Residual stress measurements

Figure 7-4 shows XRD residual stress measurements for the LSP surface are between –100 MPa and –200 MPa. For LSPwC surface residual stresses are between 0 and -100 MPa, in the longitudinal direction (S_1). This shows, despite cutting a thin sample from a laser peened block, stress relaxation was not total and some residual stresses remain. For the transverse direction (S_3) please see appendix in section 9.2.2.

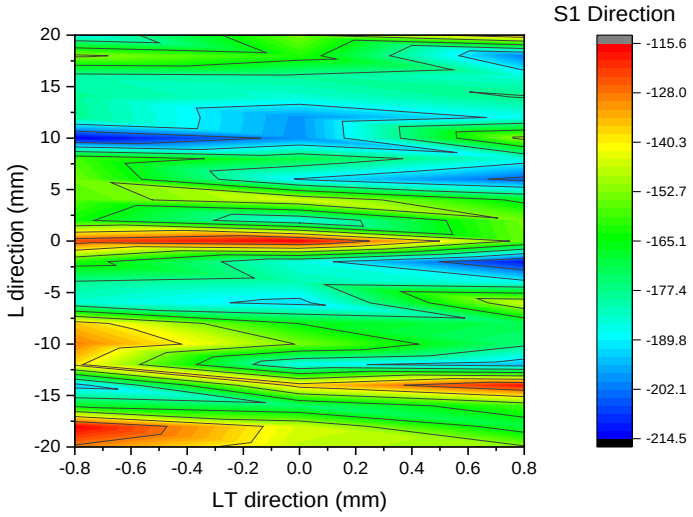

Figure 7-4 - XRD measurements of LSP residual stress in the longitudinal (S_1) direction.

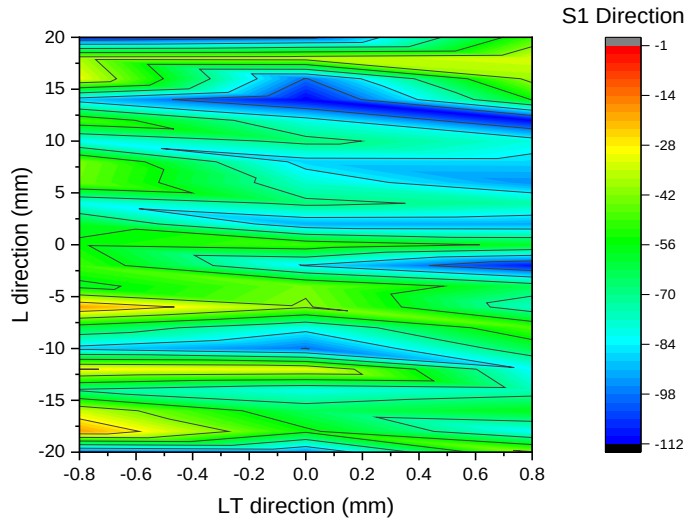

Figure 7-5 - XRD measurements of LSPwC residual stress in the longitudinal (S_1) direction.

7.1.3.2 Potentiostatic hold

Current density vs. time are shown for baseline, LSP and LSPwC Type C in Figure 7-6. The baseline sample shows two graph lines. This is due to the unexpected corrosion of only half the area (see Figure 7-7), which may have happened due to an air bubble forming early on during testing. Thus, the two baseline current density lines are calculated based on either the full area exposed or the corroded area only, and can be seen as a range of minimum and maximum possible current densities. It is very clear LSP current density is much higher than LSPwC and approximately equal or higher than baseline. This would indicate the LSP sample suffered considerably more corrosion than the other two conditions.

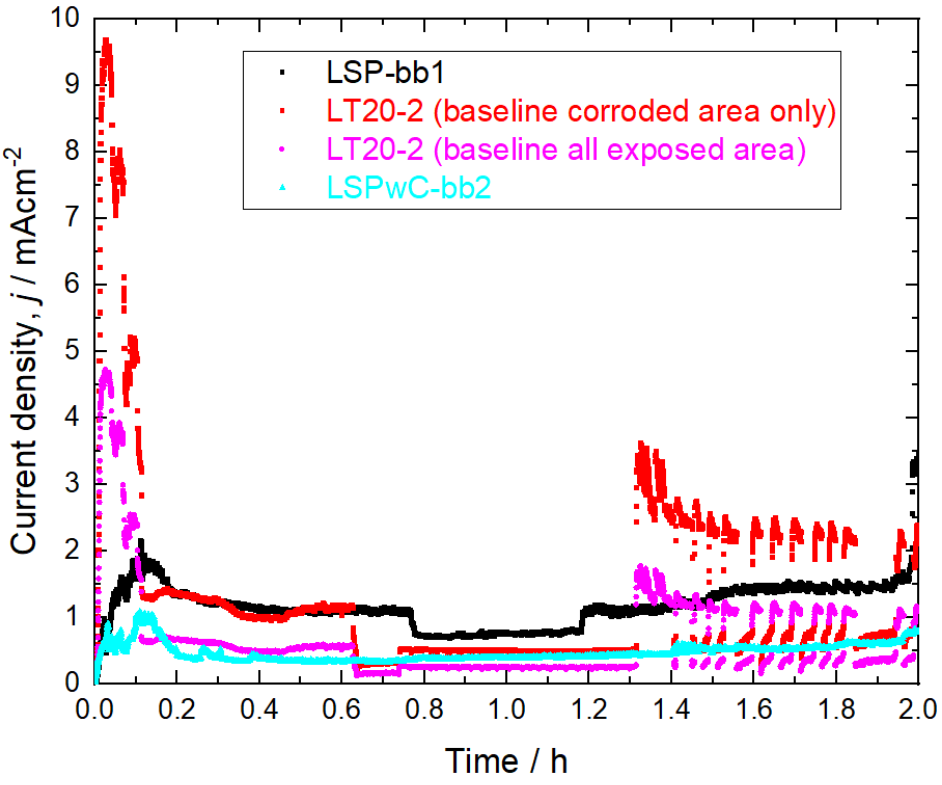

Figure 7-6 – Potentiostatic hold of untreated AA7075 (baseline), LSP and LSPwC Type C.

7.1.3.3 2-dimensional feature characterisation

Figure 7-7, Figure 7-8 and Figure 7-9 show the LSP condition was subject to significantly more corrosion degradation than baseline or LSPwC. Two-dimensional characterisation indicates LSP deepest pits reach at least 70 µm and are also considerably bigger than baseline or LSPwC. Type A tests in chapter 5.4 have shown the maximum depth is likely to be higher than what is captured by 2D methods. In contrast, both baseline and LSPwC samples appear to

show significantly smaller pits, up to 18 µm and 20 µm deep, respectively. As previously mentioned, Type A galvanostatic tested samples have shown pit depth of this size are likely to have a true pit depth closer to 50 µm.

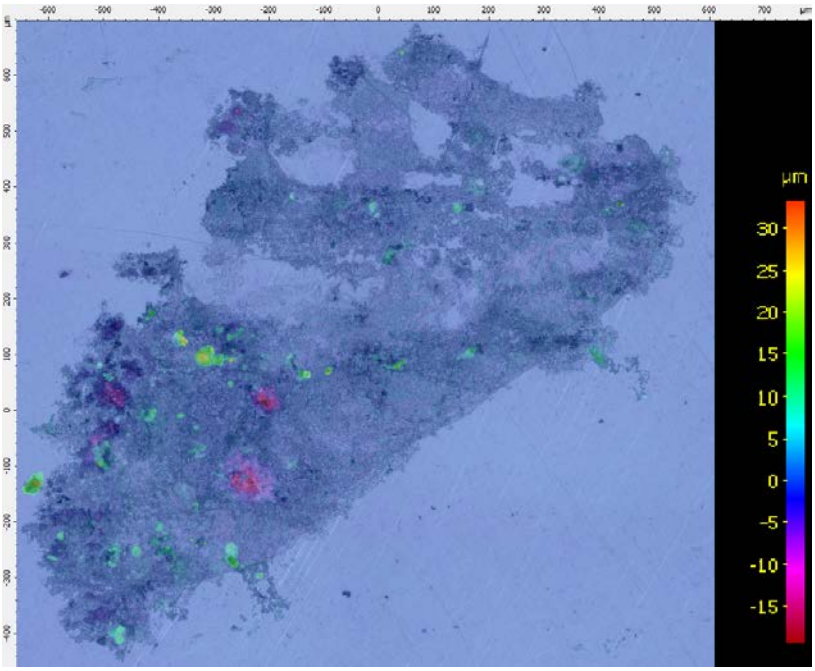

Figure 7-7 - Variable focus microscope image of Baseline Type C after potentiostatic hold at -0.655 V for 2 h, showing corrosion features.

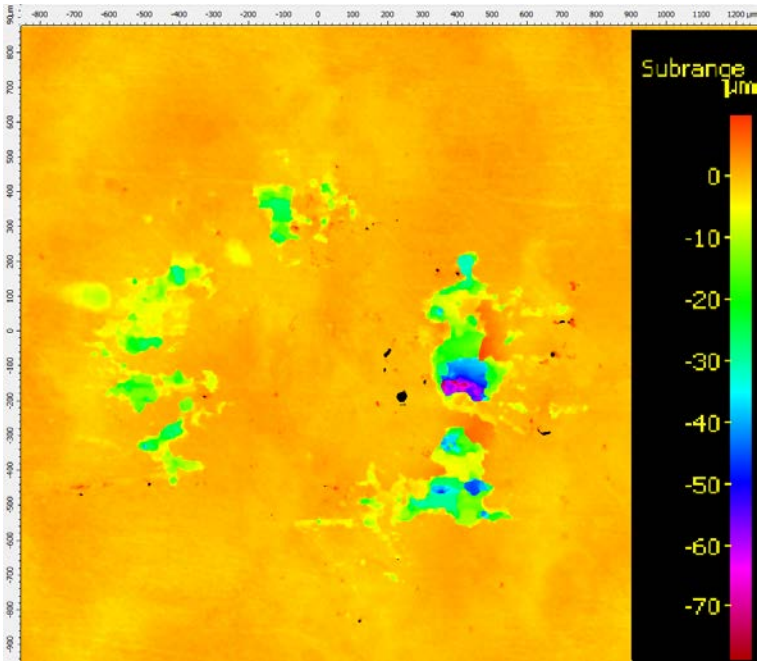

Figure 7-8 – Variable focus microscope image of LSP Type C after potentiostatic hold at -0.655 V for 2 h, showing corrosion features.

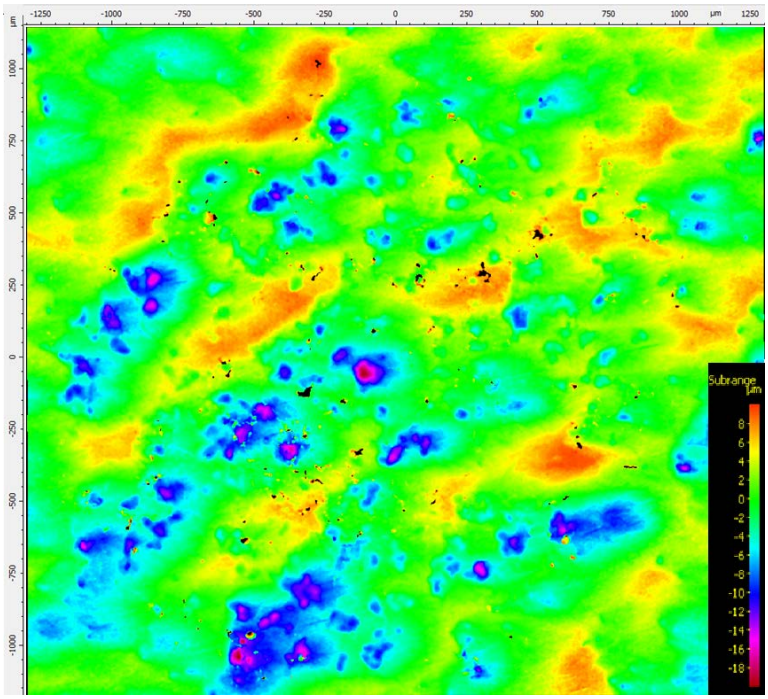

Figure 7-9 - Variable focus microscope image of LSPwC Type C after potentiostatic hold at -0.655 V for 2 h, showing corrosion features.

7.1.3.4 Three-dimensional feature characterisation

Table 7-4 compares Type C baseline maximum pit depth, width and volume captured from 2-dimensional characterisation (variable focus microscope) and 3-dimensional characterisation (X-ray CT scan), showing a significant difference in the values obtained. This shows the importance of capturing subsurface morphology with 3-dimensional characterisation techniques, as it shows pit volume, depth and width is much larger than what can be captured with two dimensional approaches.

Figure 7-10 and Figure 7-11 show a typical slice of baseline and LSP CT-scans, respectively, showing the significantly bigger pits in the LSP sample. Due to the difference in pit size from the unexpected and significantly higher exposure in LSP, the two samples' corrosion features cannot be compared in terms of absolute values, and must be compared in terms of relative morphology.

Figure 7-12, Figure 7-13, Figure 7-14, Figure 7-15, Figure 7-16 and Figure 7-17 show the distribution of surface volume, average and maximum pit branches for baseline and LSP taken from processing 3D data. It is clear the processing method has over-counted 'pits', as the total numbers of pits shown for each condition are unlikely to be realistic for the small area exposed. There is no indication of any significant differences in the distributions, suggesting no significant change in pit morphology between baseline and LSP.

Figure 7-10 – Typical slice of segmented baselines pits

Figure 7-11 – Typical slice of segmented LSP pits.

Table 7-4 – Two-dimensional and three-dimensional characterisation of Type C baseline pits after 2 h potentiostatic hold at -0.655 V.

	2D	**3D**
Deepest pit	20 µm	72 µm
Widest pit	141 µm	215 µm
Largest pit volume	34425 μm^3	835503 μm^3

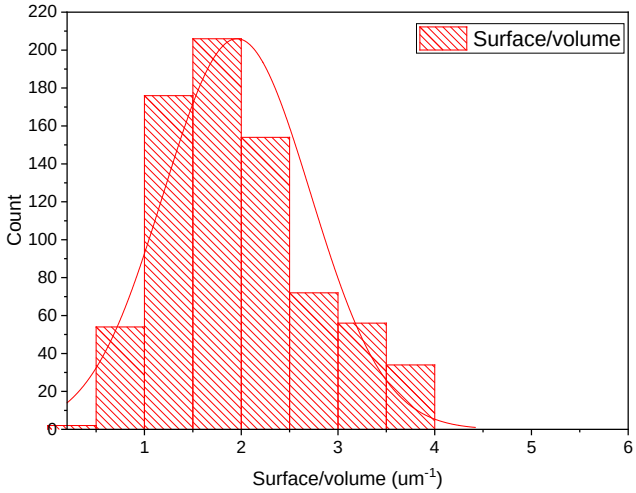

Figure 7-12 – Surface/volume distribution of Type C baseline pits after 2 h potentiostatic hold at -0.655 V.

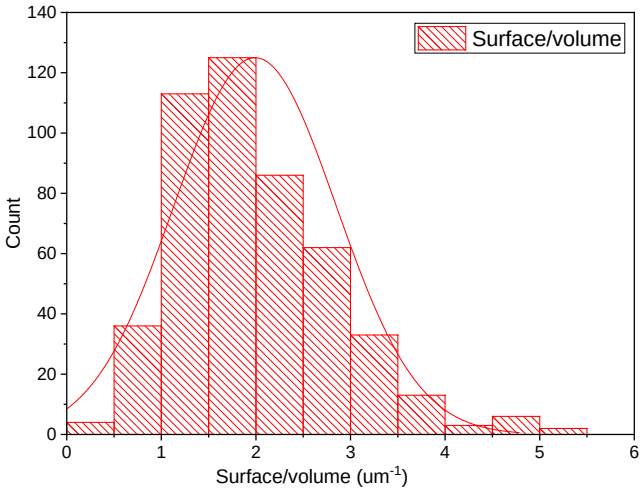

Figure 7-13 - Surface/volume distribution of Type C LSP pits after 2 h potentiostatic hold at -0.655 V.

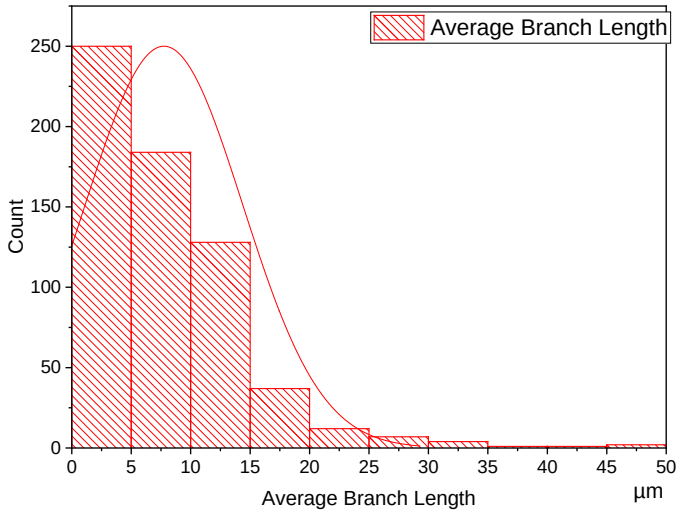

Figure 7-14 – Average branch length distribution - Type C baseline pits after 2 h potentiostatic hold at - 0.655 V.

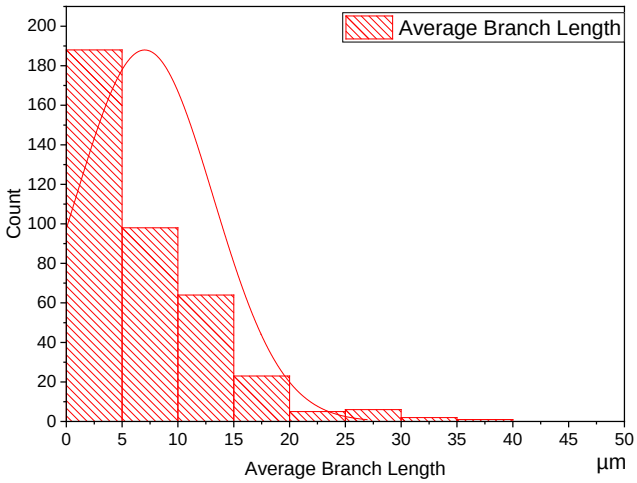

Figure 7-15 - Average branch length distribution of Type C LSP pits after 2 h potentiostatic hold at -0.655 V.

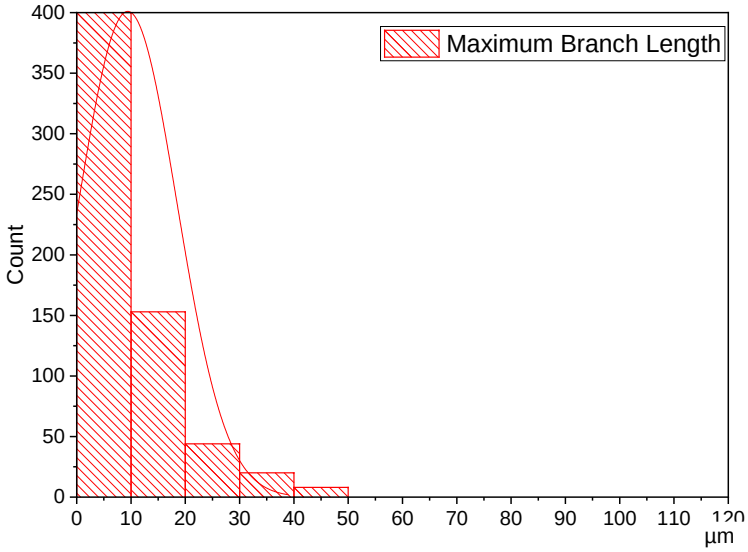

Figure 7-16 - Maximum branch length distribution of Type C baseline pits after 2 h potentiostatic hold at - 0.655 V.

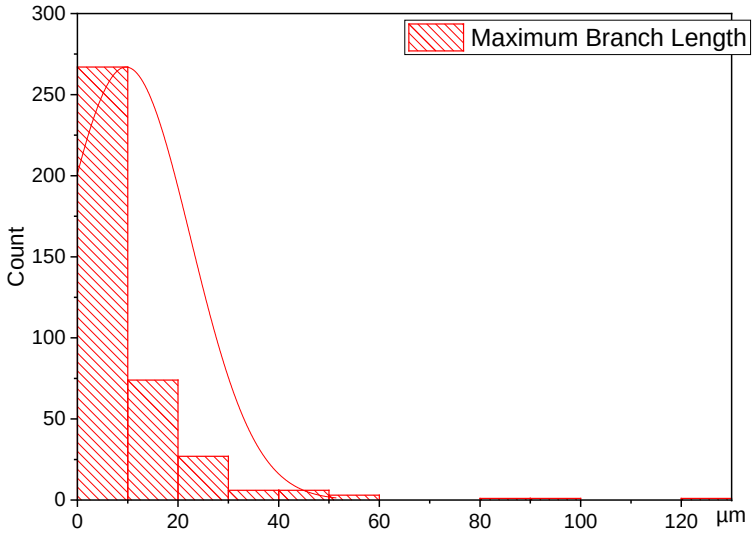

Figure 7-17 - Maximum branch length distribution of Type C LSP pits after 2 h potentiostatic hold at - 0.655 V.

7.1.3.5 Fatigue life

As mentioned previously, only one baseline fatigue test was completed, whilst LSP was started but not completed and LSPwC testing was not started. The baseline sample achieved a maximum total life (R = 0.1 + R = 0.5) of 24,562 cycles. This fatigue life is similar to what has been seen for galvanostatically corroded Type A samples, in section 5.4.6. Fatigue crack growth rates have not been calculated; however, preliminary visual analysis of X-ray CT scans suggest differentiating small cracks from pits is very difficult. Figure 7-19(A), before fatigue testing, shows corrosion pits and thin subsurface corrosion features (see annotations in Figure 7-19(A)), common in 7XXX aluminium alloy microstructure. These thin corrosion features were difficult to see as their width is close to the voxel resolution. After 8,000 cycles another baseline CT scan was performed. Data in Chapter 5 suggested fatigue cracks would be expected at this fatigue life stage. As can been seen in Figure 7-19(B), there are large cracks, indicating fatigue cracks grew very fast in the first 8000 cycles and suggesting early crack growth happened very soon after cyclic loading started. In addition, when undertaking a visual inspection of the CT scans of corrosion features, where cracks are expected to have initiated, it is difficult to differentiate the start of the crack from the corrosion features. This is likely due to both voxel resolution and the two type of features (cracks and subsurface corrosion features) being of similar size and shape.

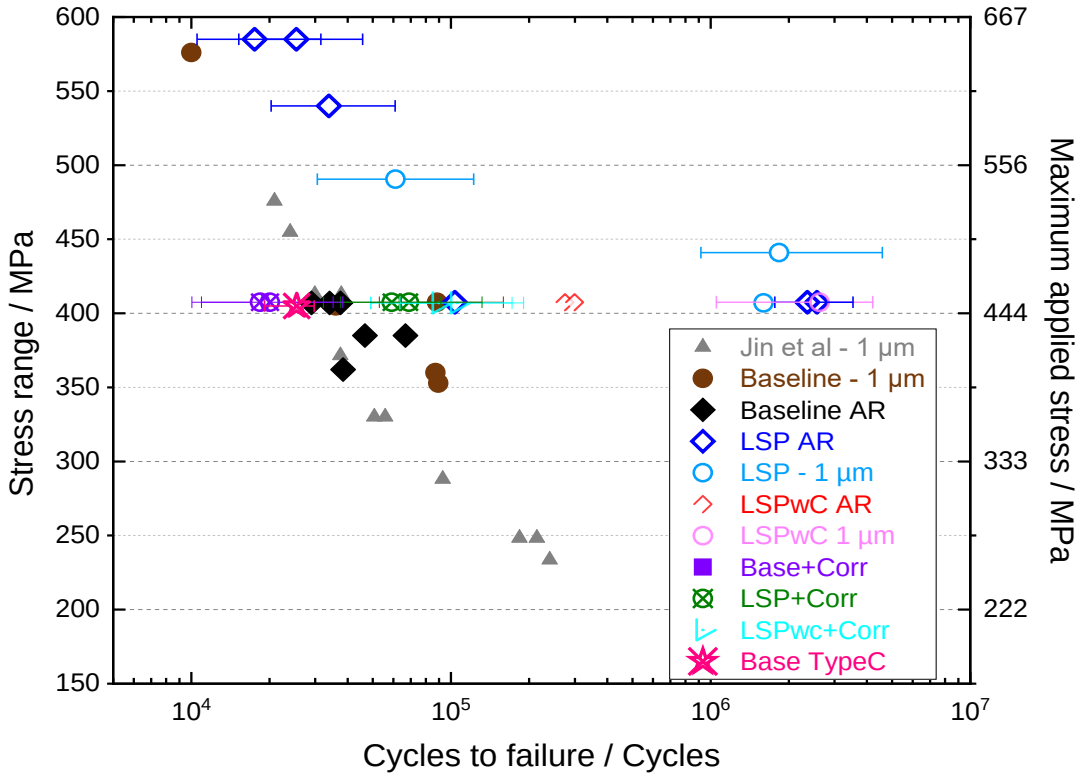

Figure 7-18 – Stress vs. number of cycles for all tests (baseline, LSP and LSPwC) including a Baseline Type C test.

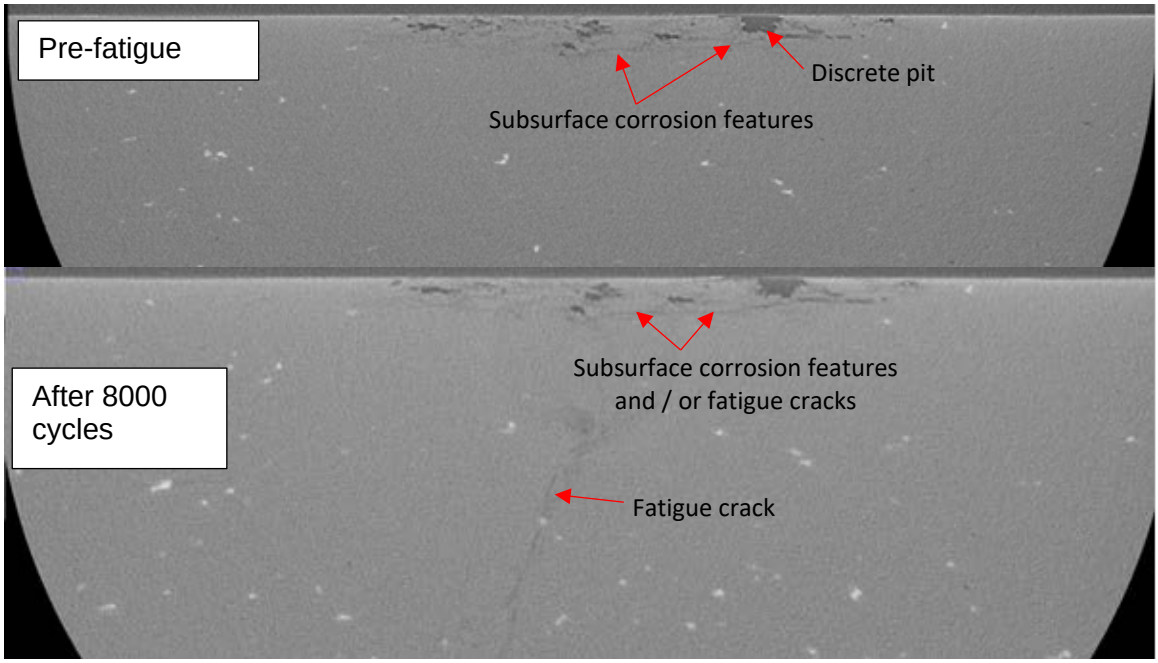

Figure 7-19 – Typical CT scan slice of baseline Type C: pre-fatigue and 8,000 cycles.

7.1.4 Discussion and follow up work recommendations

First of all, it is important to remember the Type C samples tested (one for each condition) were trials to gather initial data, and define the best methodology for this work. The second round of Type C samples, which were not completed, would have had a methodology based on the lessons learnt in the first round of testing. These lessons learnt will be discussed next.

7.1.4.1 Residual stress field relaxation

Prior to manufacturing the Type C samples the decrease in compressive residual stresses due to cutting from laser peened blocks was expected, however the extent of residual stress relaxation was unknown. XRD measurements showed residual stresses were far from negligible for LSP (-214 MPa) and LSPwC (-112 MP). These levels of residual stress would be expected to favourably affect fatigue life, and thus Type C samples are suitable for investigating laser peening residual stress effect on fatigue performance. In addition, although no subsurface residual stress measurements were performed, previous measurements on Type A samples would suggest compressive residual stresses would be present subsurface. In addition, subsurface residual stresses in LSPwC would be expected to be higher than LSP However the magnitude and depth of this is unknown.

7.1.4.2 Corrosion feature generation

The corrosion feature generation by potentiostatic hold had mixed success. It generated relatively small and discrete pits in baseline and LSPwC samples, but caused substantially larger corrosion pits in LSP. Figure 7-6 confirms LSP had more intensive exposure as it shows higher current density, approximately three times higher, than LSPwC. This large difference in exposure, and corrosion features, make it difficult to compare absolute pit morphology between the different conditions, or make valid fatigue crack morphology and behaviour comparisons. It is unclear why the LSP sample suffered considerably higher current density. One possibility is the presence of large constituent particles at the exposed surface (or near of LSP. This would have provided a site for increased localised corrosion. If this was the case, due to heterogeneous distribution of particles in the alloy, it would be difficult to ‘select’ an area without particles for exposure. A possible solution could be to select an area, and subsequently characterise the surface (and near-surface) using SEM-BEI, to understand the number of particles present and make a decision on the suitability of this surface for corrosion testing.

Another issue encountered during corrosion testing, as seen in Figure 7-7, was the partial exposure of the baseline sample. Only half the surface suffered corrosion degradation. It is likely this non-corroded area was shielded from exposure. As only one round of tests was performed, the causes for the aforementioned issues have not been isolated and identified. However, the evidence collected can help propose possible causes and solutions.

First, during initial corrosion exposure (30 minutes rest) the variation in open-circuit potential was uncharacteristically high, suggesting this was related to the experimental setup rather than the material. One possible reason for this is the challenge of exposing a very small area, where the varying local features (i.e. intermetallic numbers and sizes) can cover a large area fraction and affect potential readings. Whilst in a standard test the total area is much larger and these local features have little effect on the potential readings. The Type C potentiostatic hold tests were performed prior to the study on corrosion exposure of Type A bend bars in chapter 5. The issues with potential variability and inconsistency seen in Type C samples where positive learning outcomes and led to the successful change to galvanostatic control for Type A samples. This new approach consistently generated corrosion features. Galvanostatic control tests were not dependent on an accurate and stable potential reading, as it applies a selected current at the surface. However, these samples had considerably larger areas exposed (5 mm × 5 mm). Thus, it is not proven yet whether Type C samples under galvanostatic control will not suffer the aforementioned problems due to their smaller area.

Another possible reason for the variation in potential and feature generation, could have been air bubbles, which have been identified during corrosion testing and may have shielded some of the exposed surface, as has been seen for the half-exposed Type C baseline sample. A more bespoke electrical circuit, e.g. with more sensitive and smaller electrodes that can be placed closer to the exposed surface, may improve potential readings. Additionally, a small amount of water flow could solve any issues with bubble formation.

It is the author’s recommendation galvanostatic control is used for future corrosion pit generation as it has shown, by applying constant current, it generates features of the same size consistently for all conditions. However, in the case of Type C samples this may not be enough to solve the aforementioned issues. Including a bespoke electrical setup suited for exposure of smaller areas, and the use of water flow, may also be required.

7.1.4.3 CT-scanning processing and limitations

Although the CT scans performed have successfully captured corrosion and crack features to a 1 µm voxel resolution, Figure 7-19 indicates this may not be sufficient for accurate feature segmentation and quantitative evaluation. Features at the edges of pits, which may be intergranular cracking and/or preferential grain dissolution, can be equal or below 1 µm width, the voxel resolution. Thus, making it very difficult to segment from the rest of the material as scan noise is picked up when segmenting features. Processing commands used to remove noise, or filter unwanted features, tended to remove small corrosion features. Thus, the approach used to segment corrosion pits, which in many cases are interconnected, led to loss of information and the complex morphology not been fully captured. The consequence was corrosion features being identified as several separate features. Leading to an over-counting of pits and therefore the processed 3D data (shown in Figure 7-10 and Figure 7-11) does not represent the real morphology of the existing corrosion features. Nevertheless, considering they all have the same processing limitation, the data generated (shown in Figure 7-12, Figure 7-13, Figure 7-14, Figure 7-16, Figure 7-17) is useful as a relative quantitative comparison between different conditions.

The issues with capturing small thin features is also present in the scans containing fatigue cracks, particularly fatigue cracks near pits (as seen in Figure 7-19). Again, the voxel resolution is similar to the crack width. This makes it not only difficult to segment, but to differentiate from the small corrosion features. It was therefore difficult to accurately capture aspect ratio and early crack growth of small fatigue cracks. The best way to improve these issues is to improve voxel resolution. There are different ways this can be achieved. One approach is to increase scan time; however, this would mean time slots several days long, which can be logistically problematic. Another approach could be to decrease the sample size, but this is not recommended due to the effect of cutting samples on residual stress relaxation (and peening small samples can also be challenging). The best and recommended approach would be to perform an ex-situ, or preferably in-situ test, using a synchrotron, where high resolution 3D data can be generated throughout the experiment. This has been performed before in the literature with success [186][216][215][214]. The extent of increased voxel resolution that can be achieved with a synchrotron for this material and test setup requires investigation. If the resolution achieved can be of below 1 µm this could create a complete, time-accurate, picture of pit morphology, crack growth rates and changing crack aspect ratio throughout the life of the fatigue sample. Additionally, even if voxel resolution is not improved and continues to be a limitation, if the tests are done in-situ, scans taken against time would

make initiating cracks easy to notice, and their initiation points and paths could be tracked successfully.

7.1.4.4 Fatigue testing and performance

In terms of fatigue performance expectations, previous studies suggest these residual stress magnitudes are unlikely to change the crack initiation mechanism [125][115], whether corroded or uncorroded. Nevertheless, the findings from chapter 5 suggest a delay in crack initiation from pits, decrease in crack propagation rates and a changing crack aspect ratio.

Figure 7-18 shows baseline fatigue life was not dissimilar to Type A baseline. As with the previous tests in chapter 5, crack initiation appears to have happened shortly after dynamic loading starts. This early crack initiation from pits was not known when performing the first CT scans, leading to this crack initiation in Type C baseline being missed. In the case of LSP and LSPwC, choosing the fatigue intervals for scanning was arbitrary as the time to fatigue initiation in Type C (due to different residual stresses to Type A) was unknown. Several scans have been performed at different stages of fatigue life for LSP; however, scan processing has not been performed. LSPwC, although precorroded, has not had any CT scans or fatigue testing. It is recommended the LSP and LSPwC samples are fatigue tested to end of life and their crack initiation time identified: beach marking was performed for LSP and was planned for LSPwC. This would hopefully allow an estimation of the crack initiation time by characterising the fracture surfaces with scanning electron microscopy. If a second round of tests are performed ex-situ, the acquired knowledge from the first round of tests can be used to set specific fatigue intervals and increase the likelihood of capturing early crack initiation. Alternatively, as discussed previously, an in-situ scan using a higher resolution capability (such as a synchrotron) would be ideal.

7.2 Long-term future work recommendations

The following provide possible directions for future work based on the overall PhD project:

- Further understanding of grain refinement and grain misorientation at and below the surface of LSP and LSPwC can be used to link specific microstructure modification (grain refinement, grain deformation at the surface) to the level of residual stresses seen from each treatment. To acquire high indexing data in the most interesting areas (at and near the surface) it is recommend high resolution EBSD is performed by the novel dictionary indexing (DI) approach [181][222], as this approach has shown it can capture highly deformed grains at the surface.

- The stress range boundary between LCF and HCF could be investigated. At this boundary competing crack initiation mechanisms may be observed.

- Accurately characterise the fatigue crack shape and crack growth rates in laser peened material with subsurface crack initiation. This requires an accurate approach for identifying, or calculate, subsurface crack aspect ratio, and any variation during crack expansion. This, coupled with a literature review and/or development of accurate subsurface ΔK empirical functions, would allow for considerably more accurate crack growth rate vs. ΔK curves in laser peened material, allowing for better fatigue behaviour characterisation and fatigue life prediction. One approach to accomplish accurate crack morphology is to perform X-ray tomography in-situ. A synchrotron, for example, could allow for relatively large peened samples to be scanned in-situ, and therefore not having to make large changes to sample size, loading regime or the need for bespoke equipment.

- Another avenue for further research would be to delve deeper into the competing failure modes in laser shock peened AA7075-T651. This is to understand the influence of surface features, such as LSP-induced pits or surface roughness, on residual stress redistribution. To develop a method to predict the surface crack mechanism caused by the particular surface features within a residual stress field. This would require a way to identify, model and validate the approximate size and/or depth of a feature, for a given material and residual stress field. For instance, the threshold where it causes a reversal of crack initiation mechanism from subsurface to surface (and therefore from HCF to LCF). This could be particularly useful for industry.

- Another interesting research path would be to perform corrosion testing, as performed in this project, on a plane other than the one laser peened (LT-ST or L-ST). As mentioned in Chapter 5 discussion, a study was identified that suggested intergranular corrosion is affected by residual stresses, if these are normal to the surface being corroded. Thus, performing corrosion testing on LT-ST or L-ST planes will not only be complementary data but may also lead to more significant findings regarding laser peening effects on corrosion.

- Another important topic to consider is corrosion performance of LSPwC with an intact oxide layer (passive film). A focus on identifying the oxide layer as being specifically responsible for the corrosion improvement would validate previous literature findings suggesting this is a corrosion-enhancing mechanism in LSPwC. In addition, understanding whether fatigue performance is affected by the same corrosion-enhancing oxide layer would be important as it would give a clear understanding of the compromises that the industry may have to make when using LSPwC; or whether there is a possibility for optimisation of the oxide layer for best fatigue and corrosion performance.

- A natural next step from the work performed in Chapter 5, is to evaluate how LSP and LSPwC affects corrosion behaviour with mechanical stimuli. LSP and LSPwC would be expected to improve corrosion fatigue and SCC behaviour as residual stresses would affect the loading branch of the corrosion. Thus, understanding the extent of this improvements and whether laser peening affects any specific mechanisms would be an interesting avenue of further work.

- Finally, using a three-dimensional characterisation approach of ex-situ or in-situ testing of fatigue, corrosion, or corrosion with mechanical stimuli, in laser peened aluminium alloys could create a wealth of data on residual stress effects on pit morphology, crack morphology and/or subsurface crack growth in uncorroded and corroded aluminium alloys.

8 References

[1] Research and Technology Organisation and North Atlantic Treaty Organisation, “Corrosion Fatigue and Environmentally Assisted Cracking in Aging Military Vehicles,” 2011.

[2] US DoT FAA, *Corrosion and Corrosion Fatigue of Airframe Materials*, no. July. 2000.

[3] K. Ding and L. Ye, “General introduction,” in *Laser Shock Peening*, Elsevier, 2006, pp. 1–6.

[4] B. P. Fairand and A. H. Clauer, “Applications of laser induced stress waves,” The Society of Manufacturing Engineers, Cambridge, Massachusetts, 1978.

[5] A. H. Clauer, J. H. Holbrook, and B. P. Fairand, *Effects of laser induced shock waves on metals*. New York: Plenum Publishing Corporation, 1981.

[6] A. H. Clauer, “Laser Shock Peening for Fatigue Resistance,” *Surface Performance of Titanium*, no. 1996, pp. 217–230, 1996.

[7] P. Peyre, R. Fabbro, L. Berthe, and C. Dubouchet, “Laser shock processing of materials, physical processes involved and examples of applications,” *Journal of Laser Applications*, vol. 8, no. 3, pp. 135–141, 1996.

[8] P. Peyre, R. Fabbro, P. Merrien, and H. P. Lieurade, “Laser shock processing of aluminium alloys. Application to high cycle fatigue behaviour,” *Materials Science and Engineering: A*, vol. 210, no. 1–2, pp. 102–113, Jun. 1996.

[9] M. Newby, A. Steuwer, D. Glaser, C. Polese, D. G. Hattingh, and C. Gorny, “Synchrotron XRD Evaluation of Residual Stresses Introduced by Laser Shock Peening for Steam Turbine Blade Applications,” in *Mechanical Stress Evaluation by Neutron and Synchrotron Radiation*, 2018, vol. 4, pp. 97–102.

[10] C. S. Montross, T. Wei, L. Ye, G. Clark, and Y.-W. Mai, “Laser shock processing and its effects on microstructure and properties of metal alloys: a review,” *International*

Journal of Fatigue, vol. 24, no. 10, pp. 1021–1036, Oct. 2002.

[11] Polmear I. J., *Light Alloys: Metallurgy of the Light Metals*, Second. London: Edward Arnold, 1989.

[12] A. Mouritz, *Introduction to Aerospace Materials*. Oxford: Woodhead Publishing Limited, 2012.

[13] ASM International, "Metallurgy of Heat Treatment and General Principles of Precipitation Hardening*," *Aluminium Properties and Physical Metallurgy*, pp. 134–199, 1984.

[14] E. A. Starke and J. T. Staley, "Application of modern aluminum alloys to aircraft," *Progress in Aerospace Sciences*, vol. 32, no. 2–3, pp. 131–172, Jan. 1996.

[15] P. Rambabu, N. Eswara Prasad, V. V. Kutumbarao, and R. J. H. Wanhill, "Aluminium Alloys for Aerospace Applications," Springer, Singapore, 2017, pp. 29–52.

[16] W. Wallace, D. W. Hoeppner, and P. V Kandachar, "AGARD Corrosion Handbook Voume I: Aircraft Corrosion: Causes and case histories," Essex, 1985.

[17] M. C. Reboul and B. Baroux, "Metallurgical aspects of corrosion resistance of aluminium alloys," *Materials and Corrosion*, vol. 62, no. 3, pp. 215–233, 2011.

[18] J. P. Immarigeon *et al.*, "Lightweight materials for aircraft applications," *Materials Characterization*, vol. 35, no. 1, pp. 41–67, 1995.

[19] J. R. Davis, *Aluminum and Aluminum Alloys*. ASM International, 1993.

[20] D. L. DuQuesnay, P. R. Underhill, and H. J. Britt, "Fatigue crack growth from corrosion damage in 7075-T6511 aluminium alloy under aircraft loading," *International Journal of Fatigue*, vol. 25, no. 5, pp. 371–377, May 2003.

[21] T. S. Srivatsan, S. Sriram, D. Vee Raraghavan, V. K. Va, and S. Evan, "Microstructure, tensile deformation and fracture behaviour of aluminium alloy 7055," *Journal of Materials Science*, vol. 32, pp. 2883–2894, 1997.

[22] Alcoa, "Alloy 7075 Plate and Sheet: All Around Consistent Performance," *ALCOA Mill Products*, pp. 1–4, 2013.

[23] M.H. Lee, "Fatigue Life, Fatigue Crack Propagation and Fracture Toughness Study of

7075 Aluminum Alloy Subjected to Thermomechanical Processing," 1984.

[24] ASM International, *ASM Speciality Handbook: Aluminium and Aluminium Alloys*, Third. Ohio: ASM Internatioanl, 19993.

[25] CRP MECCANICA, "Aluminum 7075-T6; 7075-T651-Properties Sheet," 2015.

[26] CRP MECCANICA, "Aluminium 7075-T651; Aluminium 7075-T6."

[27] P. A. Rometsch, Y. Zhang, and S. Knight, "Heat treatment of 7xxx series aluminium alloys—Some recent developments," *Transactions of Nonferrous Metals Society of China*, vol. 24, no. 7, pp. 2003–2017, Jul. 2014.

[28] Y. Jin *et al.*, "The anisotropy of fatigue crack nucleation in an AA7075 T651 Al alloy plate," *Materials Science and Engineering A*, vol. 622, pp. 7–15, 2015.

[29] K. Gruenberg, B. Craig, and B. Hillberry, "A probabilistic method for predicting the variability in fatigue behavior of 7075-T6 aluminum," *AIAA*, vol. 37, no. 10, 1999.

[30] P. S. Pao, C. R. Feng, and S. J. Gill, "Corrosion fatigue crack initiation in aluminum alloys 7075 and 7050," *Corrosion Science*, vol. 56, no. 10, pp. 1022–1031, 2000.

[31] X. Fan, D. Jiang, L. Zhong, T. Wang, and S. Ren, "Influence of microstructure on the crack propagation and corrosion resistance of Al–Zn–Mg–Cu alloy 7150," *Materials Characterization*, vol. 58, no. 1, pp. 24–28, Jan. 2007.

[32] D. N. Hanlon and W. M. Rainforth, "Some Observations on Cyclic Deformation Structures in the High-Strength Commercial Aluminum Alloy AA 7150," *Metallurgical and Materials Transactions A*, vol. 29, pp. 2727–2736, 1998.

[33] S. D. Sintay, "Statistical Microstructure Generation and 3D Microstructure Geometry Extraction," *Materials Science*, 2010.

[34] K. Mohan, J. A. Sureh, P. Ramu, and R. Jayaganthan, "Microstructure and mechanical behaviour of AL 7075-T6 subjected to shallow cryogenic treatment," *ASM International*, vol. 25, no. 2, pp. 2185–2194, 2016.

[35] T. J. Harrison, B. R. Crawford, M. Janardhana, and G. Clark, "Differing microstructural properties of 7075-T6 sheet and 7075- T651 extruded aluminium alloy," *Procedia Engineering*, vol. 10, pp. 3117–3121, 2011.

[36] J. Harris, “Particle cracking damage evolution in 7075 wrought aluminium alloy under monotonic and cyclic loading conditions,” University of Georgia, 2005.

[37] J.K. Park and A.J. Ardell, “Microstructures of the Commercial 7075 Al Alloy in the T651 and T7 Tempers,” *Metallurgical Transactions A*, vol. 14A, 1983.

[38] L. K. Berg *et al.*, “GP-zones in Al-Zn-Mg alloys and their role in artificial aging,” *Acta Materialia*, vol. 49, no. 17, pp. 3443–3451, Oct. 2001.

[39] N. Birbilis and R. G. Buchheit, “Electrochemical Characteristics of Intermetallic Phases in Aluminum Alloys,” *Journal of The Electrochemical Society*, vol. 152, no. 4, p. B140, 2005.

[40] S. S. Singh, C. Schwartzstein, J. J. Williams, X. Xiao, F. De Carlo, and N. Chawla, “3D microstructural characterization and mechanical properties of constituent particles in Al 7075 alloys using X-ray synchrotron tomography and nanoindentation,” *Journal of Alloys and Compounds*, vol. 602, pp. 163–174, Jul. 2014.

[41] ASM International, “Microstructure of alloys Chapter 3,” *Aluminium Properties and Physical Metallurgy*, pp. 58–104, 1984.

[42] B.D. Obert, B. Obert, B.D. Obert, B. Obert, B.D. Obert, and B. Obert, “Quantification of Corrosion in 7075-T6 Aluminum Alloy,” *The Graduate Faculty of Texas Tech University*, p. 70, 2000.

[43] S. Suresh and R. O. Ritchie, “Propagation of short fatigue cracks,” *International Metals Reviews*, vol. 29, no. 1, pp. 445–475, 1984.

[44] N. E. Frost, K. J. Marsh, and L. P. Pook, *Metal Fatigue in Engineering - Fatigue Design Methods*, First. Mineola, New York: Dover Publications INC, 1999.

[45] S. Suresh, *Fatigue of Materials*, Second. Cambridge: University Press, 1998.

[46] R. I. Stephens, A. Fatemi, R. R. Stephens, and H. O. Fuchs, *Metal Fatigue in Engineering*, Second. Chichester: John Wiley & Sons, Inc, 2001.

[47] M. N. James, C. A. Boothroyd, J. H. Bulloch, and G. G. Garrett, “Facets on fatigue,” 1986, pp. 139–161.

[48] S.-S. Wang, G. S. Frankel, J.-T. Jiang, J.-F. Chen, S.-L. Dai, and L. Zhen, “Mechanism

of Localized Breakdown of 7000 Series Aluminum Alloys," *Journal of the Electrochemical Society*, vol. 160, no. 10, pp. C493–C502, 2013.

[49] A. Evangelou, "Oxidation-fatigue mechanisms at moderate service temperatures in single crystal turbine blade materials," University of Southampton, 2017.

[50] S. J. Maddox, "The effect of mean stress on fatigue crack propagation A literature review," *International Journal of Fracture*, vol. 1, no. 3, 1975.

[51] N. E. Frost, K. J. Marsh, and L. P. Pook, *Metal Fatigue in Engineering - Crack initiation*, First., vol. 1. Mineola, New York: Dover Publications INC, 1999.

[52] M. R. Bayoumi and A. K. Abdellatif, "Effect of surface finish on fatigue strength," *Engineering Fracture Mechanics*, vol. 51, no. 5, pp. 861–870, Jul. 1995.

[53] K. Tanaka and T. Mura, "A Theory of Fatigue Crack Initiation at Inclusions," *Metallurgical Transactions A*, vol. 13, no. 1, pp. 117–123, 1982.

[54] Tokaji k. and Ogawa T., "The growth behaviour of microstructurally small fatigue cracks in metals," *Mechanical Engineering Publications*, vol. 13, pp. 85–99, 1992.

[55] S. Pearson, "Initiation of fatigue cracks in commercial aluminium alloys and the subsequent propagation of very short cracks," *Engineering Fracture Mechanics*, vol. 7, pp. 235–247, 1975.

[56] Total Materia, "Fatigue Crack Initiation and Propagation in Al-Alloys :: Total Materia Article," *Total Materia*, 2008. [Online]. Available: https://www.totalmateria.com/page.aspx?ID=CheckArticle&site=ktn&NM=197. [Accessed: 14-Dec-2020].

[57] R. J. Bucci, ALCOA Technical Center, G. Nordmark, and E. A. Starke, "Selecting Aluminium Alloys to Resist Failure by Fracture Mechanisms," *ASM International*, vol. 19, pp. 771–812, 1996.

[58] J. D. Hochhalter, "Finite Element Simulations of Fatigue Crack Stages in AA 7075-T651," Cornell University, 2010.

[59] J. Payne, G. Welsh, R. J. Christ, J. Nardiello, and J. M. Papazian, "Observations of fatigue crack initiation in 7075-T651," *International Journal of Fatigue*, vol. 32, no. 2, pp.

247–255, Feb. 2010.

[60] E. A. DeBartolo and B. M. Hillberry, “A model of initial flaw sizes in aluminum alloys,” *International Journal of Fatigue*, vol. 23, no. SUPPL. 1, pp. 79–86, Jan. 2001.

[61] R. E. Zinkham, “Anisotropy and thickness effects in fracture of 7075-T6 and -T651 aluminum alloy,” *Engineering Fracture Mechanics*, vol. 1, no. 2, pp. 275–276, Aug. 1968.

[62] A. Turnbull and E. R. de los Rios, “The effect of grain size on the fatigue of commercially pure aluminium,” *Fatigue & Fracture of Engineering Materials and Structures*, vol. 18, no. 12, pp. 1455–1467, Dec. 1995.

[63] K. R. Trethewey and J. Chamberlain, *Corrosion for Science and Engineering*, Second. Essex: Longman Group Limited, 1988.

[64] R. A. Hays, “Corrosion Science Knowledge Area | WBDG Whole Building Design Guide,” 2017. [Online]. Available: https://www.wbdg.org/ffc/dod/cpc-source/corrosion-science-knowledge-area. [Accessed: 11-Dec-2017].

[65] PalmSens, “Polarization curve with Evan’s diagram,” *PalmSens Corrosion*, 2021. [Online]. Available: https://www.palmsenscorrosion.com/knowledgebase/tafel-plot-and-evans-diagram/polarization-curve-with-evans-diagram/. [Accessed: 01-Jan-2021].

[66] American Society for Metals, *Metals HandBook Volume 1*, 1st ed. Cleveland: American Society for Metals, 1961.

[67] Z. Ahmad, *Aluminium Alloys - New Trends in Fabrication and Applications*. InTech, 2012.

[68] C. A. Arriscorreta and D. W. Hoeppner, “Effects of prior corrosion and stress in corrosion fatigue of aluminum alloy 7075-T6,” *Corrosion*, vol. 68, no. 10, pp. 950–960, 2012.

[69] N. L. Sukiman *et al.*, *Durability and Corrosion of Aluminium and Its Alloys: Overview, Property Space, Techniques and Developments*. InTech, 2012.

[70] F. Andreatta, H. Terryn, and J. H. W. De Wit, “Corrosion behaviour of different tempers of AA7075 aluminium alloy,” *Electrochimica Acta*, vol. 49, no. 17–18, pp. 2851–2862,

2004.

[71] M. Gao, C. R. Feng, and R. P. Wei, “An Analytical Electron Microscopy Study of Constituent Particles in Commercial 7075-T6 and 2024-T3 Alloys,” *Metallurgical and Materials Transactions A*, vol. 29A, pp. 1147–1151, 1998.

[72] Q. Meng and G. S. Frankel, “Effect of Cu Content on Corrosion Behavior of 7xxx Series Aluminum Alloys,” *Journal of The Electrochemical Society*, vol. 151, no. 5, p. B271, 2004.

[73] N. Birbilis, M. K. Cavanaugh, and R. G. Buchheit, “Electrochemical behavior and localized corrosion associated with Al7Cu2Fe particles in aluminum alloy 7075-T651,” *Corrosion Science*, vol. 48, no. 12, pp. 4202–4215, 2006.

[74] P. K. Rout, M. M. Ghosh, and K. S. Ghosh, “Effect of Interrupted Ageing on Stress Corrosion Cracking (SCC) Behaviour of an Al-Zn-Mg-Cu Alloy,” *Procedia Materials Science*, vol. 5, pp. 1214–1223, Jan. 2014.

[75] S. Maitra and G. C. English, “Mechanism of Localized Corrosion of 7075 Alloy Plate,” *Metallurgic Transactions A*, vol. 12, no. 3, pp. 535–541, 1981.

[76] Z. Zhao and G. S. Frankel, “On the first breakdown in AA7075-T6,” *Corrosion Science*, vol. 49, pp. 3064–3088, 2007.

[77] Z. Zhao and G. S. Frankel, “The effect of temper on the first breakdown in AA7075,” *Corrosion Science*, vol. 49, pp. 3089–3111, 2007.

[78] D. W. Hoeppner and C. A. Arriscorreta, “Exfoliation corrosion and pitting corrosion and their role in fatigue predictive modeling: State-of-the-art review,” *International Journal of Aerospace Engineering*, vol. 2012, 2012.

[79] K. Jones and D. W. Hoeppner, “Pit-to-crack transition in pre-corroded 7075-T6 aluminum alloy under cyclic loading,” *Corrosion Science*, vol. 47, no. 9, pp. 2185–2198, Sep. 2005.

[80] K. A. Brandenburg, D. J. Hornbach, and P. W. Mason, “Use of Engineered Compressive Residual Stresses to Mitigate Stress Corrosion Cracking and Corrosion Fatigue in Sensitized 5XXX Series Aluminum Alloys,” in *Proceedings of Department of Defense*

Virtual Corrosion Conference, 2013.

[81] J. Z. Lu *et al.*, “Effects of laser peening on stress corrosion cracking (SCC) of ANSI 304 austenitic stainless steel,” *Corrosion Science*, vol. 60, pp. 145–152, Jul. 2012.

[82] J. T. Wang *et al.*, “Effects of laser shock peening on stress corrosion behavior of 7075 aluminum alloy laser welded joints,” *Materials Science and Engineering A*, vol. 647, pp. 7–14, Oct. 2015.

[83] A. Telang, A. S. Gill, S. Teysseyre, S. R. Mannava, D. Qian, and V. K. Vasudevan, “Effects of laser shock peening on SCC behavior of Alloy 600 in tetrathionate solution,” *Corrosion Science*, vol. 90, pp. 434–444, Jan. 2015.

[84] J. Yu, G. Gou, L. Zhang, W. Zhang, H. Chen, and Y. P. Yang, “Ultrasonic Impact Treatment to Improve Stress Corrosion Cracking Resistance of Welded Joints of Aluminum Alloy,” *Journal of Materials Engineering and Performance*, vol. 25, no. 7, pp. 3046–3056, Jul. 2016.

[85] R. Sundar *et al.*, “Mitigation of Stress Corrosion Cracking Susceptibility of Machined 304L Stainless Steel Through Laser Peening,” *Journal of Materials Engineering and Performance*, vol. 25, no. 9, pp. 3710–3724, Sep. 2016.

[86] M. V. Hyatt, “Effects of Residual Stresses on Stress Corrosion Crack Growth Rates in Aluminum Alloy,” *Corrosion*, vol. 26, no. 12, pp. 547–551, 1970.

[87] G. A. Hawkes, “Effect of shot peening on stress-corrosion properties and stress distribution in aluminium alloy d.t.d. 5054,” *British Corrosion Journal*, vol. 3, no. 5, pp. 258–261, 1968.

[88] U. Zupanc and J. Grum, “Effect of pitting corrosion on fatigue performance of shot-peened aluminium alloy 7075-T651,” *Journal of Materials Processing Technology*, vol. 210, no. 9, pp. 1197–1202, Jun. 2010.

[89] K. Y. Luo *et al.*, “Effects of laser shock peening with different coverage layers on fatigue behaviour and fractural morphology of Fe-Cr alloy in NaCl solution,” *Journal of Alloys and Compounds*, vol. 773, pp. 168–179, Jan. 2019.

[90] H. Wang, C. Ning, Y. Huang, Z. Cao, X. Chen, and W. Zhang, “Improvement of abrasion

resistance in artificial seawater and corrosion resistance in NaCl solution of 7075 aluminum alloy processed by laser shock peening," *Optics and Lasers in Engineering*, vol. 90, pp. 179–185, Mar. 2017.

[91] M. Abdulstaar, M. Mhaede, M. Wollmann, and L. Wagner, "Investigating the effects of bulk and surface severe plastic deformation on the fatigue, corrosion behaviour and corrosion fatigue of AA5083," *Surface and Coatings Technology*, vol. 254, pp. 244–251, Sep. 2014.

[92] W. Zhao *et al.*, "Improving the fretting and corrosion fatigue performance of 300M ultra-high strength steel using the ultrasonic surface rolling process," *International Journal of Fatigue*, vol. 121, pp. 30–38, Apr. 2019.

[93] H. Song, C. Liu, H. Zhang, X. Yang, Y. Chen, and S. B. Leen, "Experimental investigation on damage evolution in pre-corroded aluminum alloy 7075-T7651 under fatigue loading," *Materials Science and Engineering A*, vol. 799, p. 140206, Jan. 2021.

[94] K. Genel, "The effect of pitting on the bending fatigue performance of high-strength aluminum alloy," *Scripta Materialia*, vol. 57, no. 4, pp. 297–300, Aug. 2007.

[95] N. E. C. Co and J. T. Burns, "Effects of macro-scale corrosion damage feature on fatigue crack initiation and fatigue behavior," *International Journal of Fatigue*, vol. 103, pp. 234–247, Oct. 2017.

[96] S. Kim, J. T. Burns, and R. P. Gangloff, "Fatigue crack formation and growth from localized corrosion in Al-Zn-Mg-Cu," *Engineering Fracture Mechanics*, vol. 76, no. 5, pp. 651–667, Mar. 2009.

[97] J. T. Burns, J. M. Larsen, and R. P. Gangloff, "Driving forces for localized corrosion-to-fatigue crack transition in Al-Zn-Mg-Cu," *Fatigue and Fracture of Engineering Materials and Structures*, vol. 34, no. 10, pp. 745–773, 2011.

[98] K. Van Der Walde, J. R. Brockenbrough, B. A. Craig, and B. M. Hillberry, "Multiple fatigue crack growth in pre-corroded 2024-T3 aluminum," in *International Journal of Fatigue*, 2005, vol. 27, no. 10–12, pp. 1509–1518.

[99] X. D. Li, X. S. Wang, H. H. Ren, Y. L. Chen, and Z. T. Mu, "Effect of prior corrosion

state on the fatigue small cracking behaviour of 6151-T6 aluminum alloy," *Corrosion Science*, vol. 55, pp. 26–33, Feb. 2012.

[100] H. Song, C. Liu, H. Zhang, J. Du, X. Yang, and S. B. Leen, "In-situ SEM study of fatigue micro-crack initiation and propagation behavior in pre-corroded AA7075-T7651," *International Journal of Fatigue*, vol. 137, p. 105655, Aug. 2020.

[101] J. J. Medved, M. Breton, and P. E. Irving, "Corrosion pit size distributions and fatigue lives - A study of the EIFS technique for fatigue design in the presence of corrosion," *International Journal of Fatigue*, vol. 26, no. 1, pp. 71–80, Jan. 2004.

[102] D. W. Hammond and S. A. Meguid, "Crack propagation in the presence of shot-peening residual stresses," *Engineering Fracture Mechanics*, vol. 37, no. 2, pp. 373–387, Jan. 1990.

[103] P. J. Bouchard, "Residual Stresses in Lifetime and Structural Integrity Assessment," in *Encyclopedia of Materials: Science and Technology*, Elsevier, 2001, pp. 8134–8142.

[104] M. N. James, D. J. Hughes, D. G. Hattingh, G. Mills, and P. J. Webster, "Residual stress and strain in MIG butt welds in 5083-H321 aluminium: As-welded and fatigue cycled," *International Journal of Fatigue*, vol. 31, no. 1, pp. 28–40, Jan. 2009.

[105] N. Smyth, "Effect on Fatigue Performance of Residual Stress induced via Laser Shock Peening in Mechanically Damaged 2024 -T351 Alumin Cranfield, 2014.

[106] P. V Grant, J. D. Lord, P. S. Whitehead, National Physics Laboratory, and S. Ltd, "The Measurement of Residual Stresses by the Incremental Hole Drilling Technique," *Measurement Good Practice Guide*, vol. 53, no. 2, p. 63, 2006.

[107] K. Ding and L. Ye, "Physical and mechanical mechanisms of laser shock peening," in *Laser Shock Peening*, Elsevier, 2006, pp. 7–46.

[108] G. A. Webster and A. N. Ezeilo, "Residual stress distributions and their influence on fatigue lifetimes," *International Journal of Fatigue*, vol. 23, no. SUPPL. 1, pp. 375–383, Jan. 2001.

[109] C. You, "Fatigue lifing approaches for shot peened turbine components," University of

Southampton, 2017.

[110] T. S. Jun and A. M. Korsunsky, “Evaluation of residual stresses and strains using the Eigenstrain Reconstruction Method,” *International Journal of Solids and Structures*, vol. 47, no. 13, pp. 1678–1686, Jun. 2010.

[111] C. You, M. Achintha, K. A. Soady, N. Smyth, M. E. Fitzpatrick, and P. A. S. Reed, “Low cycle fatigue life prediction in shot-peened components of different geometries-part I: residual stress relaxation,” *Fatigue & Fracture of Engineering Materials & Structures*, vol. 40, no. 5, pp. 761–775, May 2017.

[112] S. Hashimi, *Comprehensive Materials Processing*. Amsterdam: Elsevier, 2014.

[113] A. . Eleiche, M. . Megahed, and N. . Abd-Allah, “The shot-peening effect on the HCF behavior of high-strength martensitic steels,” *Journal of Materials Processing Technology*, vol. 113, no. 1–3, pp. 502–508, Jun. 2001.

[114] M. Achintha, C. You, B. Y. He, K. Soady, and P. Reed, “Stress relaxation in shot-peened geometric features subjected to fatigue: Experiments and modelling,” *Advanced Materials Research*, vol. 996, pp. 729–735, 2014.

[115] A. Becker, “The Effect of Laser Shock Peening and Shot Peening on the Fatigue Performance of Aluminium Alloy 7075,” University of Cape Town, 2017.

[116] M. A. S. Torres and H. J. C. Voorwald, “An evaluation of shot peening, residual stress and stress relaxation on the fatigue life of AISI 4340 steel,” *International Journal of Fatigue*, vol. 24, pp. 877–886, 2002.

[117] P. Zhang and J. Lindemann, “Influence of shot peening on high cycle fatigue properties of the high-strength wrought magnesium alloy AZ80,” *Scripta Materialia*, vol. 52, no. 6, pp. 485–490, Mar. 2005.

[118] K. Shiozawa and L. Lu, “Very high-cycle fatigue behaviour of shot-peened high-carbon-chromium bearing steel,” *Fatigue and Fracture of Engineering Materials and Structures*, vol. 25, no. 8–9, pp. 813–822, 2002.

[119] K. A. Soady, B. G. Mellor, J. Shackleton, A. Morris, and P. A. S. Reed, “The effect of shot peening on notched low cycle fatigue,” *Materials Science and Engineering A*, vol.

528, no. 29–30, pp. 8579–8588, 2011.

[120] O. Hatamleh, J. Lyons, and F. Royce, “Laser peening and shot peening effects on fatigue life and surface roughness of friction stir welded 7075-T7351 aluminum,” *Journal of Chemical Information and Modeling*, vol. 53, no. 9, pp. 1689–1699, Mar. 2013.

[121] Y. K. Gao and X. R. Wu, “Experimental investigation and fatigue life prediction for 7475-T7351 aluminum alloy with and without shot peening-induced residual stresses,” *Acta Materialia*, vol. 59, no. 9, pp. 3737–3747, May 2011.

[122] M. Benedetti, V. Fontanari, M. Bandini, and E. Savio, “High- and very high-cycle plain fatigue resistance of shot peened high-strength aluminum alloys: The role of surface morphology,” *International Journal of Fatigue*, vol. 70, pp. 451–462, Jan. 2015.

[123] G. S. Was and R. M. Pelloux, “Effect of Shot Peening Methods on the Fatigue of Alloy 7075-T6,” *Metallurgic Transactions A*, vol. 10A, pp. 656–658, 1979.

[124] C. A. Rodopoulos, J. S. Romero, S. A. Curtis, E. R. De los Rios, and P. Peyre, “Effect of controlled shot peening and laser shock peening on the fatigue performance of 2024-T351 aluminum alloy,” *Journal of Materials Engineering and Performance*, vol. 12, no. 4, pp. 414–419, Aug. 2003.

[125] H. Luong and M. R. Hill, “The effects of laser peening and shot peening on high cycle fatigue in 7050-T7451 aluminum alloy,” *Materials Science and Engineering A*, vol. 527, no. 3, pp. 699–707, 2010.

[126] A. H. Clauer, “Laser Shock Peening, the Path to Production,” *Metals*, vol. 9, no. 6, p. 626, May 2019.

[127] K. Ding and L. (Lin) Ye, *Laser shock peening : performance and process simulations*. Woodhead, 2006.

[128] P. Liu, S. Sun, and J. Hu, “Effect of laser shock peening on the microstructure and corrosion resistance in the surface of weld nugget zone and heat-affected zone of FSW joints of 7050 Al alloy,” *Optics and Laser Technology*, vol. 112, pp. 1–7, Apr. 2019.

[129] A. Salimianrizi, E. Foroozmehr, M. Badrossamay, and H. Farrokhpour, “Effect of Laser Shock Peening on surface properties and residual stress of Al6061-T6,” *Optics and*

Lasers in Engineering, vol. 77, pp. 112–117, Feb. 2016.

[130] J. T. Wang *et al.*, “Effect of laser shock peening on the high-temperature fatigue performance of 7075 aluminum alloy,” *Materials Science and Engineering A*, vol. 704, pp. 459–468, Sep. 2017.

[131] O. Hatamleh, “The effects of laser peening and shot peening on mechanical properties in friction stir welded 7075-T7351 aluminum,” *Journal of Materials Engineering and Performance*, vol. 17, no. 281, pp. 688–694, 2008.

[132] U. Trdan, M. Skarba, and J. Grum, “Laser shock peening effect on the dislocation transitions and grain refinement of Al–Mg–Si alloy,” *Materials Characterization*, vol. 97, pp. 57–68, Nov. 2014.

[133] J. Z. Lu *et al.*, “Grain refinement of LY2 aluminum alloy induced by ultra-high plastic strain during multiple laser shock processing impacts,” *Acta Materialia*, vol. 58, no. 11, pp. 3984–3994, Jun. 2010.

[134] Y. Yang, K. Zhou, and G. Li, “Surface gradient microstructural characteristics and evolution mechanism of 2195 aluminum lithium alloy induced by laser shock peening,” *Optics and Laser Technology*, vol. 109, pp. 1–7, Jan. 2019.

[135] Y. Sano, K. Akita, K. Masaki, Y. Ochi, I. Altenberger, and B. Scholtes, “Laser Peening without Coating as a Surface Enhancement Technology,” *JLMN-Journal of Laser Micro/Nanoengineering*, vol. 1, no. 3, 2006.

[136] U. U. Trdan, J. A. Porro, J. L. Ocaña, and J. Grum, “Laser shock peening without absorbent coating (LSPwC) effect on 3D surface topography and mechanical properties of 6082-T651 Al alloy,” *Surface and Coatings Technology*, vol. 208, no. 15, pp. 109–116, 2012.

[137] U. Trdan and J. Grum, “SEM/EDS characterization of laser shock peening effect on localized corrosion of Al alloy in a near natural chloride environment,” *Corrosion Science*, vol. 82, pp. 328–338, May 2014.

[138] D. Karthik and S. Swaroop, “Laser peening without coating—an advanced surface treatment: A review,” *Materials and Manufacturing Processes*, vol. 32, no. 14, pp. 1565–

1572, Oct. 2017.

[139] H. Amar *et al.*, “Influence of the microstructure and laser shock processing (LSP) on the corrosion behaviour of the AA2050-T8 aluminium alloy,” *Corrosion Science*, vol. 53, no. 10, pp. 3215–3221, Oct. 2011.

[140] Y. K. Gao, “Improvement of fatigue property in 7050–T7451 aluminum alloy by laser peening and shot peening,” *Materials Science and Engineering: A*, vol. 528, no. 10–11, pp. 3823–3828, Apr. 2011.

[141] A. H. Clauer and D. F. Lahrman, “Laser shock processing as a surface enhancement process,” *Key Engineering Materials*, vol. 197, pp. 121–142, 2001.

[142] P. Peyre and R. Fabbro, “Laser shock processing: a review of the physics and applications,” *Optical and Quantum Electronics*, vol. 27, no. 12. Kluwer Academic Publishers, pp. 1213–1229, Dec-1995.

[143] M. Dorman, M. B. Toparli, N. Smyth, A. Cini, M. E. Fitzpatrick, and P. E. Irving, “Effect of laser shock peening on residual stress and fatigue life of clad 2024 aluminium sheet containing scribe defects,” *Materials Science and Engineering A*, vol. 548, pp. 142–151, Jun. 2012.

[144] S. Zabeen, K. Langer, and M. E. Fitzpatrick, “Effect of alloy temper on surface modification of aluminium 2624 by laser shock peening,” *Surface and Coatings Technology*, vol. 347, no. March, pp. 123–135, 2018.

[145] M. Abeens, R. Muruganandhan, K. Thirumavalavan, and S. Kalainathan, “Surface modification of AA7075 T651 by laser shock peening to improve the wear characteristics,” *Materials Research Express*, vol. 6, no. 6, pp. 1–13, Mar. 2019.

[146] A. K. Gujba and M. Medraj, “Laser peening process and its impact on materials properties in comparison with shot peening and ultrasonic impact peening,” *Materials*, vol. 7, no. 12. MDPI AG, pp. 7925–7974, 10-Dec-2014.

[147] Q. Liu, C. H. Yang, K. Ding, S. A. Barter, and L. Ye, “The effect of laser power density on the fatigue life of laser-shock-peened 7050 aluminium alloy,” *Fatigue & Fracture of Engineering Materials and Structures*, vol. 30, no. 11, pp. 1110–1124, Nov. 2007.

[148] B. P. Fairand, B. A. Wilcox, W. J. Gallagher, and D. N. Williams, “Laser shock-induced microstructural and mechanical property changes in 7075 aluminum,” *Journal of Applied Physics*, vol. 43, no. 9, pp. 3893–3895, 1972.

[149] M. Suraratchai, J. Limido, C. Mabru, and R. Chieragatti, “Modelling the influence of machined surface roughness on the fatigue life of aluminium alloy,” *International Journal of Fatigue*, vol. 30, no. 12, pp. 2119–2126, Dec. 2008.

[150] R. Hidalgo *et al.*, “Influence of Surface Finish and Porosity on the Fatigue behaviour of A356 Aluminium Casting Alloy.”

[151] R. G. Bodiford, “An investigation of the effect of surface finish on the flexure fatigue strength of 75S-T6 aluminium alloy sheet,” Georgia Institute of Technology, 1949.

[152] Z. Yongkang, Z. Shuyi, Z. Xiaorong, C. Lan, Y. Jichang, and R. Naifei, “Investigation of the surface qualities of laser shock-processed zones and the effect on fatigue life of aluminum alloy,” *Surface and Coatings Technology*, vol. 92, no. 1–2, pp. 104–109, Jun. 1997.

[153] M. Shahzad, M. Chaussumier, R. Chieragatti, C. Mabru, F. Rezai-Aria, and F. Rezai Aria, “Influence of surface treatments on fatigue life of Al 7010 alloy,” *Journal of Materials Processing Technology*, vol. 210, no. 13, pp. 1821–1826, 2010.

[154] J. Grum, U. Trdan, and M. R. Hill, “Laser shock processing of ENAW 6082 aluminium alloy surface,” *Materials Science Forum*, vol. 589, pp. 379–384, 2008.

[155] X. Q. Q. Zhang *et al.*, “Investigation on effect of laser shock processing on fatigue crack initiation and its growth in aluminum alloy plate,” *Materials & Design (1980-2015)*, vol. 65, pp. 425–431, Jan. 2015.

[156] H. Luong and M. R. Hill, “The effects of laser peening on high-cycle fatigue in 7085-T7651 aluminum alloy,” *Materials Science and Engineering A*, vol. 477, no. 1–2, pp. 208–216, 2008.

[157] O. Hatamleh, J. Lyons, and R. Forman, “Laser peening and shot peening effects on fatigue life and surface roughness of friction stir welded 7075-T7351 aluminum,” *Fatigue and Fracture of Engineering Materials and Structures*, vol. 30, no. 2, pp. 115–

130, 2007.

[158] A. M. Mostafa, M. F. Hameed, and S. S. Obayya, “Effect of laser shock peening on the hardness of AL-7075 alloy,” *Journal of King Saud University - Science*, vol. 31, no. 4, pp. 472–478, Oct. 2019.

[159] A. H. Clauer, C. T. Walters, and S. C. Ford, “The Effects of Laser Shock Processing on the Fatigue Properties of 2024-T3 Aluminum | Request PDF,” in *ASM Conference on Lasers in Materials Processing*, 1986, pp. 7–22.

[160] F. J. Carpio *et al.*, “Fatigue behaviour of laser machined 2024 T3 aeronautic aluminium alloy,” *Applied Surface Science*, vol. 208–209, no. 1, pp. 194–198, Mar. 2003.

[161] Q. Liu, “An Effective Life Extension Technology for 7xxx Series Aluminium Alloys by Laser Shock Peening (Final Report),” Victoria, Australia, 2008.

[162] A. H. Clauer, “Laser shock processinng increases fatigue life of metal parts,” *Materials and processing report*, vol. 6, no. 6, pp. 3–5, 1991.

[163] K. Shiozawa, L. Lu, and S. Ishihara, “S-N curve characteristics and subsurface crack initiation behaviour in ultra-long life fatigue of a high carbon-chromium bearing steel,” *Fatigue and Fracture of Engineering Materials and Structures*, vol. 24, no. 12, pp. 781–790, Dec. 2001.

[164] K. Shiozawa, Y. Morii, S. Nishino, and L. Lu, “Subsurface crack initiation and propagation mechanism in high-strength steel in a very high cycle fatigue regime,” *International Journal of Fatigue*, vol. 28, no. 11, pp. 1521–1532, Nov. 2006.

[165] K. Oguri, “Fatigue life enhancement of aluminum alloy for aircraft by Fine Particle Shot Peening (FPSP),” *Journal of Materials Processing Technology*, vol. 211, no. 8, pp. 1395–1399, Aug. 2011.

[166] S.-L. Lv, Y. Cui, X. Gao, and T. S. Srivatsan, “Influence of exposure to aggressive environment on fatigue behavior of a shot peened high strength aluminum alloy,” *Materials Science and Engineering A*, vol. 574, pp. 243–252, Jul. 2013.

[167] P. Peyre, V. Vignal, H. Amar, H. Song, H. Pelletier, and V. Ji, “Modification of the electrochemical properties of 2050-T8 aluminium alloys by a LSP surface treatment,”

p. 116, 2009.

[168] H. Krawiec, V. Vignal, H. Amar, and P. Peyre, “Local electrochemical impedance spectroscopy study of the influence of ageing in air and laser shock processing on the micro-electrochemical behaviour of AA2050-T8 aluminium alloy,” in *Electrochimica Acta*, 2011, vol. 56, no. 26, pp. 9581–9587.

[169] U. Trdan and J. Grum, “Investigation of corrosion behaviour of aluminium alloy subjected to laser shock peening without a protective coating,” *Advances in Materials Science and Engineering*, vol. 2015, p. 9, 2015.

[170] U. Trdan and J. Grum, “Evaluation of corrosion resistance of AA6082-T651 aluminium alloy after laser shock peening by means of cyclic polarisation and ElS methods,” *Corrosion Science*, vol. 59, pp. 324–333, 2012.

[171] U. Trdan, J. L. Ocaña, and J. Grum, “Surface Modification of Aluminium Alloys with Laser Shock Processing,” *Journal of mechanical engineering*, vol. 57, no. 5, pp. 385–393, 2010.

[172] S. Zagar and J. Grum, “Roughness, residual stresses and pitting corrosion effect on shot peened AA 7075,” *Technical Gazzette*, vol. 22, no. 6, pp. 1589–1595, 2015.

[173] ASM Aerospace Specification Metals Inc., “Aluminium 7075-T6; 7075-T651,” *MatWeb*, 2001. [Online]. Available: http://asm.matweb.com/search/SpecificMaterial.asp?bassnum=MA7075T6. [Accessed: 03-Jan-2020].

[174] University of Columbia, *Practical residual stress measurement methods*, 1st ed., vol. 1, no. 1. Vancouver: University of Columbia, 2013.

[175] S. A. Niknam and V. Songmene, “Deburring and edge finishing of aluminum alloys: A review,” in *Proceedings of the 12th International Aluminum conference (INALCO)*, 2013.

[176] D. Glaser *et al.*, “Evaluation of Residual Stresses Introduced by Laser Shock Peening in Steel using Different Measurement Techniques,” in *Mechanical Stress Evaluation by Neutron and Synchrotron Radiation*, 2018, vol. 4, pp. 45–50.

[177] J. Schindelin *et al.*, “Fiji: an open-source platform for biological-image analysis,” *Nature Methods*, vol. 9, no. 7, pp. 676–682, Jul. 2012.

[178] I. Arganda-Carreras *et al.*, “Trainable Weka Segmentation: a machine learning tool for microscopy pixel classification,” *Bioinformatics*, vol. 33, no. 15, pp. 2424–2426, Aug. 2017.

[179] W. Kapłonek, K. Nadolny, and G. M. Królczyk, “The Use of Focus-Variation Microscopy for the Assessment of Active Surfaces of a New Generation of Coated Abrasive Tools,” *Measurement Science Review*, vol. 16, no. 2, pp. 42–53, 2016.

[180] Alicona, “Alicona - High-resolution optical 3D measurement.” [Online]. Available: https://www.alicona.com/focus-variation/. [Accessed: 02-Sep-2018].

[181] S. Singh, Y. Guo, B. Winiarski, T. L. Burnett, P. J. Withers, and M. De Graef, “High resolution low kV EBSD of heavily deformed and nanocrystalline Aluminium by dictionary-based indexing,” *Scientific Reports*, vol. 8, no. 1, p. 10991, Dec. 2018.

[182] F. J. Humphreys, “Grain and subgrain characterisation by electron backscatter diffraction,” *Journal of Materials Science*, vol. 36, no. 16. Springer, pp. 3833–3854, 15-Aug-2001.

[183] Oxford Instruments HKL, “CHANNEL 5,” Denmark, 2007.

[184] F. Bachmann, R. Hielscher, and H. Schaeben, “Grain detection from 2d and 3d EBSD data-Specification of the MTEX algorithm,” *Ultramicroscopy*, vol. 111, no. 12, pp. 1720–1733, Dec. 2011.

[185] E. Broitman, “Indentation Hardness Measurements at Macro-, Micro-, and Nanoscale: A Critical Overview,” *Tribology Letters*, vol. 65, no. 23, 2017.

[186] T. O. Mbuya, “Analysis of microstructure and fatigue micromechanisms in cast aluminium piston alloys,” University of Southampton, 2011.

[187] Y. Zhao *et al.*, “3D Characterisation of the Fe-rich intermetallic phases in Al-5%Cu alloys by synchrotron X-ray microtomography and skeletonisation,” *Scripta Materialia*, vol. 146, no. 15, pp. 321–326, 2018.

[188] E. N. Landis and D. T. Keane, “X-ray microtomography,” *Materials Characterization*,

vol. 61, no. 12, pp. 1305–1316, Dec. 2010.

[189] Instron, “Instron Bluehill 3 Testing Software - Instron.” [Online]. Available: http://www.instron.co.uk/en-gb/products/materials-testing-software/bluehill-software. [Accessed: 14-Oct-2018].

[190] “Aluminum 7075-T6; 7075-T651.” [Online]. Available: http://www.matweb.com/search/DataSheet.aspx?MatGUID=4f19a42be94546b686bbf43f79c51b7d&ckck=1. [Accessed: 16-Nov-2020].

[191] S. . Curtis, J. S. Romero, E. . de los Rios, C. . Rodopoulos, and A. Levers, “Predicting the interfaces between fatigue crack growth regimes in 7150-T651 aluminium alloy using the fatigue damage map,” *Materials Science and Engineering: A*, vol. 344, no. 1–2, pp. 79–85, Mar. 2003.

[192] G. Ivetic *et al.*, “Characterisation of fatigue and crack propagation in laser shock peened open hole 7075-T73 aluminium specimens,” in *ICAF 2011 Structural Integrity: Influence of Efficiency and Green Imperatives - Proceedings of the 26th Symposium of the International Committee on Aeronautical Fatigue*, 2011, pp. 855–866.

[193] M. Mhaede, Y. Sano, I. Altenberger, and L. Wagner, “Fatigue Performance of Al7075-T73 and Ti-6Al-4V : Comparing Results after Shot Peening , Laser Shock Peening and Ball- Burnishing,” *Proc. Shot peening - ICSP11*, pp. 2–7, 2011.

[194] U. Zupanc and J. Grum, “Surface integrity of shot peened aluminium alloy 7075-T651,” *Strojniski Vestnik/Journal of Mechanical Engineering*, vol. 57, no. 5, pp. 379–384, 2011.

[195] V. Pandey, J. K. K. Singh, K. Chattopadhyay, N. C. C. S. S. Srinivas, and V. Singh, “Influence of ultrasonic shot peening on corrosion behavior of 7075 aluminum alloy,” *Journal of Alloys and Compounds*, vol. 723, pp. 826–840, Nov. 2017.

[196] T. R. Simes, S. G. Mellor, and D. A. Hills, “A note on the influence of residual stress on measured hardness,” *The Journal of Strain Analysis for Engineering Design*, vol. 19, no. 2, pp. 135–137, Apr. 1984.

[197] T. Y. Tsui, W. C. Oliver, and G. M. Pharr, “Influences of stress on the measurement of mechanical properties using nanoindentation: Part I. Experimental studies in an

aluminum alloy," *Journal of Materials Research*, vol. 11, no. 3, pp. 752–759, 1996.

[198] M. K. Khan, M. E. Fitzpatrick, S. V. Hainsworth, and E. L., "Effect of residual stress on the nanoindentation response of aerospace aluminium alloys," *Computational Materials Science*, vol. 50, no. 10, pp. 2967–2976, Aug. 2011.

[199] M. K. Khan, M. E. Fitzpatrick, S. V. Hainsworth, A. D. Evans, and L. Edwards, "Application of synchrotron X-ray diffraction and nanoindentation for the determination of residual stress fields around scratches," *Acta Materialia*, vol. 59, no. 20, pp. 7508–7520, Dec. 2011.

[200] A. G. Sanchez *et al.*, "Effects of laser shock peening on the mechanisms of fatigue short crack initiation and propagation of AA7075-T651," *International Journal of Fatigue*, vol. 143, p. 106025, Feb. 2021.

[201] N. E. DOWLING, C. A. CALHOUN, and A. ARCARI, "Mean stress effects in stress-life fatigue and the Walker equation," *Fatigue & Fracture of Engineering Materials & Structures*, vol. 32, no. 3, pp. 163–179, Mar. 2009.

[202] T. Zhao and Y. Jiang, "Fatigue of 7075-T651 aluminum alloy," *International Journal of Fatigue*, vol. 30, no. 5, pp. 834–849, 2008.

[203] S. P. Lynch, "Progression markings, striations, and crack-arrest markings on fracture surfaces," *Materials Science and Engineering A*, vol. 468–470, no. SPEC. ISS., pp. 74–80, Nov. 2007.

[204] T. J. Stannard, J. J. Williams, S. S. Singh, A. S. Sundaram Singaravelu, X. Xiao, and N. Chawla, "3D time-resolved observations of corrosion and corrosion-fatigue crack initiation and growth in peak-aged Al 7075 using synchrotron X-ray tomography," *Corrosion Science*, vol. 138, pp. 340–352, Jul. 2018.

[205] A. S. S. Singaravelu *et al.*, "3D Time-Resolved Observations of Fatigue Crack Initiation and Growth from Corrosion Pits in Al 7XXX Alloys Using In Situ Synchrotron X-ray Tomography," *Metallurgical and Materials Transactions A: Physical Metallurgy and Materials Science*, vol. 51, no. 1, pp. 28–41, Jan. 2020.

[206] B. Y. He, K. a Soady, B. G. Mellor, a Morris, and P. a S. Reed, "Effects of shot peening

on short crack growth rate and resulting low cycle fatigue behaviour in low pressure turbine blade material," *Materials Science and Technology*, vol. 29, no. 7, pp. 788–796, 2013.

[207] X. Liu and G. S. Frankel, "Effects of compressive stress on localized corrosion in AA2024-T3," *Corrosion Science*, vol. 48, no. 10, pp. 3309–3329, 2006.

[208] B. M. H. M. Elkandari, "Excimer Laser Surface Melting Treatment on 7075-T6 Aluminium Alloy for Improved Corrosion Resistance," University of Manchester, 2012.

[209] C. P. Chan, T. M. Yue, and H. C. Man, "The effect of excimer laser surface treatment on the pitting corrosion fatigue behaviour of aluminium alloy 7075," *Journal of Materials Science*, vol. 38, no. 12, pp. 2689–2702, Jul. 2003.

[210] M. M. Pariona, V. Teleginski, K. Dos Santos, E. L. R. Dos Santos, A. A. De Oliveira Camargo De Lima, and R. Riva, "AFM study of the effects of laser surface remelting on the morphology of Al-Fe aerospace alloys," *Materials Characterization*, vol. 74, pp. 64–76, Dec. 2012.

[211] K. D. Ralston, D. Fabijanic, and N. Birbilis, "Effect of grain size on corrosion of high purity aluminium," *Electrochimica Acta*, vol. 56, no. 4, pp. 1729–1736, Jan. 2011.

[212] F. A. Almuaili, S. A. McDonald, P. J. Withers, A. B. Cook, and D. L. Engelberg, "Strain-induced reactivation of corrosion pits in austenitic stainless steel," *Corrosion Science*, vol. 125, pp. 12–19, Aug. 2017.

[213] F. A. Almuaili, S. A. McDonald, P. J. Withers, and D. L. Engelberg, "Application of a Quasi In Situ Experimental Approach to Estimate 3-D Pitting Corrosion Kinetics in Stainless Steel," *Journal of The Electrochemical Society*, vol. 163, no. 13, pp. C745–C751, Sep. 2016.

[214] S. P. Knight, M. Salagaras, A. M. Wythe, F. De Carlo, A. J. Davenport, and A. R. Trueman, "In situ X-ray tomography of intergranular corrosion of 2024 and 7050 aluminium alloys," *Corrosion Science*, vol. 52, no. 12. Pergamon, pp. 3855–3860, 01-Dec-2010.

[215] M. Ghahari *et al.*, "Synchrotron X-ray radiography studies of pitting corrosion of

stainless steel: Extraction of pit propagation parameters," *Corrosion Science*, vol. 100, pp. 23–35, 2015.

[216] B. J. Connolly *et al.*, "X-ray microtomography studies of localised corrosion and transitions to stress corrosion cracking X-ray microtomography studies of localised corrosion and transitions to stress corrosion cracking," *Materials Science and Technology*, vol. 22, no. 9, pp. 1076–1085, 2013.

[217] W. Tian, S. Li, B. Wang, J. Liu, and M. Yu, "Pitting corrosion of naturally aged AA 7075 aluminum alloys with bimodal grain size," *Corrosion Science*, vol. 113, pp. 1–16, Dec. 2016.

[218] N. Easter Cruz Co, "The Effect of Corrosion Damage Morphology on fatigue Crack Initiation and Small Crack Propagation of AA70750-T7451," 2018.

[219] R. Bonzom and R. Oltra, "Droplet cell investigation of intergranular corrosion on AA2024," *Electrochemistry Communications*, vol. 81, no. October, pp. 84–87, 2017.

[220] X. Zhao, G. S. Frankel, B. Zoofan, and S. I. Rokhlin, "In Situ X-Ray Radiographic Study of Intergranular Corrosion in Aluminum Alloys," no. November, pp. 1012–1018, 2003.

[221] M. Doube *et al.*, "BoneJ: Free and extensible bone image analysis in ImageJ," *Bone*, vol. 47, no. 6, pp. 1076–1079, 2010.

[222] M. De Graef, "A dictionary indexing approach for EBSD," *IOP Conference Series: Materials Science and Engineering*, vol. 891, p. 012009, Aug. 2020.

[223] H. M. Flower, *High Performance Materials in Aerospace*, 1st ed. London: Chapman * Hall, 1995.

[224] M. J. Starink and S. C. Wang, "A Model for the Yield Strength of Overaged Al-Zn-Mg-Cu Alloys," 2003.

[225] R. Mächler, P. J. Uggowitzer, C. Solenthaler, R. M. Pedrazzoli, and M. O. Speidel, "Structure, mechanical properties, and stress corrosion behaviour of high strength spray deposited 7000 series aluminium alloy," *Materials Science and Technology*, vol. 7, no. 5, pp. 447–451, May 1991.

[226] T. Engdahl, V. Hansen, P. J. Warren, and K. Stiller, "Investigation of fine scale

precipitates in Al-Zn-Mg alloys after various heat treatments," 2002.

[227] T. S. Srivatsan, S. Sriram, D. Vee Raraghavan, V. K. Va, and S. Evan, "Microstructure, tensile properties and fracture behaviour of aluminium alloy 7150," *Journal of Materials Science*, vol. 27, pp. 4772–4781, 1992.

[228] C. Stampfl, M. Veronica Ganduglia-Pirovano, K. Reuter, and M. Scheffler, "Catalysis and corrosion: the theoretical surface-science context," *Surface Science*, vol. 500, no. 1–3, pp. 368–394, Mar. 2002.

[229] University of Cambridge, "DoITPoMS - TLP Library Kinetics of Aqueous Corrosion." [Online]. Available: https://www.doitpoms.ac.uk/tlplib/aqueous_corrosion/index.php. [Accessed: 22-Feb-2018].

9 Appendices

9.1 Appendix A: Literature review

9.1.1 Appendix A1: 7XXX aluminium alloys

9.1.1.1 Manufacturing steps

The first step is casting, where the aluminium alloy's chemical composition is created. The solidification process can lead to micro and macro segregation as well as the formation of insoluble coarse particles (often containing unwanted iron or silicon). Homogenization, typically carried out at 450 – 500°C is performed to eliminate micro-scale segregation from casting. In this step, dispersoids particles are also formed from elements such as Cr, Mg and Zr. These dispersoids reduce grain growth and inhibit recrystallisation in the following manufacturing steps. The next step, hot rolling, could also be replaced by forging or extrusion, but for simplicity only hot rolling will be discussed. This step is used to change the common 1 m thickness casts into a more manageable thickness. This tends to leave elongated pancake grain structures. Coarse particles tend to be pre-cracked during hot rolling, as well as dispersed in the rolling direction as stringers. These particles have detrimental effects on fatigue and corrosion performance and are discussed in more detail in the following sections. Dynamic recovery also occurs during hot rolling, where dislocations re-arrange themselves into sub-grains. Some recrystallisation also occurs, where grains nucleate and grow within deformed grains. Following rolling, the solution treatment step (at approx. 480°C) dissolves particles from past processing steps. Some further recovery or recrystallisation can occur, and thus there is a compromise to be had between dissolving as many undesirable soluble particles as possible whilst minimising grain nucleation and growth as recrystallised grains are considered undesirable for fatigue performance. The next step, quenching, produces a super-saturated solid solution which will subsequently form strengthening precipitates. It is often performed rapidly to increase the subsequent nucleation of fine scale strengthening particles η' (semi-coherent $MgZn_2$) whilst minimising the formation of coarse precipitates η (incoherent $MgZn_2$) and diffusion of strengthening particles into grain boundaries. The former (η) decreases the effectiveness of strengthening precipitates and therefore alloy strength, whilst the latter ($MgZn_2$ in grain boundaries) promotes intergranular corrosion. The final step is 'ageing', typically done at 100 – 200°C, where the size and spacing of the nucleated

precipitates varies due to growth and coherent precipitates ($MgZn_2$) become semi-coherent (but can also become incoherent) to the aluminium matrix, and there is an overall increase in precipitate volume fraction [27][41][54].

9.1.1.2 7XXX Strengthening precipitates

GP zones can also precipitate into semi coherent T' and equilibrium T precipitates, which are $Mg_{32}(Al, Zn)_{49}$ and irregular in morphology, unlike the platelet shaped η precipitates [223]. Nevertheless, T precipitates occur at ageing temperatures in excess of 200°C and thus are not generally thought to contribute to strengthening commercial alloys as these are aged at temperatures below 180 °C [224]. T6, peak aged, and T7, over-aged, are some of the most common ageing tempers used in the aerospace industry. Recent work indicates that for T6 the main precipitates phases are a mixture of η' and η, whilst in T7 the main precipitate is η [225][226]. However, Srivatsan [227] found AA7150-T77 strengthening precipitates were mainly semi-coherent η' with few equilibrium η precipitates in the matrix and grain boundaries.

9.1.2 Appendix A2: Fatigue theory

9.1.2.1 Strain life approach

The strain life approach is found to be more appropriate when significant plastic deformation occurs. Here stresses are high enough to cause plastic deformation, particularly around stress concentrations. The Coffin-Mason relationship indicates a power law relationship between the fatigue life and plastic strain [45]:

Equation 9-1:

$$\frac{\Delta \boldsymbol{E_p}}{\mathbf{2}} = \boldsymbol{\varepsilon_f'}(\mathbf{2}\boldsymbol{N_f})^{\boldsymbol{c}}$$

Where ε_f' is known as the fatigue ductility coefficient and c is the fatigue ductility exponent.

The elastic strain amplitude must be included to use the strain life approach:

Equation 9-2:

$$\frac{\Delta \boldsymbol{\varepsilon}}{\mathbf{2}} = \frac{\Delta \boldsymbol{\varepsilon_e}}{\mathbf{2}} + \frac{\Delta \boldsymbol{\varepsilon_p}}{\mathbf{2}}$$

The elastic strain is expressed in terms of a modified Basquin equation:

Equation 9-3:

$$\frac{\Delta\varepsilon_e}{2} = \frac{\sigma_f'}{E}(2N_f)^b$$

Where E is the Young Modulus, as:

Equation 9-4:

$$\frac{\Delta\varepsilon_e}{2} = \frac{\Delta\sigma}{2E} = \frac{\Delta\sigma_a}{E}$$

By combining the contributions from both the elastic and the plastic strain ranges, we reach the equation of which the strain life approach is based:

Equation 9-5:

$$\frac{\Delta\boldsymbol{\varepsilon}}{\mathbf{2}} = \frac{\boldsymbol{\sigma_f'}}{\mathbf{2}}(\mathbf{2}\boldsymbol{N_f})^{\boldsymbol{b}} + \boldsymbol{\varepsilon_f'}(\mathbf{2}\boldsymbol{N_f})^{\boldsymbol{c}}$$

9.1.3 Appendix A3: Corrosion theory

9.1.3.1 Fundamental theory

Corrosion can take place in various environments such as in the atmosphere, in solution and in the soil. The basic mechanism involves removal of valence electrons from the metal atoms, which become cations that transfer into the adjacent solution, and then often more stable compounds such as iron oxide (commonly termed rust) may form. This basic mechanism is called an anodic reaction, and for the corrosion process to proceed there must be a corresponding cathodic reaction that accepts the electrons. Corrosion of a metal brings it to its thermodynamic ground state under the existing environmental conditions [228].

Oxidation is the removal of electrons from a species, a reduction is the addition of electrons, and a redox reaction is a reaction in which there is transfer of electrons from one species to another. The electron transfer may be accompanied by other events, such as atom or ion transfer, but the net effect is electron transfer and hence a change in oxidation number of an element [63]. In simple terms, the anode is where oxidation occurs.

9.1.3.2 Gibbs free energy and cell potential relationship

A cell in which the overall cell reaction has yet to achieve chemical equilibrium can do electrical work as the reaction drives electron flow. When a spontaneous reaction takes place in a Galvanic cell, electrons are 'deposited' in one electrode (anode) and collected from another (cathode), and so there is a net current which can be used to do electrical work, W_e. From thermodynamics the maximum electrical work done ($W_{e,max}$) at constant temperature and pressure is equal to the change in electrochemical Gibbs energy for the net reaction: ΔG. The relationship between the electrochemical Gibbs (free) energy of the reaction and the cell potential is:

Equation 9-6:

$$\Delta \boldsymbol{G} = -zFE_{cell}$$

Where, F is the Faraday constant (units: 96485 C mol^{-1}), E_{cell} is the electrical potential of the cell, and z is the stoichiometric coefficient of the electrons in the half-cell reactions into which the cell reaction can be divided. This is the key expression connecting electrical measurements and thermodynamic properties. It follows from this equation that a negative reaction Gibbs energy corresponds to a spontaneous cell reaction [63].

9.1.3.3 Kinetics of corrosion reactions

Consider the generalised electrochemical reaction (a simple electrode process):

$$\mathrm{R} \rightleftharpoons \mathrm{O} + \mathrm{ze}^{-}$$

A chemical reaction such as this one increase its reaction rate increase if the temperature is increased. This temperature – reaction relationship is expressed in the Arrhenius equation [63][229] :

Equation 9-7:

$$k = Ae^{\frac{-G^{\ddagger}}{RT}}$$

Where k is the rate constant, T is the absolute temperature, A is a constant, $G^{\ddagger}$ is the activation energy and R is the universal gas constant. The activation energy is the minimum energy required for a corrosion reaction to happen.

The symbol for polarisation is usually η. To differentiate this from the 7XXX series alloys age precipitates (eta). The symbol for polarisation will be η_p:

Equation 9-8:

$$\eta_{\mathrm{p}} = E - E_0$$

Where E_0 is the equilibrium potential of the reaction.

The overall effect of polarisation is to lower the activation energy ($G^{\ddagger}$) of the forward (anodic) reaction by '$G = \alpha z F \eta_{\mathrm{p}}$' [63][229]. Thus, Equation 9-7 can be re-written to add the new activation energy caused by the overpotential:

Equation 9-9:

$$k = Ae^{\left(\frac{-\Delta G^{\ddagger} + \alpha z F \eta_p}{RT}\right)}$$

Where α is the transfer coefficient (note that α will exhibit values between 0 and 1, and in many cases it is usually taken as 0.5) for the anodic process. Note that for the cathodic process α would be replaced by '1-α' [63].

Equation 9-9 can be modified as follows:

$$k = \mathrm{A}\mathrm{e}^{\left(\frac{-\Delta \mathrm{G}^{\ddagger}}{RT}\right)}\mathrm{e}^{\left(\frac{\alpha z F \eta_{\mathrm{p}}}{RT}\right)}$$

If we introduce k_0, the reaction rate at equilibrium conditions, where:

Equation 9-10:

$$k_0 = Ae^{\left(\frac{-\Delta G^{\ddagger}}{RT}\right)}$$

We can introduce Equation 9-10 into Equation 9-9:

Equation 9-11:

$$k = k_0 \mathrm{e}^{\left(\frac{\alpha z F \eta_{\mathrm{p}}}{RT}\right)}$$

The electrochemical chemical reaction involves the release of electrons. The magnitude of the heterogeneous electrochemical rate constant is strongly influenced by the magnitude of the applied potential at the metal electrode. Equation 9-11 can be expressed either in terms of a rate constant or in terms of a current density ($j, \mathrm{A\ cm^{-2}}$), where '$j = zFk$'. Thus:

Equation 9-12:

$$j = i_0 e^{\left(\frac{\alpha z F \eta_p}{RT}\right)}$$

Where j_0 is the exchange current density, which is the current density flowing in both directions (cathodic and anodic current) at equilibrium conditions, per unit area. This tells us that current density can be a direct measure for the rate of corrosion reaction [63][229].

If we want to measure the electrochemical cell's current in an experiment, which is equal to the anodic current minus the cathodic current (the cathodic current would be running in the opposite direction the anodic current) we can apply Equation 9-12 into Equation 9-13, as follows:

Equation 9-13:

$$j_{\mathrm{m}} = j_{\mathrm{a}} - j_{\mathrm{c}}$$

Where i_{m} is the current density measured experimentally in an electrochemical cell, j_{a} the magnitude of the anodic current density and j_{c} the magnitude of the cathodic current density. Insert Equation 9-12 into Equation 9-13 and we have:

Equation 9-14:

$$j_{\mathrm{m}} = j_0 e^{\left(\frac{\alpha z F \eta_p}{RT}\right)} - i_0 e^{\left(\frac{(1-\alpha) z F \eta_p}{RT}\right)}$$

Equation 9-14 is known as the Butler-Vomer equation and is an important equation, as it indicates the relationship between the current measured experimentally and the level of polarisation in the electrochemical cell. This relationship can be expressed in other forms that can be useful for experimental techniques:

For a specific temperature and reaction, we can group the following constants together into one symbol:

Equation 9-15:

$$\boldsymbol{A'_a = \frac{\alpha z F}{RT}}$$

Equation 9-16:

$$\boldsymbol{A'_c = \frac{(1-\alpha) z F}{RT}}$$

Then introduce Equation 9-15 and Equation 9-16 into Equation 9-12 for the cathodic and anodic current densities, respectively:

Equation 9-17:

$$\boldsymbol{j_a = i_0 e^{(A'_a \eta_p)}}$$

Equation 9-18:

$$\boldsymbol{j_c = i_0 e^{(A'_c \eta_p)}}$$

Taking natural logarithms and then converting to base 10 logarithm:

Equation 9-19:

$$\log_{10}\left(\frac{j_a}{j_0}\right) = \beta_a \eta_p$$

Where $\beta_{\mathrm{a}} = \frac{2.303}{\mathrm{A}'_a}$, which accounts for the change from natural to base 10 logarithm. Thus, we now have the following important result for the anodic process, which can be written in linear form ($y = mx + c$):

Equation 9-20:

$$\eta_{p_a} = \beta_{\mathrm{a}} \log_{10} j_{\mathrm{a}} - \log_{10} j_0$$

For the cathodic process, $\beta_{\mathrm{c}} = \frac{2.303}{\mathrm{A}'_c}$:

Equation 9-21:

$$\eta_{\mathrm{p_c}} = \beta_{\mathrm{c}} \log_{10} i_c - \log_{10} i_0$$

Equation 9-20 and Equation 9-21 are known as the Tafel equations for the anodic and cathodic processes, respectively. If we plot these linear equations (see Figure 9-1), we can see the theoretical anodic and cathodic processes and how these lines intersect at the exchange current density, when there is zero polarisation:

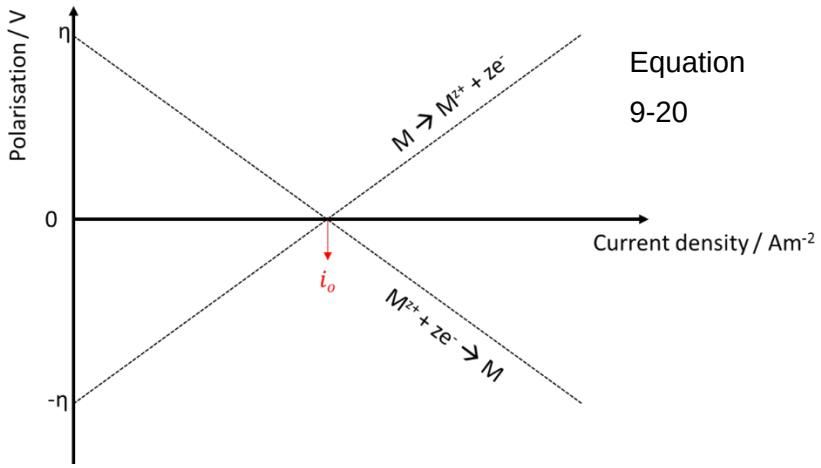

Figure 9-1 – Graph of Equation 9-20 and Equation 9-21: Theoretical Tafel equations for the anodic and cathodic currents.

The theoretical Tafel plots cannot be measured experimentally as the anodic and cathodic current densities cannot be measured separately in an electrochemical cell. Instead, the experimentally measured current is the total current, which is the sum of the anodic and cathodic currents. Thus, if we replace Equation 9-13 into Equation 9-20, and with some minor re-arrangement, we get the following:

Equation 9-22:

$$\boldsymbol{\eta_{p_a} = \beta_a ln\left(\frac{i_{meas} + i_c}{i_0}\right)}$$

9.1.3.4 Pourbaix Diagram

Using some of the corrosion properties of a specific metal, we can construct a predictive diagram that can give us information on how a metal behaves, from an electrochemical point of view, when potential and pH are changed, for a specific electrolyte, and temperature and pressure conditions. This is called the Pourbaix diagram, and can be used to understand whether a metal may corrode, passivate or be immune to corrosion [63].

The Pourbaix diagram (see Figure 9-2) is another useful tool for practical electrochemistry and as guidance for engineers wanting to understand what kind of materials they can use for their specific applications and conditions.

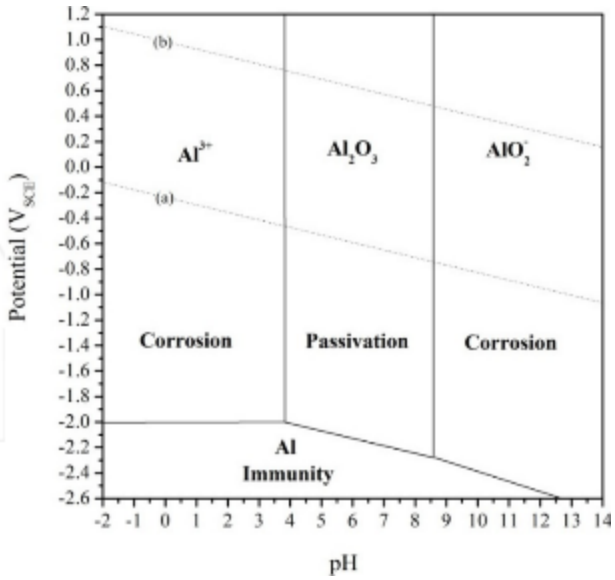

Figure 9-2 - Pourbaix Diagram of Aluminium [69].

9.2 Appendix B: Material Characterisation

9.2.1 Surface profiles by variable focus optical microscope.

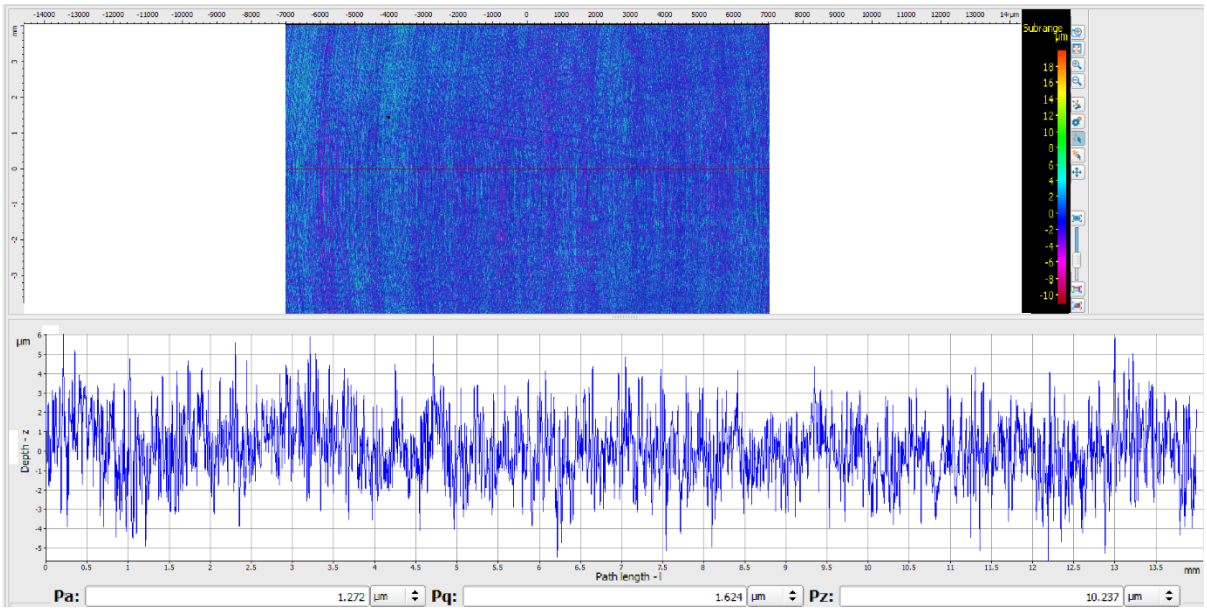

Figure 9-3 - Primary profile of Baseline in L direction. From variable focus optical microscope

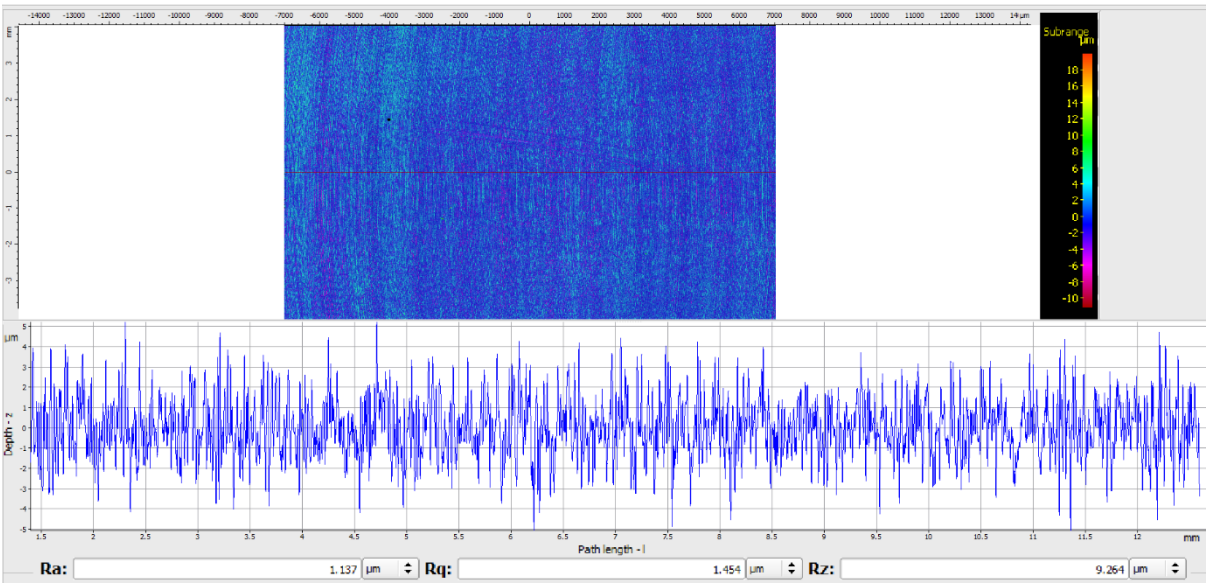

Figure 9-4 - Roughness profile of baseline in L direction. From variable focus optical microscope

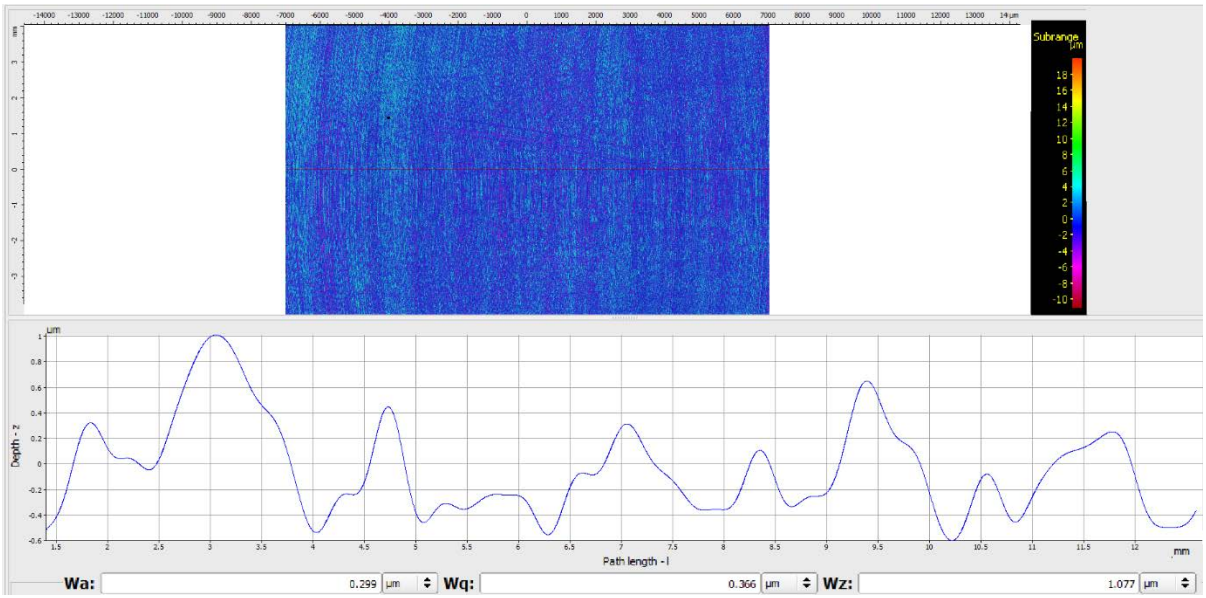

Figure 9-5 - Waviness profile of baseline in L direction. From variable focus optical microscope.

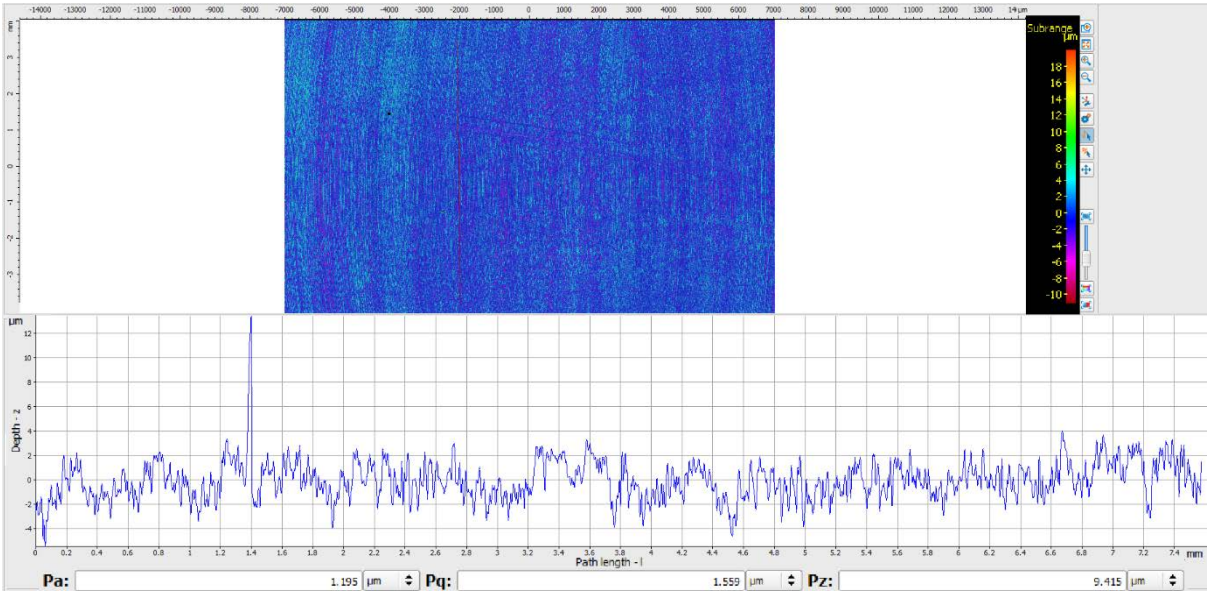

Figure 9-6 – Primary profile of baseline in LT direction. From variable focus optical microscope.

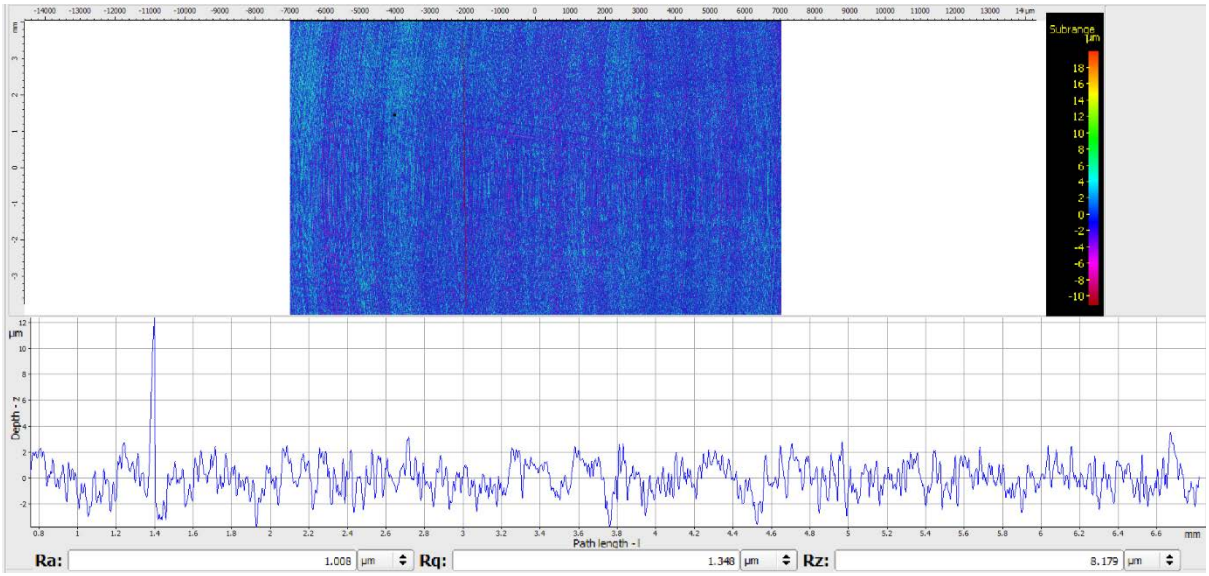

Figure 9-7 - Roughness profile of baseline in LT direction. From variable focus optical microscope.

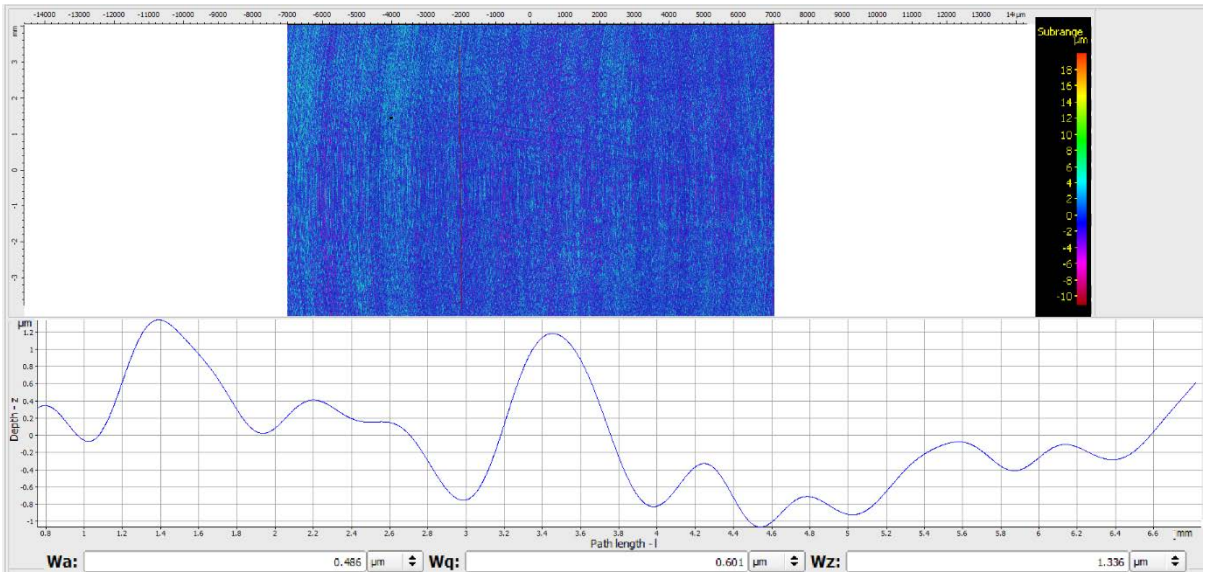

Figure 9-8 - Waviness profile of baseline in LT direction. From variable focus optical microscope.

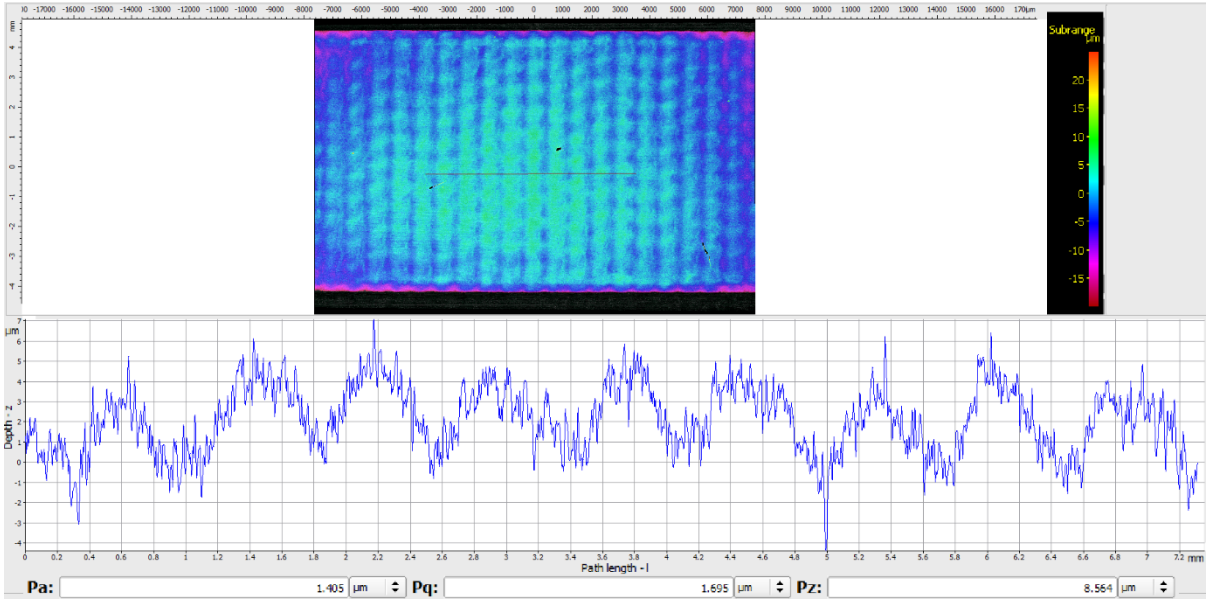

Figure 9-9 - Primary profile of LSP in L direction. From variable focus optical microscope.

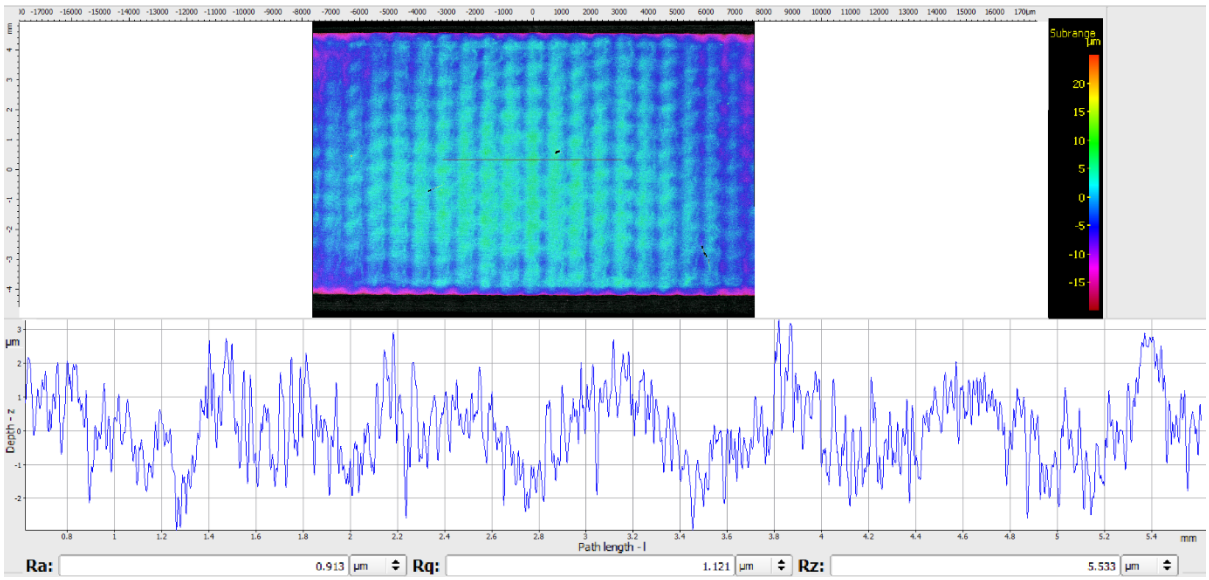

Figure 9-10 - Roughness profile of LSP in L direction. From variable focus optical microscope.

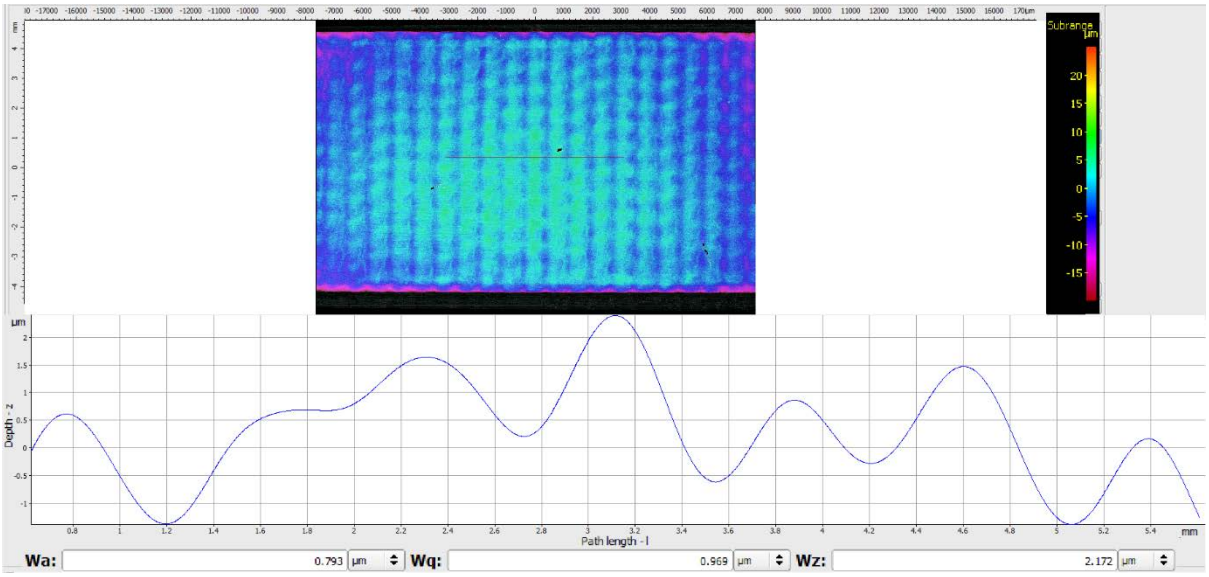

Figure 9-11 - Waviness profile of LSP in L direction. From variable focus optical microscope.

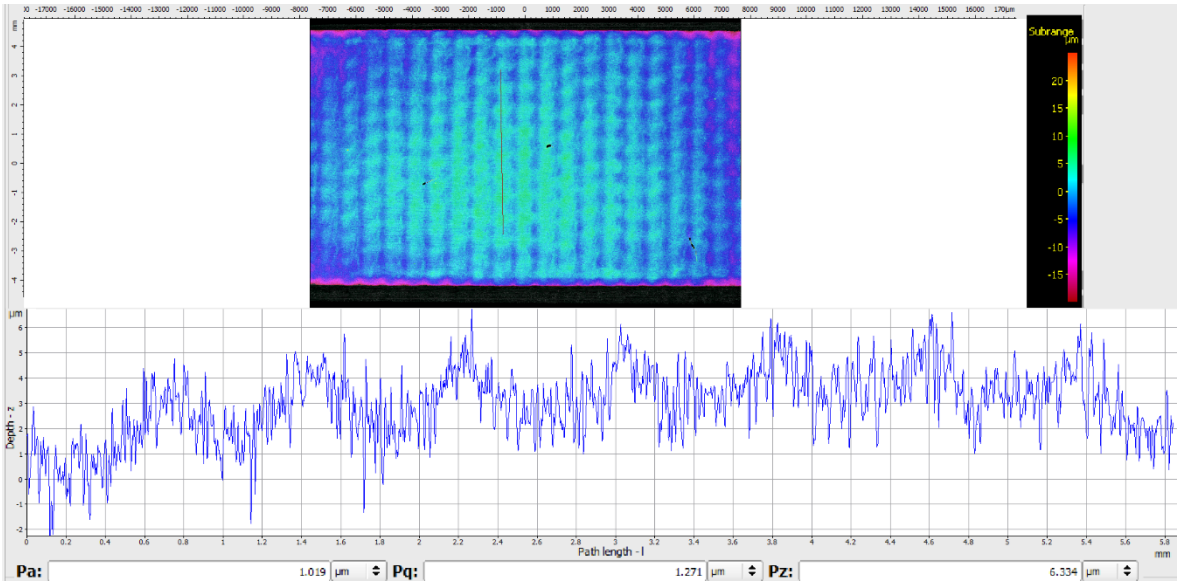

Figure 9-12 - Primary profile of LSP in LT direction. From variable focus optical microscope.

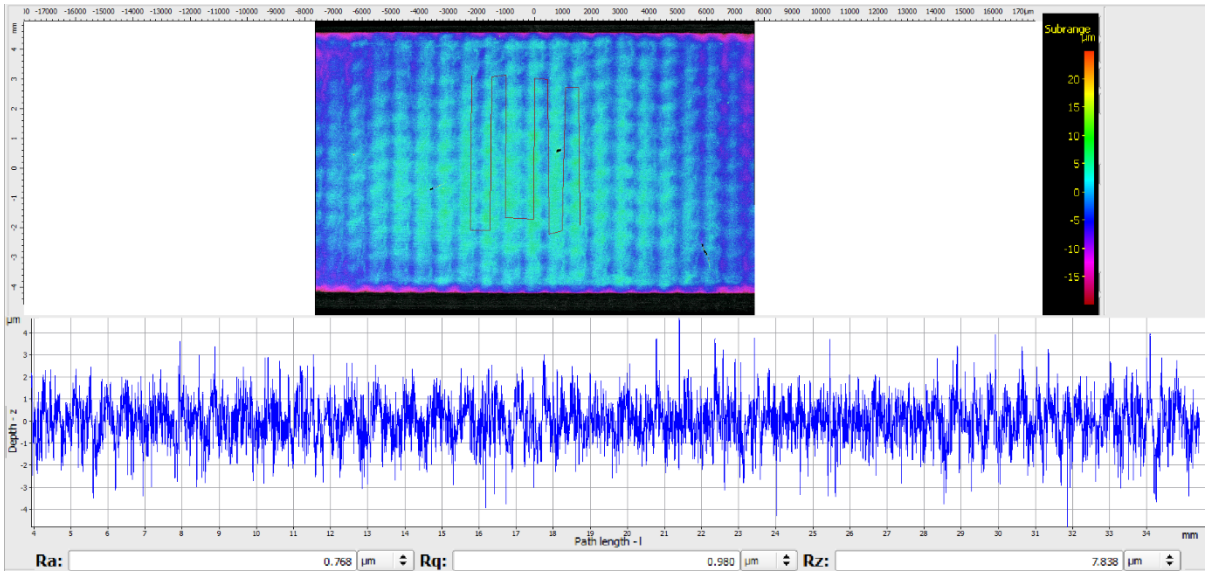

Figure 9-13 - Roughness profile of LSP in LT direction. From variable focus optical microscope.

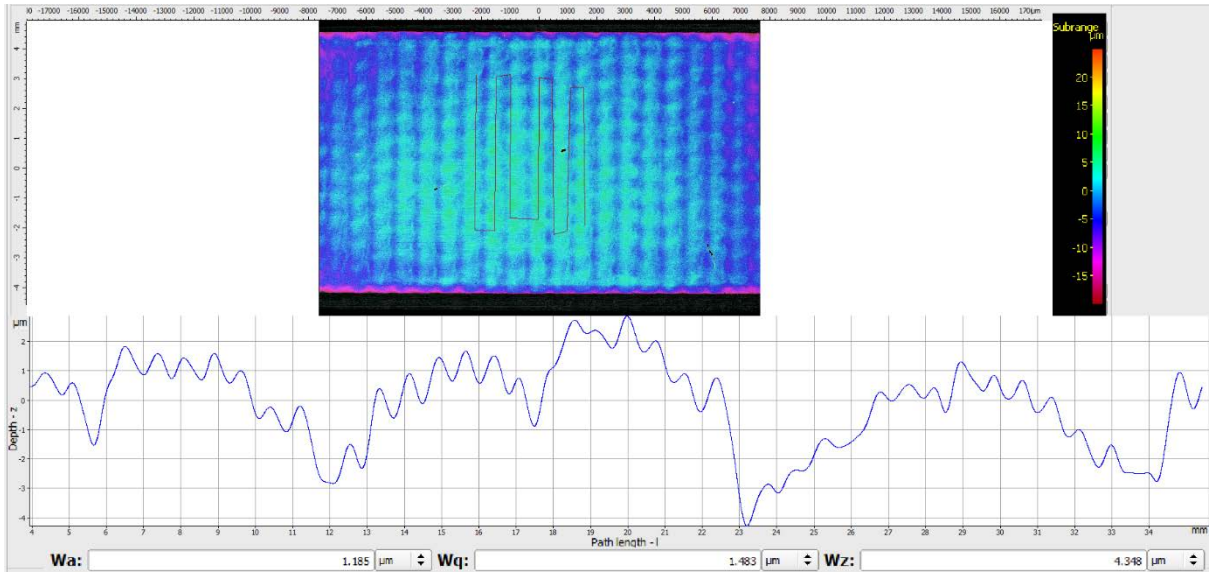

Figure 9-14 - Waviness profile of LSP in LT direction. From variable focus optical microscope.

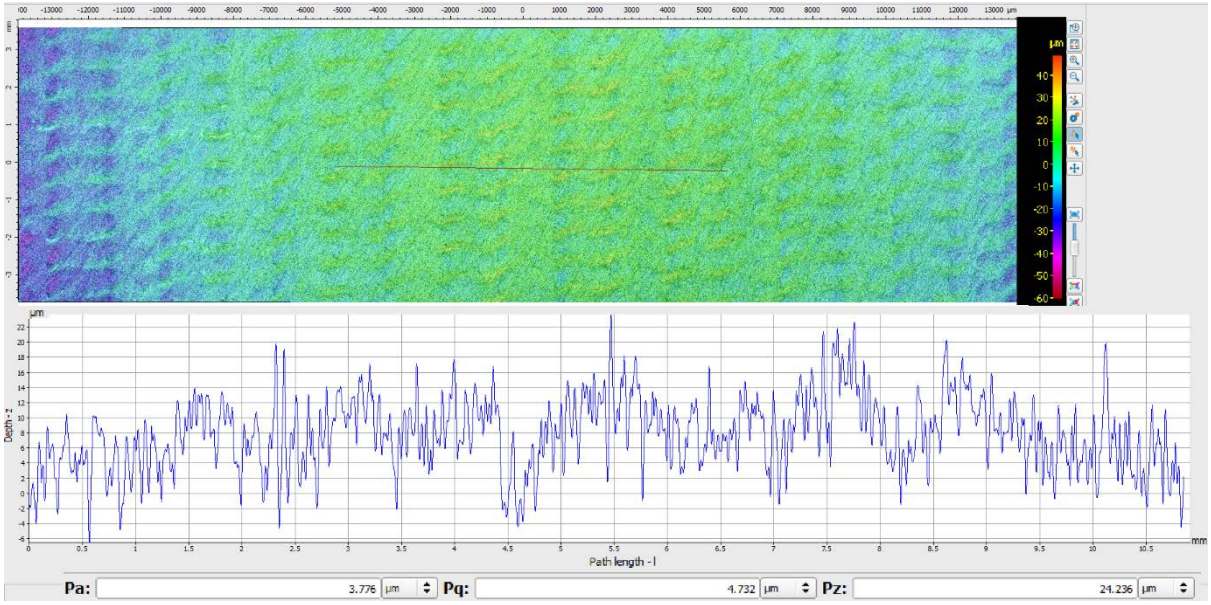

Figure 9-15 - Primary profile of LSPwC in L direction. From variable focus optical microscope.

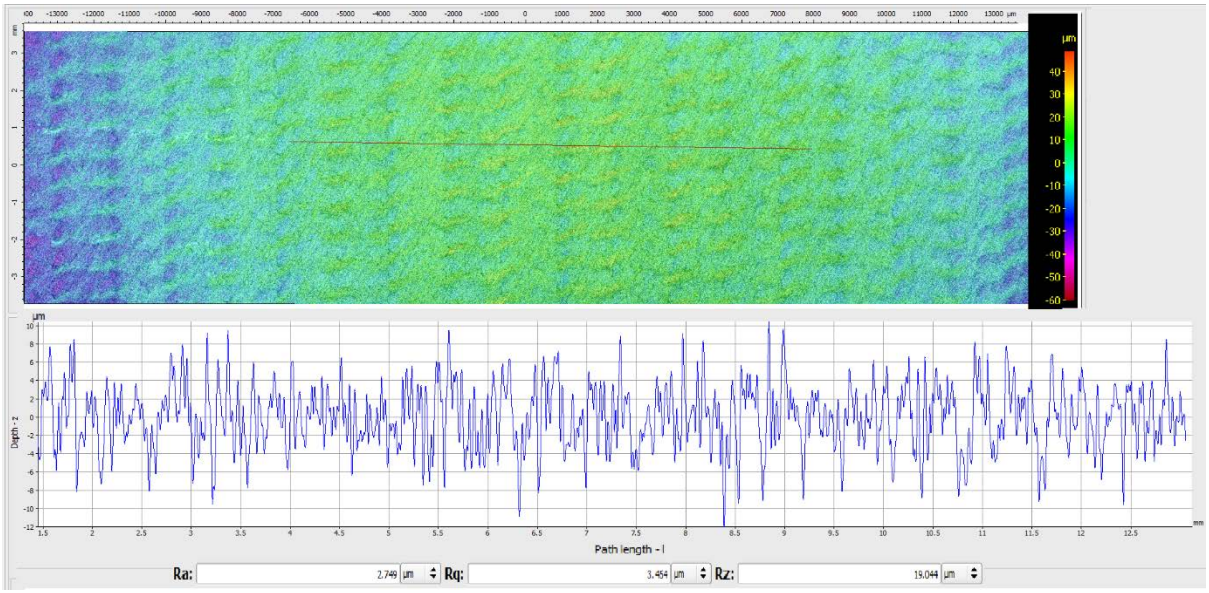

Figure 9-16 – Roughness profile of LSPwC in L direction. From variable focus optical microscope.

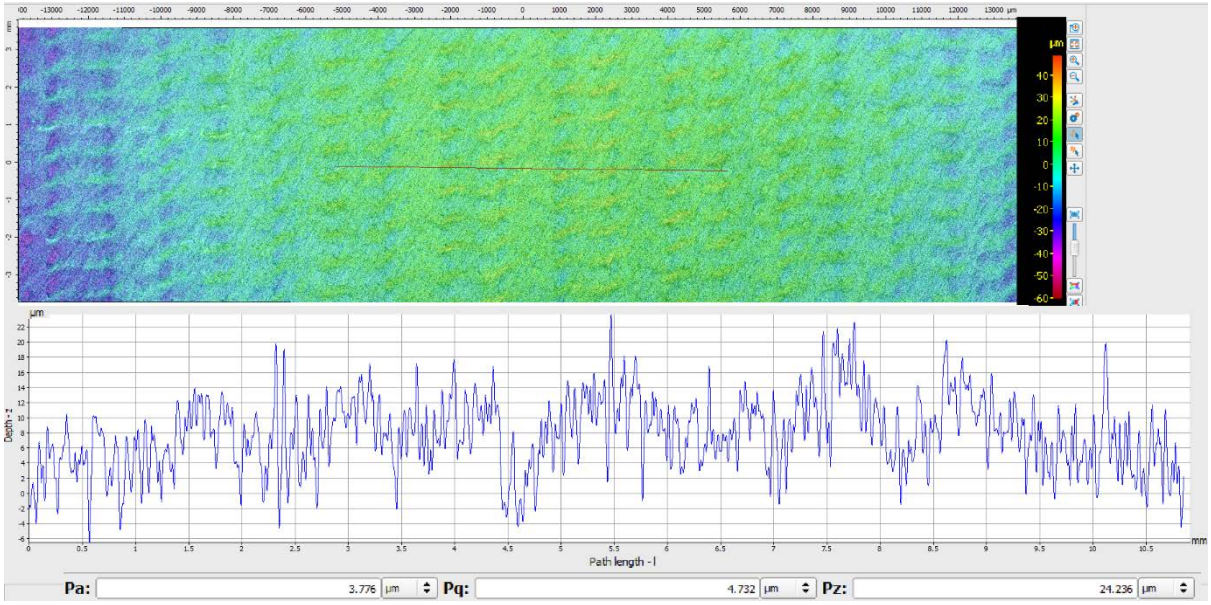

Figure 9-17 - Waviness profile of LSPwC in L direction. From variable focus optical microscope.

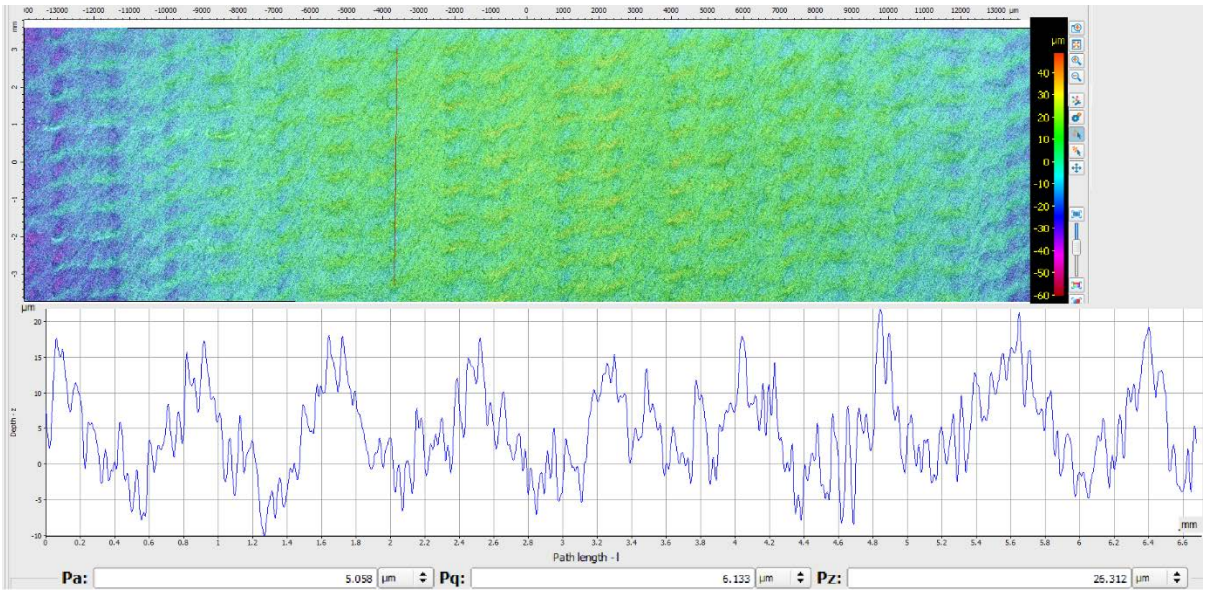

Figure 9-18 - Primary profile of LSPwC in LT direction. From variable focus optical microscope.

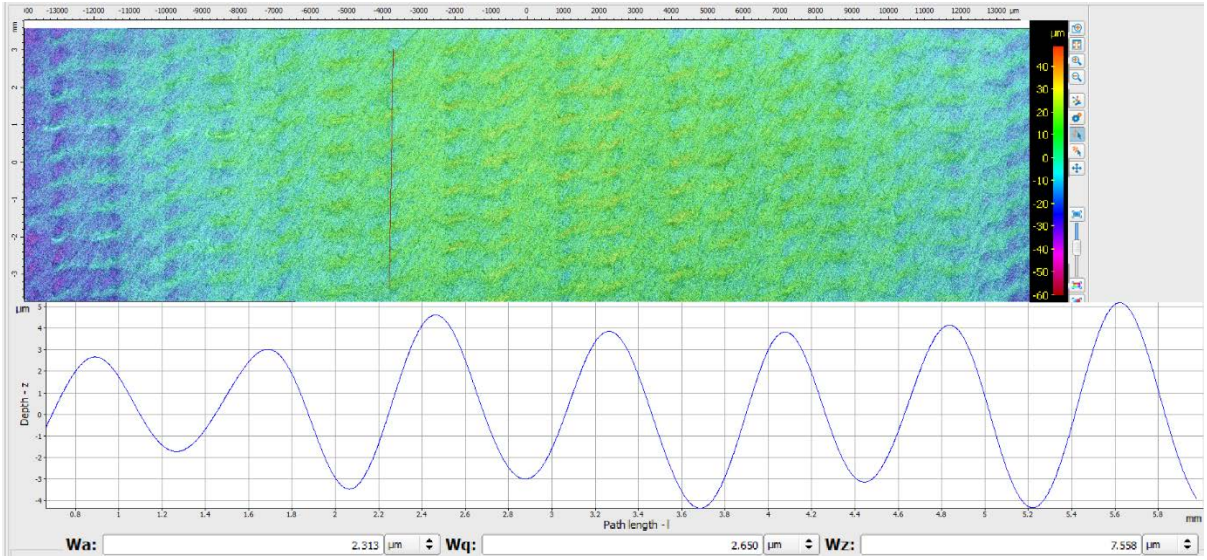

Figure 9-19 - Waviness profile of LSPwC in LT direction. From variable focus optical microscope.

9.2.2 Appendix C: Computed tomography work

9.2.2.1 Programme code

The code imports an image sequence that already has thresholded features (this would be pits and any other features of similar greyscale, e.g. porosity, noise, artefacts) and removes all features that do not have at least one pixel at 0 – 10 µm from the surface.

Table 9-1 – Python code to remove features that are not pits.

```
from PIL import Image
import os, glob
import numpy as np

def load_image_sequence(path):
	#path is the name of the folder containing the image stack (as a stack of tiffs)
	stack_string=[]
	for tif in glob.glob("{0}*.tif".format(path)):
		stack_string.append(tif)

	stack_string.sort()

	stack_list=[]
	for tif in stack_string: #loads each tif in stack as a numpy array of grey values
		temp = Image.open(tif)
		stack_list.append(np.array(temp))
		temp.close()
	stack=np.dstack(stack_list)
	return stack

def save_as_im_sequence(a_stack,dir='./'):
	for i in range(np.shape(a_stack)[2]):
		slice = a_stack[:,:,i]
		result = Image.fromarray(slice)
		result.save('{0}/{1}.tif'.format(dir,i))
```

```
path = './coloured_pits/' #coloured pits is an image where each connected objected has a unique grey value

I = load_image_sequence(path) # I is an array representing the image (the data you have loaded)

no_pits=np.max(I) #One max number (prior to loop)

good_pits = np.zeros(np.shape(I)) #shape of path (coloured pits) but only zeroes

for p in range(1,no_pits+1): #start loop, from 1 to last pit greyvalue (have to use +1)
   print(no_pits-p)              #This is just to keep tracking of what's going on, not part of fundamental code
   indxs = np.where(I==p)     #For pit in loop, find which coordinates have greyvalue p (P happens to be whatever p we are at the loop)
   ys = indxs[0]                #Creating variable with only y coordinates of pixels which have grey value p
   if np.min(ys)<=10: #change this value to determine distance from surface cut off. min is to find the min y coordinate of all the pixels with grey value p
      good_pits[I==p]=255  #Fill in good_pits with value 255 in coordinates of the pit (which is p loop) given it has past above test.

save_as_im_sequence(good_pits.astype('uint8'),dir='./good_pits/')
```

9.2.2.2 XRD measurements in LT direction

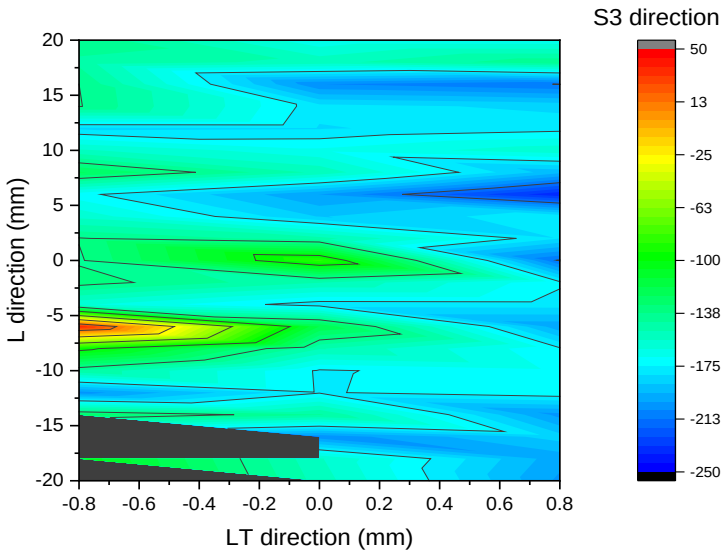

Figure 9-20 – XRD measurements of LSP residual stress in the transverse (S_3) direction.

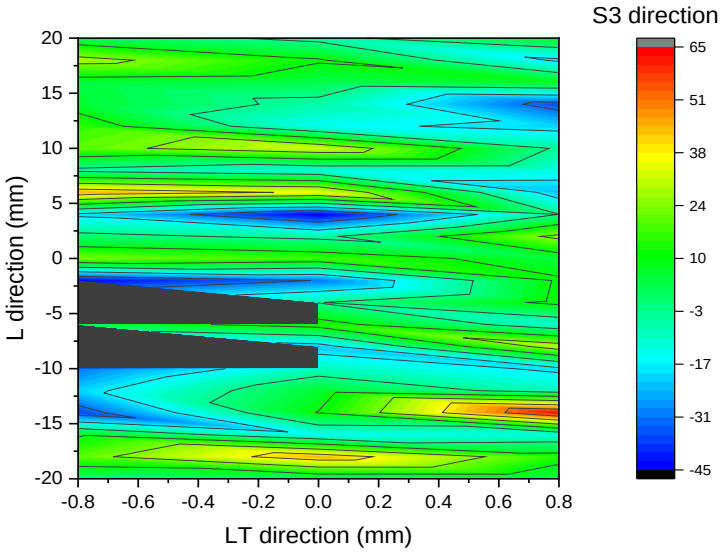

Figure 9-21 - XRD measurements of LSPwC residual stress in the transverse (S_3) direction.

9.2.2.3 Data location

All samples are located in the nCATS laboratory, in desiccators and boxes labelled ‘Alvaro Sanchez’. Table 9-2 lists the type and number of samples available. All test data, including CT scans, are available in a selected hard drive given to Professor Philippa Ann Reed. Some of the available laser peened samples are not only from the CSIR, but also from the HiLASE Centre, an institute belonging to the Czech Academy of Sciences. In addition, there are small and large samples of untreated AA7037-T7452, an alloy of interest at the start of the project which was supplied by Airbus.

Table 9-2 – List of material, sample type and numbers.

Material	Number	Number	Comments
AA7075-T651 CSIR	Baseline Type A	+10	
	LSP Type A	4	
	LSPwC Type A	7	
	LSP Type B	+20	
	LSPwC Type B	+25	
	Baseline Type C	1	Polished to 1µm
	LSP Type C	1	
	LSPwC Type C	2	One pre-corroded
AA7075-T651 HiLASE	LSP Type A 2.5 GW cm^{-2}	5	
	LSP Type A 4 GW cm^{-2}	4	Two tested by IP student Tom Buckingham.
	LSP Block 2.5 GW cm^{-2}	1	Block – from which +30 Type B samples can be removed
	LSP Type B 4 GW cm^{-2}	+20	Block was cut: Several tested performed by IP student Freeman Kong
AA7037-T7452	Component sections	4	Large component blocks
	Baseline Type A	8	